

Multiscale design of bioadhesive platforms for next-generation applications in surgery and healthcare

by

Sarah J. Wu

B.S., Mechanical Engineering
Massachusetts Institute of Technology, 2019

S.M., Mechanical Engineering
Massachusetts Institute of Technology, 2021

Submitted to the Department of Mechanical Engineering
in partial fulfillment of the requirements for the degree of

Doctor of Philosophy in Mechanical Engineering

at the

MASSACHUSETTS INSTITUTE OF TECHNOLOGY

September 2024

©2023 Sarah J. Wu. This work is licensed under a [CC BY-SA 2.0](https://creativecommons.org/licenses/by-sa/2.0/). The author hereby grants to MIT a nonexclusive, worldwide, irrevocable, royalty-free license to exercise any and all rights under copyright, including to reproduce, preserve, distribute and publicly display copies of the thesis, or release the thesis under an open-access license.

Authored by: Sarah J. Wu
Department of Mechanical Engineering
August 8, 2024

Certified by: Xuanhe Zhao
Professor of Mechanical Engineering, Thesis Supervisor

Authored by: Nicolas Hadjiconstantinou
Chairman, Department Committee on Graduate Theses

Multiscale design of bioadhesive platforms for next-generation applications in surgery and healthcare

by

Sarah J. Wu

Submitted to the Department of Mechanical Engineering on August 8, 2024
in partial fulfillment of the requirements for the degree of

Doctor of Philosophy in Mechanical Engineering

Abstract

Bioadhesives—materials capable of adhering to biological tissues—hold significant promise as transformative tools in healthcare, offering the ability to repair tissues with ease and minimal damage. These materials present numerous opportunities in surgery and human-machine interfaces, creating a broad landscape of applications that has captivated clinical and scientific interest alike. Still, there remain open challenges surrounding their reliability, biocompatibility, usability, and versatility. These include weak adhesion with wet tissues, foreign body response, cumbersome application processes, and limited customizability. This dissertation presents a multiscale framework for addressing these obstacles, encompassing design strategies on the molecular, polymer network architecture, macroscale device, and application process levels. The implementation of this framework is demonstrated through the development of two pioneering bioadhesive platforms: (1) a multifunctional patch for minimally invasive surgery, and (2) a 3D printable bioadhesive for fabricating tunable, application-specific devices. Together, these platforms expand the design space for creating robust and versatile tissue repair solutions and biomedical devices.

Thesis Committee

Xuanhe Zhao, PhD
Committee Chair
Professor of Mechanical Engineering, MIT

Elazer R. Edelman, MD, PhD
Edward J. Poitras Professor of Medical Engineering & Science, MIT
Professor of Medicine, Harvard Medical School

Ellen T. Roche, PhD
Associate Professor of Mechanical Engineering and Medical Engineering & Science, MIT

Acknowledgements

To be sitting here (at a river-facing window in Hayden Library) writing the acknowledgements for my PhD thesis feels nothing short of surreal. After five years in the Soft Active Materials Lab, nine years total at MIT, thousands of treks through the Infinite Corridor, countless nights in the Stud, and a handful of tent parties, I've emerged at last with a coffee dependency and a dissertation. For the latter, I have many people to thank.

My thesis supervisor, Prof. Xuanhe Zhao: for his colossal support and belief in me, and his infectious passion to make “grand societal impacts.”

My thesis committee, Prof. Elazer Edelman and Prof. Ellen Roche: for their wealth of insights over the years. Elazer, for pioneering research in this field and challenging me to consider all the complexities of tissue adhesion. Ellen, for serving as a mentor since the 2.009 days and making this thesis more practical.

Everyone in the SAMs lab: for being the people I talked to and worked with daily over the past five years. What a journey it has been. Hyunwoo, for teaching me much of what I know about materials, adhesion, and rabbits. Heejung, for being a diligent collaborator and, more importantly, a kindhearted friend. Shucong, for being a trustworthy source of advice (in all realms of research and life). Jaehun, Chase, and Bastien, for keeping the lab from blowing up! Thanks also to Christina, John, and Morgan for making sure we always got the supplies we needed, cakes included.

The team at BWH (Dr. Raphael Bueno, Dr. Blair Marshall, Dr. Robert Padera, Dr. Ahmed Sadek, and Lori Foley): for working so hard to bring my adhesives to new levels with the pig studies.

Dr. Christoph Nabzdyk: for providing the valuable clinical expertise which inspired the minimally invasive tissue sealing patch, and for always offering to discuss ideas, even amid busy nights at the hospital.

Prior to becoming a graduate student, I was fortunate to learn from an extraordinary cast of role models who mentored me throughout my earlier years at the Institute.

Prof. Seok-Hyun Yun and Dr. Sheldon Kwok: for three unforgettable years working on the Cell Laser project. Sheldon, for telling me I should apply for a PhD (and setting a very high standard for what it means to do one).

Prof. Bob Langer, Dr. Giovanni Traverso, and Dr. Farhad Javid: for generously giving a wide-eyed freshman a shot at mechanical design and research.

Prof. Doug Lauffenburger and Dr. Shannon Hughes: for teaching me how to ask and answer scientific questions.

And long before that, my kindergarten and second grade teachers, Miss Takamoto and Ms. Rumi: for nurturing my curiosity and making learning fun.

Last but not least, my friends and family: for making life enjoyable and meaningful. My mom, for being the first to help me through any issue, big or small. My dad (the original Dr. Wu), for teaching me to appreciate the finer things in life, including the Red Sox, IPAs, and good engineering. And my sister, Chloe, for being my lifelong confidante, role model, and best friend.

Contents

Abstract.....	2
Acknowledgements.....	1
List of Figures.....	7
1. Introduction.....	10
1.1. Significance of bioadhesives in surgery and healthcare.....	10
1.2 Scope of the thesis.....	11
1. Strategies and challenges for tissue adhesion.....	13
2.1. Tissue adhesion mechanics.....	13
2.1.1. Design strategies for interfacial linkages.....	15
2.1.2. Design strategies for energy dissipation.....	19
2.1.3. Energy dissipation in the tissue.....	21
2.2. Biological challenges.....	21
2.2.1. Adhesion in a wet environment.....	22
2.2.2. Dynamic movement.....	23
2.2.3. Immune response and allergies.....	24
2.2.4. Bacterial activity.....	24
2.2.5. Mechanical mismatch.....	25
2.2.6. Difficulty of access.....	25
2.2.7. Biodegradability, clearance, and removability.....	27
2.3. Experimental methods.....	28
2. Minimally invasive tissue sealing (MITS) patch.....	31
3.1. Overview.....	31
3.1.1. Clinical motivation.....	31
3.1.2. Proposed solution.....	31
3.2. Material design.....	32
2.2.1. Bioadhesive material.....	32
2.2.2. Hydrophobic fluid.....	34
2.2.3. Antifouling material.....	34
3.3. Patch architecture design.....	37
3.3.1. Thermodynamic conditions.....	38
3.4. Methods and results.....	41

3.4.1. Preparation of the multilayer patch	41
3.4.2. Adhesion characterization	42
3.4.3. Mechanical properties.....	46
3.4.4. Antifouling Performance	48
3.4.5. Biocompatibility and biodegradation	52
3.5. Design for minimally invasive surgical applications	55
3.5.1. Origami-inspired approach	55
3.5.2. Balloon catheter-based delivery	56
3.5.3. Stapler-based delivery	57
3.5.4. Ex vivo demonstrations	58
3.6. Discussion	61
3. Preclinical study: Minimally invasive bronchopleural fistulae	62
4.1. Overview	62
4.1.1. Clinical motivation	62
4.1.2. Current challenges	62
4.1.3. Proposed solution	63
4.2. Methods and results.....	63
4.2.1. Bioadhesive patch.....	63
4.2.2. Animal model	64
4.2.3. Study results	68
4.3. Discussion	70
4. Three-dimensional printing of bioadhesives	74
5.1. Overview	74
5.1.1. Clinical motivation	74
5.1.2. Proposed solution	74
5.2. Methods and results.....	76
5.2.1. Material design	76
5.2.2. Mechanical tunability	83
5.2.3. Biocompatibility and biodegradability	85
5.2.4. In vivo defect repair.....	88
5.2.5. Detailed methods	93
5.3. Bio-integrated device fabrication.....	100

5.3.1. Bioelectronic patch	101
5.3.2. Drug delivery patches	101
5.4. Discussion	103
5. Future landscape of bioadhesive technology.....	104
6.1. Bioadhesive bioelectronics.....	107
6.2. Bioadhesive chemical biosensors.....	108
6.2.1 Epidermal biochemical sensors	109
6.2.2. Intraoral biochemical sensors	109
6.2.3. Ocular biochemical sensors	110
6.3. Bioadhesive drug delivery.....	110
6.5. Bioadhesive photonic devices	112
6.6. Bioadhesive ultrasound	112
6.4. Bioadhesive mechanical support.....	113
6.7. Bioadhesive thermal stimulators	114
6.8. Other practical considerations	118
6.8.1. Human factors.....	119
6.8.2. Cost and Complexity	120
6.8.3. Purification and sterilization.....	120
6.8.4. Shelf stability	120
6.8.5. Sustainability	120
6. Concluding remarks.....	122
7. References	123

List of Figures

Figure 1-1. Traditional and emerging bioadhesive applications.....	11
Figure 2-1. Design strategies for tissue adhesion	14
Figure 2-2. Key considerations related to the biological environment.....	22
Figure 2-3. General advantages and disadvantages of various bioadhesive form factors	27
Figure 2-4. Experimental test setups for evaluating adhesion performance.....	30
Figure 3-1. Schematic of the minimally invasive tissue sealing (MITS) patch.....	32
Figure 3-2. Chemical structures of poly(acrylic acid) and chitosan.	33
Figure 3-3. PAA-NHS ester reaction scheme.	33
Figure 3-4. Antifouling properties of zwitterionic materials	35
Figure 3-5. Fabrication strategy for producing a zwitterionic polymer-interpenetrated polyurethane film.....	36
Figure 3-6. Scanning electron micrographs (SEMs) of the microtextured bioadhesive surface ..	38
Figure 3-7. 3D reconstruction of confocal micrographs.	38
Figure 3-8. Schematics of the wetting configurations for a system comprising air, the bioadhesive substrate, silicone oil, blood, and tissue.....	39
Figure 3-9. Schematic of the combined blood-repelling and adhesion mechanism	40
Figure 3-10. Blood resistance of the liquid-infused patch.....	42
Figure 3-11. Characterization of blood repellence and adhesion performances of the multilayer patch under varying applied pressures.....	43
Figure 3-12. Representative images for the quantification of blood entrapment	44
Figure 3-13. Shear stress vs. displacement curves.....	44
Figure 3-14. Experimental setup for the adhesion characterization of the multilayer patch and tissues submerged in blood.	45
Figure 3-15. Comparison of adhesion performances of the multilayer patch and various commercially-available tissue adhesives.	46
Figure 3-16. Mechanical characterization of the composite patch.	47
Figure 3-17. Engineering stress vs. stretch curves for the zwitterionic-interpenetrated polyurethane layer and a pure zwitterionic hydrogel.....	48
Figure 3-18. Fracture toughness of a pure zwitterionic hydrogel and the zwitterionic-interpenetrated elastomer layer.....	48

Figure 3-19. FTIR spectra of the zwitterionic layer and unmodified pristine hydrophilic PU.....	49
Figure 3-20. In vitro biocompatibility of the MITS patch.....	51
Figure 3-21. In vitro fibrin deposition	51
Figure 3-22. In vivo biocompatibility.....	53
Figure 3-23. <i>In vivo</i> inflammation scoring	54
Figure 3-24. <i>In vivo</i> stability.....	54
Figure 3-25. Photographs showing the multilayer patch in the plastically-deformable dry glassy state	55
Figure 3-26. Folding schematic for a triangular sleeve and a pleated cylindrical sleeve with “wings” for integrating the bioadhesive patch with a balloon catheter	56
Figure 3-27. Photographs showing the deployment mechanism using an esophageal balloon catheter.....	57
Figure 3-28. Folding schematic for integration with a surgical stapler.....	58
Figure 3-29. Photographs showing the deployment mechanism of the MITS patch using an articulating linear stapler.....	58
Figure 3-30. <i>Ex vivo</i> demonstrations of minimally invasive delivery and application of the multilayer bioadhesive patch by balloon catheters	60
Figure 3-31. <i>Ex vivo</i> demonstrations of minimally invasive delivery and application of the multilayer bioadhesive patch using a surgical stapler.....	61
Figure 4-1. Schematic of bioadhesive patch and application	64
Figure 4-2. Endoscopic footage of defect creation and patch placement.	66
Figure 4-3. Burst pressure measurement setup for the dissected trachea specimen	67
Figure 4-4. Histological images of subcutaneous tissue 14 days after implantation of the bioadhesive	69
Figure 4-5. Partially degraded bioadhesive patch adjacent to tracheal defect.....	70
Figure 4-6. Outcomes of the animal study.....	72
Figure 5-1. Fabrication and adhesion of the 3D printable bioadhesive	75
Figure 5-2. Representative stress-strain curves of samples prepared using varying ratios of PU-PAA to PU in the 3D printing ink.....	76
Figure 5-3. Synthesis and material characterization of the 3D printable tissue adhesive.....	77

Figure 5-4. Images of the synthesized PU-PAA material and solutions of varying polymer content.....	78
Figure 5-5. Shelf stability of the PU-PAA polymer	78
Figure 5-6. FTIR spectra for materials prepared using different precursor compositions.....	79
Figure 5-7. ¹ H NMR spectra for PU-PAA prepared using varying precursor ratios of acrylic acid (AA) and PU	80
Figure 5-8. Swelling of the printed tissue adhesive material.....	81
Figure 5-9. Swelling of an adhered 3D printed mesh.	81
Figure 5-10. Adhesion performance and mechanical tunability of the 3D printable tissue adhesive.....	82
Figure 5-11. Representative burst pressure curves of 3D printed patches with and without backing layer.....	83
Figure 5-12. Representative stress-strain curves for 3D printed samples with varying gap width to filament diameter ratios	84
Figure 5-13. Representative stress-strain curves for 3D printed samples with different alignment angles between filaments	85
Figure 5-14. In vitro biocompatibility.	86
Figure 5-15. Biocompatibility and sutureless repair of defects in rat models	86
Figure 5-16. In vitro degradation of PU-PAA	87
Figure 5-17. In vivo wound sealing of tracheal defects in rats.....	88
Figure 5-18. Micro-CT observation of tracheal healing in rats	89
Figure 5-19. In vivo wound sealing of colonic defects in rats.....	90
Figure 5-20. Liquid-infused 3D printed patches for blood-resistant tissue sealing. a, Illustrated schematic and photograph of the liquid-infused 3D printed patch.....	91
Figure 5-21. Wetting configurations and energy criteria for the liquid-infused adhesive system comprising air, the tissue adhesive material, oleic acid, and tissue.....	92
Figure 5-22. Experimental setups characterizing adhesion performance	96
Figure 5-23. Potential applications of the 3D printable tissue adhesive platform.....	102
Figure 6-1. The landscape of emerging technologies	105
Figure 6-2. Emerging applications, key properties, and examples	106
Figure 6-3. Multifaceted practical considerations of bioadhesives	119

1. Introduction

1.1. Significance of bioadhesives in surgery and healthcare

Modern medicine is impossible to imagine without the ability to repair and reconnect tissues. Since the era of ancient civilizations, humans have found innovative methods to close wounds, from using ant jaws and thorns to bone needles and intestines.^{1,2} These primitive forms of tissue closure formed the basis for surgical sutures, which continue to be regarded as the gold standard today. Despite their extensive use, sutures suffer from notable limitations. For instance, suturing is time-consuming and demands a high level of surgical skill, which is problematic in time-sensitive and anatomically complex procedures such as hemorrhagic injuries or minimally invasive surgeries. To expedite wound closure, surgical staplers were adopted throughout the late 1900s, offering rapid application and facilitating less invasive procedures.³ Nonetheless, staplers also have their share of disadvantages, including a high incidence of device malfunctions and adverse effects such as leakages and tissue tearing.^{4,5} Moreover, the pointwise, tissue-penetrative modality of both sutures and staples is intrinsically damaging to tissues and can result in poor healing.

Bioadhesives, referring to materials that can form adhesion with biological tissues, present a promising alternative to the traditional tissue attachment techniques.⁶⁻⁹ These materials offer numerous advantages, such as ease of application, minimal tissue trauma, and tissue-specific tunability. Moreover, compared to the discrete mechanical anchors provided by sutures or tacks, bioadhesives can establish conformal and intimate interfaces, positioning them as attractive tools for bridging biomedical devices with tissues.

First-generation bioadhesives, including fibrin and cyanoacrylate glues, were primarily developed for achieving hemostasis and serving as adjunctive support to surgical sutures.¹⁰⁻¹² Recent years have seen significant efforts dedicated toward improving their adhesion performance, as well as realizing advanced properties such as reversible adhesion, self-healing behavior, and electrical conductivity.¹³⁻¹⁶ Along with the development of advanced capabilities, the applications of bioadhesives have expanded beyond wound repair and tissue sealing, holding promise for diverse tissue-interfacing technologies such as electrophysiological recording and stimulation, drug delivery, mechanical modulation, and deep tissue imaging, among others (**Figure 1-1**).

Amid these exciting developments, bioadhesive technologies face many open questions and challenges. How can we design bioadhesives that work reliably in different environments, especially in the presence of biological fluids and dynamic tissue movement? What are the practical considerations of bioadhesive production to enable widespread adoption in clinical practice? How can we tailor the properties of bioadhesives to unlock their multifunctional roles in advanced biomedical applications? These and other challenges provide a stimulating, interdisciplinary research landscape for the development of bioadhesives in the years to come.

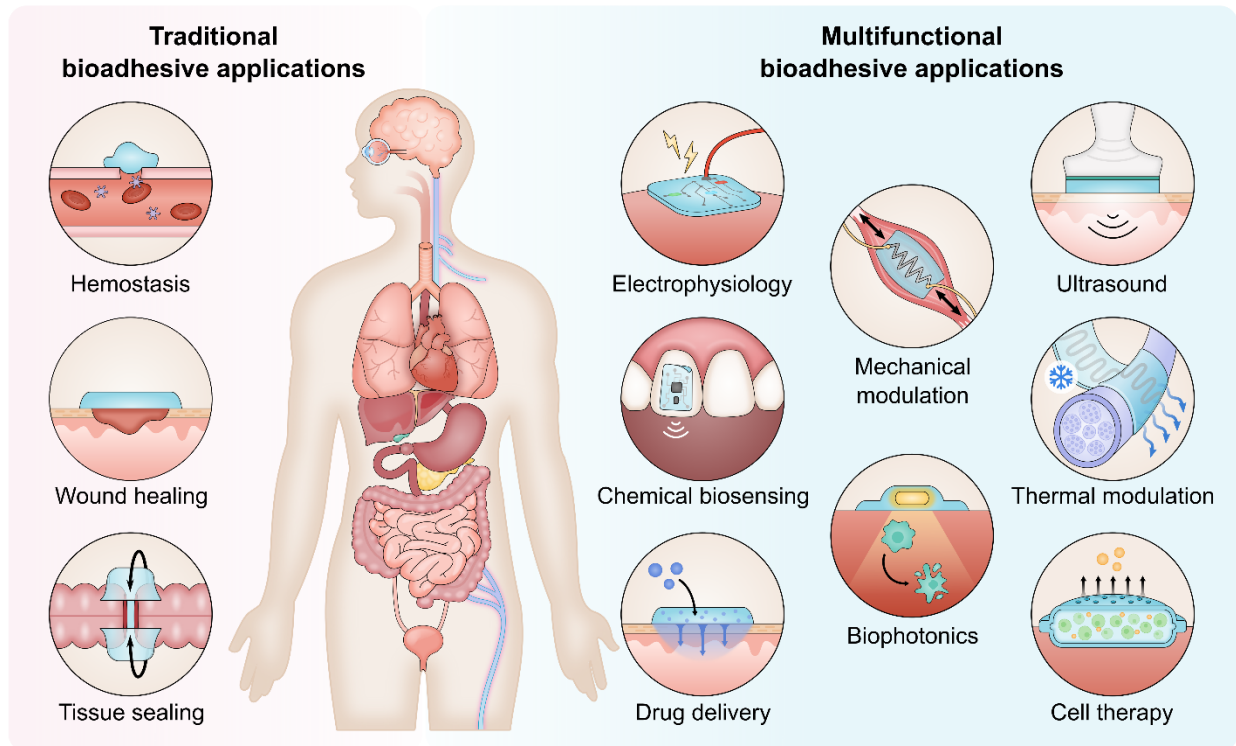


Figure 1-1. Traditional and emerging bioadhesive applications.

1.2 Scope of the thesis

The goal of this thesis is to describe a multiscale framework for developing functional and practical bioadhesive platforms by encompassing design strategies on the material, application process, and translational levels. On the molecular and polymer network scale, the incorporation of certain chemical groups or polymer network architectures can be leveraged to provide specific chemical reactivities and material properties. On the mesoscale, the structure or form factor of the bioadhesive can be considered for imparting multifunctional properties (for example, when combined with multiple materials) or specific adhesion mechanisms. On the macroscale, the manner in which the bioadhesive is combined with devices determines how it can be used in the clinic.

In the following chapter (Chapter 2), we establish a background for the fundamental mechanisms of tissue adhesion, along with design and analysis strategies. A set of the key biological challenges and limitations of bioadhesives is also summarized. Chapter 3 describes the design and development of a minimally invasive tissue sealing (MITS) patch, which features a blood-resistant liquid-infused surface to enable hemostatic tissue sealing, as well as a zwitterionic-interpenetrated backing to resist fouling. Chapter 4 focuses on a preclinical case study for minimally invasive bronchopleural fistula repair involving large animal studies. In Chapter 5, a 3D printable bioadhesive is proposed for fabricating highly tunable patches and devices. Chapter 6 provides a perspective on the potential applications of bioadhesives in technologies dedicated to monitoring, modulating, and enhancing physiological functions and pathologies. Through a systematic discussion, future design prospects and guidelines are highlighted. Additional practical

considerations underlying the usability and commercialization of bioadhesives throughout their lifecycle are also discussed.

2. Strategies and challenges for tissue adhesion

2.1. Tissue adhesion mechanics

Tissue adhesion is a complex process involving physical and chemical interactions between the bioadhesive material (the adhesive) and the biological tissue of interest (the adherend), as well as each of their bulk properties. This section outlines various guiding principles and implementation strategies for achieving tissue adhesion.

From the basis of fracture mechanics, debonding between two adhered substrates involves the initiation and propagation of a crack along the interface (adhesive failure) or in either material (cohesive failure) (**Figure 2-1**). The energy required for interfacial fracture is described by the *interfacial toughness* Γ (also called the *interfacial fracture energy* or *practical work of adhesion*), which is given by,

$$\Gamma = G_c = -\frac{dU}{dA} \quad (2.1)$$

where U is the total potential energy of the system, A is the undeformed crack area, and G_c is the critical energy release rate.¹⁷⁻¹⁹ Note that unlike tensile toughness, which is measured in units of energy per volume, the unit for interfacial toughness is energy per area, or J m^{-2} .

Most bioadhesives and biological tissues are soft materials ($10^2 \sim 10^6$ Pa in elastic modulus) which dissipate energy under deformation. The contribution of mechanical dissipation plays a large role in the resulting interfacial toughness. Quantitatively, the total interfacial toughness can be expressed as the summation of three components (**Figure 2-1a**): Γ_0 , which is the intrinsic work of adhesion due to interfacial bonds; Γ_A , the mechanical energy dissipated in the bulk adhesive; and Γ_T , the mechanical energy dissipated in the tissue.^{19,20}

$$\Gamma = \Gamma_0 + \Gamma_A + \Gamma_T \quad (2.2)$$

In view of Eqn. (2.2), tough adhesion can be achieved by incorporating strong interfacial linkages to confer a high Γ_0 , along with energy dissipation mechanisms in the bulk adhesive to increase the contribution from Γ_A . Γ_T is determined by the mechanical properties of the native tissue and is therefore less readily tunable, although it is worth noting that Γ_T may change depending on the dimensions of the adhesive-tissue interface and the amount of energy absorbed by the bioadhesive. Because Γ_0 and Γ_A can be directly adjusted by tuning interfacial or cohesive material properties, bioadhesive design is typically focused on strategies for tuning these two terms.

The strength of interfacial interactions and the mechanical properties of the bioadhesive and the tissue altogether determine the failure mode of adhesion (**Figure 2-1b**). If the bioadhesive matrix or the tissue are weak or brittle, cohesive failure in one of the substrates is likely to occur. Otherwise, failure at the interface due to disrupted interfacial linkages is the dominant mode.

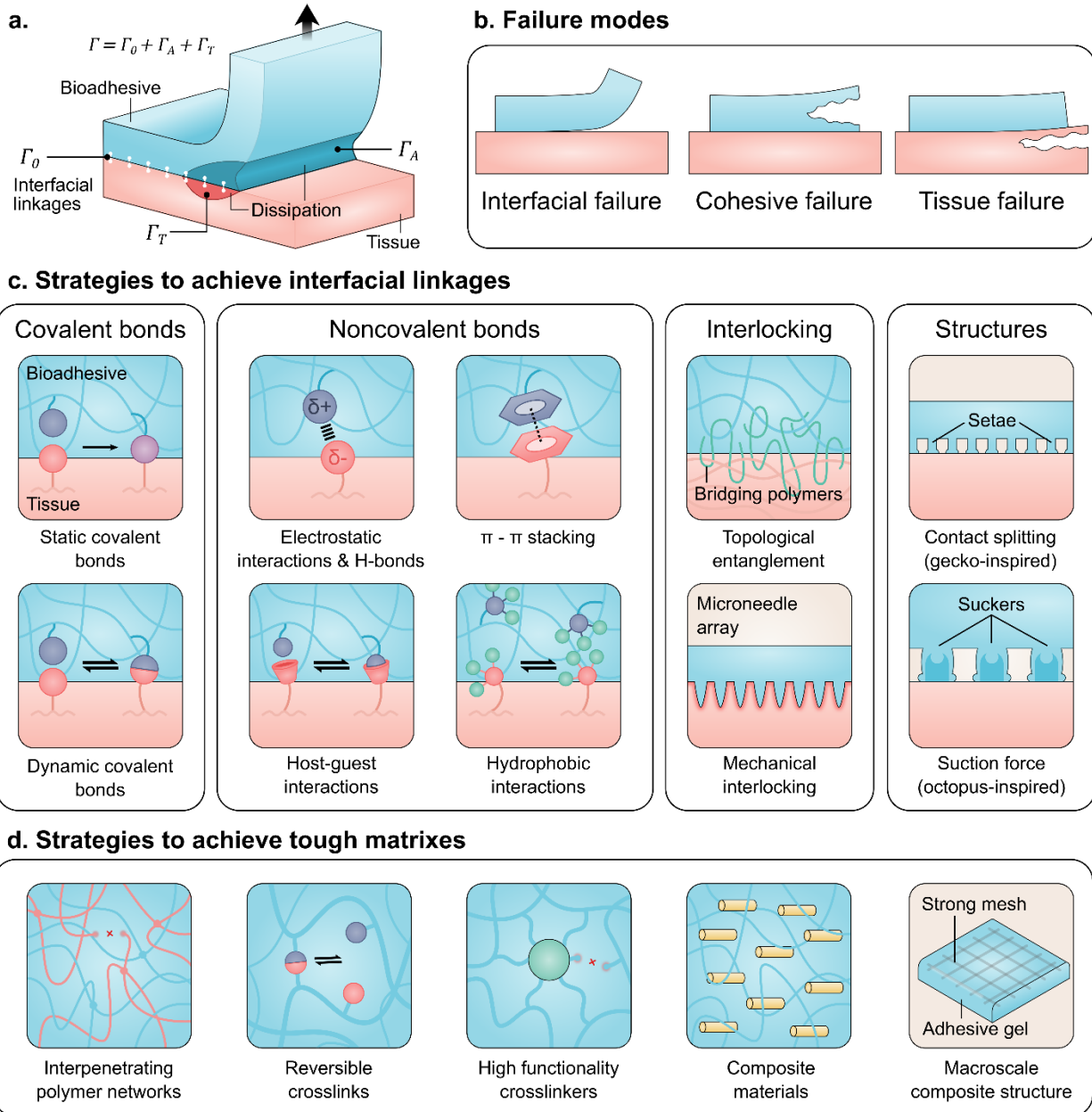


Figure 2-1. Design strategies for tissue adhesion. (a) The interfacial toughness of an adhered system depends on Γ_0 , the intrinsic work of adhesion due to interfacial bonds; Γ_A , the energy dissipated in the bulk adhesive; and Γ_T , the energy dissipated in the tissue. (b) Three possible adhesion failure modes: interfacial failure, cohesive failure, and tissue failure. To design for tough adhesion, both strong interfacial linkages and a dissipative bioadhesive matrix are desired. (c) Representative strategies to achieve interfacial linkages and increase the interfacial work of adhesion. (d) Representative strategies to achieve tough bioadhesive matrixes by incorporating energy dissipation mechanisms.

2.1.1. Design strategies for interfacial linkages

Interfacial interactions between bioadhesives and tissues are significantly influenced by both the chemical composition of the materials involved and the geometrical characteristics of the interface. Intermolecular interactions play a dominant role in determining the intrinsic work of adhesion (Γ_0), which is a measure of the energy required to separate two surfaces per unit area of contact without any external forces acting on them. In general, a higher intrinsic work of adhesion indicates stronger and more stable interfacial bonding, leading to improved adhesion performance. Beyond intrinsic adhesion, physical attributes of the interface such as surface roughness and architected protrusions can have a profound effect on the overall adhesion behavior. This section provides an overview of the primary strategies employed to modulate the interface in bioadhesive systems: intermolecular interactions, polymer entanglements, mechanical interlocking, contact splitting, and suction force (**Figure 2-1c**).

Intermolecular Interactions

Proteins comprising tissues contain chemical functional groups such as amines, carboxylic acids, hydroxyls, and thiols (also called sulfhydryls), which can form intermolecular interactions with reactive groups in bioadhesives.²¹ These interactions can be covalent or non-covalent in nature, depending on the specific functional groups involved. Covalent interactions, which possess high bond dissociation energies relative to non-covalent interactions, are often targeted as the primary strategy for achieving strong and stable tissue adhesion.^{9,22–24} Typical reactive groups which can be incorporated into bioadhesives to form covalent linkages include cyanoacrylates, isocyanates, N-hydroxysuccinimide (NHS) and NHS esters, and catechol groups. For example, cyanoacrylates can react rapidly with tissue surface nucleophiles, such as amines and hydroxyls, to form covalent bonds. Isocyanates can also react with surface nucleophiles to form covalent urethane bonds.²⁵ NHS can react with primary amines to form amide bonds, often with the aid of the coupling agent 1-ethyl-3-(3-(dimethylamino)propyl) carbodiimide (EDC).^{26,24} Catechol groups can undergo oxidative crosslinking pathways to bond with amine and thiol groups.^{27,28} The net strength of these bonds depends on the specific tissue surface and its constituent chemical functional groups.⁸

Compared to traditional covalent bonds, which are kinetically stable and require a large energy input to break, dynamic covalent bonds exhibit intermediate bond dissociation energies and can undergo exchange reactions under certain pH and temperature conditions. As a result, dynamic covalent bonds can be utilized to achieve reversible interfacial linkages.^{29,30} These bonds are increasingly being incorporated into bioadhesives due to their ability to self-heal and remodel after being disrupted, which can be particularly valuable in applications where the bioadhesive is subject to continuous mechanical stress or deformation. Examples of dynamic covalent bonds include disulfide bonds, boronic ester bonds, imine bonds (also named Schiff bases), and hemithioacetal bonds.^{31–34} In addition to their ability to self-heal, dynamic covalent bonds offer a tool to design bioadhesives with stimulus-responsive reversible adhesion, which can enable the retrieval or repositioning of misplaced bioadhesives without damaging the underlying tissue.¹³

Apart from covalent interactions, many bioadhesives rely on the interplay of non-covalent intermolecular interactions to adhere with tissues. Despite their relative weakness, non-covalent interactions play an important role in achieving fast interfacial bonding and contributing to adhesion stability. Non-covalent interactions in tissue adhesion include electrostatic interactions,

hydrogen bonds, π - π stacking, host-guest interactions, and hydrophobic interactions.³⁵ For example, bioadhesives possessing hydrogen bond-forming capabilities can interact with various chemical groups on tissue surfaces (e.g., amines, carboxyl, and thiol groups) and establish strong supramolecular adhesion, even without covalent linkages.^{36,37}

Often, a combination of covalent and non-covalent interactions is used to impart tissue adhesion. A prime example of this approach can be seen in the adhesion strategy of marine mussels. Mussels are renowned for their ability to adhere to a variety of surfaces and withstand wet, dynamic environments (much to the dismay of boat owners). Their remarkable adhesive capability arises from mussel foot proteins (mfps) which contain a high proportion of phenolic residues, such as 3,4-dihydroxy-l-phenylalanine (DOPA), tyrosine, and tryptophan. These aromatic residues participate in a diverse array of bonding types, including bidentate hydrogen bonds, metal-ion coordination, π - π stacking, and various covalent bonds involving quinones, the oxidized form of DOPA.³⁸ This repertoire of covalent and non-covalent interactions has served as inspiration for the development of mussel-inspired bioadhesives based on catechol chemistry, which continues to be a lively area of research.³⁹⁻⁴⁴ For more detailed information, common chemical strategies for introducing tissue adhesive intermolecular interactions have been discussed at length in several topical reviews.^{9,21,29}

Topological Entanglement

Topological entanglement between bioadhesive polymers and tissues provides a physical mechanism that can contribute to the interfacial work of adhesion without relying on specific reactive group chemistries. Topological entanglement refers to the phenomenon in which polymer chains diffuse into and become physically entwined with the substrate, forming a network of interlocks that can be viewed as molecular stitches.^{33,34} The entanglement of bioadhesive polymer chains is governed by the molecular weight and flexibility of the polymers, as well as the charge and topology of the tissue surface. Note that topological entanglement requires the adherend to have a porous microstructure to allow for the diffusion of stitching polymers.

Various polymers have been employed as stitching polymers to accomplish topological adhesion with tissues. One example is poly(acrylic acid) (PAA), a water-soluble polymer that has a high density of carboxylic acid side chains, enabling the formation of coordination complexes with metal ions.⁴⁷ When PAA is dissolved in an aqueous solution and applied to the surface of a porous adherend, the polymers diffuse into the substrate. Upon the introduction of a trivalent metal ion such as iron(III), the entangled PAA chains crosslink and form a network of stitches.⁴⁸ Other polymers that have been leveraged as stitching polymers include biopolymers such as chitosan, alginate, and hyaluronic acid.^{26,48}

A drawback of the topological entanglement mechanism is the diffusion-limited rate of adhesion. Tissues with low permeability can be challenging for bridging polymers to interpenetrate, resulting in slow and weak adhesion. One potential strategy to accelerate and promote the formation of topological entanglements is to leverage an ultrasound transducer to induce cavitation and actively embed adhesive polymers into the tissue.^{49,50}

Mechanical Interlocking

In addition to the molecular stitches described above, another physical adhesion mechanism involves the formation of mechanical interlocks between the bioadhesive and the tissue. Mechanical interlocking can occur on various scales through a number of strategies, including the use of flowable polymers to infiltrate tissue surface irregularities, the geometric design of bioadhesive surface structures, and the use of pores to promote tissue ingrowth. In general, mechanical interlocking can enhance adhesion by increasing the contact area between substrates and provoking additional energy expenditure during crack propagation.⁵¹

A classic example of mechanical interlocking can be seen with pressure sensitive adhesives (PSAs), which typically take the form of tapes composed of viscoelastic polymers such as acrylics and silicones.⁵² When a small amount of pressure is applied, the viscoelastic polymers flow around the peaks and troughs of the adherend surface, creating mechanical interlocks. PSAs have been widely commercialized for epidermal applications by companies such as DuPont™, 3M™, and Elkem.^{53–55} Recently, 3M unveiled a new acrylate-based PSA marketed to stick to skin for up to 28 days, expanding the previous wear time by two weeks.⁵⁶ Despite the commercial popularity of epidermal PSAs, their development for internal applications has been hindered by their inability to bind to surfaces coated with body fluids.⁵⁷

To enable mechanical interlocking with the surface roughness of wet tissues, bioadhesives can be patterned with micro- or macro-scale surface features, such as microneedles and hooks.⁵⁸ The adhesion performance of these structured bioadhesives is heavily reliant on the geometric design of their protrusions, which determine the required penetration force and the pull-out force.⁵⁹ Anchoring architectures, such as barbed or swellable microneedle tips, can be employed to increase the adhesion strength, especially in shear.^{60–62} This anchoring effect physically impedes with crack propagation while simultaneously increasing the contact area between the adhesive and the tissue. Moreover, these surface features not only enable adhesion but also can also create micro-channels through the tissue surface, facilitating the efficient delivery of drugs, vaccines, and cosmetics.^{63–67} The mechanical and geometrical properties of microneedles and barbs should be evaluated to ensure that they maintain their structure during skin insertion.⁶⁸ It may also be important to account for variations in tissue properties across different body regions and individuals, as they can impact the desired adhesion performance and therapeutic effects of micro-needle type bioadhesives. Numerical simulations have been employed as a tool for predicting skin penetration behavior. However, the specific contributions of microneedles and similar structures to adhesion energy have received limited attention in the literature. Elucidating how certain geometrical parameters might impact crack propagation and overall adhesion would offer a more thorough understanding of their adhesive mechanisms.

From a different approach of mechanical interlocking, self-adhesive implantable devices have been designed by crafting porous surfaces on implants, allowing for soft tissue ingrowth and interdigitation.^{69–71} For example, titanium alloy implants have been modified using methods such as electron beam manufacturing, sandblasting, and acid etching to produce penetrable tissue interfaces.^{71,72} However, because this strategy relies on slow biological processes to achieve mechanical stability, its practical use cases are largely confined to the long-term integration of dental and orthopedic implants.^{73,74}

Contact Splitting

The remarkable capability of geckos to cling to almost any surface has inspired a family of adhesives known as gecko-mimetic adhesives, which are being exploited for various applications including medical bioadhesives.^{75,76} The working principle of these adhesives is based on the hierarchical structure of the gecko foot, which is covered with millions of tiny hairs called setae. Each seta is further divided into hundreds of branches called spatulae that interact with the surface at the molecular level via van der Waals forces.⁷⁷⁻⁷⁹ The sum of these van der Waals interactions over millions of setae gives rise to a surprisingly large attachment force that is relatively insensitive to the surface chemistry of the adherend. The central design principle underlying gecko adhesion is the notion of contact splitting, i.e., the division of a large contact area into many finer contact areas.^{80,81} Contact splitting strategically improves adaptability to surface irregularities and increases the effective adhesion force. This can be understood from the framework of contact mechanics. Following the Johnson-Kendall-Roberts (JKR) contact model, the adhesion force of a hemispherical contact F is directly proportional to its radius R .⁸² Conversely, the density of these contacts per unit area is inversely proportional to the square of the radius, scaling as $1/R^2$. Consequently, by replacing a single large contact with n self-similar smaller ones, the adhesion force F' can be enhanced to:⁸¹

$$F' = \sqrt{n}F \quad (2.3)$$

Another notable attribute of the gecko foot is the anisotropy of its structures, which give rise to anisotropic shear frictional forces and an adhesion energy highly dependent on the peeling angle.⁸³ This feature enables the gecko to achieve a strong grip in certain directions, yet also detach its feet with near-zero detachment forces. For this reason, gecko-inspired adhesives are also often referred to as frictional adhesives.

Borrowing from the adhesion strategy of the gecko, researchers have fabricated adhesive surfaces with synthetic nanopillar setae. These nanostructured surfaces can be chemically functionalized, such as with a coating of oxidized dextran, to promote chemical crosslinking with tissues and further stabilize adhesion.⁷⁶ However, gecko-inspired bioadhesives generally struggle to adhere strongly to wet surfaces with reduced friction. Altering the micropillar geometry, such as by incorporating mushroom-shaped tips, has demonstrated improved adhesion performance in both dry and wet conditions.⁸⁴ Besides tuning their shape, fabricating pillars with regions of different elastic moduli (e.g., a soft tip and stiff base) can be beneficial for simultaneously achieving conformal contact with rough surfaces and overall mechanical robustness.⁸⁵ However, the introduction of added geometric or material complexities poses manufacturing challenges and may limit high-volume production.⁸⁶

Suction Force

Another source of inspiration from nature is the octopus, whose arms are decorated with hundreds of suckers which can grip a variety of objects underwater, from hard rocks to soft and slippery fish.⁸⁷ Interest in the utility of octopus suckers for wet adhesion has given rise to octopus-mimetic bioadhesives which rely on the formation of suction force to attach to substrates.⁸⁸⁻⁹⁴ The strength of attachment is influenced by the pressure differentials generated by the suckers, which is dependent on their geometry and elasticity.⁹⁵ In addition to the suction provided by these protuberances, the outer part of the octopus sucker is covered with an array of soft, microscale wrinkles. These wrinkles drain water at the interface and increase the contact area between the

sucker and the substrate, enhancing the net adhesion force. Inspired by this anatomical feature, researchers have developed an octopus-mimetic patch containing adhesive suckers outfitted with wrinkles to drain and capture water.⁹⁶ Overall, bioadhesives based on suction force offer several unique advantages, including the ability to adapt to rough surfaces and reversibly attach to both wet and dry substrates. Nonetheless, this family of bioadhesives has been relatively less explored, possibly due to the complexity of manufacturing suction cup architectures and the easy loss of suction.

2.1.2. Design strategies for energy dissipation

Returning to Eqn. (2.2), another important factor in determining the interfacial toughness is Γ_A , the energy dissipated in the adhesive during the process of delamination. To increase Γ_A , energy dissipation mechanisms can be intentionally designed into the polymer network architecture of the bioadhesive (**Figure 2-1d**). This can take the form of fracturing sacrificial polymer chains, breaking reversible crosslinks, using high functionality crosslinkers, and pulling out embedded fibers or fillers.^{97,98}

Fracture of Polymer Chains

Short polymer chains can impart toughness in a network by providing sacrificial bonds. As the bioadhesive is deformed, the short chains around the process zone fracture and dissipate mechanical energy. To maintain strength in addition to toughness, interpenetrating polymer networks (IPNs) have been employed as strategic architectures.⁹⁹⁻¹⁰¹ An IPN generally involves the interpenetration of a long-chain and a short-chain network that are separately crosslinked. Under loading, the brittle short-chain network dissipates energy while the intact long-chain network maintains the integrity of the material. The implementation of IPN architectures with reactive surface functional groups has produced tough bioadhesive hydrogels with exceptional interfacial toughness.^{24,102,103} However, rupturing of the short-chain network usually induces permanent damage, resulting in limited fatigue resistance.

Reversible Crosslinks

Another approach to introducing energy dissipation is to incorporate reversible crosslinks into the bioadhesive matrix.¹⁰⁴ Similar to how reversible bonds, such as physical interactions and dynamic covalent bonds, can provide self-healing behavior at the interface, reversible crosslinks in the bulk matrix can dissociate under loads and allow stretched polymer chains to relax, dissipating energy. Their reversibility allows for crosslinks to reform after breaking, thereby maintaining the energy dissipation mechanism over multiple loading cycles. For instance, mussel-inspired bioadhesives contain catechol groups which participate in various non-covalent interactions among one another in the bulk material (e.g., hydrogen bonding and π - π stacking). The dynamic formation and breakage of these non-covalent interactions provide stretchability and toughness.¹⁰⁵

High Functionality Crosslinkers

Functionality refers to the number of polymer chains that can be crosslinked by a single crosslinker. Conventional physical and chemical crosslinkers typically have low functionalities, meaning there is often only a single polymer chain bridging two adjacent crosslinks.⁹⁷ As a result, the network can fracture when single polymer chains are ruptured under deformation and connections between crosslinks are compromised. To circumvent this issue, high functionality crosslinkers (e.g., with functionalities exceeding 100) can be incorporated into polymer networks, yielding multiple polymer chains with varied lengths connecting adjacent crosslinks. This design allows for the dissipation of energy through the fracture of relatively shorter chains, while longer chains retain their structural integrity, thus imparting elasticity to the material. Representative high-functionality crosslinkers include two-dimensional nanomaterials such as clay nanosheets and graphene.¹⁰⁶ However, high concentrations of nanoclays and graphene can have adverse effects on cells; therefore, their incorporation into bioadhesive materials should be carefully assessed to ensure their compatibility with cellular systems.^{107–109}

Composite Materials

Composite materials, such as the natural composites of tissues embedded with collagen fibrils, often possess superior toughness than their constituents alone.^{110–113} The working principle of toughening due to fiber reinforcement is based on the dissipation of energy that results from the sliding, debonding, and fracture of fibers under mechanical loads. The incorporation of fibers can also act to reduce the swelling ratio of the composite by restricting the amount of water that is able to penetrate the denser structure, which can mitigate swelling-induced weakening. For example, cellulose fibers (CFs) integrated into a gelatin and alginate-based bioadhesive formulation were found to increase the cohesiveness of the matrix, significantly improving the burst strength of the bioadhesive.¹¹⁴ However, caution is warranted in using CFs for internal bioadhesives due to their non-biodegradability in humans.¹¹⁵

In general, the mechanical properties, orientation, and volume fraction of fibers or fillers in the polymer network are key parameters that influence the resulting mechanical properties of the composite. For instance, uniformly aligned fibers can give rise to anisotropic toughness and strength, while randomly dispersed fibers result in an isotropic toughening effect. Another design parameter is the aspect ratio of the fibers. Longer fibers can provide higher toughness and crack resistance but may also lead to reduced flexibility and stretchability. For fibers that exhibit strong inter-fiber interactions (e.g., hydrogen bonding), the use of processing aids or coupling agents may be necessary to prevent the fibers from aggregating.^{116,117}

Besides fibers and fillers, macroscale composite structures such as hydrogel-mesh composites or bilayer patches can also be employed to provide mechanical reinforcement to bioadhesive materials.^{118,119} For instance, hydrogel-mesh composites combine the load-bearing capacity of a surgical mesh, such as those used for hernia repair, with a bioadhesive hydrogel, resulting in a structure that can maintain adhesion and cohesion under large mechanical stresses.¹¹⁸ Similarly, heterogeneous bilayer patches comprising a bioadhesive layer bonded to a secondary material with favorable mechanical properties can yield improved toughness. For example, integrating a bioadhesive hydrogel with a thin backing layer of hydrophilic polyurethane has been employed to create bioadhesive patches with enhanced strain capacity and flexibility.¹¹⁹ For bilayer structures, the equilibrium swelling ratios of the individual components should ideally be similar to avoid

curling of the patch when hydrated, which can lead to the patch collapsing in humid environments or delaminating from tissue surfaces.

2.1.3. Energy dissipation in the tissue

As biological tissues are viscoelastic and poroelastic in nature, they too contribute to the energy dissipated under loading.^{120,121} An array of biological factors give rise to the nonlinear elastic behavior observed in tissues. Prominent among these factors are collagen, proteoglycans, elastin, and fluid content.¹²² Collagen fibers, abundant in connective tissues, impart viscoelastic properties through mechanisms such as sliding and reorientation. Proteoglycans within the extracellular matrix establish a hydration layer around collagen fibrils, facilitating load transfer and energy dissipation.¹²³ Elastin, a resilient structural protein, is present in large amounts in highly elastic tissues and has the ability to repetitively deform and recoil under strain.¹²⁴ Fluids residing within the extracellular matrix contribute to stress dissipation and load distribution via movement within the porous structure. The resulting fluid pressurization and viscous drag give rise to flow-dependent poroelastic properties.¹²⁵ Collectively, these factors work in concert to absorb and redistribute mechanical energy, allowing tissues to withstand dynamic loads. Notably, variations in the composition and arrangement of these components across different tissue types result in tissue-specific viscoelastic properties. Although tissues possess these energy dissipation mechanisms, in general, the relative contribution of Γ_T is low compared to the energy dissipated in the bioadhesive (Γ_A).¹²⁶ Nonetheless, the elastic and dissipative properties of the tissue influence the energy dissipation within the bioadhesive, as they can impact the size of the dissipation zone and the relative deformation of the bioadhesive. Consequently, such variations may contribute to the significant differences in adhesion performance of bioadhesive materials when applied to different tissue types.¹²⁶

2.2. Biological challenges

In practice, bioadhesives face a variety of complex biological challenges which often impede their tissue bonding performance in vivo compared to in laboratory settings. These challenges highlight areas where there exists a major need for technological innovation, motivating the development of new and improved bioadhesives. This section examines the main challenges imposed by the biological environment: adhesion in a wet environment, dynamic tissue movement, the immune response, bacterial activity, mechanical mismatch, difficult-to-access application sites, and biodegradation (**Figure 2-2**).

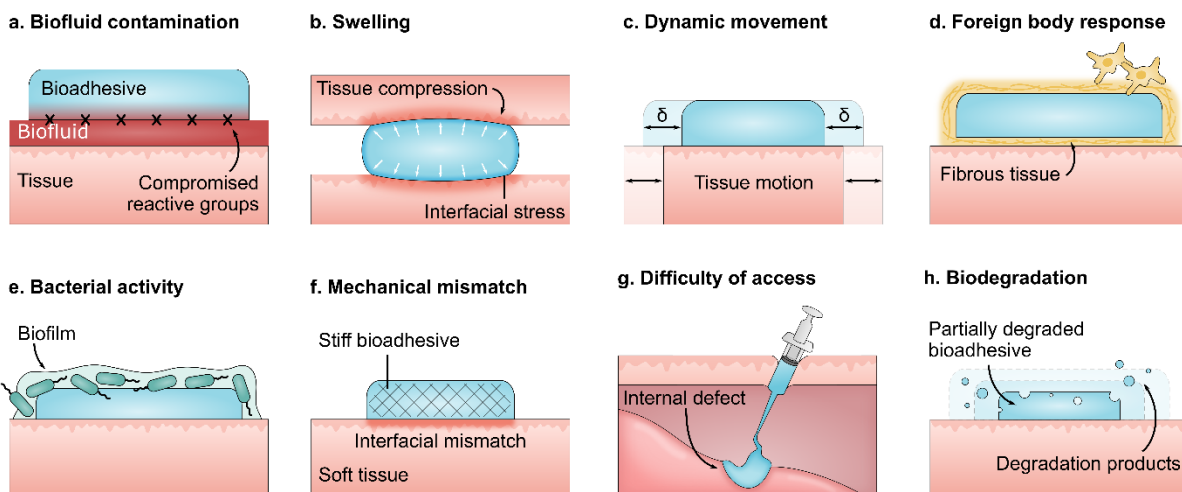


Figure 2-2. Key considerations related to the biological environment. (a) Premature contamination by biofluids can compromise reactive groups on the bioadhesive surface, rendering it non-adhesive. (b) Excessive swelling of the bioadhesive can give rise to interfacial stress, weakening the strength of adhesion, and adversely compress surrounding tissues. (c) Dynamic tissue movement imposes repeated deformations on the bioadhesive, which may cause it to fracture or delaminate. (d) Excessive inflammation as a result of the foreign body response can lead to fibrotic capsule formation and poor healing. (e) Bacterial activity can give rise to biofilm formation and infectious complications. (f) Mechanical mismatch between the bioadhesive and tissue can lead to interfacial stress concentrations and interfere with organ function. (g) Difficult-to-access internal defects may require specialized bioadhesive form factors or delivery methods. (h) The bioadhesive should undergo biodegradation at a suitable pace and induce minimal cytotoxicity with its degradation products.

2.2.1. Adhesion in a wet environment

Inside the body, fluids are ubiquitous. Most internal tissues are lined with a layer of interfacial water which provides lubrication, hydration, and other functions essential for their physiology. However, biofluids also present a major obstacle for tissue adhesion, as they can physically block tissue contact, slow down diffusion, or compromise reactive groups in the bioadhesive (**Figure 2-2a**). For instance, NHS esters are susceptible to hydrolysis.¹²⁷ Achieving fast and robust adhesion with wet tissues has historically been one of the grand challenges for bioadhesive development.

A promising wet adhesion strategy is to remove the interfacial water from the tissue surface using a dry-crosslinking mechanism, in which the bioadhesive material is applied in a dry or dehydrated state to allow quick absorption of the interfacial water as the adhesive becomes hydrated.¹²⁸ This enables near-immediate consolidation with the tissue, allowing rapid formation of intermolecular bonds.²⁴ Although this strategy can accelerate adhesion formation compared to diffusion-limited bioadhesives (e.g., within a few seconds vs. several minutes), a downside of the dry-crosslinking mechanism is its sensitivity to hydration, as the interfacial wicking effect can be compromised if the dry bioadhesive becomes prematurely hydrated before reaching the tissue surface.

An idea for circumventing premature fouling by biofluids involves coating the bioadhesive with a protective layer of liquid that is immiscible with the contaminating biofluids.¹²⁹ The implementation of this approach employs a hydrophobic liquid, such as a silicone or mineral oil, to serve as a dynamic physical barrier that prevents the underlying bioadhesive surface from directly contacting environmental fluids. The hydrophobic liquid can then be expelled at the tissue surface under sufficient dewetting pressure.¹³⁰ In liquid-infused systems, the solid surface typically features nano- or micro-scale structures that stabilize the wetting of the lubricating liquid. For example, the solid surface can take the form of a porous, sponge-like substrate, a microparticle-embedded surface, or a woven mesh.^{130–132} This strategy can also be adapted to create bioadhesive pastes by suspending bioadhesive particles in a protective fluid, allowing the paste to be directly applied to actively bleeding wound sites.¹³³ The main advantage of these liquid-infused systems is that they allow the bioadhesive to leverage water-sensitive reactive groups without necessitating a dry, open-access surgical field, improving their practical applicability.

Another consequence of adhesion in wet environments is the swelling of hydrophilic bioadhesives, which can give rise to interfacial stresses and compress surrounding tissues (**Figure 2-2b**). The latter concern of tissue compression is especially detrimental for applications in spaces sensitive to volume expansion, such as near nerves.^{134–136} The effects of swelling can be mitigated by increasing the crosslinking degree, incorporating thermosensitive polymers, or introducing hydrophobic functional groups, although these alterations may also impact the overall adhesion performance and mechanical properties of the bioadhesive.^{137,138} For pre-formed bioadhesive patches, stretching the bioadhesive to its equilibrium swelling ratio prior to application can cancel out the effects of swelling without altering its material composition.^{119,139} However, this technique is limited by the stretchability of the bioadhesive network in its initial state, which may be less than its equilibrium swelling ratio.

2.2.2. Dynamic movement

Many tissues in the body are constantly moving and stretching, which can cause bioadhesive materials undergoing tissue-induced deformations to fail (**Figure 2-2c**). Overcoming this challenge requires bioadhesives to be designed with high flexibility, extensibility, and fatigue resistance. To this end, introducing energy dissipation and self-healing mechanisms can be useful for designing tough, stretchable, and self-healing materials (e.g., the strategies discussed in Section 2). Moreover, the use of fibers/fillers or high functionality crosslinkers to introduce high-energy phases can increase the fatigue threshold of bioadhesives.¹⁸

The lungs are an illustrative example of a challenging, dynamic application site. Lung tissues are highly elastic to accommodate large cyclic changes in volume during inspiration and expiration. Air leaks following surgical lung resection are a cause of major breathing complications, but effective methods for sealing them have remained somewhat elusive. Sutures and staples pose the risk of creating additional leak points, since they puncture through tissue, while common commercial sealants lack the proper extensibility or tensile strength to support inflation and deflation. Leveraging the properties of elastin, researchers engineered a highly elastic lung sealant by crosslinking recombinant human tropoelastin (the subunit of elastin).^{140,141} The resulting formulation was found to outperform commercial sealants in rat and porcine lung defect models, demonstrating the importance of bioadhesive elasticity for repairing dynamic tissues.

In addition to the mechanical properties of the bioadhesive, the time required to form adhesion is a crucial property for adhering to actively moving tissues. Tissue movement can displace or fracture a bioadhesive before it reaches full adhesive or cohesive strength, depending on the kinetics of relevant processes such as diffusion, bond formation, and gelation. Some strategies that may be incorporated to minimize the time it takes to form adhesion include employing stimuli-responsive materials (e.g., light-activated polymerization), using pre-formed patches to eliminate the need for in situ matrix formation, fabricating surface structures that enhance the wetting behavior and interfacial contact with the tissue, or implementing the dry-crosslinking mechanism described in Section 3.1. Still, slow adhesion formation remains a common challenge among bioadhesives.

2.2.3. Immune response and allergies

The foreign body reaction (FBR) to implanted biomaterials is a fundamental biological challenge which underlies the failure of many materials and devices (**Figure 2-2d**).¹⁴² Adverse consequences of FBRs include fibrotic scarring and the development of post-surgical adhesions.¹⁴³ For implanted devices, fibrous tissues that form between the device and the physiological environment can also substantially interfere with biosensing, mass transport, and signal transmission. To minimize the FBR, some bioadhesive materials have been designed to incorporate molecules that inhibit protein adsorption and cell adhesion, such as zwitterionic polymers.^{144–146} Bioadhesives can also serve as carriers for anti-inflammatory drugs which can be released at the interface to modulate the local tissue response and minimize fibrotic encapsulation. However, strategies based on the release of pharmacological substances are only effective in the short term, and fibrosis can still arise after their therapeutic effects wear off. An alternative strategy to alleviate the FBR involves altering the shape or surface topography of implanted materials.^{147,148} Such geometrical parameters appear to have a profound effect on macrophage behavior and capsular contracture. It was recently reported that implants having an average surface roughness of 4 μm are associated with minimal inflammation, which may serve as a basis for the development of deliberately textured bioadhesives.¹⁴⁷

Besides the FBR, the potential allergenicity of bioadhesive materials poses a substantial concern for individuals who may be sensitive to specific proteins or antigens. For example, bioadhesives containing components derived from animal sources such as collagen, gelatin, albumin, or fibrin may induce anaphylactic reactions in allergic patients.^{149–151} Although synthetic polymers are generally associated with lower allergenicity, they too can elicit allergic responses.¹⁵² In view of this risk, applying personalized medicine approaches to bioadhesive development may be a valuable strategy to tailor formulations to individual patients based on their specific medical needs.¹⁵³ In the future, screening patients for potential allergies to bioadhesive components (including specific polymers, crosslinkers, and other additives) and adjusting the formulation of a bioadhesive accordingly could be performed prior to a clinical intervention to minimize the risk of adverse reactions. To effectively carry out such an approach, establishing a library of various components of bioadhesive formulations, their alternatives, and their effects on material properties would be necessary to optimize the patient-specific safety of bioadhesives.

2.2.4. Bacterial activity

The potential for biomaterials to support bacterial activity is a major concern that can pose the risk of infections and related complications (**Figure 2-2e**). To mitigate the occurrence of microorganism attachment and proliferation, bioadhesive materials can be designed to incorporate bacteria-repellent or antiadhesive properties.¹⁵⁴ Materials with intrinsic antibacterial properties, such as metals (e.g., copper, silver, and gold) or ceramics (e.g., zinc oxide, magnesium oxide, and titanium oxide), may be incorporated into the adhesive matrix to inhibit bacterial growth. Additionally, chitosan has been shown to produce antibacterial effects.¹⁵⁵ Besides bulk material strategies, tuning the surface properties of bioadhesive patches can be employed to introduce antiadhesive interfaces.¹⁵⁶ For example, incorporating highly hydrophilic moieties such as zwitterionic polymers can reduce bacterial attachment by increasing the energetic cost of disrupting surface-associated water molecules.^{157,158} Furthermore, modifying the surface topography of implants has been shown to impact biofilm formation.^{159,160} To this end, developing fabrication methods to controllably introduce optimized topographical features may be an effective strategy for hindering bacterial activity.

2.2.5. Mechanical mismatch

When considering the mechanical properties of bioadhesive materials, the similarity or mismatch in properties between the bioadhesive and the tissue adherend can significantly influence the performance of the adhesive bond. In the case of a substantial mechanical mismatch, stress concentrations at the interface can lead to tissue damage or premature failure (**Figure 2-2f**). For example, cyanoacrylate bioadhesives, which form rigid and brittle matrixes upon polymerization, are prone to delaminating from soft tissues due to their limited flexibility.¹⁶¹ This illustrates the importance of targeting mechanical compatibility between the bioadhesive and the tissue. On the other hand, however, highly deformable bioadhesives may be ineffective at keeping wound edges together, hindering tissue repair. One strategy to reconcile these confounding material requirements for soft tissue sealing is to implement a gradient in elastic modulus along the bioadhesive, such that the tissue-material interface is mechanically well-matched (i.e., softer) while the wound-covering portion is resistant to excessive deformation (i.e., stiffer).¹⁶²

Besides affecting adhesion performance, the mechanical properties of the bioadhesive can have profound effects on tissue mechanics and organ function. For instance, in the context of blood vessels which experience continuous pulsatile pressures from blood flow, compliance matching between the bioadhesive and the vessel can be crucial for maintaining proper hemodynamics.¹⁶³ A compliance mismatch may disrupt blood flow or induce turbulence, potentially altering perfusion or promoting thrombus formation.¹⁶⁴ Furthermore, the tissues comprising blood vessels (and most tissues in general) are elastically anisotropic, which may also impact flow behavior.¹⁶⁵ Also worth considering is how the disease state of tissues may alter their physical (and chemical) properties, thereby influencing the performance of a bioadhesive. Certain pathologies have been linked to changes in tissue mechanics; for example, cardiomyopathy can lead to stiffening of the heart tissue.¹⁶⁶ Developing strategies to fabricate bioadhesives with programmable, anisotropic mechanical properties, such as by electrospinning or 3D printing, may enable better tissue and patient specificity.

2.2.6. Difficulty of access

The challenge of physically accessing certain tissue sites poses a distinct hurdle in the application of bioadhesives (**Figure 2-2g**). This may arise due to the nature of the procedure (e.g., minimally invasive vs. open access) or the anatomical structure (e.g., within deep tissue compartments or hollow structures), and can be prohibitive to the use of common forms of bioadhesives, requiring specialized application strategies. Injectable formulations, including glues, pastes, and hydrogel microparticles, have emerged as the prevailing strategy for achieving minimally invasive delivery.^{117,167-169} Injectable bioadhesives must be formulated to possess the proper rheological properties to flow through a narrow syringe, and undergo phase transitions or crosslinking processes to establish cohesive matrixes in situ.⁴³ While injectable bioadhesives offer notable adaptability, in situ matrix formation carries several limitations, including slow adhesion formation and low cohesive strength.

For the minimally invasive delivery of pre-formed bioadhesives, origami-inspired patches have been proposed, drawing inspiration from the art of paper folding.¹³⁰ These bioadhesives are designed to be collapsed or folded prior to delivery, facilitating insertion through small access ports, and subsequently expand and adhere at the target site using minimally invasive end-effectors. Designing bioadhesives amenable to origami techniques requires that they retain their folded shape prior to insertion and conform with the tissue upon deployment. While this strategy can achieve fast and robust adhesion in difficult-to-access tissue targets, its versatility is constrained by geometric limitations.

A unique approach to deliver a bioadhesive coating to the deep branches of the airway involves the inhalation of bioadhesive microparticles.¹⁷⁰ These microparticles are administered using a dry powder inhaler and deposited along the airway, where they undergo swelling and crosslinking to form a hydrogel shield. The resulting bioadhesive layer can serve as a physical barrier against pathogens or deliver drugs directly to the respiratory system.

As has become apparent throughout the discussions thus far, the choice of bioadhesive form factor plays a central role in determining its suitability for specific applications. Bioadhesives have been developed in a wide array of shapes and forms, each of which carries distinct advantages and disadvantages, which are summarized in **Figure 2-3**. The most suitable choice depends strongly on the intended use and delivery method.


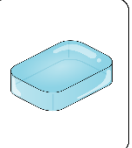
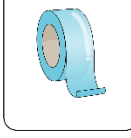
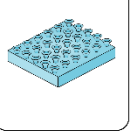
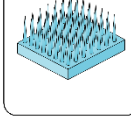
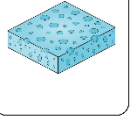
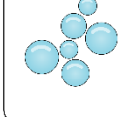
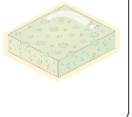
Glues & pastes		Hydrogel patches	
	<ul style="list-style-type: none"> - Conform to curved and rough surfaces - Suitable for minimally invasive surgery (injection) 		<ul style="list-style-type: none"> - Preformed matrix provides easy & fast application - Adept for sealing large gaps and defects - Can be loaded with drugs, etc.
	<ul style="list-style-type: none"> - May have slow in situ matrix formation - Difficult to spatially control application 		<ul style="list-style-type: none"> - Limited shape complexity - Requires open access for application
Pressure-sensitive tapes		Biomimetic patches	
	<ul style="list-style-type: none"> - Form fast and reversible adhesion - Adhesive to a wide range of engineering materials 		<ul style="list-style-type: none"> - Rely on physical mechanisms to form adhesion, enabling reusability/reversibility - Adapt to rough surfaces
	<ul style="list-style-type: none"> - Poor performance with wet tissues - Can cause skin irritation or maceration 		<ul style="list-style-type: none"> - May require complex manufacturing steps - Low peeling forces
Microneedle patches		Sponges	
	<ul style="list-style-type: none"> - Can penetrate mucus barriers - Provide access to interstitial fluid through the skin 		<ul style="list-style-type: none"> - Macroporous structure can quickly absorb & drain body fluids (e.g., blood)
	<ul style="list-style-type: none"> - May cause tissue damage - May require complex manufacturing steps 		<ul style="list-style-type: none"> - Matrix is generally weak/brittle - Not suitable for preventing leaks
Microparticles		Liquid-infused systems	
	<ul style="list-style-type: none"> - Suitable for minimally invasive delivery (injection or inhalation) - Can be loaded with drugs, etc. 		<ul style="list-style-type: none"> - Robust against contamination by body fluids - Enables pressure-triggerable adhesion
	<ul style="list-style-type: none"> - Not suitable for sealing large holes - Difficult to spatially control application 		<ul style="list-style-type: none"> - May require complex surface patterning steps - Risk of embolization of lubricating fluid droplets
	General advantages		General disadvantages

Figure 2-3. General advantages and disadvantages of various bioadhesive form factors. Each form factor possesses distinct pros and cons, and their suitability depends on the target application and delivery method.

2.2.7. Biodegradability, clearance, and removability

The ultimate fate of a bioadhesive from the angles of biodegradation, clearance, and removability is a critical design consideration, especially for bioadhesives used internally.^{171,172} At a high level, bioadhesives should be designed to degrade at a pace that allows them to provide the necessary support during tissue repair, but eventually undergo degradation without causing a chronic immune response (**Figure 2-2h**).

The rate and process of biodegradation depend on the characteristics of the material and the physiological environment where it resides. Biodegradation can be driven by chemical, physical, and biological mechanisms, resulting in a multitude of factors that contribute to its process. Three main mechanisms of polymer degradation in the body are oxidative, hydrolytic, and enzymatic degradation.^{100,173} Oxidative degradation occurs during the inflammatory response when recruited immune cells produce reactive oxygen species, resulting in the scission of polymer chains.^{174,175} Hydrolytic degradation arises when hydrolysable bonds (e.g., esters, amides, and carbonates) are cleaved by water, breaking down the polymer into oligomers and monomers. The rate of hydrolytic degradation can be tuned by modifying the morphological and hydrophilic characteristics of the bioadhesive. Finally, enzymatic degradation occurs through the catalysis of hydrolysis by endogenous enzymes, which accelerates biodegradation.^{176,177} Enzyme activity is influenced by

pH and temperature, which can vary across different anatomical sites. Overall, the design of specific chemical and surface characteristics modulates biodegradation. As these properties themselves change over the course of degradation, the interplay of biodegradation mechanisms is a dynamic process. Due to the multitude of influencing factors, it is difficult to accurately predict the timeline of in vivo biodegradation using in vitro experiments.

In certain physiological environments, biodegradation poses a substantial challenge to tissue repair. For example, the pancreas secretes a highly degradative juice containing a variety of digestive enzymes which, when leaked, can damage surrounding tissues and deteriorate suture or bioadhesive materials.^{178,179} The use of synthetic bioadhesives or enzyme inhibitors may potentially hinder this aggressive degradation process; however, the design of degradation-resistant bioadhesives which can withstand pancreatic juice, as well as gastric juice and bile, remains a prominent challenge.

As a product of the biodegradation process, clearance of implanted biomaterials from the body is essential to minimize adverse effects and interference with normal physiological processes. In general, biodegradation products can be eliminated via renal or hepatic routes. Designing bioadhesives with appropriate physicochemical properties and molecular sizes can facilitate their clearance and minimize the potential for long-term accumulation. The toxicity of biodegradation products is also a concern, exemplified by the release of cytotoxic formaldehyde from cyanoacrylate-based adhesives.¹⁸⁰

Removability is another important consideration for bioadhesives intended for short-term applications. Most internal applications disfavor the requirement of a secondary surgery to retrieve an implanted bioadhesive; however, for epidermal adhesion, it is often desirable to remove the bioadhesive on demand without causing damage to the underlying skin. Atraumatic detachment can be achieved through various mechanisms, such as using external triggers (e.g., heat, light, or specific chemical reactions) that weaken the adhesive interface, or employing adhesion strategies that rely on nondestructive physical interactions (e.g., PSAs, gecko-mimetic adhesives, and octopus-inspired adhesives).

2.3. Additional material selection considerations

Thus far, we have broadly discussed various material selection considerations from the lenses of mechanical properties, biocompatibility, and biodegradability. Worth noting are several additional considerations that may impact the adhesion performance and practical application of a bioadhesive material.

A key factor that influences the effectiveness of a bioadhesive is the kinetics of matrix formation and interfacial bond formation. Many flowable bioadhesives are composed of multiple components that interact at the time of application to form a cohesive matrix. The rate at which this crosslinking occurs can significantly affect the usability of the adhesive. Rapid crosslinking is generally advantageous for adhering to dynamic tissues and preventing displacement of the bioadhesive; however, it can also be difficult to control. For example, cyanoacrylate-based adhesives tend to polymerize very quickly upon contact with water, which can be useful in emergency scenarios, but also risks imprecise application. In contrast, slow crosslinking offers finer placement and allows for readjustments, but may be impractical in time-sensitive surgical

contexts. The appropriate time window of adhesion is influenced by the specific clinical application. Bioadhesives targeting the heart, lungs, or other dynamic organs should be designed to have sufficiently fast crosslinking kinetics relative to the characteristic timescale of tissue movement. Note that this time may vary depending on the surgical conditions (e.g., the level of anesthesia) and the physiology of the individual patient. In general, reaction kinetics may be controlled by tuning the type and concentration of crosslinking agent(s), the availability of crosslinking sites in the bioadhesive material system, the pH of the reactive solutions, and the intensity of external triggers such as UV light (for photochemical crosslinking).

The rheological properties of a bioadhesive also play a pivotal role in its adhesion performance, as they determine its ability to flow and conform to irregular tissue surfaces and mechanically interlock with surface asperities. In this regard, the viscosity of a bioadhesive precursor should be carefully tuned: overly viscous materials may not effectively penetrate or conform to tissues, while excessively fluid ones may wash away or form insufficient adhesion. Furthermore, the shear-thinning behavior of a flowable bioadhesive is an important property for ensuring that it can be administered through the narrow tip of a syringe while maintaining sufficient structure to avoid washout from the application site.¹⁸¹ The incorporation of rheology modifiers, such as pectin or nanomaterials, is one strategy that can be used to adjust shear-thinning properties.^{182,183}

For preformed bioadhesives (e.g., patches, tapes), the adhesion formation time is largely determined by the time it takes for the bioadhesive material to form direct tissue contact. Employing hydrophilic materials that can undergo rapid hydration has been an effective strategy to remove interfacial biofluids and enforce fast tissue-material consolidation, enabling tissue adhesion within seconds.²⁴

2.4. Experimental methods

Tissue adhesion is dependent on contributions of factors that can vary widely, such as tissue surface chemistry (which influences the strength of the interfacial linkages) and mechanical properties (which influences how much energy is dissipated in both the adhesive and the adherend). Therefore, when it comes to performing adhesion characterization experiments, the choice of substrate will play a prominent role in the measured outcome. Using biological tissues sourced from animals is often regarded as the gold standard due to their proximity to in vivo human tissues. However, the intrinsic variability of tissue properties depending on factors such as fat composition, storage conditions, and tissue age undermines the repeatability of using tissues as substrates. To perform more standardized comparisons, synthesized biopolymer-based substrates (e.g., gelatin- or collagen-based hydrogels) could be used to assess adhesion with reduced batch-to-batch variability. However, measurements based on lower-fidelity substrates may be less effective at representing in vivo adhesion performance. In general, a combined approach can be effective: starting with a lower-fidelity but more consistent substrate to quantitatively benchmark performance deltas between adhesives, then using biological tissues to further validate their adhesion capability.

Adhesion is most commonly quantified using one or more of the following experimental tests based on standards established by the American Society for Testing and Materials (ASTM): the T-peel test (ASTM F2256, measuring interfacial toughness); the lap shear test (ASTM F2255, measuring shear strength), the tensile test (ASTM F2258, measuring tensile strength); and the burst

test (ASTM F2392, measuring burst pressure). The experimental setups and corresponding data outputs are illustrated in **Figure 2-4**. For soft tissues and bioadhesives, a stiff backing can be used to minimize elongation of the detached portion in the T-peel and lap-shear tests. Depending on the target application of a certain bioadhesive, specific adhesion tests may have greater clinical relevance than others. For example, it would be appropriate to evaluate sealants designed to prevent air or fluid leakages by measuring their burst pressure with relevant tissues.

The viscoelastic nature of polymeric materials and tissues, combined with the rate dependence of bond dissociation processes, introduces another aspect to consider: the rate at which peeling forces are applied affects the force required to initiate failure.^{126,184} In practical terms, the rate dependence of peeling forces has implications for the durability of a bioadhesive on different tissues and their ease of removal. In general, at low peel rates the adhesive interface experiences time to relax, resulting in a lower force required for failure. Conversely, at high peel rates the interface is subjected to rapid stress increases, leading to a higher force for failure. When conducting experiments to measure adhesion energy, it becomes useful to account for the rate dependence behavior of peeling forces. To consistently measure a lower bound of the interfacial toughness, a sufficiently low peel rate should be applied to capture the steady state behavior.

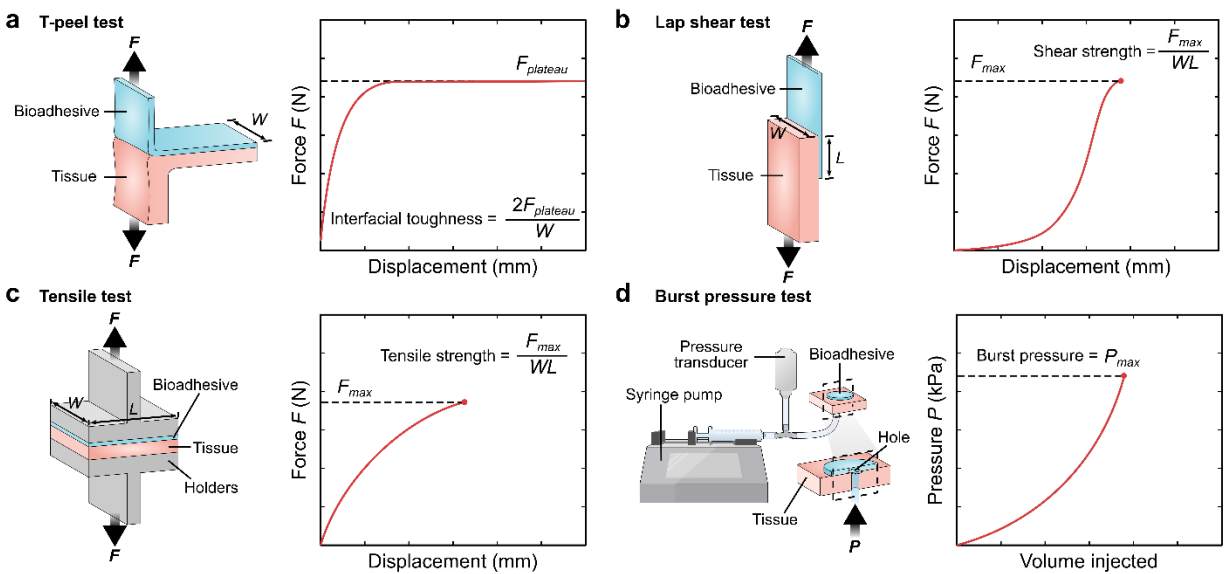


Figure 2-4. Experimental test setups for evaluating adhesion performance. (a) T-peel test based on ASTM F2256 for measuring interfacial toughness. (b) Lap shear test based on ASTM F2255 for measuring shear strength. (c) Tensile test based on ASTM F2258 for measuring tensile strength. (d) Burst pressure test based on ASTM F2392 for measuring burst pressure.

3. Minimally invasive tissue sealing (MITS) patch

3.1. Overview

3.1.1. Clinical motivation

Over the past several decades, advancements in imaging, endoscopic instrumentation, and robotic technologies have enabled general surgery to evolve toward less invasive procedures, resulting in substantial improvements in patient outcomes such as decreases in blood loss, operation and recovery times, and postoperative pain. Despite these innovations, the transition from open to minimally invasive surgery (MIS) comes with significant challenges, particularly for procedures of greater complexity. One critical challenge in MIS is the ability to connect tissues. Current methods for repairing and sealing injured tissues remain largely based on the traditional approaches of sutures and staples; however, these modalities have inherent drawbacks which are often amplified in minimally invasive settings. Compared to conventional open surgical procedures, the use of endoscopic equipment can limit visualization, depth perception, range of motion, and haptic feedback. Consequently, complex manipulations such as suturing and knot-tying are difficult to achieve, necessitating a high level of surgical skill and specialized dexterous tools. Moreover, both sutures and staples can be mechanically damaging to tissues and are prone to leakage and separation. The associated postoperative complications, such as an anastomotic leak, can have devastating clinical consequences for patients and often require conversion to open surgery in order to achieve definitive surgical repair.

While bioadhesives offer the potential to overcome these limitations, existing commercially-available bioadhesives have significant drawbacks. Bioadhesives in the forms of liquids and glues can be easily displaced or diluted in dynamic physiological environments. On the other hand, hydrogel or patches can be difficult to maneuver without open surgical access. Both form factors may also suffer from contamination by blood or mucus as they travel through minimally invasive channels, rendering them ineffective before they can be applied to the target site. Additional clinical concerns include inflammatory responses, such as postoperative adhesion formation, and perioperative infectious complications.^{8,185,186} In particular, postoperative adhesions represent major clinical complications following pericardial, abdominal, and intrauterine surgery. Characterized by fibrous bands of scar tissue creating abnormal seams between organ surfaces, adhesions can lead to loss of tissue function and often require substantial surgical reintervention (i.e., adhesiolysis procedures).

3.1.2. Proposed solution

To address the specific challenges described above, a multiscale design approach was employed with the following aims:

1. To achieve fast, strong adhesion to wet tissue surfaces;
2. To resist contamination by body fluids;
3. To mitigate postoperative inflammatory and infectious complications;

4. To allow facile delivery and application using minimally invasive surgical instruments.

This chapter of the thesis describes the design, development, and experimental results of a solid patch featuring multiple functional layers: (1) a bioadhesive substrate, (2) a protective hydrophobic matrix, and (3) an antifouling non-adhesive backing (**Figure 3-1**). To start, these three components are designed on a material level to achieve their individual target functionalities. Then, through mesoscale design of a multilayer patch architecture, the components are synergistically combined to yield a patch possessing multiple functionalities. Finally, on the macroscale design level, an origami-inspired approach is used to design deployable form factors that can be coupled with minimally invasive surgical instruments.

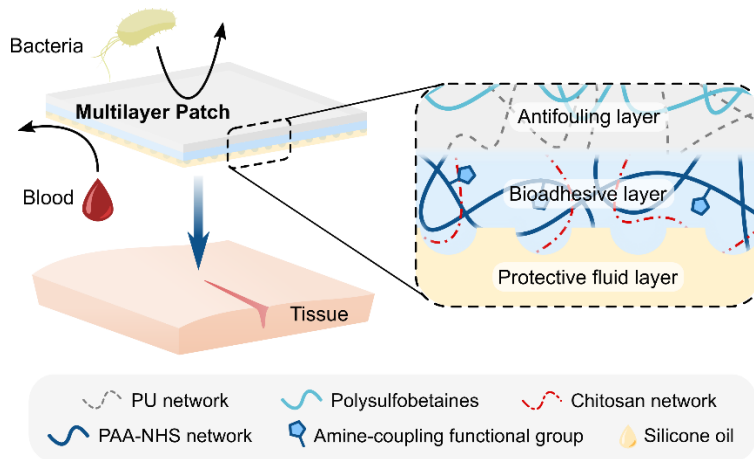


Figure 3-1. Schematic of the minimally invasive tissue sealing (MITS) patch. The patch comprises a textured bioadhesive fused with an antifouling polymer layer on the non-adhesive side, and is wetted with a hydrophobic fluid layer on the adhesive side to repel body fluids en route to the target site.

3.2. Material design

2.2.1. Bioadhesive material

The bioadhesive material system described in this work is a double-network hydrogel comprised of poly(acrylic acid) grafted with *N*-hydroxysuccinimide ester (PAA-NHS ester) and chitosan.^{24,130} Poly(acrylic acid) is a highly hydrophilic polymer which is rich with ionizable carboxylic acid side chains (**Figure 3-2a**). PAA-based materials are therefore capable of rapidly absorbing water and forming a high density of hydrogen bonds, creating fast interfacial linkages. NHS ester functionalization further increases the interfacial bond strength, by providing the polymer with groups that can form covalent bonds with primary tissue amines. Grafting of NHS esters to PAA can be carried out using carbodiimide (EDC/NHS) crosslinker chemistry: first, carboxylic acid groups on PAA react with EDC to form an active intermediate. The unstable intermediate reacts with NHS (or water-soluble Sulfo-NHS) to form an amine-reactive NHS ester, which can later conjugate to primary amines to form a stable amide bond (**Figure 3-3**).¹⁸⁷

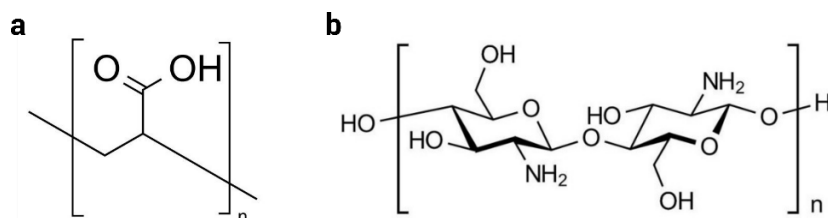


Figure 3-2. Chemical structures of (a) poly(acrylic acid) and (b) chitosan.

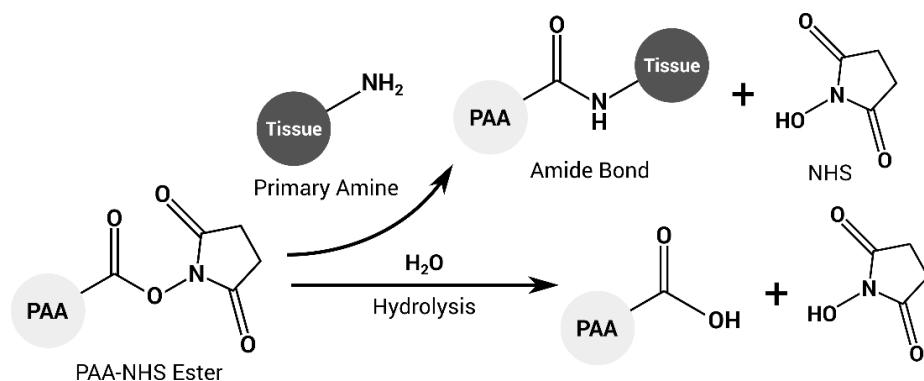


Figure 3-3. PAA-NHS ester reaction scheme for the formation of an amide bond between primary amines in proteins contained on tissue surfaces (upper), and the competing hydrolysis reaction (lower).

The second key component in the bioadhesive material is chitosan, a natural polysaccharide derived from chitin (**Figure 3-2b**)^{188,189}. Chitosan has been employed in a wide variety of biomedical applications, including as microspheres for drug delivery, coatings for orthopedic implants, scaffolds for tissue engineering, and various forms of bioadhesive materials. In addition to exhibiting favorable properties such as biocompatibility, non-toxicity, non-antigenicity, and low reactivity, the chemical structure of chitosan contains cationic amino groups which can form electrostatic interactions with tissue surfaces. Moreover, chitosan can be degraded by enzyme-catalyzed hydrolysis and is thus an excellent candidate for biomedical applications.

Drawing from the advantages of both polymers, the bioadhesive material used in this work is an interpenetrating network (IPN) of PAA-NHS ester and chitosan. As described in Section 2.1.2, the IPN architecture provides an energy dissipation mechanism for the material, making it tough. The material is prepared via photopolymerization of the precursor solution, which contains the monomers, α -ketoglutaric acid as a photo-initiator, and poly(ethylene glycol dimethacrylate) (PEGDMA) as a biodegradable crosslinking agent.

To reduce the time to form adhesion, the PAA-NHS ester/chitosan network employs a dry-crosslinking mechanism^{24,130}: first, the dry material is brought into contact with the wet tissue surface, and the highly hydrophilic PAA chains enable the material to rapidly absorb interfacial water. Removal of the interfacial water occurs within seconds, which causes the material to swell (equilibrium water content of around 92% by volume) and quickly form physical crosslinks with

the tissue. Owing to the carboxylic acid side chains of PAA, a high density of hydrogen bonds between the material and the tissue can be achieved. Electrostatic interactions between moieties of both PAA and chitosan further contribute to the short-timescale adhesion strength. The second part of the dry-crosslinking mechanism entails formation of covalent amide bonds between the NHS ester groups grafted on PAA and primary amine residues which are abundant on tissue surfaces. This covalent coupling is key to the long-term stable adhesion of the material.

2.2.2. Hydrophobic fluid

The liquid infiltrating the microtextured substrate plays a key role in the overall design of the LIS. For the liquid to maintain stability through the process of being maneuvered within the body, viscosity is an important parameter. While higher viscosity fluids tend to remain more stable when infiltrated into a textured substrate, they can also lead to greater frictional forces with immiscible liquids, resulting in a reduction in the repelled droplet velocity.^{190,191} Furthermore, current designs and applications of liquid-infused films typically have the singular aim to maintain the protective overlayer indefinitely; however, in this case, the ultimate fate of the lubricating layer is to be removed from the interface in order to expose the underlying adhesive material for tissue contact. Therefore, the pressure threshold required to squeeze out the interfacial oil should not be too excessive, as this could potentially cause tissue damage. The lubricating fluid must also be immiscible with blood and other body fluids, exhibit good chemical affinity with the bioadhesive substrate, and not induce secondary wound contamination or have toxic effects. Based on these requirements, silicone oil (100 cSt) was selected as the lubricating fluid for the liquid-infused bioadhesive system.

Regarding the biosafety of silicone oils, some silicone oils are routinely used as medical lubricants for minimally invasive devices and implants, as well as intraocular tamponades during vitreoretinal surgery (albeit in small quantities).¹⁹² In general, it has been reported that silicone oils with a higher average molecular weight tend to exhibit greater biocompatibility due to a lower tendency to emulsify. Future iterations of the liquid-infused bioadhesive design may benefit from investigating the performance of naturally derived oils, such as soybean and vegetable oils, which could provide greater biodegradability (for example, the liquid-infused system described in Chapter 5).

2.2.3. Antifouling material

The third component of the multilayer patch resides on the non-tissue-facing side which interacts with the surrounding physiological environment. This layer takes the form of a flexible and stretchable elastomer film interpenetrated with zwitterionic polymers. Its key function is to provide an antifouling surface to mitigate inflammatory responses and infectious complications.

Zwitterions describe unique molecules containing an equal number of separate positively- and negatively-charged functional groups. Naturally-occurring zwitterionic materials are abundant in biological systems (e.g., amino acids) and play distinct functional roles based on their charge group interactions. Synthetic zwitterionic materials were first reported in the 1950s.¹⁹³ Since then, zwitterionic materials have been used for a wide range of applications. Most notably, zwitterionic polymers have been found to exhibit remarkable antifouling properties due to their ability to attract

a tight hydration shell while minimally disrupting the hydrogen-bonding structure of free water molecules.^{158,194–199} Disturbance of this hydration shell carries a high energy cost which precludes the surface adsorption of bacteria and biomolecules (**Figure 3-4**). Owing to these features, zwitterionic polymers are attractive candidates for mitigating fouling by proteins, cells, and bacteria which are associated with clinical complications such as infection, blood coagulation, and postoperative adhesion formation.

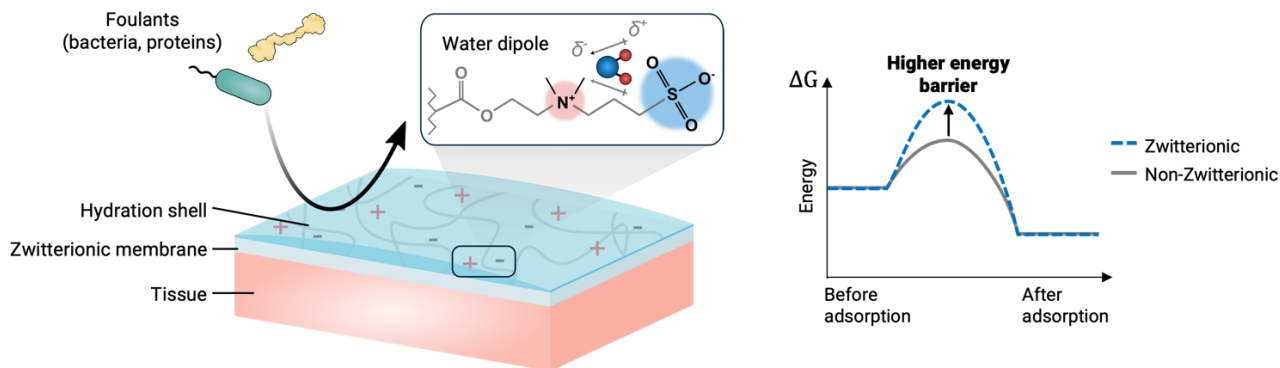


Figure 3-4. Antifouling properties of zwitterionic materials. Foulant adsorption is prevented due to the formation of a tightly bound hydration layer caused by electrostatic interactions between water molecules and the charged ionic groups. Representative reaction coordinate diagram showing the increased energy barrier for adsorption associated with displacing the hydration shell surrounding a zwitterionic material.

Two of the most commonly-used zwitterionic monomers contain cationic trimethyl ammonium groups and are classified as sulfobetaine (SB) and carboxybetaine (CB) based on their corresponding anions (sulfonate and carboxylate). Of these, SB monomers are more easily prepared and thus have a lower production cost, while CB monomers present greater design flexibility due to their amenability for functionalization of the $-\text{COOH}$ groups.¹⁵⁸ Both moieties exhibit strong hydration behavior, which is a requisite for preventing protein adsorption. Despite their remarkable antifouling performance, poly(sulfobetaine) (pSB) and poly(carboxylbetaine) (pCB) based hydrogels typically suffer from poor mechanical properties, such as low toughness and stretchability, which hinders their long-term robustness and stability in physiological environments. Here, a strategy for interpenetrating zwitterionic polymers into the surface of an elastomer film is presented. This strategy achieves antifouling surface modification while maintaining the elasticity and mechanical strength of the bulk elastomer.

For the bulk material of the antifouling layer, thermoplastic polyurethane is an excellent candidate owing to its flexibility and strength, as well as its commercial availability. Medical-grade polyurethanes featuring a range of mechanical properties are widely manufactured for use in the preparation of different types of medical devices, including implants, artificial organs, and device coatings.²⁰⁰ Here, a hydrophilic ether-based polyurethane which has undergone biocompatibility testing is used (purchased from AdvanSource Biomaterials). The polyurethane is soluble in 95 v/v % ethanol, and the solution can be readily spin coated into a thin, flat film.

The zwitterionic surface-interpenetration process is depicted in **Figure 3-5**. First, the base film is created by spin-coating a solution containing polyurethane and a hydrophobic photoinitiator (specifically, benzophenone). After the film is fully dried, it is submerged into an aqueous solution containing the zwitterionic monomer (e.g., SB or CB monomers) and a hydrophilic photoinitiator (e.g., α -ketoglutaric acid). Due to the insolubility of the hydrophobic initiator in aqueous solution, it remains embedded in the polyurethane film and does not diffuse into the zwitterionic solution. Polymerization of the zwitterionic solution occurs under UV irradiation, during which the hydrophobic initiators contained at the surface of the polyurethane film serve as grafting agents for the zwitterionic polymers to crosslink with the polyurethane chains.²⁰¹ In the reaction solution, the hydrophilic initiators assist in the polymerization of the zwitterionic monomers. After reaction, the film is thoroughly washed for several days to remove unreacted zwitterionic monomers and ungrafted polymers. The resultant film bears zwitterionic polymers interpenetrated at the surface, which can be experimentally validated using chemical analysis methods.

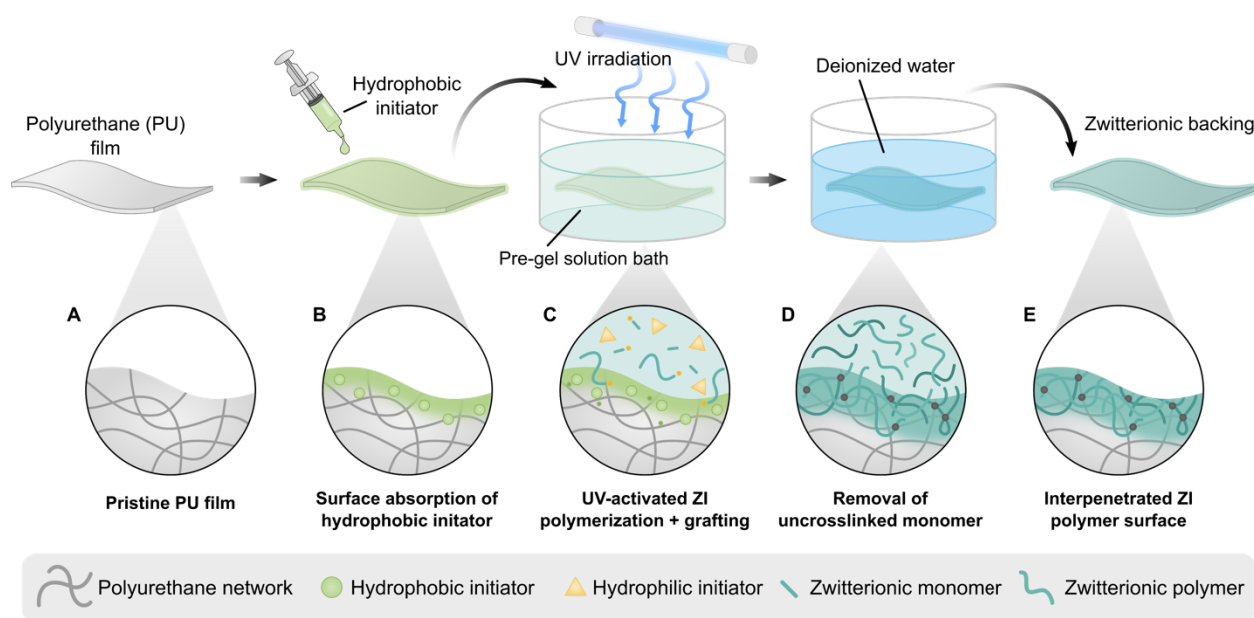


Figure 3-5. Fabrication strategy for producing a zwitterionic polymer-interpenetrated polyurethane film. (a) A thin film of hydrophilic PU is treated with a hydrophobic initiator (i.e., benzophenone). (b) The treated PU film is submerged in a precursor solution containing the zwitterionic monomer and hydrophilic initiator, then cured in a UV chamber. (c) The sample is washed in a large volume of deionized water, yielding (e) a zwitterionic-interpenetrated polyurethane film.

3.3. Patch architecture design

To achieve a stable yet dynamic fluid matrix to resist blood contamination, the surface of the bioadhesive layer was designed to promote liquid infiltration.

Textured liquid-infused surfaces have been reported to show excellent antifouling behavior, with broad applications ranging from anti-icing surfaces to biofilm-resistant catheters and implants.^{129,190,191,202–205} The basic principle behind liquid-infused surfaces (LIS), also known as slippery liquid-infused porous surfaces (SLIPS), lies in the tethering of a liquid to a surface, stabilized by surface chemistry and topographical effects, to provide a physical barrier which precludes adsorption to and fouling of the solid surface. The design of liquid-infused surfaces draws inspiration from nature: carnivorous *Nepenthes* pitcher plants possess leaves with special surface properties adapted to capture prey.²⁰⁶ These surfaces feature a highly regular microstructure of ridges projecting from the pitcher wall. When wet, the microstructure is remarkably effective at locking in a slippery fluid layer, so that the pitcher leaf becomes covered by a thin, stable liquid film which causes insects to slide into the digestive region by a process known as aquaplaning. The high wettability of *Nepenthes* leaves is attributed to a combination of hydrophilicity and surface microtopography.

By harnessing design principles similar to those exhibited by the *Nepenthes* pitcher plant, synthetic versions of slippery liquid-infused surfaces can be produced which exhibit superior non-wetting behavior compared to typical solid-phase superhydrophobic surfaces (e.g. those based on the lotus effect).²⁰² The presence of a smooth liquid interface mitigates droplet pinning, allowing immiscible liquids to be roll off. Liquid-infused surfaces are created by fabricating a solid substrate featuring a nano- or micro-scale topography, which promotes wetting of a lubricating liquid via capillary wicking and increased contact area with the solid. The stability of the liquid-infused surface and its effectiveness in repelling immiscible liquids are governed by interfacial energy relations.

In this work, the bioadhesive layer features a micro-scale surface topography consisting of embedded bioadhesive microparticles (**Figures 3-6 and 3-7**). The micro-scale surface structure further plays a secondary role in adhesion by contributing mechanical interlocking effects. Friction between the roughened bioadhesive surface and the tissue substrate during the initial stages of contact and adhesion can also act to prevent sliding and displacement of the adhesive during the adhesion process.²⁰⁷

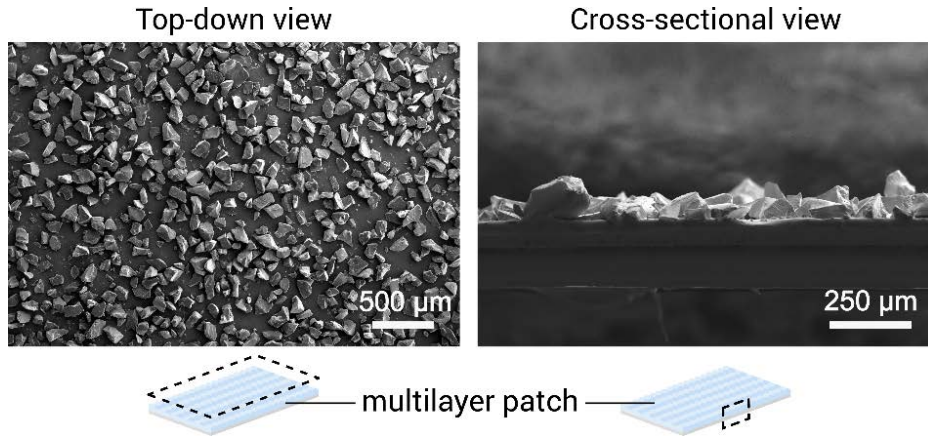


Figure 3-6. Scanning electron micrographs (SEMs) of the microtextured bioadhesive surface from a top-down (left) and cross-sectional (right) point of view. The surface is prepared by embedding cryogenically grinded bioadhesive microparticles prior to complete drying of the substrate. A lubricating fluid is later impinged into the microtopography to form a stable hydrophobic matrix.

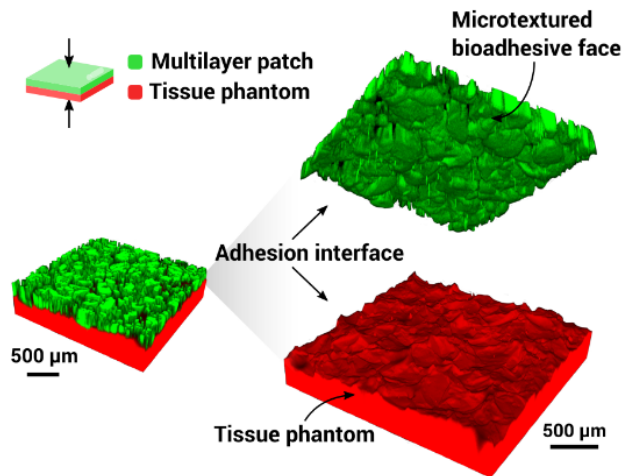


Figure 3-7. 3D reconstruction of confocal micrographs at the interface of adhesion between the microtextured bioadhesive face (green) and a gelatin-based tissue phantom (red).

3.3.1. Thermodynamic conditions

Smith *et al.* described the fundamental energy relations which govern the morphology of the liquid-substrate contact line.¹⁹¹ The design of a fluid-repellent liquid-infused surface generally requires consideration of the interactions between four phases present in the system: the lubricant, the ambient air, the liquid to be repelled, and the solid substrate (**Figure 3-8**). Here, the corresponding system components are silicone oil, air, contaminating body fluids (e.g., blood), and the bioadhesive material, respectively. An additional material—the biological tissue—should

also be considered for analysis of interactions at the tissue surface. These components will be denoted by subscripts o for oil, b for blood, a for air, ad for adhesive, and t for tissue.

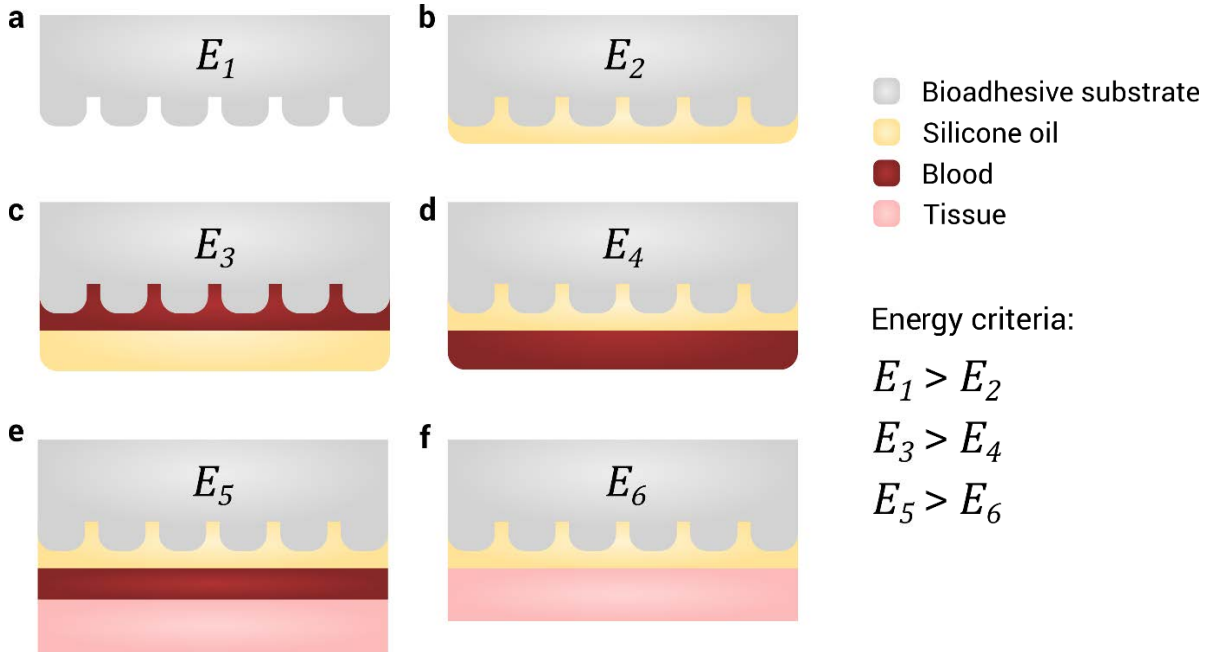


Figure 3-8. Schematics of the wetting configurations for a system comprising air, the bioadhesive substrate, silicone oil, blood, and tissue.

The microparticles embedded in the bioadhesive surface can be treated as a close-packed model of uniform hemispheres with radius R and packing density $D = \pi\sqrt{3}/6$ (i.e., hexagonal packing). The ratio of total surface area to the projected area is $r = \frac{4\pi R^2}{6\sqrt{3}R^2} = \frac{2\pi}{3\sqrt{3}}$.

First, to determine the stable configuration of the liquid-infused bioadhesive in air, we compare the total surface energies (denoted E_n) of two different configurations (a , b) consisting of the bioadhesive substrate, the lubricating fluid, and air. For the lubricant to infiltrate the bioadhesive surface, we require:

$$E_1 > E_2 \quad (3.1)$$

Applying Young's equation, this condition becomes:

$$r \cos \theta_{o/ad(a)} > 1 \quad (3.2)$$

where $\theta_{o/ad(a)}$ denotes the apparent contact angle of the silicone oil on the adhesive substrate in air.

By a similar treatment, for the bioadhesive surface to be preferentially wetted by the silicone oil in the presence of blood, the energies of configurations c and d can be compared:

$$E_3 > E_4 \Leftrightarrow \gamma_{o/a} \cos \theta_{o/ad(a)} - \gamma_{b/a} \cos \theta_{b/ad(a)} > 0 \quad (3.3)$$

where $\gamma_{x/y}$ denotes the interfacial energy between substances x and y .

Finally, we compare the total surface energies of two configurations (e , f) at the tissue surface to ensure the repulsion of blood by the silicone oil matrix. The corresponding energy relation that must be satisfied is:

$$E_5 > E_6 \Leftrightarrow \gamma_{\frac{o}{b}} + \gamma_{o/a} \cos \theta_{o/t(a)} - \gamma_{b/a} \cos \theta_{b/t(a)} > 0 \quad (3.4)$$

The conditions summarized by Eqns. (3.1)-(3.4) provide a toolkit for designing an effective blood-repellent liquid-infused bioadhesive system. System energies can be approximated by measuring the relevant contact angles, interfacial energies, and geometrical parameters. The values of the parameters for the present system are $\gamma_{o/a} = 20.9 \text{ mN m}^{-1}$, $\gamma_{b/a} = 72.0 \text{ mN m}^{-1}$, $\gamma_{o/b} = 40 \text{ mN m}^{-1}$, $\theta_{o/ad(a)} = 4.5^\circ$, $\theta_{b/ad(a)} = 96^\circ$, $\theta_{o/t(a)} = 4.2^\circ$, $\theta_{b/ad(a)} = 84^\circ$.²⁰⁸⁻²¹¹ Substitution of these values into the equations confirm that the energy criteria for stable oil infiltration and blood repellency at the tissue interface are satisfied.

Ultimately, the hydrophobic fluid layer should be removed from the bioadhesive/tissue interface to allow adhesion to occur (**Figure 3-9**). Dewetting of the textured surface occurs under the influence of externally applied pressure.

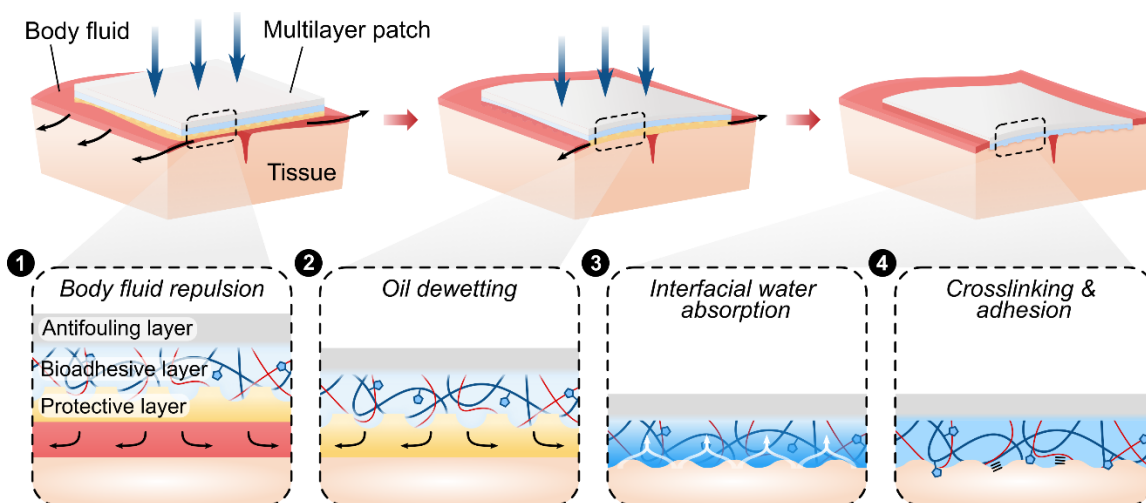


Figure 3-9. Schematic of the combined blood-repelling and adhesion mechanism. (1) As the patch is maneuvered toward the tissue, the infused silicone oil layer repels blood and prevents contamination of the bioadhesive layer. (2) External pressure application drives interfacial dewetting between the bioadhesive and the tissue substrate. (3) The bioadhesive layer makes contact with the tissue surface and undergoes rapid hydration, forming physical crosslinks. (4) Covalent bonds form between NHS ester functional groups in the bioadhesive network and primary amines on the tissue surface.

3.4. Methods and results

3.4.1. Preparation of the multilayer patch

Preparation of the bioadhesive Layer

For the 30 w/w % acrylic acid, 2 w/w % chitosan (HMC+ Chitoscience Chitosan 95/500, 95 % deacetylation), 1 w/w % acrylic acid N-hydroxysuccinimide ester, 0.2 w/w % α -ketoglutaric acid, and 0.05 w/w % Poly(ethylene glycol dimethacrylate) (PEGDMA; $M_n = 550$) were dissolved in deionized water. For fluorescent microscopic visualization of the bioadhesive layer, fluorescein-labeled chitosan was used. The precursor solution was poured on a glass mold with spacers (the thickness is 210 μm unless otherwise mentioned) and cured in a UV chamber (284 nm, 10 W power) for 30 min. Right after curing, dry bioadhesive microparticles were sifted through a 100 μm sieve over the surface of the bioadhesive hydrogel. The resulting bioadhesive hydrogel with surface-embedded microparticles was then thoroughly dried and sealed in plastic bags with desiccant (silica gel packets) and stored at $-20\text{ }^\circ\text{C}$ prior to assembly with the non-adhesive layer.

Preparation of the bioadhesive microparticles

A bioadhesive film was first prepared by casting, curing, and drying the precursor solution described above. The fully dried bioadhesive material was then cryogenically grinded at 30 Hz frequency for 2 min. The resulting bioadhesive microparticles were sealed in plastic bags with desiccant and stored at $-20\text{ }^\circ\text{C}$ until use.

Preparation of the zwitterionic-interpenetrated elastomer

10 w/w % hydrophilic PU (HydroMedTM D3, Advansource Biomaterials) and 0.1 w/w % benzophenone dissolved in ethanol/water mixture (95:5 v/v) was spin-coated at 200 rpm. The spin-coated film was dried under airflow overnight, then submerged into an aqueous solution containing 35 w/w % [2-(Methacryloyloxy)ethyl]dimethyl-(3-sulfopropyl)ammonium hydroxide (DMAPS) and 5 w/w % α -ketoglutaric acid for 10 min, followed by curing in a UV chamber (284 nm, 10 W power) for 1 h. The resultant film was thoroughly washed in a large volume of deionized water for 3 days to remove unreacted reagents, then thoroughly dried under airflow.

Assembly of the multilayer Patch

To combine the zwitterionic layer with the bioadhesive layer, a thin layer of 5 w/w % hydrophilic PU solution in ethanol/water mixture (95:5 v/v) was spin-coated at 400 rpm over the flat surface of the bioadhesive layer. The zwitterionic layer was then pressed on top and the entire assembly was thoroughly dried. The hydrophilic PU solution served as an adhesive between the zwitterionic layer and the bioadhesive layer by interpenetrating and drying between the two layers. To introduce the hydrophobic fluid layer, silicone oil (100 cSt viscosity) was first sterilized by filtration through a sterile membrane with 0.2 μm pore size to remove bacteria and other microorganisms. The sterilized silicone oil was then impinged on the microtextured surface of the bioadhesive layer.

3.4.2. Adhesion characterization

Blood resistance

To evaluate the protective capacity of the silicone oil-infused bioadhesive surface, samples of the patch with and without silicone oil were submerged in blood and their fouling behaviors were compared (**Figure 3-10**). When submerged in a porcine blood bath, the patch without the silicone oil layer is immediately wetted by the blood and loses its adhesive capability, whereas the patch with the protective silicone oil layer resists blood contamination and remains intact. To further investigate the effect of the surface microtopography on the stability of the fluid layer, patches with flat and microtextured bioadhesive surfaces were subjected to vigorous shaking in a porcine blood bath. While the multilayer patch with a flat bioadhesive surface shows substantial blood contamination after shaking, the patch comprising a microtextured surface exhibits robust protection of the bioadhesive layer against vigorous blood flow, supporting the significance of the microtextured design of the bioadhesive layer in order to achieve stable contaminant-repellent properties (**Figure 3-10b**).

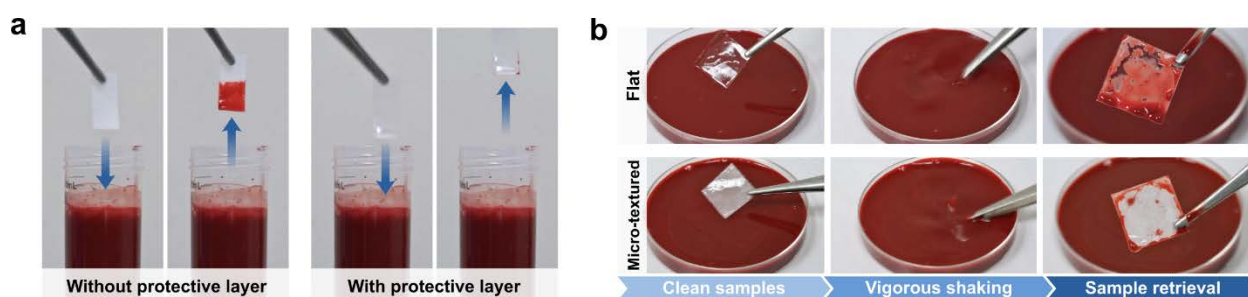


Figure 3-10. Blood resistance of the liquid-infused patch. (a) Photographs of multilayer patches with and without the hydrophobic fluid layer before and after submerging in a porcine blood. (b) Photographs of the multilayer patches with flat and microtextured bioadhesive layers before and after vigorously shaking in a porcine blood bath.

Interfacial fluid entrapment

To determine the optimal pressure conditions for removing interfacial blood and maximizing the contact area of adhesion, the amount of residual blood entrapped between patches and gelatin hydrogel tissue phantoms was quantified following adhesion under varying applied pressures covered with porcine blood (**Figures 3-11** and **3-12**). The gelatin hydrogel tissue phantoms were prepared by dissolving 10 w/w % gelatin (300 bloom) in deionized water at 40 °C, pouring the solution into a glass mold with 5 mm spacers, and then cooled at room temperature for 1 h. A sample of the multilayer patch (25.4 mm in width and 25.4 mm in length) was coated with silicone oil (100 cSt viscosity), then placed onto a gelatin hydrogel tissue phantom submerged in blood with the hydrophobic oil layer facing downward. The multilayer patch was pressed against the tissue phantom at varying applied pressures using a mechanical testing machine (2.5 kN load-cell,

Zwick/Roell Z2.5) for 5 s. The blood entrapped at the adhered patch-tissue phantom interface was visualized by taking photographs. To quantify the blood-entrapped area, the photographs were processed and analyzed by using ImageJ (**Figure 3-12**).

The adhesive shear strength of patches adhered to blood-covered porcine skin tissues under the same varying pressures was also measured (**Figure 3-11c** and **3-13**). As the applied pressure increases, the area of entrapped blood decreases while the adhesive shear strength increases. When the applied pressure exceeds 77.5 kPa, the amount of entrapped blood and the adhesive shear strength both reach plateau values, indicating that a threshold pressure of 77.5 kPa can effectively repel most of the interfacial blood and activate optimal adhesion of the multilayer patch. Notably, this level of pressure (i.e., around 100 kPa) can be readily applied by surgical end effectors such as staplers and balloons.

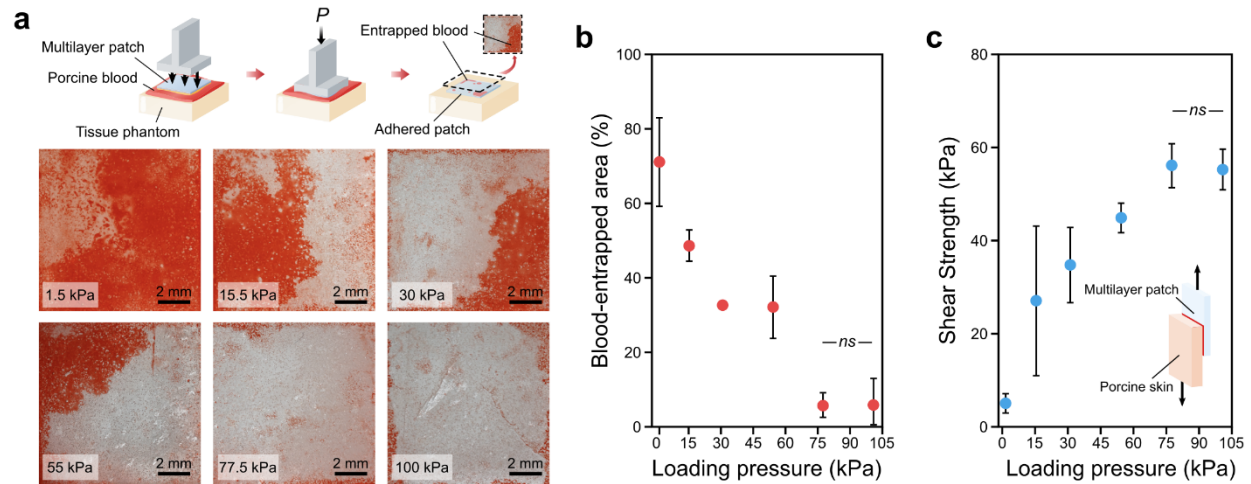


Figure 3-11. Characterization of blood repellence and adhesion performances of the multilayer patch under varying applied pressures. (a) Representative photographs of the interfaces between the adhered multilayer patches and tissue phantom gelatin hydrogels. (b) Percentage of blood-entrapped area at the interface as a function of applied pressure. (c) Shear strength of adhered multilayer patches and blood-covered porcine skin as a function of applied pressure. Values in (b,c) represent the mean and the standard deviation ($n = 2$). P values are determined by a Student's t-test; * $p \leq 0.05$; ** $p \leq 0.01$; *** $p \leq 0.001$.

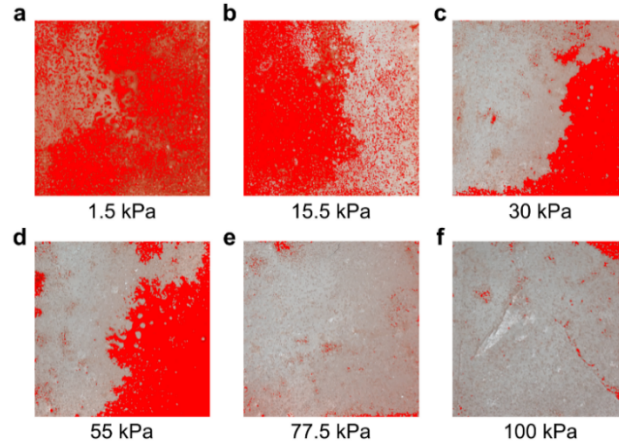


Figure 3-12. Representative processed images for the quantification of blood entrapment at the area of adhesion between the patches and blood-covered gelatin hydrogel tissue phantom compressed at (a) 1.5 kPa, (b) 15.5 kPa, (c) 30 kPa, (d) 55 kPa, (e) 77.5 kPa, and (f) 100 kPa for 5 s. Photographs were processed by globally thresholding in ImageJ, then analyzed to quantify the percentage of blood-entrapped area.

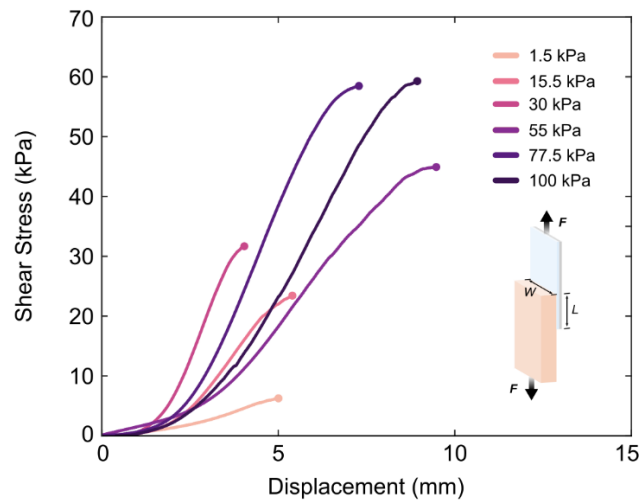


Figure 3-13. Shear stress vs. displacement curves for lap-shear tests of multilayer patches adhered to blood-covered porcine skins with varying applied pressures (1.5, 15.5, 30, 55, 77.5, and 100 kPa) for 5 s.

Quantitative adhesion characterization

To quantitatively evaluate the ability of the multilayer patch to form adhesion in blood, samples of the patch were adhered with porcine skin tissues submerged in a blood bath using an applied pressure of 77.5 kPa, and quantitatively assessed by 180-degree peel tests (ASTM F2256), lap-

shear tests (ASTM F2255), and tensile tests (ASTM F2258) to measure the interfacial toughness, shear strength, and tensile strength of the adhered samples, respectively (**Figure 3-14**).

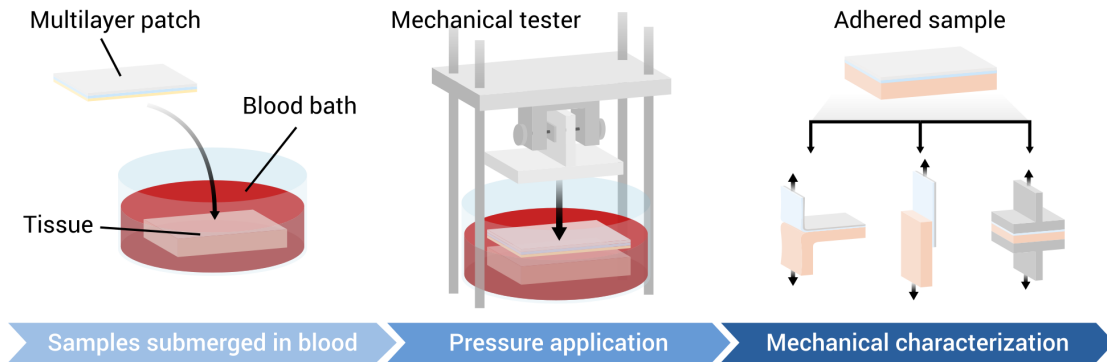


Figure 3-14. Experimental setup for the adhesion characterization of the multilayer patch and tissues submerged in blood. First, a sample of porcine tissue is covered with heparinized porcine blood. The multilayer patch is placed in the blood bath, then a mechanical tester applies a controlled pressure to adhere the patch to the tissue. After 5 s of pressure application, the adhered sample is collected for mechanical characterization to measure interfacial toughness, shear strength, or tensile strength, following ASTM standards F2256, F2255, and F2258.

The interfacial toughness, shear strength, and tensile strength of porcine skin tissues adhered using various commercially-available tissue adhesives were measured as well, including fibrin-based Tisseel, albumin-based Bioglue, polyethylene glycol (PEG)-based Coseal, and cyanoacrylate-based Histoacryl (**Figure 3-15**). Compared to these commercially-available tissue adhesives, the multilayer patch resists blood contamination and achieves significantly higher interfacial toughness ($536.7 \pm 93.4 \text{ J m}^{-2}$), shear strength ($56.1 \pm 4.7 \text{ kPa}$), and tensile strength ($65.0 \pm 8.0 \text{ kPa}$).

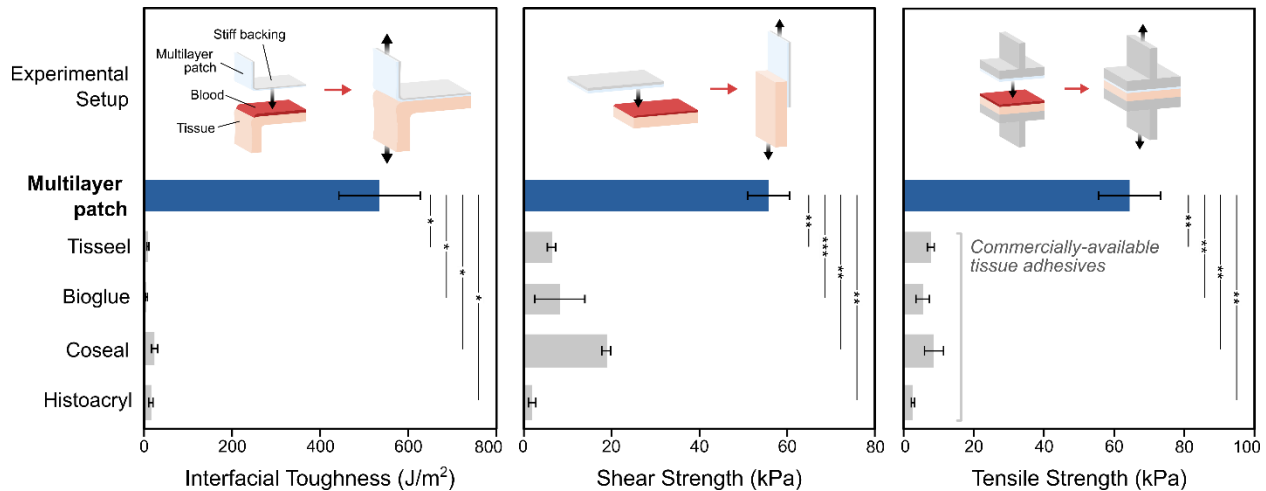


Figure 3-15. Comparison of adhesion performances of the multilayer patch and various commercially-available tissue adhesives, adhered to porcine skin coated with porcine blood. Values represent the mean and the standard deviation ($n = 3$). P values are determined by a Student's t -test; ns, not significant ($p > 0.05$); * $p \leq 0.05$; ** $p \leq 0.01$; *** $p \leq 0.001$.

3.4.3. Mechanical properties

Mechanical properties of the composite patch

The tensile properties and fracture toughness of the samples were measured using pure-shear tensile tests of thin rectangular samples (10 mm in length, 30 mm in width, and 0.5 mm in thickness) with a mechanical testing machine (20-N load-cell, Zwick/Roell Z2.5). All tests were conducted with a constant tensile speed of 50 mm min^{-1} . The fracture toughness of the samples was calculated based on tensile tests of unnotched and notched samples (**Figure 3-16**). The measured shear modulus of the fully assembled multilayer patch is 70 kPa, and the measured fracture toughness of the multilayer patch is $2,100 \text{ J m}^{-2}$.

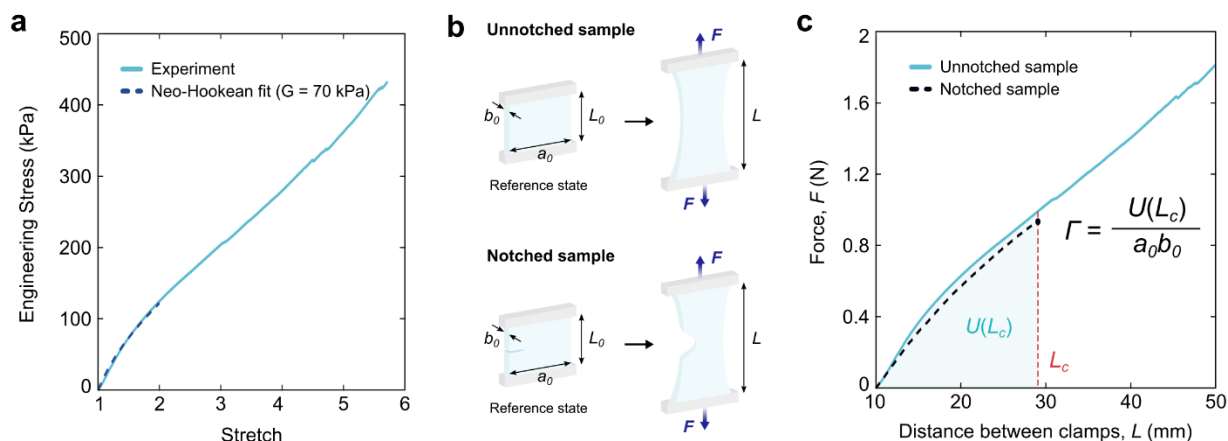


Figure 3-16. Mechanical characterization of the composite patch. (a) Engineering stress vs. stretch curve of the multilayer patch. The measured shear modulus of the multilayer patch is 70 kPa. (b) Schematic illustrations of a pure-shear test for unnotched and notched samples. (c) Force vs. distance between clamps curves for the unnotched and notched antifouling face. L_c indicates the critical distance between the clamps at which the notch turns into a running crack. The measured fracture toughness of the multilayer patch is $2,100 \text{ J m}^{-2}$.

Mechanical properties of the antifouling layer

The fracture toughness of the zwitterionic-interpenetrated polyurethane layer was compared with a pure zwitterionic hydrogel (**Figures 3-17 and 3-18**). To prepare the zwitterionic hydrogel, 50 w/w % DMAPS, 0.5% w/w % Irgacure 2959, and 0.5% w/w % PEGDMA were dissolved in deionized water. The precursor solution was then poured on a glass mold with 1 mm spacers and cured in a UV chamber (284 nm, 10 W power) for 60 min. Compared to the zwitterionic hydrogel (fracture toughness 0.35 J m^{-2} and stretchability less than 1.5 times of the original length), the zwitterionic-PU layer exhibits superior mechanical properties (fracture toughness around 420 J m^{-2} and stretchability over 3.5 times of the original length).

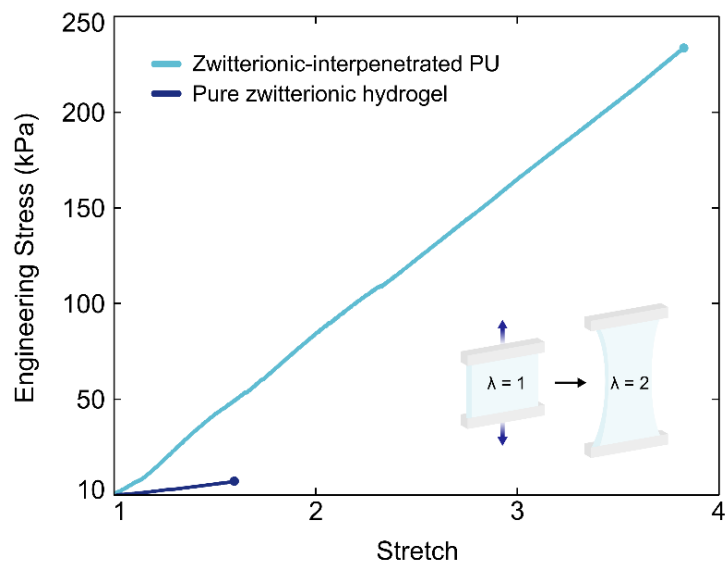


Figure 3-17. Engineering stress vs. stretch curves for the zwitterionic-interpenetrated polyurethane layer and a pure zwitterionic hydrogel.

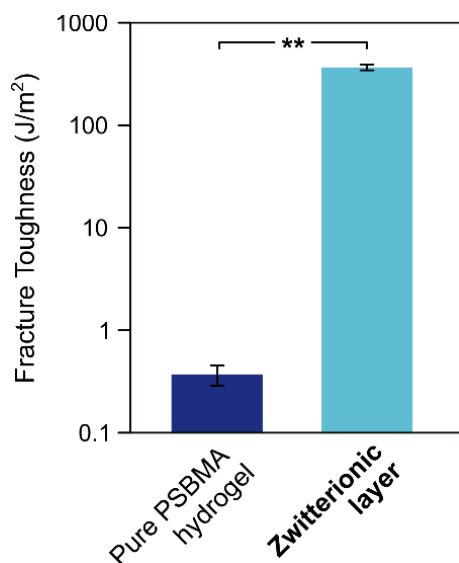


Figure 3-18. Fracture toughness of a pure zwitterionic hydrogel (0.35 J m⁻²) and the zwitterionic-interpenetrated elastomer layer (420 J m⁻²).

3.4.4. Antifouling Performance

Chemical characterization

To verify the presence of polysulfobetaines in the zwitterionic-interpenetrated polyurethane film, the surface was characterized by a transmission Fourier transform infrared spectroscope (FTIR

6700, Thermo Fisher) using a Germanium attenuated total reflectance (ATR) crystal (55 deg) (Figure 3-19). Compared to pristine PU, the FTIR spectrum for the zwitterionic-interpenetrated PU shows strong absorbance peaks at 1020 cm^{-1} and 1180 cm^{-1} , which correspond to vibrations of the sulfonate group ($-\text{SO}_3^-$) present in the sulfobetaine.¹⁹⁶

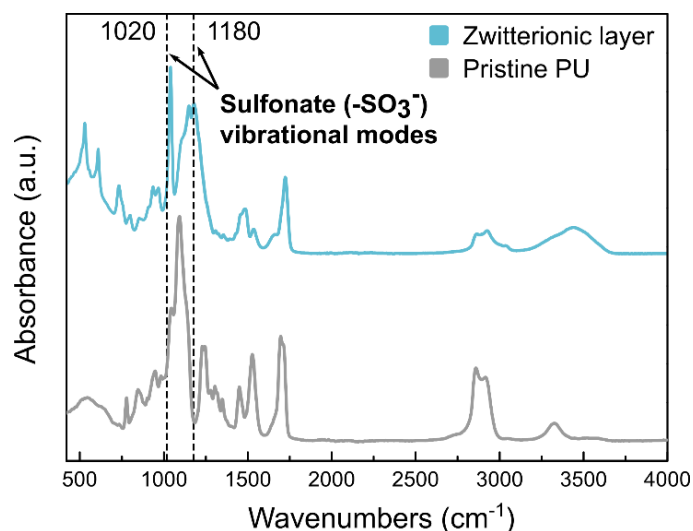


Figure 3-19. FTIR spectra of the zwitterionic layer and unmodified pristine hydrophilic PU; peaks at 1020 cm^{-1} and 1180 cm^{-1} correspond to vibrational modes of the sulfonate group ($-\text{SO}_3^-$).

Bacterial adhesion

To characterize the antifouling performance of the zwitterionic layer, its capability to mitigate *in vitro* bacterial adhesion was evaluated (Figure 3-20). Bacterial attachment to implanted materials can lead to biofilm formation and surgical site infection, which cause significant patient morbidity and substantial healthcare costs due to the need for additional procedures and antimicrobial therapies. To evaluate the antimicrobial performance of the zwitterionic layer, various patches with non-adhesive faces comprised of a hydrophobic polymer (polydimethylsiloxane, PDMS), a hydrophilic polymer (pristine hydrophilic PU), and the zwitterionic-interpenetrated elastomer were incubated with a green-fluorescent protein (GFP)-expressing *Escherichia coli* (*E. coli*).

An engineered *Escherichia coli* (*E. coli*) strain that constitutively expresses green fluorescent protein (GFP) was prepared by following a previously reported protocol and cultured in Luria-Bertani broth (LB broth) overnight at 37 °C. 1 μL of bacteria culture diluted in 1 mL of fresh LB broth was placed on samples (1 cm \times 1 cm) and incubated for 24 h at 37 °C.²⁰¹ After incubation, the samples were taken out and rinsed with phosphate buffered saline (PBS) to remove the free-floating bacteria, and imaged with a fluorescence microscope (Eclipse LV100ND, Nikon). The number of adhered *E. coli* on the samples per unit area (mm^2) were counted by ImageJ. In contrast to the patches featuring hydrophobic ($\sim 1,370$ counts mm^{-2}) and hydrophilic non-adhesive layers ($\sim 1,360$ counts mm^{-2}), the patch with the zwitterionic layer exhibits a significantly lower level of *E. coli* adhesion (~ 0.9 counts mm^{-2}).

Thrombogenicity

The antifouling performance of the zwitterionic layer was further assessed by evaluating its capacity to resist the adsorption of fibrinogen in porcine whole blood. Surface attachment of fibrinogen leads to the formation of a fibrin meshwork, which serves as the basis of a blood clot. Thus, the surface coverage of fibrin can indicate the potential for a biomaterial to induce platelet accumulation, activation, and thrombus formation, which are undesirable for applications in which the bioadhesive interfaces with a bloodstream. Samples with non-adhesive layers comprised of a hydrophobic polymer (PDMS), a hydrophilic polymer (pristine hydrophilic PU), and the zwitterionic-interpenetrated elastomer were submerged in a blood bath containing heparinized porcine whole blood spiked with Alexa Fluor 488-tagged fibrinogen.²¹²

A 5 v/v % solution of fetal bovine serum (FBS) in PBS used to block the wells of a 24-well plate for 30 min. The wells were rinsed with PBS, then 6 mm-diameter samples were placed in the blocked wells. The samples were submerged in porcine blood spiked with Alexa Fluor[®] 488-labeled human fibrinogen conjugate (66 μg fibrinogen mL^{-1} blood, Thermo Fisher) and incubated on a shaker in 220 rpm at room temperature for 60 min. The samples were gently rinsed in PBS and fixed for 1 hour in 2.5 v/v% glutaraldehyde in 0.1 M phosphate buffer. The samples were then imaged with a fluorescence microscope (Eclipse LV100ND, Nikon) and analyzed by using ImageJ.

Exhibiting similar behavior to the results for bacterial adhesion, the patch with the zwitterionic layer shows significantly lower levels of fibrin deposition ($\sim 0.1\%$ areal coverage) compared to the patches with hydrophobic ($\sim 3.09\%$ areal coverage) and hydrophilic faces ($\sim 2.16\%$ areal coverage) (**Figure 3-21**). These results suggest a lower thrombogenic risk associated with the zwitterionic material in contact with whole blood.

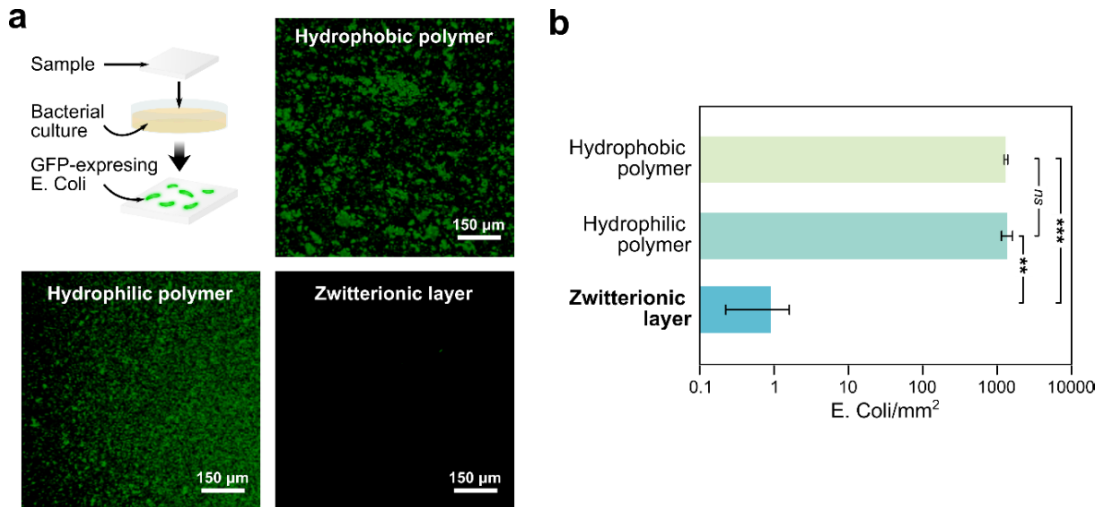


Figure 3-20. (a) Representative fluorescent micrographs of GFP-expressing *E. Coli* adhered to a hydrophobic polymer (PDMS), a hydrophilic polymer (PU), and the zwitterionic layer following 24 h incubation. (b) The number of adhered *E. Coli* per mm² for each substrate.

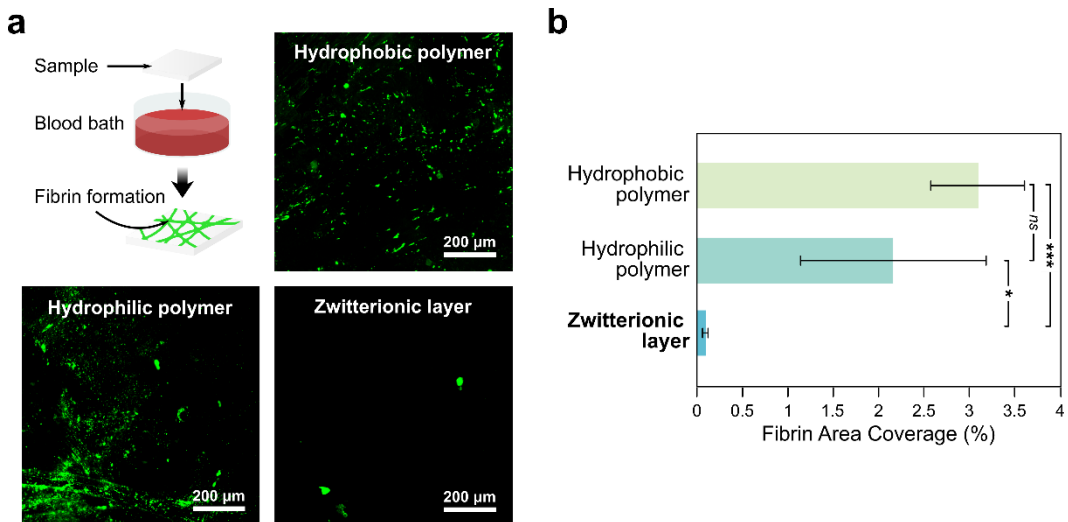


Figure 3-21. (a) Representative fluorescent micrographs of fibrin network formation on a hydrophobic polymer (PDMS), a hydrophilic polymer (PU), and the zwitterionic layer after 60 min of exposure to porcine whole blood spiked with fluorescently-tagged fibrinogen. (b) Fibrin area coverage (%) for each substrate.

3.4.5. Biocompatibility and biodegradation

In vivo implantation

All animal surgeries were reviewed and approved by the Committee on Animal Care at the Massachusetts Institute of Technology. Female Sprague Dawley rats (225-250 g, Charles River Laboratories) were used for all *in vivo* studies. Before implantation, the multilayer patch was prepared using aseptic techniques and was further sterilized for 3 hours under UV light. For implantation in the dorsal subcutaneous space, rats were anesthetized using isoflurane (1–2% isoflurane in oxygen) in an anesthetizing chamber. Anesthesia was maintained using a nose cone. The back hair was removed and the animals were placed over a heating pad for the duration of the surgery. The subcutaneous space was accessed by a 1-2 cm skin incision per implant in the center of the animal's back. To create space for implant placement, blunt dissection was performed from the incision towards the animal shoulder blades. multilayer patches with hydrophobic polymer (PDMS) faces ($n = 4$), hydrophilic polymer (pristine hydrophilic PU) faces ($n = 4$), and zwitterionic faces ($n = 4$) with the size of 10 mm in width and 20 mm in length were placed in the subcutaneous pocket created above the incision without detachment. The incision was closed using interrupted sutures (4-0 Vicryl, Ethicon) and 3-6 ml of saline were injected subcutaneously. Up to four implants were placed per animal ensuring no overlap between each subcutaneous pocket created. After 2 or 4 weeks following the implantation, the animals were euthanized by CO₂ inhalation. Subcutaneous regions of interest were excised and fixed in 10% formalin for 24 hours for histological analysis.

To evaluate the biocompatibility and *in vivo* antifouling performance of the multilayer patch, the fibrous capsule formed in response to a variety of patches was measured and compared. As described in the preceding section, rats were implanted with patches containing non-adhesive layers comprised of a hydrophobic polymer (PDMS), a hydrophilic polymer (pristine hydrophilic PU), and the zwitterionic-interpenetrated elastomer. At time points of 2 and 4 weeks following implantation, the tissues were collected and fixed and submitted for histological processing and Masson's Trichrome staining. The thickness of fibrous capsule was measured under a bright-field digital microscope (Eclipse LV100ND, Nikon) based on histology slides of each sample.

The formation of a thick fibrotic encapsulation around the surgical site is highly undesirable and can result in complications such as organ stricture and postoperative adhesions.^{185,213} After 2 weeks of implantation, histological analysis shows that the patch containing the zwitterionic layer exhibits a significantly thinner fibrous capsule around the patch ($145 \pm 29 \mu\text{m}$) compared to the patches with hydrophobic ($574 \pm 125 \mu\text{m}$) and hydrophilic polymer layers ($185 \pm 16 \mu\text{m}$) (**Figure 3-22a**). After 4 weeks of implantation, the patch with the zwitterionic layer maintains a similar thickness of fibrous capsule around the patch ($135 \pm 7 \mu\text{m}$) to the 2-week results, whereas the patches with hydrophobic ($1163 \pm 138 \mu\text{m}$) and hydrophilic ($307 \pm 73 \mu\text{m}$) polymer layers exhibit significantly thicker fibrous capsules than their respective 2-week results (**Figure 3-22b**).

In summary, these results suggest that the zwitterionic layer of the multilayer patch possesses favorable capacities to resist excessive fibrosis around the injury site.

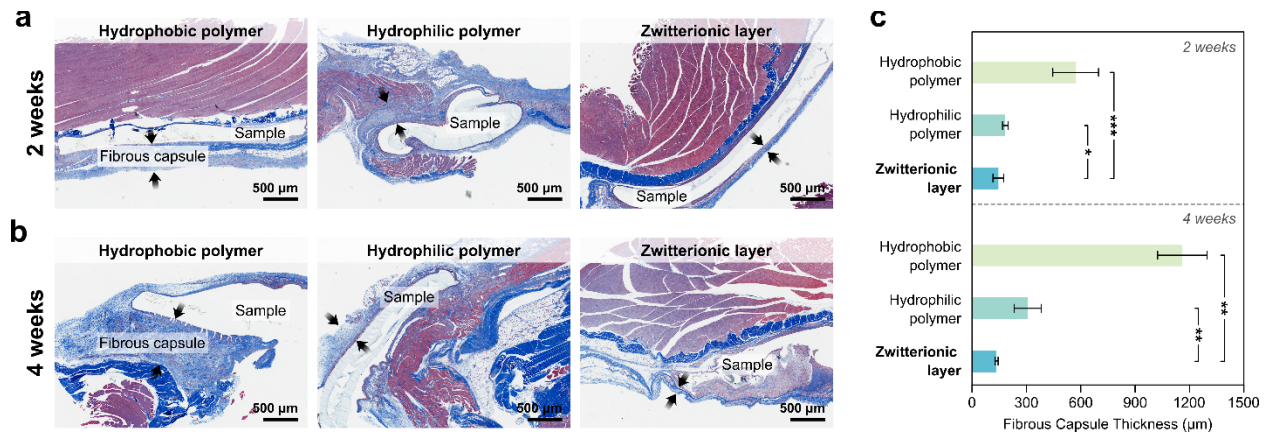


Figure 3-22. Biocompatibility of the MITS patch. (a,b) Representative histological images stained with Masson's trichrome for *in vivo* rat dorsal subcutaneous implantation of patches with non-adhesive faces comprised of a hydrophobic polymer (PDMS, left), a hydrophilic polymer (PU, middle), and the zwitterionic layer (right) after 2 weeks (a) and 4 weeks (b). (c) Fibrous capsule thickness formed around the implanted samples after *in vivo* the implantation. Values in (c) represent the mean and the standard deviation ($n = 4$). P values are determined by a Student's t -test; * $p \leq 0.05$; ** $p \leq 0.01$; *** $p \leq 0.001$.

Inflammation scoring

To further investigate the *in vivo* biocompatibility of the multilayer patch, histological images of the implanted samples were submitted for histological analysis and evaluated by a blinded pathologist (**Figure 3-23**). The degree of inflammation at the implantation site for the zwitterionic layer-containing patch received average scores of 1.33 and 1.67 after 2 and 4 weeks, respectively, which fall within the “very mild” to “mild” inflammation range. These results indicate that the multilayer patch elicits low levels of acute and chronic inflammation.

Biostability

The multilayer patch exhibits stability for several weeks at the implantation site *in vivo* (**Figure 3-24**). Because the bioadhesive layer is comprised of PAA-NHS ester crosslinked with biodegradable linkages and the biopolymer chitosan, it can be left to undergo enzymatic biodegradation within the body if it is intended to be implanted without recurrent surgery. The degradation rate can be tuned by changing the type of biopolymer used in the bioadhesive material (e.g., gelatin or alginate instead of chitosan) or the ratio of crosslinking agent used.

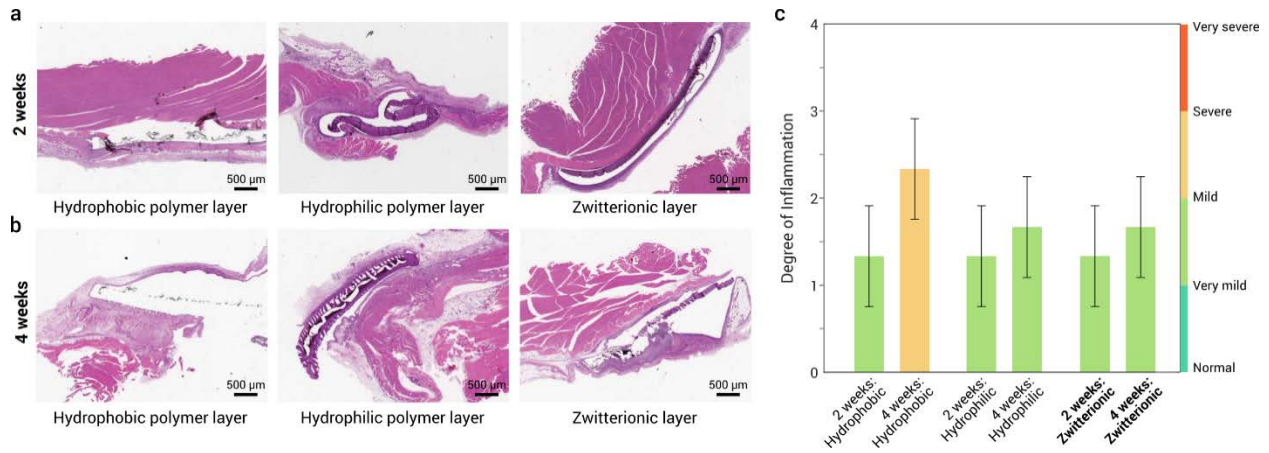


Figure 3-23. *In vivo* inflammation scoring of the multilayer patch. Representative H&E histological images of multilayer patches with non-adhesive layers comprised of a hydrophobic polymer, a hydrophilic polymer, and a zwitterionic-interpenetrated elastomer layer implanted into the dorsal subcutaneous spaces of rats after a) 2 weeks and b) 4 weeks. c) Histological evaluation of the degree of inflammation at the implantation sites by a blinded pathologist. Degree of inflammation is scored wherein 0 = normal, 1 very mild, 2 = mild, 3 = severe, and 4 = very severe. Values represent the mean and standard deviation ($n = 3$).

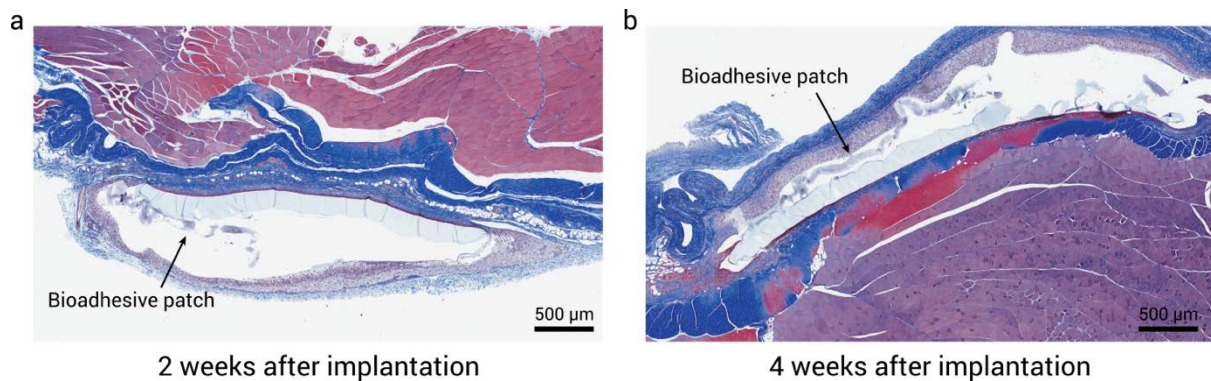


Figure 3-24. *In vivo* stability of the multilayer patch. Representative histological images stained with Masson's trichrome of samples implanted into the dorsal subcutaneous spaces of rats for a) 2 weeks and b) 4 weeks. At 4 weeks after implantation, the bioadhesive patch begins to exhibit visual signs of gradual degradation and decomposition.

3.5. Design for minimally invasive surgical applications

Beyond the functional requirements which guided the material properties and stack-up of the patch, the macroscale form factor of the MITS patch was driven by the goal of enabling a minimally invasive delivery process. This section discusses the process-level design considerations and describes prototypical device-coupled systems developed for ex vivo defect repair.

3.5.1. Origami-inspired approach

For the patch to be usable in minimally invasive surgical procedures, it should be able to be carried through narrow spaces and triggered to dewet and adhere on demand. To enable this process, inspiration was drawn from origami: the Japanese art of paper folding. The tape-like form-factor of the multilayer patch allows it to be folded into compact, three-dimensional shapes that are programmed to expand upon actuation of surgical end effectors.

Plastic-to-rubbery state transition

The basis of the origami-inspired design strategy lies in the transition of the bioadhesive polymer network from the glassy state, during which it can maintain a deformed shape, to the rubbery state, during which the strain at its folded hinges is released. The general strategy is alike that of shape memory polymers (SMPs), which are pre-deformed into temporal shapes in the glassy phase with the intent of recovering their original shapes in response to an external stimulus, such as temperature. Here, the dry bioadhesive material is in the glassy state at room temperature. When the patch is folded, the elastomer is constrained by the bioadhesive material due to its higher rigidity, such that the creases are held in place. Hydration of the bioadhesive material is the driving stimulus for the phase transition, which occurs upon tissue contact when interfacial water is absorbed. Hydration works by lowering the glass transition temperature of the material. As a result, the patch returns to the soft rubbery state and conforms to the tissue surface (**Figure 3-25**).

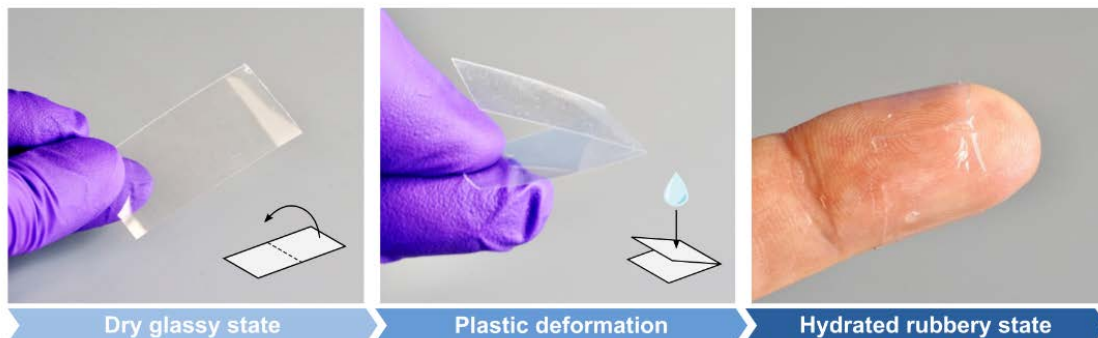


Figure 3-25. Photographs showing the multilayer patch in the plastically-deformable dry glassy state. Upon hydration, the folded patch transitions to the rubbery state and becomes a soft, conformable hydrogel.

3.5.2. Balloon catheter-based delivery

Balloon catheters have been used for a broad range of applications in various systems of the body, such as for angioplasty, stent delivery, and balloon occlusion. These devices are well-suited for the endoluminal delivery and precise deployment of medical devices and biomaterials in hollow structures (e.g., trachea, esophagus) and large vessels. To be made compatible with balloon catheter-based delivery, the patch can be folded into a sleeve circumscribing the uninflated balloon with the oil-impinged layer oriented radially outward (**Figure 3-26** and **3-27**). Once positioned at the defect site, inflation of the balloon will drive it to expand and cause the bioadhesive patch to unfold, making contact with the luminal tissue. The radial pressure exerted by the balloon on the bioadhesive and the tissue triggers the dewetting and adhesion of the bioadhesive, resulting in rapid endoluminal sealing. In a proof-of-concept prototype shown in **Figure 3-25a**, the bioadhesive patch was folded into a simple tri-faced sleeve for coupling with esophageal and Foley catheters. Alternatively, the sleeve can also take the form of a cylinder with numerous pleated “wings” (**Figure 3-25b**). In order to secure the positioning of the sleeve on the balloon, removable stabilizing elements (e.g., stiffening members which dissolve or fracture upon deployment) can be incorporated which restrict movement, bunching, or rotation during travel through the lumen.

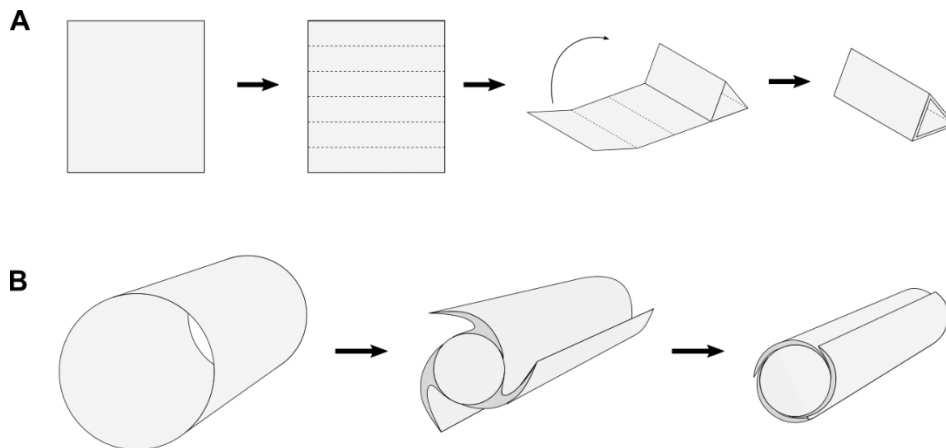


Figure 3-26. Folding schematic for (a) a triangular sleeve and (b) a pleated cylindrical sleeve with “wings” for integrating the bioadhesive patch with a balloon catheter. The numbers of edges and wings may vary.

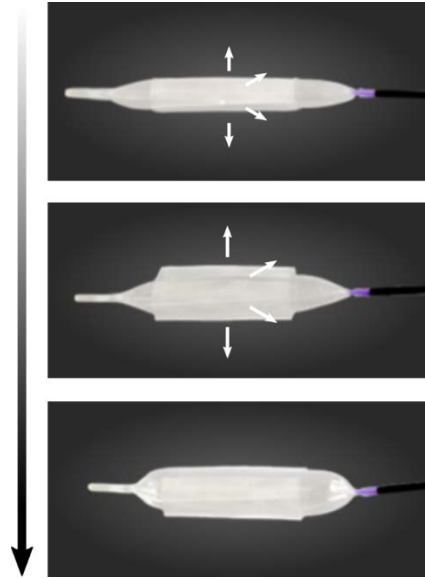


Figure 3-27. Photographs showing the deployment mechanism using an esophageal balloon catheter.

3.5.3. Stapler-based delivery

A common surgical instrument in endoscopic surgery is the articulating stapler, which is designed to cut and seal segments of tissue by clamping the desired tissue site between an anvil and a stapler cartridge, firing parallel lines of staples, and then actuating a blade to cut the tissue in between the two staples lines. While surgical staplers have substantial device failure rates when used to firing staples, the ability to maneuver surgical staplers through small ports and actuate the jaws to lock and apply firm compression provides these devices with versatile utility, including the potential to apply the multilayer patch.

To enable stapler-based minimally invasive delivery, the multilayer patch can be cut into various-sized strips and loaded in a folded origami sleeve designed to wrap around the anvil and cartridge units of the stapler (**Figure 3-28**). Once the stapler jaws are positioned around the site of the tissue injury, actuation of the stapler compresses the multilayer patches against the tissue surface, triggering adhesion and sealing of the defect (**Figure 3-29**).

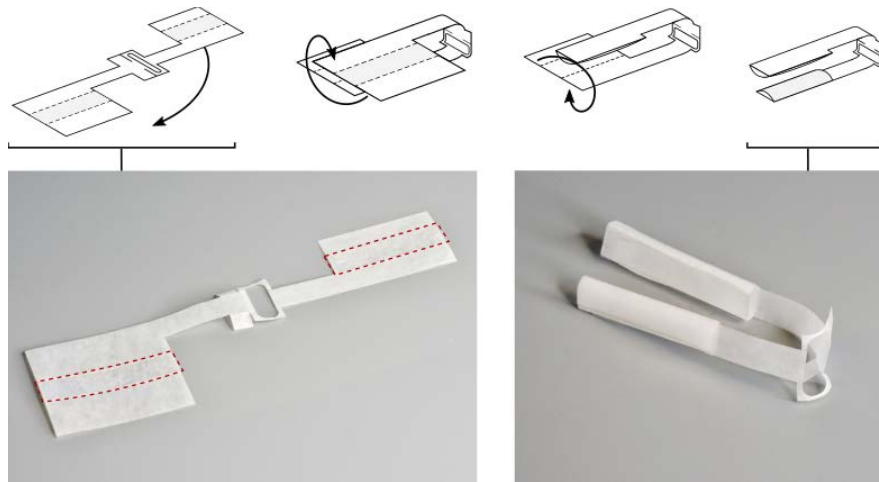


Figure 3-28. Folding schematic for integration with a surgical stapler.

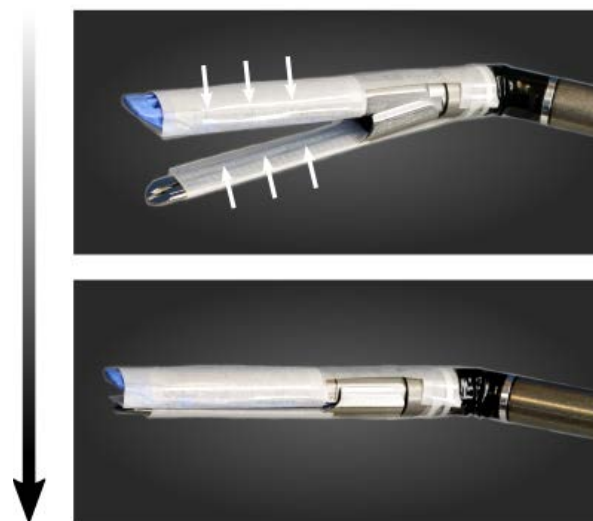


Figure 3-29. Photographs showing the deployment mechanism of the MITS patch using an articulating linear stapler.

3.5.4. Ex vivo demonstrations

To explore the translational potential of the multilayer patch, various proof-of-concept demonstrations using *ex vivo* porcine models were performed according to the two deployment strategies described above: tracheal defect repair, esophageal defect repair, aortic defect repair, and intestinal defect repair (**Figures 3-30** and **3-31**). All *ex vivo* experiments were reviewed and approved by the Committee on Animal Care at the Massachusetts Institute of Technology. All porcine tissues and organs for *ex vivo* experiments (skin, trachea, aorta, esophagus, intestine) were purchased from a research-grade porcine tissue vendor (Sierra Medical Inc.).

Tracheal defect model

For the *ex vivo* tracheal defect model, a 5 mm circular transmural defect was created in the wall of a porcine trachea (with intact lungs) using a biopsy punch. The upper portion of the trachea was connected to tubing through which air was pumped to the lung lobes. A multilayer patch was folded into an origami sleeve and fitted with a Foley catheter (ReliaMed). The assembled balloon was inserted into the lumen of the damaged trachea. Once the multilayer patch was located at the position of the defect, the balloon was inflated by introducing air into the catheter. Pressure was held for 5 seconds prior to deflation and removal of the balloon (**Figure 3-30a**). After sealing of the tracheal defect, air was pumped through the trachea to check for the hermetic sealing of the trachea. It was observed that the application and adhesion of the multilayer patch restored the previously compromised inflation capability of the lungs (**Figure 3-30b**).

Esophageal defect model

The esophageal defect repair model was similar to that for tracheal defect repair. Briefly, 5 mm circular transmural defect was punched in the wall of a porcine esophagus with a biopsy punch. Water was flowed through the esophagus using a tubing and a peristaltic pump (Thermo Fisher) to visualize leakage through the defect. A multilayer patch was folded into an origami sleeve and fitted with an esophageal catheter (Boston Scientific), then deployed at the defect site. After sealing of the esophageal defect, water was pumped through the trachea to check the fluid-tight sealing of the esophagus (**Figure 3-30c**). The esophageal seal withstood the pumping of water without leakage at supraphysiological pressures over 300 mm Hg.

Aortic defect model

The Foley catheter method described for the tracheal defect repair model was further used to achieve hemostatic sealing in an *ex vivo* aorta. Porcine blood was flowed through the aorta using a tubing and a peristaltic pump (Thermo Fischer) to visualize leakage through the defect (**Figure 3-30d**). As with the esophageal seal, the aortic seal withstood the pumping of water without leakage at supraphysiological pressures over 300 mm Hg. For all endoluminal delivery models, an endoscopic camera (DEPSTECH) was used for visualization.

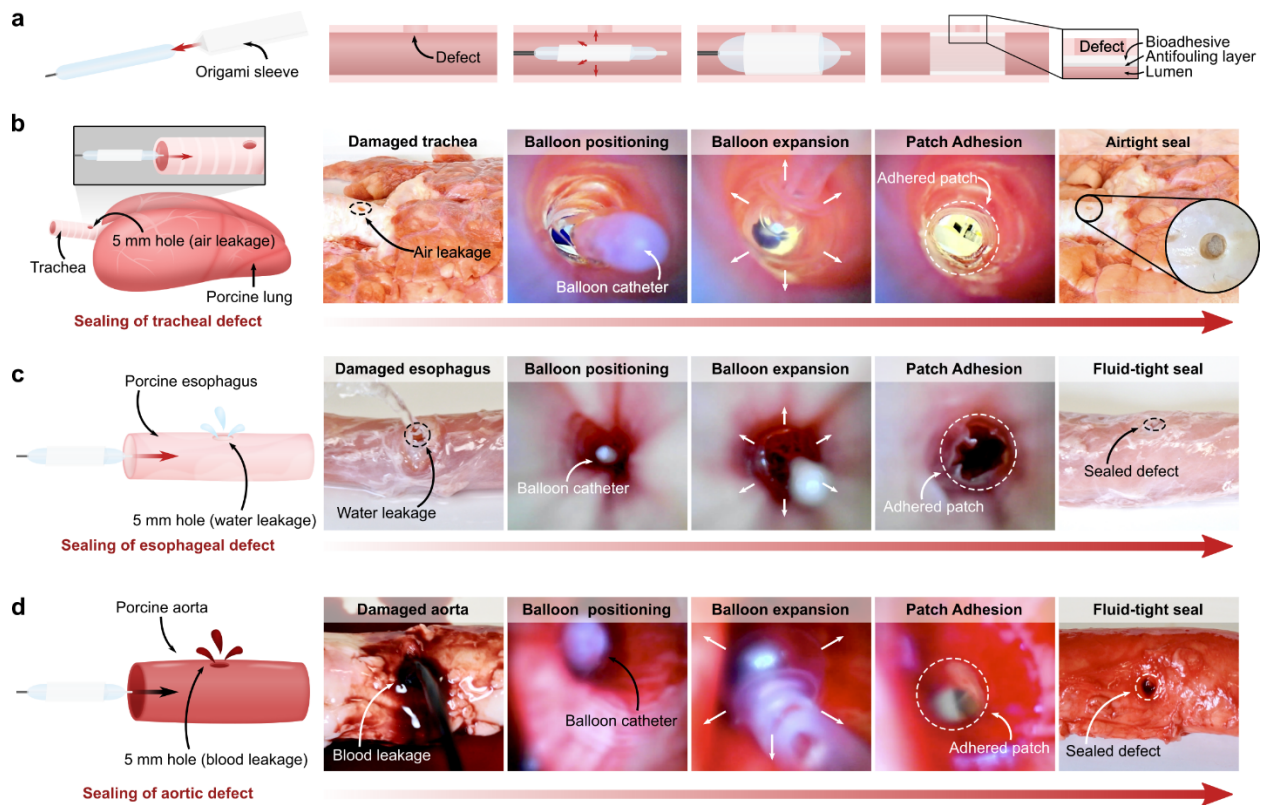


Figure 3-30. *Ex vivo* demonstrations of minimally invasive delivery and application of the multilayer bioadhesive patch by balloon catheters. (a) Schematic illustrations of the origami patch integration and endoluminal delivery process using a balloon catheter. (b) Macroscopic and endoscopic photographs taken during the process of sealing of a porcine tracheal defect, (c) esophageal defect, and (d) aortic defect.

Intestinal defect model

For the intestinal defect repair model, a 5 mm circular defect was created through the walls of a porcine small intestine using a biopsy punch. A patch-loaded origami sleeve was folded and introduced to an articulating linear stapler (Ethicon). The assembled stapler was navigated to the defect site and actuated to apply compression for 5 seconds, before opening the jaws and retracting the stapler (**Figure 3-31a,b**). The repaired intestine was connected to a pump and inflated to check for fluid-tight sealing of the bowel. To simulate a minimally invasive surgical setting, the experiment was repeated inside a dark chamber with holes, using endoscopic camera footage to guide the process (**Figure 3-31c**). As represented by these *ex vivo* demonstrations, the multilayer patch can potentially serve as a primary sealing and repair modality for various organ defects. Alternatively, it can act as an adjunct on top of a suture or staple line to support an anastomosis, especially in patients at high risk of anastomotic failure.

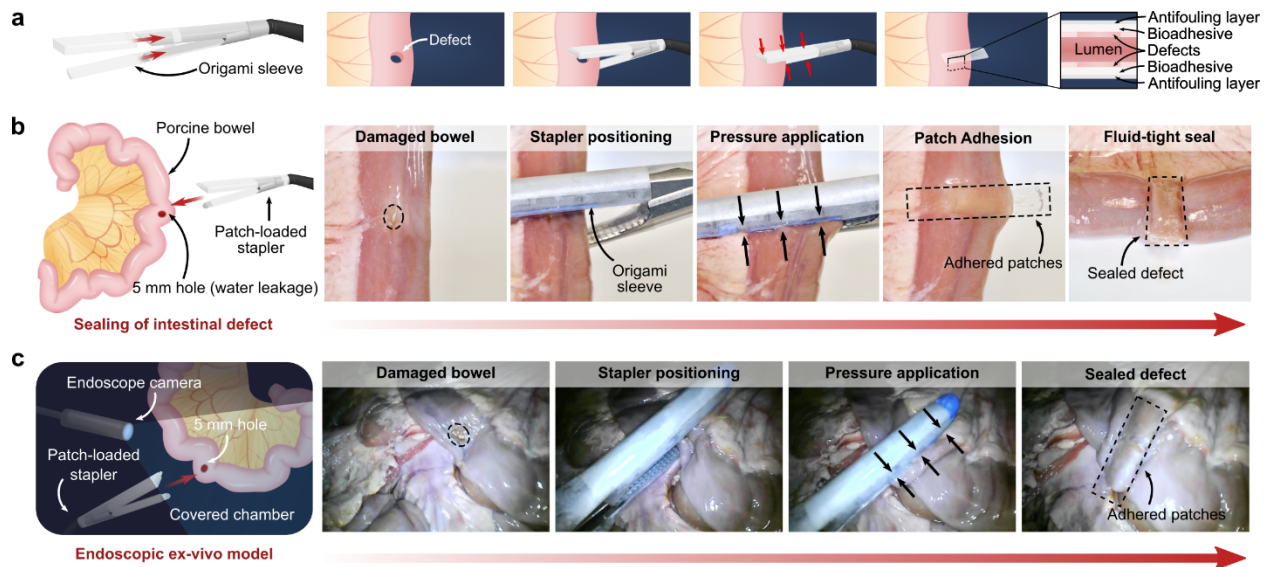


Figure 3-31. *Ex vivo* demonstrations of minimally invasive delivery and application of the multilayer bioadhesive patch using a surgical stapler. (a) Schematic illustrations of the patch integration and delivery process using an articulating linear stapler. (b) Macroscopic photographs of the linear sealing of a porcine intestinal defect (c) Endoscopic footage of the sealing of a porcine intestinal performed in a dark, covered chamber to mimic a minimally invasive surgical procedure.

3.6. Discussion

In this Chapter, the development of a multifunctional patch was described with the principal goal of addressing the multifaceted clinical needs for improved minimally invasive tissue repair techniques. By employing a multilayered architecture comprising various materials and structures, the resulting patch is capable of achieving a wide range of functionalities: (1) fast, robust, and fluid-tight tissue adhesion through adoption of a dry-crosslinking mechanism; (2) resistance to contamination by body fluids through integration of a liquid-infused protective matrix which can be removed under sufficient pressure; and (3) mitigation of post-implantation fouling by bacteria and biomolecules associated with infection, thrombosis, and fibrosis through the creation of a zwitterionic-interpenetrated elastomer. Taking advantage of the material properties and tape-like form factor of the patch, various origami-based manufacturing techniques have been demonstrated which enable the potential application in diverse minimally invasive procedures.

While the experimental characterizations, *ex vivo* demonstrations, and *in vivo* small animal models have thus far shown promising results, more work will need to be done to rigorously investigate the long-term biocompatibility and treatment efficacy of the multilayer patch. Furthermore, the customizability of the patch opens doors to future designs and deployment strategies. Ideally, the form factor, material properties, and constituent layers of the patch should be optimized for specific clinical indications.

4. Preclinical study: Minimally invasive bronchopleural fistulae

4.1. Overview

Following the development of the MITS patch outlined in Chapter 3, a specific clinical use case for repairing airway defects was investigated via preclinical pig studies in collaboration with a thoracic surgical team at Brigham and Women's Hospital. This Chapter discusses the motivation, patch delivery system, and results of this investigation.

4.1.1. Clinical motivation

Tracheal or Central Bronchopleural fistulae (BPF) are communications between the airway and pleural space. While these can occur anywhere in the airway, centrally located bronchopleural fistulas (i.e. distal tracheal, mainstem-bronchi, or lobar-bronchi) present potentially challenging complications after thoracic surgeries.^{1,2} BPF can occur after any pulmonary resection, but most commonly occur after pneumonectomy. They occur after pneumonectomies, lobectomies, and segmentectomies at rates of 1.5-7%, 0.5-1.2%, 0.3% respectively.² Right pneumonectomy is associated with higher rates of BPF than left pneumonectomy (8.6% vs 2.3%).³ This difference is likely secondary to anatomical and vascular differences between the right and left mainstem bronchi, which predisposes right bronchial stumps to ischemia and exposed staple lines.² Preoperative risk factors for the development of BPF include advanced age, poor pulmonary reserve, diabetes, weight loss, pulmonary infections, chronic steroid use, and neoadjuvant radiotherapy.^{1,2,4,5} Intra-operative risk factors include long bronchial stumps, stump devascularization, radical lymph node dissection, the extent of resection, lack of stump reinforcement, and spillage of infected contents.^{2,5} Postoperative risk factors include prolonged mechanical ventilation, prolonged postoperative air leak, and pneumonia.^{2,5} Though rare, the occurrence of central BPF is associated with high morbidity and mortality. Up to 80% of post-pneumonectomy empyema's are thought to be secondary to centrally located BPF.^{2,5} BPF have reported mortality rates between 10-71%.^{1-3,6}

4.1.2. Current challenges

Due to the varying presentations and time course of BPF, therapeutic interventions are case-dependent. Initial management of BPF includes bronchoscopic evaluation of the bronchial stump with close inspection of mucosal irregularities, granulation tissue, or frank dehiscence.² BPF closure options depend on patient status, BPF location, and timing.^{1,2,4} Once identified, BPFs are managed initially by drainage of the pleural space.² In select patients with small (<5mm), favorably located fistulae, attempts at bronchoscopic management can be attempted. Bronchoscopic closure techniques include fibrin glue, plugs, or stenting.⁷⁻¹⁰ Surgical options for closure of BPF include debridement and primary closure with reinforcement of the bronchial stump with a vascularized tissue flap (i.e. serratus anterior, latissimus dorsi, intercostal muscle, omental).^{1,2} With persistent or chronic BPF with concomitant empyema, open thoracic windows such as the Clagett window

or Eloesser flaps are considered.^{1, 2, 4, 11} Success rates for BPF closure are also highly variable and depend on fistula size, patient status, concomitant disease, and type of closure. As such, treatment options for central BPF remain challenging.

Existing tissue adhesives are generally insufficient and/or difficult to apply minimally invasively during a thoracotomy. For example, commercially-available adhesives (e.g., fibrin glues, albumin-based adhesives, poly-ethylene glycol-based adhesives), nanoparticle solutions, and mussel-inspired adhesives exhibit slow adhesion formation (longer than 1 min) and weak adhesion on wet surfaces (interfacial toughness less than 20 J m⁻²). Cyanoacrylate adhesives also suffer from high cytotoxicity and inflexibility after curing. It is fair to state that there are no current products that are effective or clinically indicated (by the FDA or otherwise) to improve the sealing of any thoracic anastomosis or reinforcement of airway or esophageal repairs.

4.1.3. Proposed solution

To limit the number of new materials being investigated in this study, the implantable patch was simplified to comprise only the bioadhesive material (i.e., no hydrophobic fluid or antifouling backing). However, to facilitate delivery and application through trocars using minimally invasive tools, a new stack-up was designed (**Figure 4-1**). This design, which comprises a bioadhesive patch coupled with a removable sponge substrate via a water-soluble PVA solution, improves the process of handling and applying pressure to the patch.

4.2. Methods and results

4.2.1. Bioadhesive patch

All chemicals were obtained from Sigma-Aldrich unless otherwise mentioned and used without further purification. For preparation of the bioadhesive patch, acrylic acid (AAc), polyvinyl alcohol (PVA) (M_w = 146,000 to 186,000, 99+ % hydrolyzed), polyethylene glycol dimethacrylate (PEGDMA) (M_n = 550), acrylic acid N-hydroxysuccinimide ester (Aac-NHS ester), and α -ketoglutaric acid were used. As a removable applicator for the patch, foam sponges (Fisher Scientific) were used after autoclaving for sterilization. Low molecular weight PVA (M_w = 9,000 to 10,000, 80% hydrolyzed) was used for the soluble binder between the bioadhesive patch and the applicator sponge.

To prepare the bioadhesive patch, 35 w/w % Aac, 7 w/w % high molecular weight PVA, 0.2 w/w % α -ketoglutaric acid, and 0.05 w/w % PEGDMA were added into nitrogen-purged deionized water. Then, 30 mg of Aac-NHS ester was dissolved per 1 ml of the above stock solution to prepare a precursor solution (equivalent to 1% of dry bioadhesive weight). The precursor solution was then poured on a glass mold with 150- μ m spacers and cured in a UV chamber (354 nm, 12 W power) for 30 min. After curing, to couple the bioadhesive patch to the applicator sponges, 10 w/w % low molecular weight PVA dissolved in water was used as a binding agent. The patches were then thoroughly dried before being cut into pieces (approximately 1 cm x 1 cm area, 100- μ m thickness) and stored with desiccant (silica gel packets) at -20 °C until use.

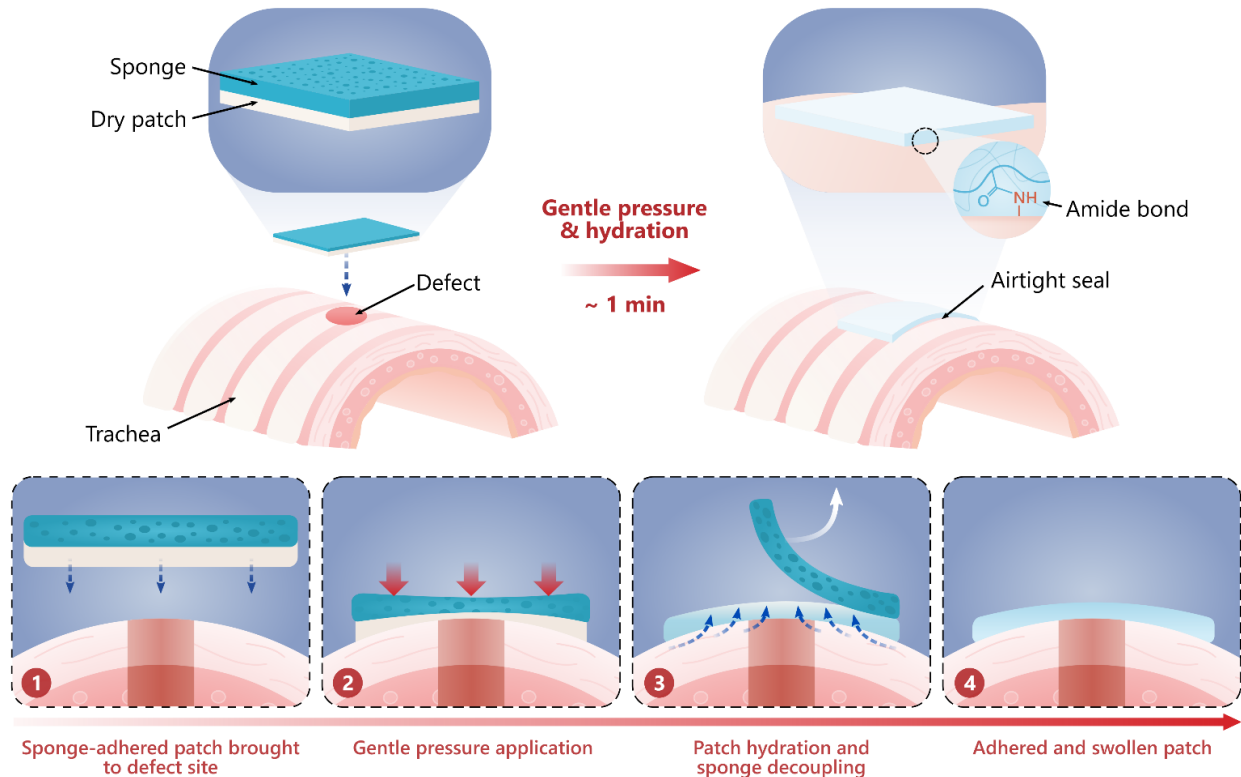


Figure 4-1. Schematic of bioadhesive patch and application. The patch is applied as a dry, tape-like film that transitions into a soft hydrogel after adhesion. To facilitate handling, the patch is coupled to a removable, porous sponge backing with a water-soluble adhesive. The patch forms tissue adhesion via intermolecular interactions and covalent amide bonds within a minute under gentle pressure. (1) Sponge-adhered patch brought to defect site. (2) Gentle pressure application. (3) Patch hydration and sponge decoupling. (4) Adhered and swollen patch.

4.2.2. Animal model

Nine 12-16 week (30-45 kg) Yorkshire swine underwent right VATS with the creation of a 1-5 mm full thickness defect in the distal trachea. Two additional swine were used for model optimization and not included in analysis. Cases in which the patch could not be successfully placed became control animals. In control animals, the defect was left untreated ($n = 3$). For experimental animals, the defect was sealed with the bioadhesive patch and checked for air leak under endoscopic visualization ($n = 6$). After a two-week survival period, the pigs were euthanized, tracheal specimens were harvested, and mechanical burst testing with histological evaluation was performed. A single sample of the novel bio-adhesive patch material (approximately 1 cm x 1 cm area, 100 μm thickness) was implanted subcutaneously in one animal to assess any site-specific differences in biocompatibility. All experiments were approved by the Institutional Animal Care and Use Committee of the Brigham and Women's Hospital, and animals were cared for in coordination with veterinary technicians at in compliance with the Principles of Laboratory Animal Care formulated by the National Society of Medical Research and the Guide for the Care and Use of Laboratory Animals.

Model creation and patch placement

Twenty-four hours prior to surgery, a 2-5 mcg/kg/hr fentanyl patch was applied trans-dermally. After overnight fast, animals were premedicated with subcutaneous injection of telazol 4.4 mg/kg (reconstituted to 100 mg/ml with 5ml of sterile water), xylazine 2.2 mg/kg, and atropine 0.02-0.04 mg/kg. Once sedated, swine were anesthetized with inhaled 1-4% isoflurane, and intubated with a 5.5-7.5 mm endotracheal tube. After desired level of anesthesia was achieved, animals were placed in a right lateral decubitus position and prepped and draped in sterile fashion. Cefazolin 20-25 mg/lg was then administered for prophylaxis. After injection of local anesthetic, a VATS approach was utilized to gain entry to the right chest. One 12 mm chest port and 2-3 x 5 mm chest ports were placed in the 3-6th intercostal spaces in lateral chest near the axilla. Using standard thoracoscopic instruments, tracheal dissection was performed and vagus nerve was identified and preserved. Branches of azygous vein were identified and ligated if necessary to facilitate adequate tracheal exposure (**Figure 4-2a**). Next, a 1-5 mm full-thickness defect was created in the distal trachea using a combination of puncture, electrocautery, and scissors (**Figure 4-2b**). For non-patched control animals, the defect was left untreated ($n = 3$). For patched experimental animals, mechanical ventilation was temporarily held and the defect was sealed with the novel bioadhesive patch and checked for air leak under direct visualization ($n = 6$). To deploy the patches, they were inserted through the 12mm port into the operative field with their blue sponge backing (**Figure 4-2c**). The patches were placed directly on top of the defect and pressure was applied for 1-2 minutes. The patches were then submerged with saline to hydrate the patch, dissociate the backing, and check for air leaks. The sponge backing was removed and the patches were left adhered to the tracheal wall (**Figure 4-2d**). Finally, chest tubes were placed via the 12mm port incision, the right lung was inflated under direct visualization, and the remaining port sites were closed. One-way Heimlich valves were then secured on the chest tubes. Finally, anesthesia was terminated, swine were extubated and clinically monitored throughout the postoperative period.

Postoperative management

Postoperatively, swine were fed and clinically monitored for signs of pain, infection, or respiratory distress. Meloxicam 0.4 mg/kg was given daily until chest tube removal. Chest tubes were maintained and routinely checked for air leaks. Upon resolution of air leak, chest tubes were removed under sedation with telazol 2.2 mg/kg and xylazine 1.1 mg/kg. Animals were survived for two weeks. Signs of pain, respiratory distress, or infection were addressed on a case-by-case basis in direct coordination with the veterinary staff.

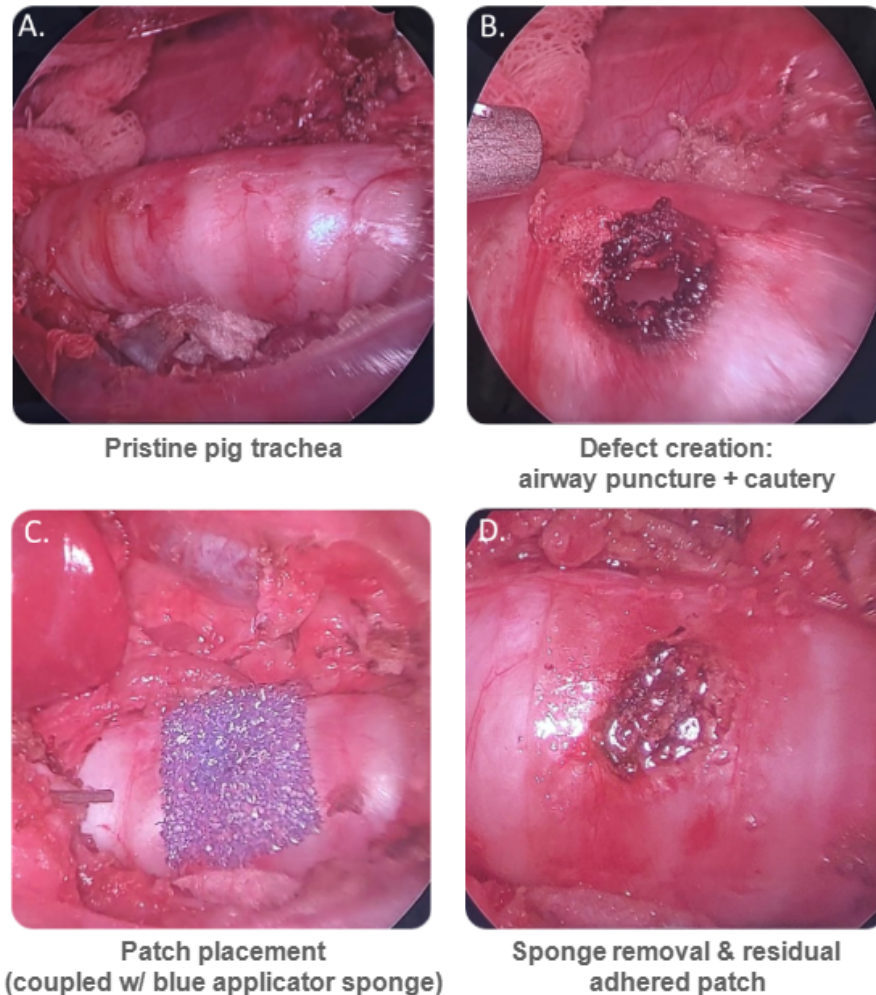


Figure 4-2. Endoscopic footage of defect creation and patch placement. (a) Tracheal dissection. (b) Creation of the tracheal defect. (c) Deployment of the bioadhesive patch. (d) Final patch placement with application sponge decoupled.

Endpoint analysis

Two weeks after the initial model creation and patch placement procedure, swine underwent a terminal harvest procedure. Animals were sedated with subcutaneous injection of telazol 4.4 mg/kg (reconstituted to 100 mg/ml with 5ml of sterile water), xylazine 2.2 mg/kg, and atropine 0.02-0.04 mg/kg and euthanized with Pentobarbital euthanasia solution (Euthasol, Fatal Plus, etc.); 100 mg/kg IV (0.22 mL/kg IV). A median sternotomy was performed for thoracic exposure and bilateral thoracic cavities were examined. After proximal and distal ligation of major vessels, the trachea, heart, lungs were removed en-bloc and examined. The tracheal specimen was then dissected and removed for mechanical testing proximally from the sub-laryngeal area to the subcarinal mainstem bronchi. After completion of mechanical testing (described below), the tracheal specimen, along with specimens from the right lung, left lung, mediastinal lymph nodes, right ventricle, left ventricle, liver, and spleen were fixed in formalin for pathological evaluation.

Additionally, pleural, pericardial, and chest wall specimens were collected in animals that showed gross signs of intrathoracic infection.

Mechanical Testing

To measure burst pressure of the excised tracheas, a syringe pump (Harvard Apparatus) was used to inject water into the excised porcine trachea at a rate of 5 ml min^{-1} while the applied pressure was monitored by a pressure gauge (Omega PX409) (modified ASTM F2392-04). A pipe-to-tube fitting was used to connect the upper end of the trachea to the water source, and surgical clamps were used to seal the lower end. The burst pressure was recorded as the maximum pressure prior to water leakage. For cases in which the trachea withstood over 200 mm Hg without bursting, the test was stopped and the burst pressure was recorded as $>200 \text{ mm Hg}$ (**Figure 4-3**).

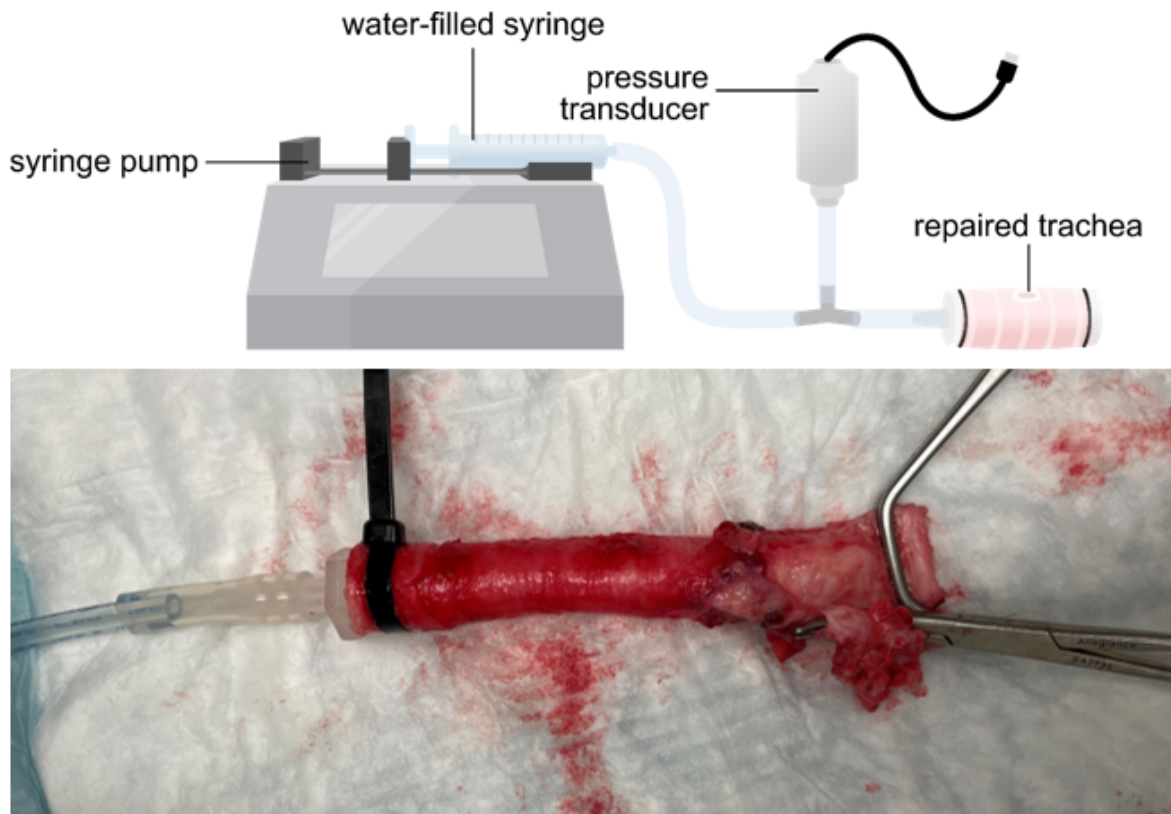


Figure 4-3. Burst pressure measurement setup for the dissected trachea specimen.

Histological Evaluation

Tissues were fixed in 10% neutral buffered formalin, dehydrated through a series of graded ethanols and xylene, embedded in paraffin, sectioned to 5 μm thickness and stained with hematoxylin and eosin (H&E) and Masson trichrome using standard histologic methods.

4.2.3. Study results

Survival

Two of three non-patched control animals (66%) and five of six patched experimental animals (83%) survived to the two-week endpoint ($p = 0.57$). One non-patched control animal was euthanized after an episode of respiratory distress on postoperative day 2 that did not resolve after chest tube suctioning and replacement. One patched experimental animal was euthanized after showing signs of a systemic infection (fever, emesis, lethargy) on postoperative day 4 that did not resolve with antibiotics, fluid resuscitation, and antipyretics.

Complications

Complications observed in the postoperative period included respiratory distress ($n = 4$) and systemic infection ($n = 3$). All of the non-patched control animals ($n = 3$) and half of patched experimental animals ($n = 3$) experienced postoperative complications ($p = 0.13$). Control group complications included respiratory distress ($n = 2$) and infection ($n = 1$). Patched experimental complications included respiratory distress ($n = 1$) and infection ($n = 2$). Detailed summaries of all experiments including complications, outcomes, necropsy findings, and histology findings are described in **Table 4-1**.

Mechanical Testing

Tracheal specimens from all animals that survived to the two-week endpoint underwent mechanical burst-pressure testing ($n = 7$). Tracheal specimens from all experimental animals ($n = 5$) that survived to the two-week endpoint sustained intraluminal pressures >200 mmHg.

Histological Evaluation

The subcutaneously implanted bioadhesive patch sample demonstrated only mild surrounding inflammation in a standard foreign body response to a biodegradable implantable material at 14 days (**Figure 4-4**). There was a thin layer of macrophages with rare foreign body giant cells at the interface between the remaining material and the host subcutaneous tissue, with viable, vascularized granulation tissue comprising the implant capsule. There was no evidence of tissue necrosis, acute inflammation, infection or hypersensitivity reaction.

Gross and pathologic evaluation showed no evidence of patch incorporation on 4 of the 6 experimental animals. The remaining two experimental animals showed gross and histologic evidence of patch incorporation to the surrounding tracheal tissue. Histologic evaluation of the tracheal samples (**Figure 4-5**) demonstrated a similar tissue response to the implanted material including only mild chronic inflammation. The soft tissue of the trachea showed healing with granulation tissue, cartilage regeneration and re-epithelialization of the airway lumen. There was no evidence of necrosis, acute inflammation, infection or hypersensitivity reaction. Even in areas where the patch folded on itself leading to a higher concentration of polymer mass, there was appropriate healing with only mild inflammation and no evidence of tissue necrosis.

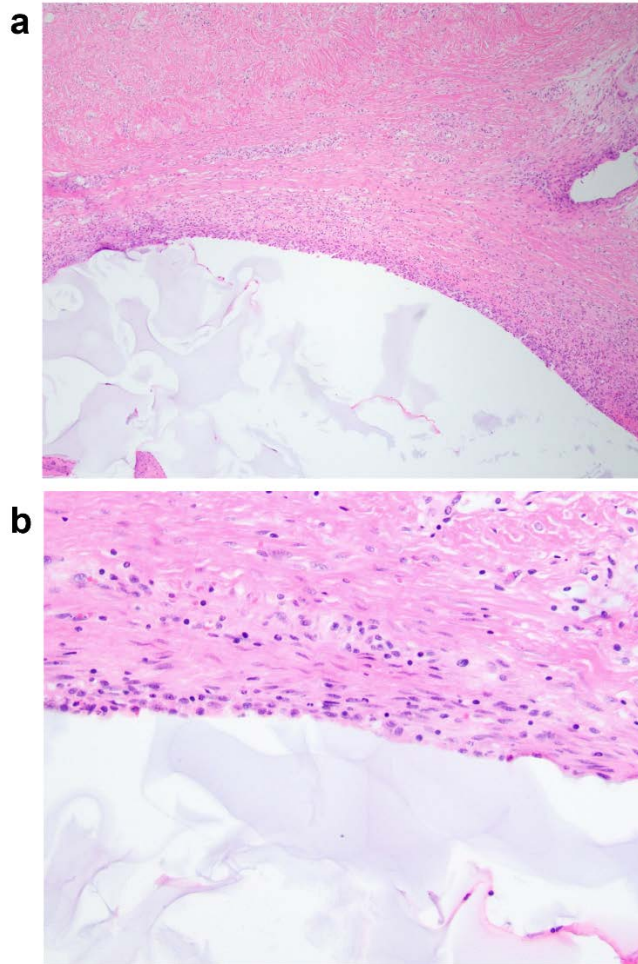


Figure 4-4. Histological images of subcutaneous tissue 14 days after implantation of the bioadhesive. (a) Low power photomicrograph demonstrating a thin foreign body reaction with mild chronic inflammation, granulation tissue and no evidence of acute inflammation or necrosis surrounding the polymer (P) (H&E stained section, 40x original magnification). (b) High power photomicrograph of polymer-tissue interface demonstrating a thin layer of macrophages surrounded by granulation tissue and no evidence of acute inflammation or eosinophilic reaction. (H&E stained section, 200x original magnification).

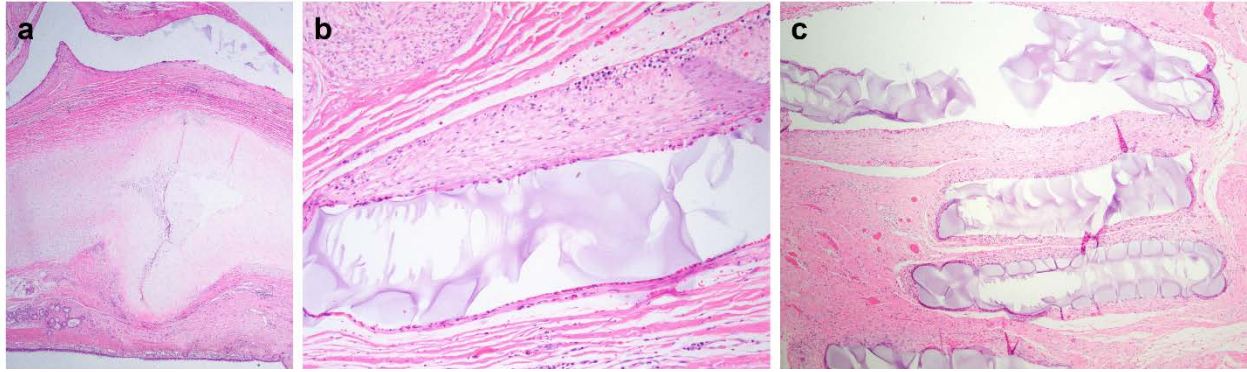


Figure 4-5. Partially degraded bioadhesive patch adjacent to tracheal defect. (a) Low power photomicrograph demonstrating biodegradable polymer (P) overlying tracheal cartilage (T) with evidence of regeneration (area of thickening). The mucosal tissue also shows evidence of healing with regeneration of the tracheal epithelial layer (arrows) adjacent to the tracheal lumen (L) (H&E stained section, 20x original magnification). (b) Medium power photomicrograph demonstrating a thin foreign body capsule with minimal inflammation surrounding the polymer (P). A nearby peripheral nerve (N) is normal with no pathologic change (H&E stained section, 100x original magnification). (c) Low power photomicrograph demonstrating area of folding of polymer (P) showing the same mild foreign body response with granulation tissue and mild chronic inflammation with no adverse tissue effects due to the excess material concentration (H&E stained section, 40x original magnification).

4.3. Discussion

To summarize, there were a total of nine animals in this study: six patched experimental animals and three non-patched controls. The construction and delivery process of the patch was iteratively refined and updated throughout the study based on surgical feedback. **Figure 4-6** summarizes the clinical and histologic outcomes, and **Table 1** provides detailed outcomes for each animal. All of the control animals ($n = 3$) and half of our experimental animals ($n = 3$) developed postoperative complications. While there were not enough animals to see statistical significance, there was an observable trend toward lower complication rates in the experimental animals which showed evidence of patch incorporation on histologic review. Evidence of patch incorporation was only observed grossly, and on histologic evaluation in 33% of the experimental animals ($n = 2$). This suggests that during the healing process, the patches may have dislodged for the remaining four experimental animals. Neither of the two animals which showed evidence of patch incorporation developed any complications during the postoperative period. After noticing this trend of complications, the team reviewed surgical videos to evaluate the technical success of patch deployment. The two animals in which the patch fully incorporated to the surrounding scar tissue had the most successful intraoperative deployments of the patch (good adhesion, no edge or corner peeling, and good seal). This may indicate that good technical deployment is essential for the patch to adequately seal and integrate to the healing defect. These findings also suggest a trend towards fewer complications of persistent air leak and respiratory infection in animals with well-placed patches. Furthermore, the patch exhibited stronger adhesion with tissues in the subcutaneous space

compared to the tracheal surface (despite identical deployment methods), indicating tissue-dependent adhesion behavior.

Regarding the infectious complications observed in 33% of the animals, there are several potential contributing factors. The animal models were sedated, anesthetized, and mechanically ventilated, but were not paralyzed. As such, the team was unable to completely prevent air movement across the distal tracheal defect during the patch placement procedure. This opens the potential to introduce respiratory airway secretions and respiratory flora into the chest. Further, the swine were housed and clinically monitored for signs of respiratory distress or infection in pens per institutional regulations. However, these pens did not have the capabilities of continuous vital monitoring (SPO₂, HR, BP). Additionally, the pens did not have oxygen delivery, wall suction, or chest tube drainage system capabilities. As such, chest tubes were managed using one-way Heimlich valves with intermittent manual suctioning based on clinical presentation. With additional supportive cares such as IV antibiotics, oxygen therapy, chest tube drainage systems with wall suction, continuous pulse oximetry, some of the observed complications could likely have been avoided. Respiratory and infectious complications are known and expected complications associated with any thoracic surgery. The ACSOG Z0030 trial analyzed 1,023 patients who underwent any pulmonary resection for early stage lung cancer and found that 5.5%, 2.5%, and 1.1% of patients developed postoperative respiratory failure, pneumonia, and empyema respectively.¹⁵

The histologic findings of the patch material in both the subcutaneous tissue and in the trachea demonstrated the expected benign foreign body reaction to a degradable material, consistent with previous experience with this material in other anatomic sites.^{12, 13} Polymeric material was still present at 14 days. While it would be speculation to suggest that the polymer actually stimulated regeneration, the material clearly provided both a sealant function and a permissive environment for soft tissue and cartilaginous healing of the tracheal wall in the cases where it remained attached to the tracheal wall. One potential concern with any biodegradable material is toxicity to the tissue from degradation products if they are released in excess from too much starting material, at an elevated concentration or at too fast a rate. One sample demonstrated folding (**Figure 4-4C**), simulating a situation where there was an excess of material in a confined space. Even in this sample, the tissue reaction demonstrated only mild chronic inflammation with good healing and no adverse local effects speaking to the biocompatibility of this novel material in soft tissue.

The present study had several limitations. As described previously, the bioadhesive patch itself was adjusted throughout the study, entailing minor changes in patch properties such as patch size, shape, and backing. Deployment approaches, including chest port sizes and surgical tools, were also tuned throughout the process. These changes enabled improvement in patch placement and sealing; however, the variability between cases detract from consistency in the results and therefore the ability to draw conclusions with statistical confidence. Furthermore, the clinical monitoring abilities were limited and may have inflated rates of infection, chest tube dislodgement, and respiratory distress seen in the animal cohort.

This animal study highlighted both strengths and weaknesses of the bioadhesive patch. Given the favorable biological outcomes in the most successful patch placement cases, the bioadhesive material presents a promising platform for addressing bronchopleural fistulas. However, inconsistent deployment success and apparent migration of the patch in other cases highlight that there is room to improve in both material and process design.

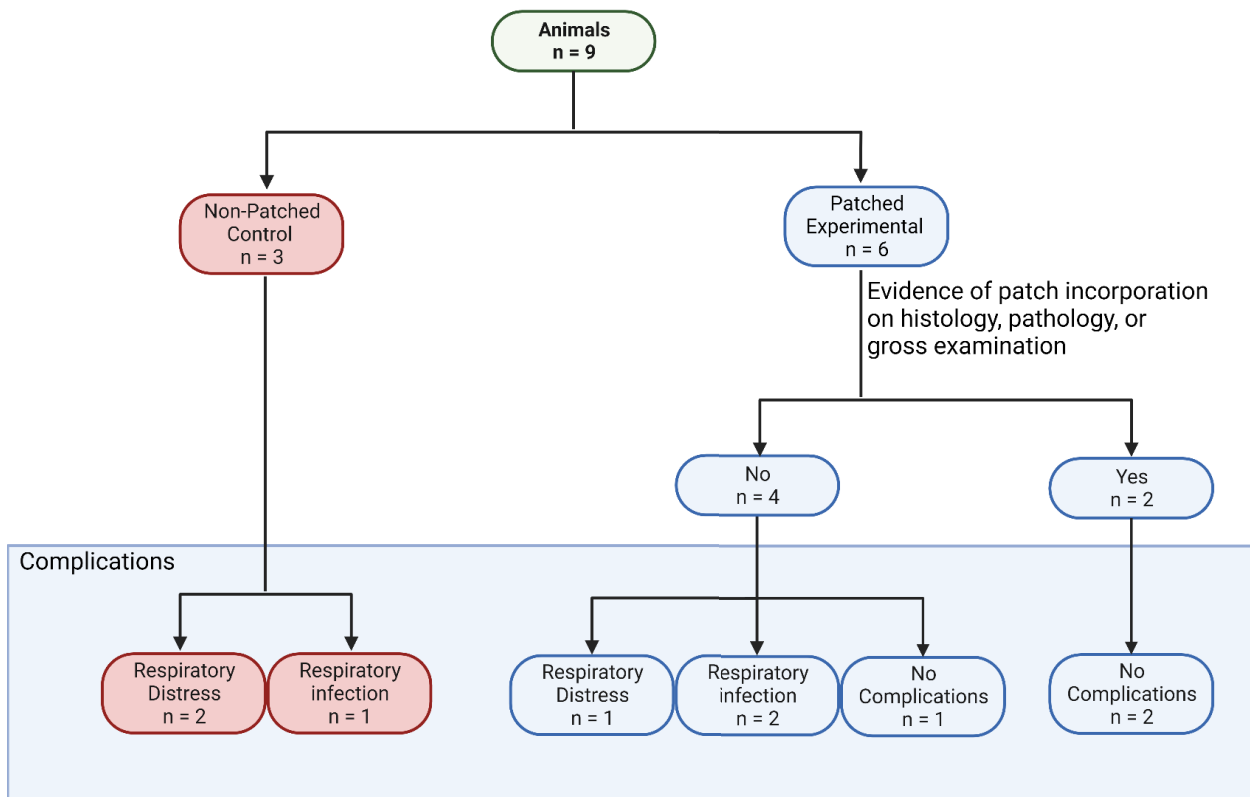


Figure 4-6. Outcomes of the animal study.

Table 4-1. Summary of case details.

Animal	Group	Success of patch placement	Clinical Complication	Complication management	2-week Survival	Burst pressure (mmHg)	Necropsy Findings	Histologic findings
09-2	Control	N/A	Respiratory distress	Chest tube suctioning	Yes	209	Trachea healed	Healed tracheal defect with granulation tissue and mild chronic inflammation
23-1	Patch	Poor	Respiratory Distress	Chest tube suctioning and Heimlich valve replacement	Yes	351	Trachea healed. Patch found in surrounding scar tissue	Healing tracheal defect with moderate chronic inflammation and foreign body giant cell reaction to likely aspirated material or surgical contaminant; patch material separate from tracheal defect with surrounding organizing fibrin and minimal inflammation
25-1	Patch	Good	None	N/A	Yes	331	Trachea healed. Fibrinous scar surrounding defect	Healed tracheal defect and overlying patch with granulation tissue and mild chronic inflammation
29-4	Control	N/A	Respiratory Distress	Chest tube suctioning and replacement	No	N/A	Significant subcutaneous emphysema in the neck surrounding trachea	Open tracheal defect with acute inflammation and fibrin deposition
29-1	Patch	Good	None	N/A	Yes	240	Small subclinical chest wall abscess. Patch contained within abscess.	Healing tracheal defect with no patch material but moderate to severe acute and chronic inflammation overlain by fibrous capsule; patch material separate with acute inflammation consistent with abscess
30-1	Patch	Great	Infection	Antibiotics, Antipyretics, IV fluids	No	N/A	Tracheal defect identified and unhealed. Right lung atelectatic. Right pleura thickened. Gray exudate noted in the pleural space.	Open tracheal defect with acute inflammation and fibrin deposition
30-5	Patch	Great	None	N/A	Yes	252	Trachea healed. Patch adhered to trachea.	Healed tracheal defect and overlying patch with granulation tissue and mild chronic inflammation
36-9	Control	N/A	Infection	Antibiotics, Antipyretics	Yes	351	Trachea healed.	Healing tracheal defect with moderate chronic inflammation and fibrosis; subcutaneous patch material with typical foreign body reaction and mild chronic inflammation
35-14	Patch	Poor	Inadvertent airway injury during initial procedure, Infection	Antibiotics, Antipyretics	Yes	351	Trachea healed. Pericardium thickened.	Healing tracheal defect without evidence of patch material

5. Three-dimensional printing of bioadhesives

5.1. Overview

5.1.1. Clinical motivation

As discussed in previous Chapters, bioadhesive hydrogels, such as the material developed for the MITS patch, are promising candidates for realizing tough adhesion and good biocompatibility^{24,26,133,13,214}. However, typical mold-casted hydrogels provide limited manufacturing freedom over their shapes and properties, constraining their versatility and offering little room for development toward more customized, application-specific technologies. This can be particularly limiting when considering the wide variety of tissue properties and anatomical geometries which set the context for real-life clinical scenarios.

3D printing has become a forefront technology for manufacturing biomedical products with controlled architectures, proving useful for constructing devices customized for different host tissues or functionalities^{215,216}. While there have been significant efforts toward developing 3D printable biomaterials for tissue scaffolds, prosthetics, and pharmaceuticals, the potential for 3D printing tissue adhesives has remained largely unexplored^{217–219}. A main obstacle lies in the challenging set of material properties required to ensure both printability and high adhesion performance: a printable tissue adhesive must possess proper rheological properties for layer stacking (e.g., shear thinning behavior and sufficient yield stress) while retaining its adhesive properties through the printing and post-processing steps²²⁰.

5.1.2. Proposed solution

This Chapter presents a direct-ink-write 3D printable (3DP) tissue adhesive ink that enables the additive manufacturing of elastic structures with tunable geometries and robust tissue adhesive properties (**Figure 5-1a-c**). Specifically, a polymer network is developed comprised of poly(acrylic) acid functionalized with *N*-hydroxysuccinimide ester (PAA-NHS ester) interpenetrated with and grafted to a hydrophilic polyurethane (PU). A key innovation of this material is the ability to process it into a viscoelastic ink by dissolution in a benign solvent (30 v/v % water and 70 v/v % ethanol), making it amenable to extrusion-based 3D printing (**Figure 5-1d-e**). The polymer constituents are selected based on design principles for achieving rapid and robust adhesion: specifically, leveraging hydrophilic moieties to enable rapid adhesion, and incorporating strong interfacial linkages and bulk energy dissipation mechanisms to enhance interfacial toughness^{19,24,26} (**Figure 5-1f**). Owing to a high density of charged carboxylic acid groups, the hydrophilic PAA chains facilitate rapid interfacial water uptake and can quickly consolidate with tissue surfaces to form intermolecular bonds^{24,200,221}. Reactive NHS ester groups further contribute to tissue adhesion by interacting with primary amines on tissues to form covalent amide bonds. Meanwhile, the hard segments in PU interact via dynamic hydrogen bonding, providing an energy dissipation mechanism under deformation¹⁹ (**Figure 5-1g**). Previously, a commercially-available thermoplastic ether-based hydrophilic PU has demonstrated favorable biocompatibility and mechanical properties (i.e., high stretchability and toughness)^{24,119,130,139}. Here, this off-the-shelf material is leveraged as a base polymer in the tissue adhesive to impart

these favorable properties to the resulting graft interpenetrating network. The elastomeric mechanical properties of the resulting polymer make it suitable for conforming to varying wound geometries and bearing loads in dynamic tissues (**Figure 5-1e** and **Figure 5-2**). 3D printing of this material creates a streamlined and versatile fabrication platform for designing tissue adhesive structures for tissue repair and bio-integrated devices.

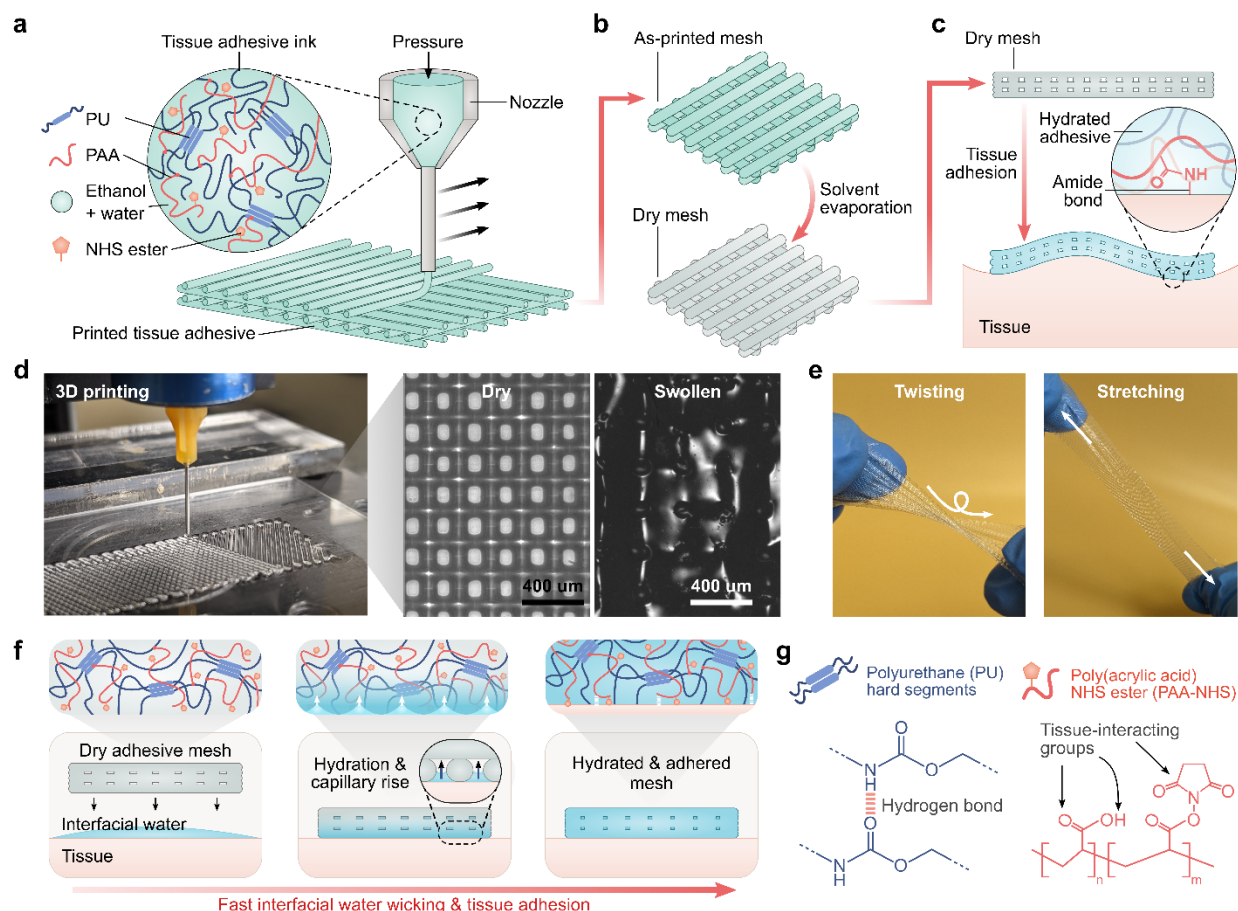


Figure 5-1. Fabrication and adhesion of the 3D printable bioadhesive. (a-c) Schematic illustration of the 3D printing overview. A tissue adhesive ink is extruded using direct-ink-write 3D printing and dried to obtain an adhesive mesh patch. The mesh is then applied in the dry state to a hydrated tissue surface, where it achieves adhesion by forming covalent amide bonds with primary amines on the tissue surface. (d) Photograph of the 3D printing process and micrographs of a 3D printed mesh patch in dry and swollen states. (e) Photographs of as-printed patches being twisted and stretched, demonstrating their flexibility. (f) Schematic illustration of the adhesion mechanism. Interfacial water is swiftly removed via hydration of the material and capillary rise through the mesh pores, which enables rapid consolidation with tissues. The formation of intermolecular and covalent bonds stabilizes adhesion. (g) Primary chemical moieties of the 3D printable tissue adhesive copolymer: polyurethane (PU) and poly(acrylic acid) (PAA) coupled with NHS ester.

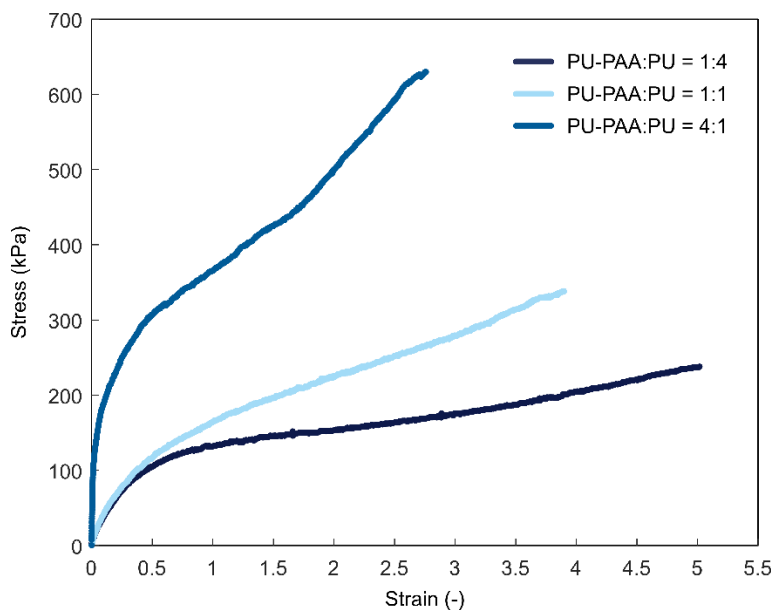


Figure 5-2. Representative stress-strain curves of samples prepared using varying ratios of PU-PAA to PU in the 3D printing ink. Samples containing different weight ratios of PU-PAA to PU were 3D printed and their tensile properties were measured in their dry state.

5.2. Methods and results

5.2.1. Material design

Synthesis of the tissue adhesive material

The synthesis of the PU-PAA graft interpenetrating network is achieved using a photoinitiated polymerization method (**Figure 5-3a**). Briefly, UV-assisted synthesis is carried out in a one-pot solution containing PU, acrylic acid, α -ketoglutaric acid, and benzophenone. α -ketoglutaric acid functions as an initiator for the polymerization of acrylic acid, and benzophenone functions as an initiator for producing radical sites in the PU, which can give rise to covalent grafting of PAA to PU^{201,222–224}. Next, the PAA-grafted PU (PU-PAA) product is purified by dialysis in ethanol followed by water to remove unreacted reagents, and then fully dried to obtain a shelf-stable polymer (**Figures 5-4, 5-5**). FTIR analysis of the material substantiates the roles of both initiators in the incorporation of PAA, reflected in the peak around 1710 cm^{-1} associated with the C=O stretching in carboxylic acid (**Figure 5-6**)²⁰¹. The content of acrylic acid and PU in the precursor solution was determined based on achieving a large ratio of PAA:PU in the final product. Specifically, a 4:1 AA:PU weight ratio in the precursor solution was found to produce materials within the upper limit of final PAA content (**Figure 5-7**). Prior to 3D printing, the PAA-PU solutions may be blended with PU to further tune the PU content of the ink as desired. This method of polymerizing and crosslinking PAA with PU prior to 3D printing enables the facile direct-ink-writing of tissue adhesive inks which require no further post-processing besides from drying. This contrasts with 3D printing a hydrogel precursor requiring post-processing (e.g., UV curing,

chemical crosslinking) which increases the complexity of fabrication and removal of residual monomers.

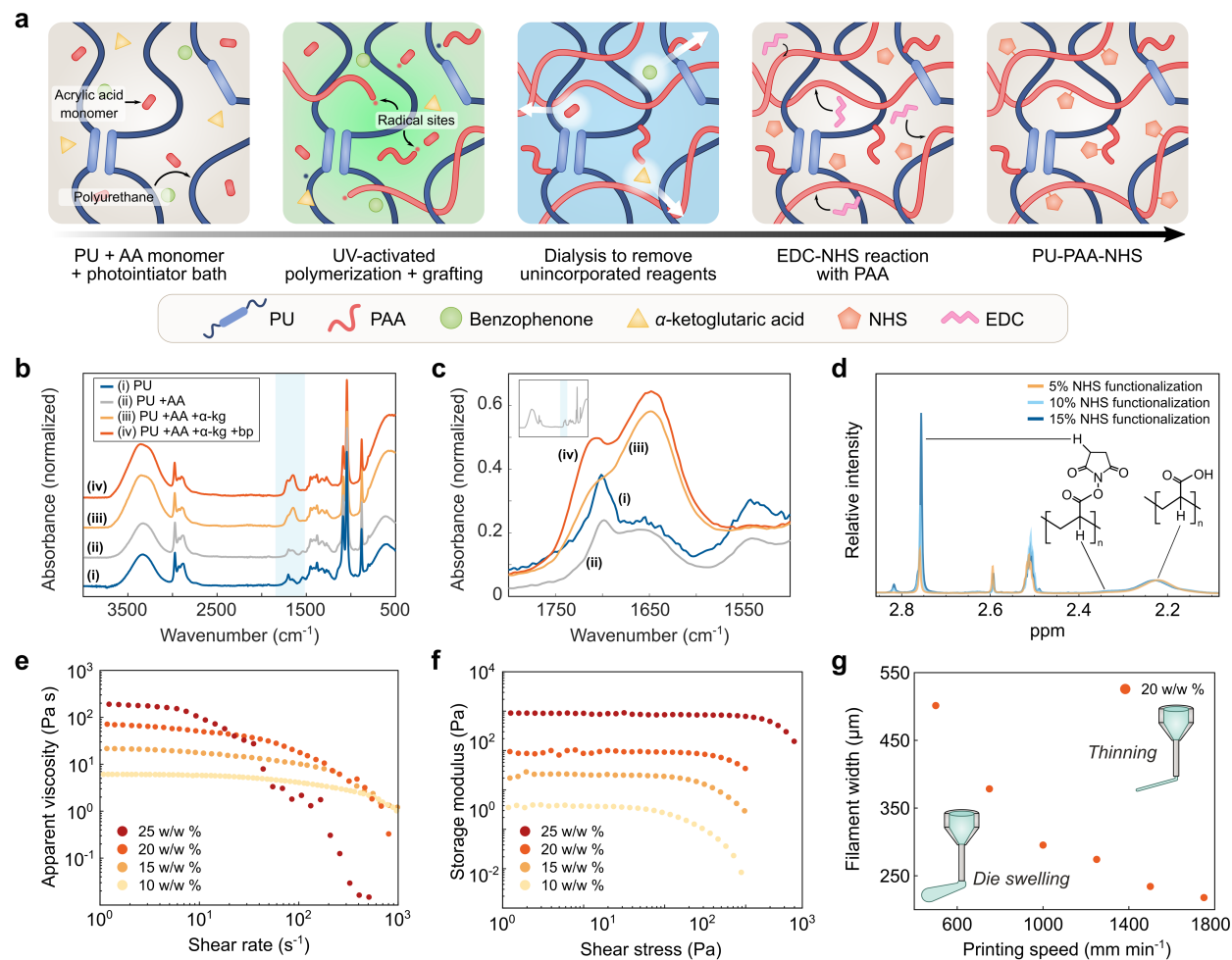


Figure 5-3. Synthesis and material characterization of the 3D printable tissue adhesive. (a) Illustrated schematic of the tissue adhesive synthesis process. (b-c) FTIR spectra for materials prepared using different precursor compositions. Each spectrum was normalized based on the peak at 2900 cm^{-1} . (d) ^1H NMR spectra for tissue adhesive samples with varying degrees of NHS functionalization. Each spectrum was normalized based on the peak around 2.22 ppm (attributed to PAA), and the degree of NHS functionalization was estimated by integrating the NHS alkyl peak around 2.76 ppm with respect to the normalized peak. (e) Apparent viscosity of tissue adhesive inks as a function of shear stress for varying polymer concentrations. (f) Shear storage modulus as a function of shear stress for varying polymer concentrations. (g) Filament width as a function of printing speed for the tissue adhesive ink comprising 15 w/w % PU-PAA and 5 w/w % PU extruded through a $200 \mu\text{m}$ -diameter nozzle under 250 kPa of pressure.

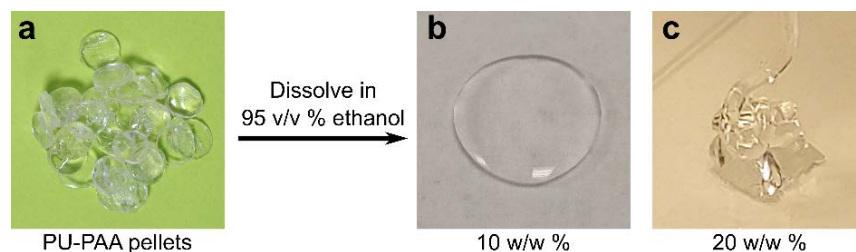


Figure 5-4. Images of the synthesized PU-PAA material and solutions of varying polymer content. a, PU-PAA pellets obtained after synthesis, purification, and drying. b-c, PU-PAA solutions of 10 w/w % (b) and 20 w/w % (c) concentrations. As the polymer concentration increases, the inks transition from spreading freely to having suitable yield stress for 3D printing.

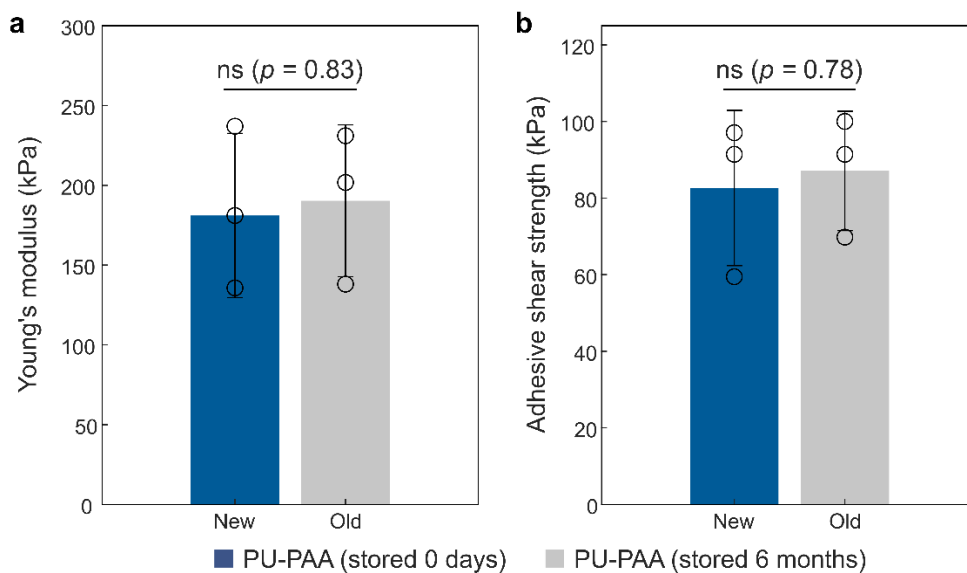


Figure 5-5. Shelf stability of the PU-PAA polymer. (a) Young's modulus and (b) adhesive shear strength of samples printed using newly synthesized PU-PAA and PU-PAA stored in ambient conditions for 6+ months. Values represent the mean and standard deviation ($n = 3$ independent samples). Statistical significance and p values were determined using a two-tailed Student's t -test with unequal variance: ns indicates $p > 0.05$.

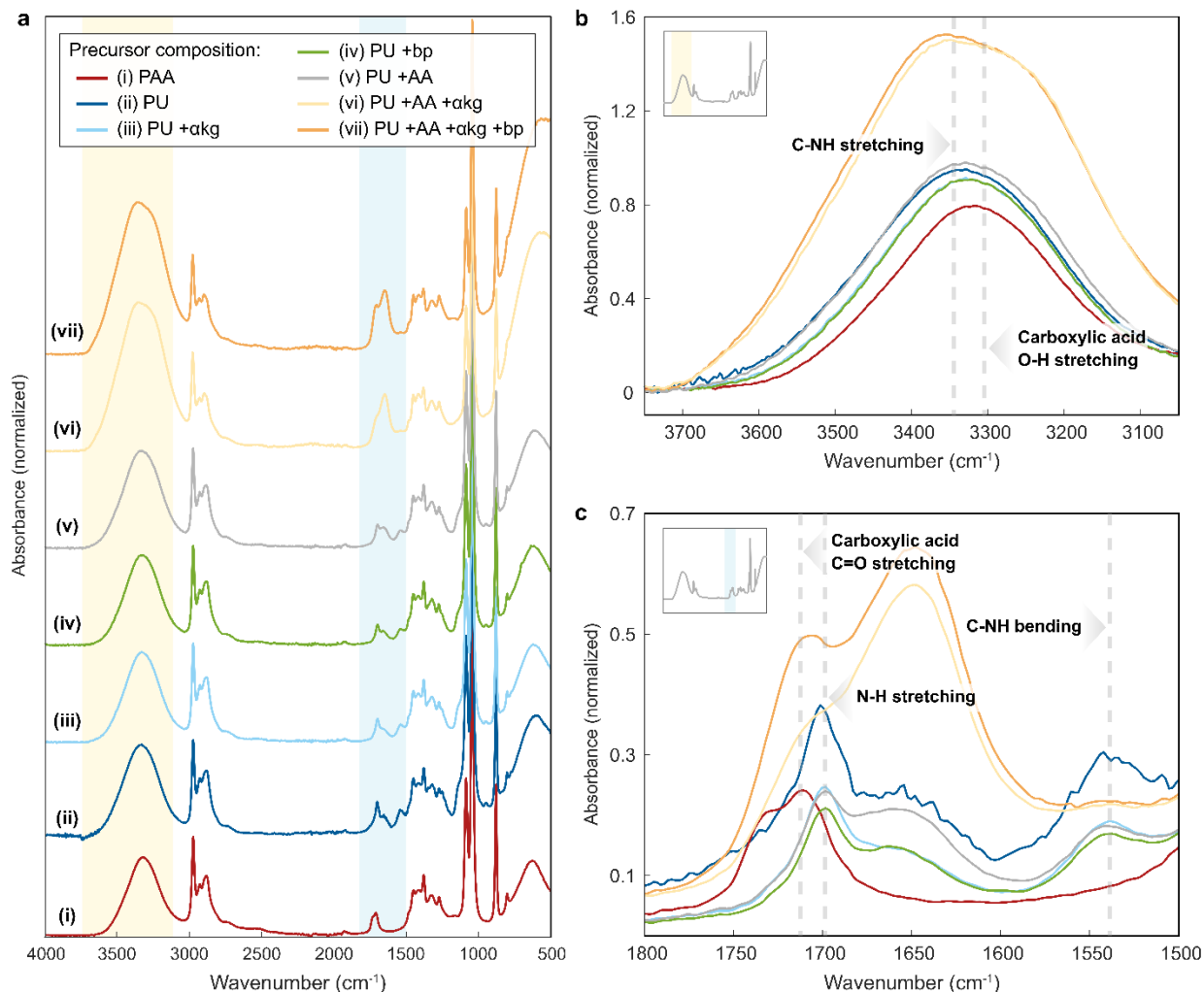


Figure 5-6. FTIR spectra for materials prepared using different precursor compositions. (a) Full FTIR spectra for samples prepared from precursors containing (i) PAA alone, (ii) PU alone, (iii) PU and α -ketoglutaric acid (α -kg), (iv) PU and benzophenone (bp), (v) PU with acrylic acid (AA) and no initiator, (vi) PU with AA and α -kg, and (vii) PU with AA, α -kg, and bp. Each spectrum is normalized based on the peak at 2900 cm^{-1} . (b) Zoomed-in spectra for a frequency range of $3700\text{--}3100\text{ cm}^{-1}$. (c) Zoomed-in spectra for a frequency range of $1800\text{--}1500\text{ cm}^{-1}$.

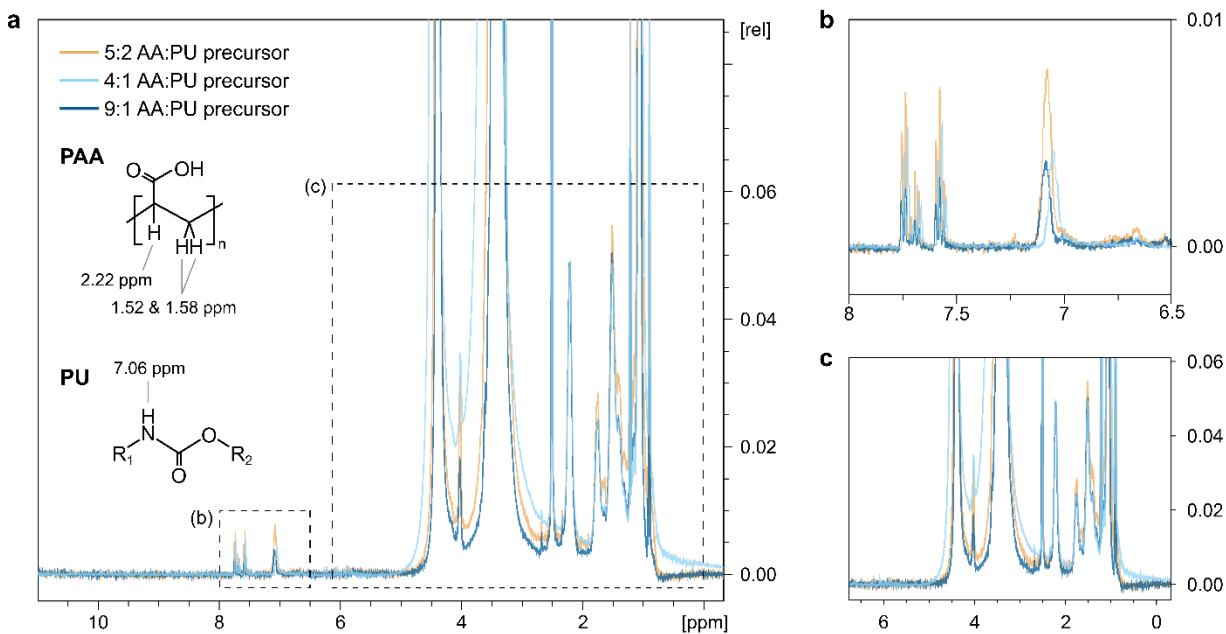


Figure 5-7. ^1H NMR spectra for PU-PAA prepared using varying precursor ratios of acrylic acid (AA) and PU. Precursor solutions containing varying AA:PU weight ratios of 5:2, 4:1, and 9:1 PAA:PU were used to synthesize PU-PAA. The final products were purified to remove unincorporated monomers and oligomers, then characterized using ^1H NMR. (a) Full NMR spectra of all three samples normalized based on the peak around 2.22 ppm (attributed to PAA). (b) Zoomed-in spectra from 8 to 6.5 ppm. The peak at 7.06 ppm is attributed to the nitrogen-attached hydrogen in PU. (c) Zoomed-in spectra from 6 to 0 ppm.

3D printing and adhesive performance

To convert the synthesized PU-PAA into a printable ink, a high concentration of PU-PAA is first dissolved in an aqueous ethanol solution, yielding a viscous resin. The PU-PAA resin is then mixed with 3-(dimethylamino)propylcarbodiimide (EDC) and *N*-ethyl-*N'*-(*N*-hydroxysuccinimide) (NHS) to introduce NHS ester functional groups in the PAA chains, yielding around 10% NHS functionalization of the carboxylic acid groups (**Figure 5-3d** and **Figure 5-7**). The direct-ink-write printing method requires that the ink be able to flow through a fine nozzle under pressure, retain its shape after extrusion, and support layer stacking²²⁰. It was found that inks comprising a total polymer concentration below 15 w/w % are prone to spreading, which compromises shape fidelity, whereas inks with polymer concentration exceeding 25 w/w % are difficult to extrude due to clogging in the printing nozzles. Inks within the intermediate range of concentrations (e.g., a composition of 15 w/w % PU-PAA, 5 w/w % PU) exhibit suitable properties for 3D printing (**Figure 5-3e-g**). The filament and pore dimensions can be controlled by tuning the extrusion pressure and printing head speed (**Figure 5-3g**). Following deposition onto a substrate, the printed structures are dried with no further processing required. After adhering to tissues, the printed material equilibrates in wet physiological environments with an equilibrium swelling ratio of

around 1.75 (Figures 5-8, 5-9). The bulk material can achieve high interfacial toughness ($>350 \text{ J m}^{-2}$) and shear strength ($>140 \text{ kPa}$) after being adhered to porcine skin (Figure 5-10).

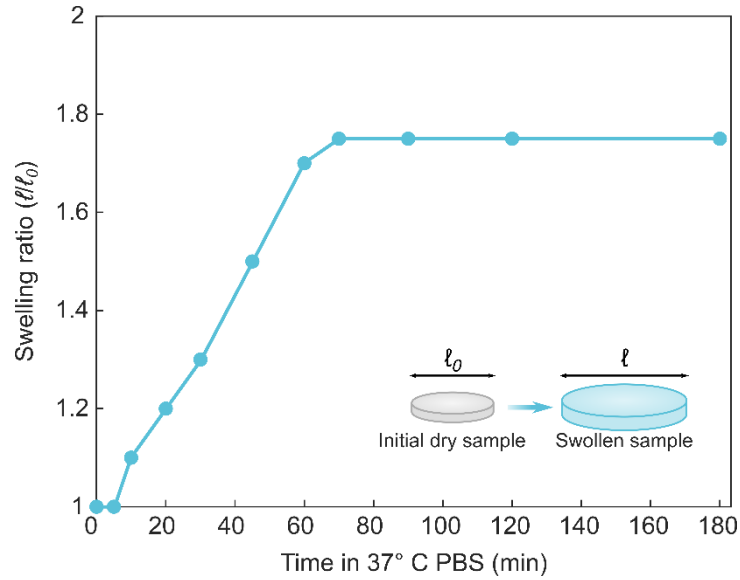


Figure 5-8. Swelling of the printed tissue adhesive material. Swelling ratio of a disk-shaped tissue adhesive sample vs. time immersed in PBS at 37° C (initial diameter $l_0 = 10 \text{ mm}$). Three independent experiments were conducted with similar results.

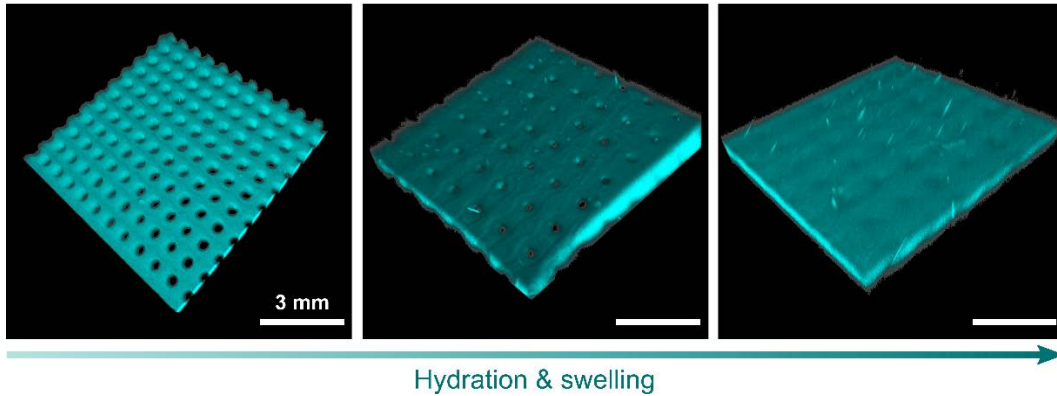


Figure 5-9. Swelling of an adhered 3D printed mesh. To visualize swelling using fluorescent confocal microscopy, the tissue adhesive ink was mixed with blue fluorescent latex microbeads prior to 3D printing. The lattice-patterned patch was adhered to a gelatin hydrogel and immersed in saline solution. Hydration and swelling of the mesh patch over the course of ~15 minutes led to visible shrinkage of the pores.

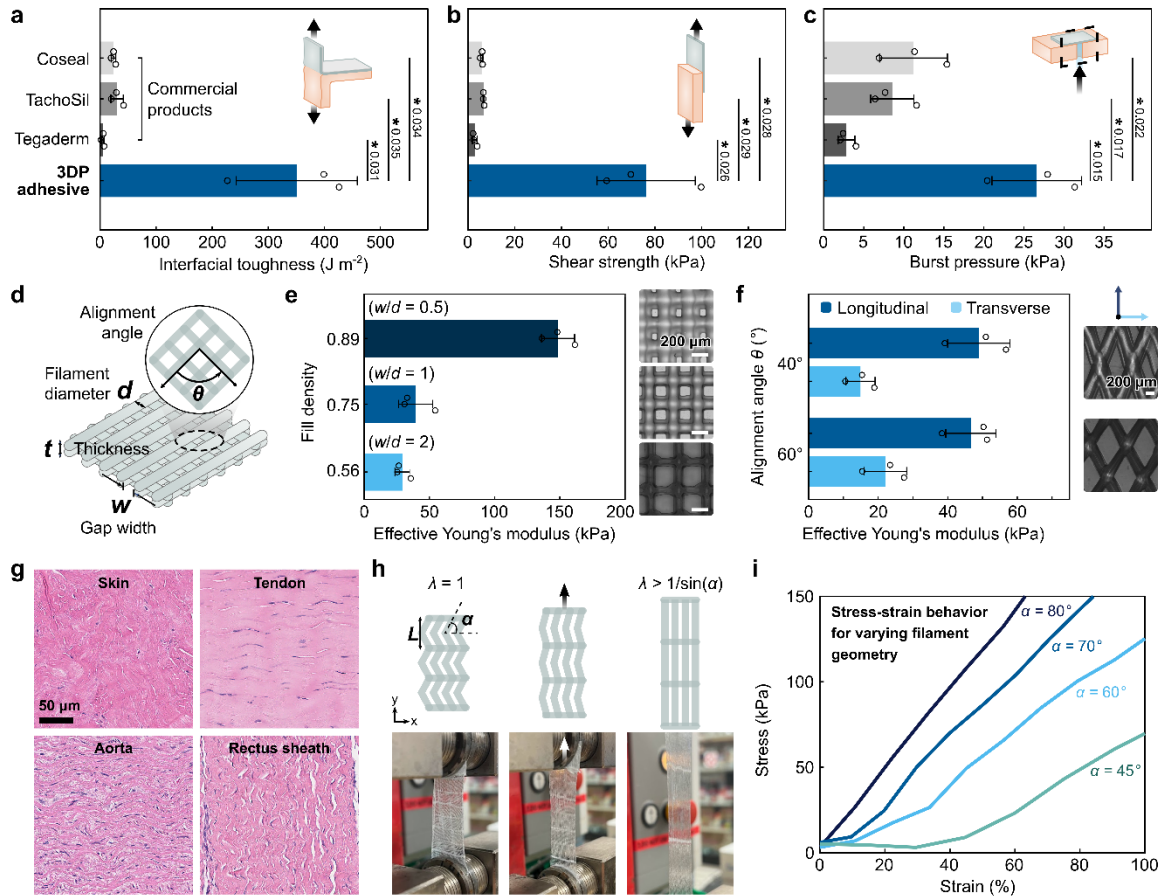


Figure 5-10. Adhesion performance and mechanical tunability of the 3D printable tissue adhesive. (a-c) Adhesion characterization of the tissue adhesive material and commercially available tissue adhesives adhered to porcine skin for interfacial toughness (a), shear strength (b), and burst pressure (c). All measurements were taken 30 minutes after initial adhesion to allow for swelling and equilibration. (d) Tunable geometric parameters of printed mesh lattice structures. (e) Effective initial Young's moduli for 3D printed meshes with varying fill density. (f) Effective anisotropic Young's moduli for 3D printed meshes with varying alignment angles between alternating printed layers. (g) Histological images stained with H&E of different types of porcine tissues featuring distinct collagen fibril patterns. (h) Illustrated schematic and corresponding photographs of uniaxial stretching for a collagen fiber-inspired patch featuring a 3D printed waveform pattern. For a pattern with bend angle α , the corresponding transition stretch between straightening and bending of the fibers is $\lambda = 1/\sin(\alpha)$. (i) Experimental stress-strain curves for 3D printed patches having different angles α of 80° (dark blue), 70° (medium blue), 60° (light blue), and 45° (teal). The corresponding theoretical transition strains for these angles are around 2%, 6%, 15%, and 41%, respectively. Values and error bars in a-f represent the mean and standard deviation ($n = 3$). Statistical significance and p values were determined by two-sided paired t -tests: ns $p > 0.05$; $*$ $p \leq 0.05$; $**$ $p \leq 0.01$; $***$ $p \leq 0.001$.

The 3D printability of the optimized tissue adhesive ink allows direct ink writing of lattice-patterned mesh patches designed for sealing tissue defects. Mesh structures, whose voids enhance flexibility and facilitate mass transport, make rational form factors for conforming to tissues. Furthermore, the removal of interfacial water at the adhesive-tissue interface is facilitated by capillary effects and drainage through the pores²²⁵. To fabricate fluid-tight sealant patches, a mesh pattern was printed directly onto a thin layer of PU to provide a flexible backing layer. The resulting patch can achieve fluid-tight sealing of 3 mm-diameter defects in ex vivo porcine skin, sustaining burst pressures of over 26 kPa (**Figure 5-10c** and **Figure 5-11**) For reference, this is substantially higher than most physiologically relevant pressures, including hypertensive systolic blood pressure (17-19 kPa) and intrathoracic pressures (6-8 kPa)²²⁶⁻²²⁸.

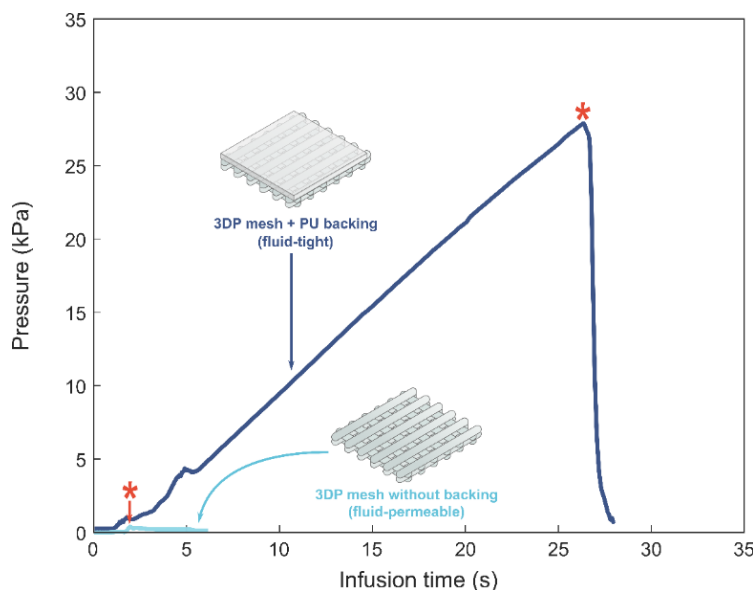


Figure 5-11. Representative burst pressure curves of 3D printed patches with and without backing layer. Lattice patterns printed onto a thin layer of PU achieved fluid-tight seals with porcine skin, sustaining burst pressures exceeding 20 kPa (main Fig. 3c). Without backing the backing layer, the patches formed fluid-permeable adhesive interfaces. For the representative curves, * indicates the burst pressure.

5.2.2. Mechanical tunability

Varying the geometric parameters, such as the filament density or the angle of alignment between filaments, can alter the mechanical properties of the mesh and introduce anisotropic or tunable nonlinear behavior (**Figures 5-10d-f**, **Figure 5-12**, and **5-13**). Considering the range of properties observed in different biological tissues, mechanical tunability may be a useful tool for designing a well-matched tissue-material interface and guiding cell interactions or tissue mechanics (**Figure 5-10g**)²²⁹. For example, inspired by the wavy collagen fibrils in tissues which give rise to nonlinear stress-strain behavior, patches were generated featuring waveforms that generate tissue-like J-shaped stress-strain responses (**Figure 5-10h-i**). Depending on the arclength of the wave

(determined here by the bend angle α and period L), the printed structures exhibit varying stiffening behavior corresponding to shifts in the transition between straightening of the wavy fibers to stretching-dominated deformation. The experimental J-shaped stress-strain curves plotted in **Figure 5-10i** show different transition points for patterns having different bend angle α , which are in close approximation with the theoretical transition stretch of $\lambda = 1/\sin(\alpha)$, indicating that the 3D printing platform can be leveraged as an avenue for developing patches with programmable nonlinear mechanical properties. In turn, these mechanical properties have the potential to influence the biological response to the implanted material.

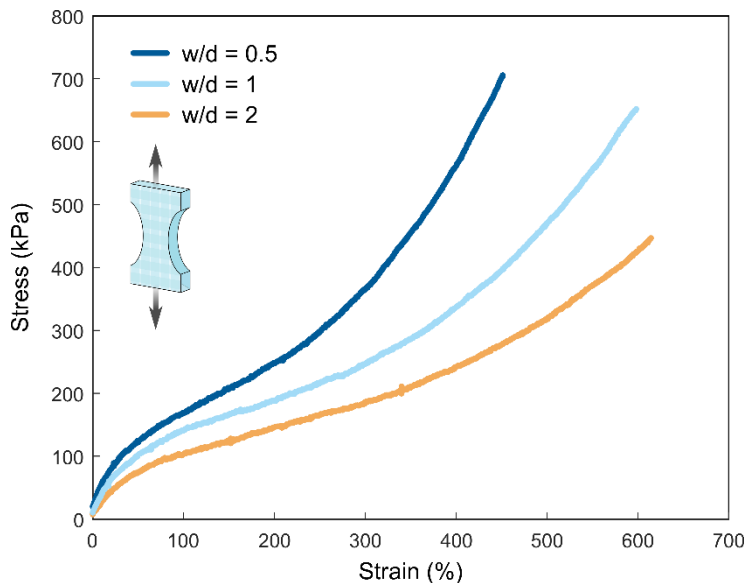


Figure 5-12. Representative stress-strain curves for 3D printed samples with varying gap width (w) to filament diameter (d) ratios. Tensile tests of 3D printed tissue adhesive meshes with w/d ratios of 0.5, 1, and 2 were measured (with d fixed at $200\ \mu\text{m}$). All measurements were taken with the materials in a fully hydrated state, following submersion in PBS at $37\ ^\circ\text{C}$ for 20-30 minutes.

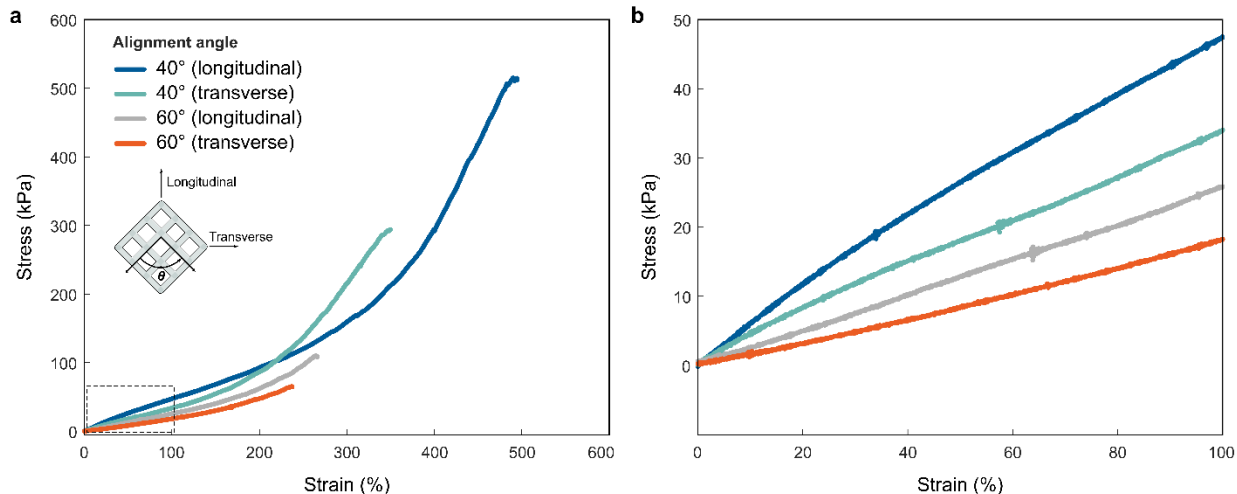


Figure 5-13. Representative stress-strain curves for 3D printed samples with different alignment angles between filaments. a, Full stress-strain curves for samples with angles of alignment of 40° and 60°. b, Zoomed-in plot depicting the initial stress-strain slope of each representative sample. All measurements were taken with the materials in a fully hydrated state, following submersion in PBS at 37 °C for 20-30 minutes.

5.2.3. Biocompatibility and biodegradability

To evaluate the biocompatibility of the 3D printed tissue adhesive, *in vitro* cell and *in vivo* animal studies were performed. Quantitative analysis using a LIVE/DEAD assay of mouse fibroblast cells co-cultured with medium (DMEM) soaked with the 3D printed patch reveals high cell viability comparable to a pristine control media group ($P = 0.41$) and other commercially available tissue adhesives ($P = 0.35$ for Tachosil and $P = 0.71$ for Coseal) (**Figure 5-14**). The *in vivo* biocompatibility and biodegradability was further characterized by performing subcutaneous implantations of the 3D printed patch in rats (**Figure 5-15a**). After 2- and 4-weeks post-implantation, the implanted material and adjacent tissues were harvested for histological analysis. The 3D printed patch shows mild inflammation at both time points, with a gradual decrease of the implant volume at 4 weeks due to hydrolytic degradation (**Figure 5-15a** and **Figure 5-16**)²³⁰. Subcutaneous implantation of a commercial product (Tachosil) as a control showed comparable levels of inflammation and relatively faster *in vivo* degradation.

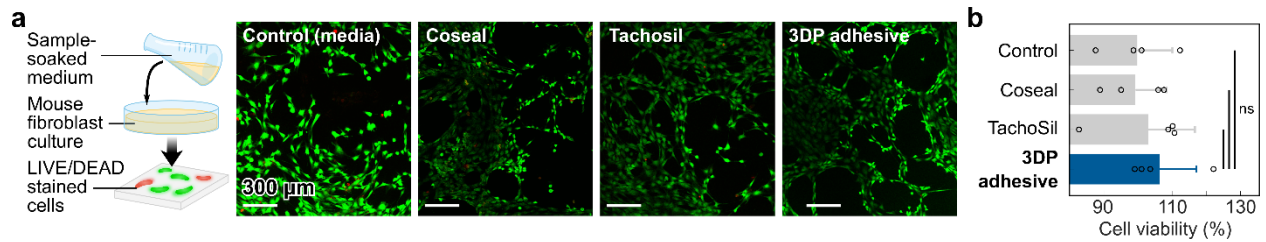


Figure 5-14. In vitro biocompatibility. (a) Representative in vitro LIVE/DEAD staining and (b) quantitative cell viability analysis of 3T3 mouse fibroblasts cultured with Dulbecco's modified Eagle's medium (DMEM, control) and DMEM soaked with Coseal, TachoSil, and the 3D printed patch. Values and error bars represent the mean and standard deviation ($n = 4$ independent samples). Statistical significance and p values were determined using a two-tailed Student's t -test with unequal variance: ns indicates $p > 0.05$.

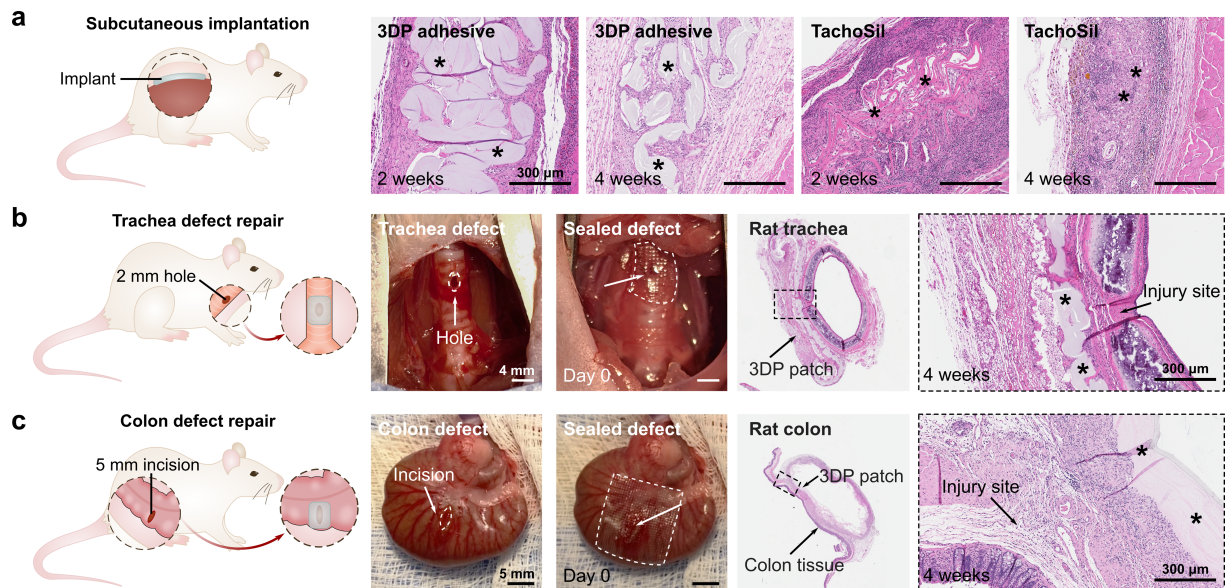


Figure 5-15. Biocompatibility and sutureless repair of defects in rat models. (a) Representative histological images stained with H&E after 2 and 4 weeks following the subcutaneous implantation of 3D printed patches and TachoSil in rats. (b) Representative photographs and histological images stained with H&E of rat trachea defect repaired using the 3D printed patch after 4 weeks. (c) Representative photographs and histological images stained with H&E of rat colon repaired using the 3D printed patch after 4 weeks. In the histological images, * represents the implanted material.

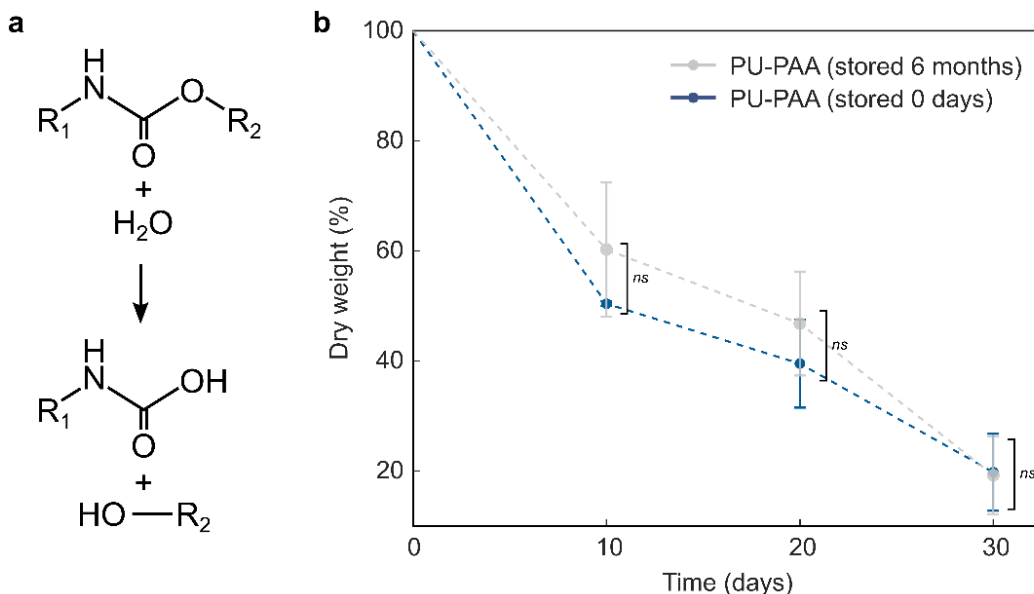


Figure 5-16. In vitro degradation of PU-PAA. (a) General hydrolytic degradation of polyurethane. (b) Degradation profiles. Samples of PU-PAA were submerged in 37 °C PBS and shaken continuously at 60 rpm. At days 10, 20, and 30, the samples were removed, dried thoroughly at 70 °C, and weighed. No significant difference in degradation was found between freshly synthesized samples and samples which were stored in ambient conditions for 6 months prior. Values represent the mean and standard deviation ($n = 3$ independent samples). Statistical significance and p values were determined using a two-tailed Student's t -test with unequal variance: ns indicates $p > 0.05$.

5.2.4. In vivo defect repair

Next, the applicability of the 3D printed patch for sealing tissue defects as assessed, specifically focusing on two scenarios: air-leaking tracheal defects and fluid-leaking colon defects (**Figure 5-15b-c**). Defects in the airway and gastrointestinal (GI) tract can be life-threatening conditions that often require significant patient management or surgical treatment^{231,232}. For the trachea, current options for defect repair are limited because sutures apply high tensions susceptible to cartilage tearing and can allow air leaks through gaps between punctures, and flowable sealants may be aspirated into and obstruct the airway. Considering these challenges, the flexible, preformed 3D printed mesh is a favorable form factor for achieving tracheal defect repair. To investigate its tissue sealing potential, the 3D printed patch was applied over 2 mm long x 1 mm wide oval-shaped defects in rat tracheas (**Figure 5-15b**). After 10 s of gentle pressure application, the patch formed a circumferential seal around the defect, achieving air-tight adhesion and restoring air ventilation to the lungs. Histological analysis of the tissues harvested after 4 weeks post-implantation indicates that the defects were repaired by the 3D printed patch with no visible sign of leakages or tracheal narrowing (**Figures 5-17, 5-18**). The patch remains partially degraded at the site of implantation after 4 weeks with mild inflammation, consistent with the subcutaneous implantation study.

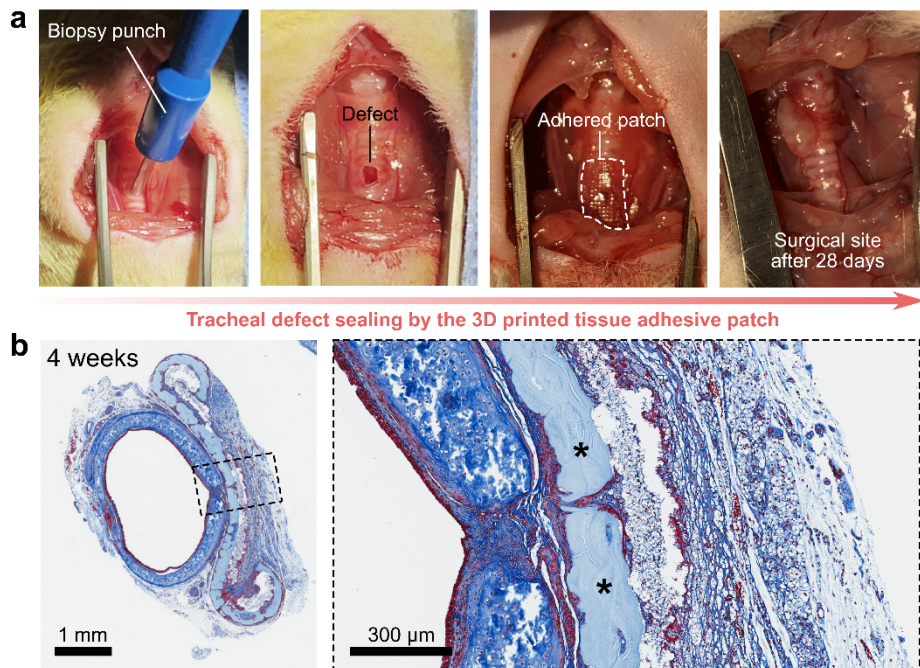


Figure 5-17. In vivo wound sealing of tracheal defects in rats. (a) Experimental photographs for the rat tracheal defect-repair model. A 1-mm diameter biopsy punch was used twice to create a 2 mm x 1 mm oval-shaped hole, which was sealed with a 3D printed patch. The defects remained sealed for 28 days post-surgery. (b) Representative histology images of the tracheas harvested after 28 days stained with Masson's trichrome stain. * indicates the adhesive. Three independent experiments were conducted with similar results.

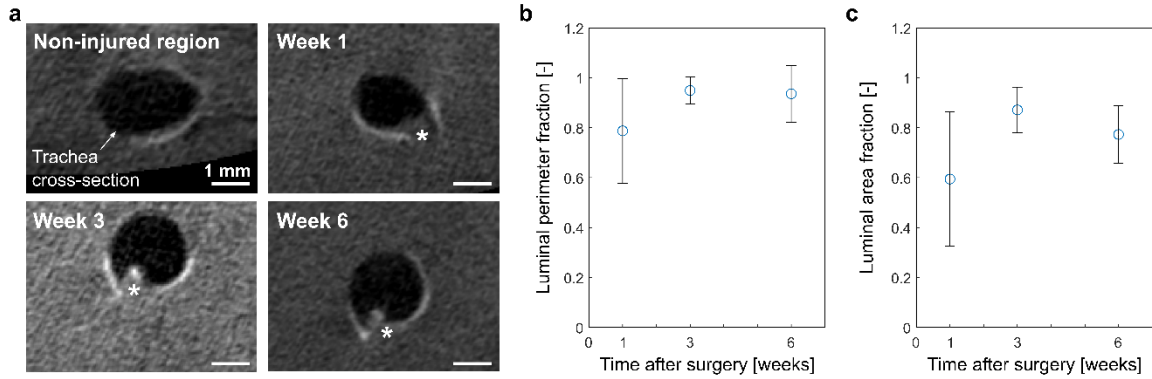


Figure 5-18. Micro-CT observation of tracheal healing in rats. (a) Representative micro-CT scans of an injured rat trachea repaired with a 3D printed patch. * indicates the defect site. (b) Luminal perimeter fraction as a function of time after surgery. Luminal perimeter fraction was computed using ImageJ by measuring the ratio of the injured trachea cross-sectional perimeter to the non-injured perimeter for each animal. (c) Luminal area fraction as a function of time after surgery. Luminal area fraction was computed using ImageJ by measuring the ratio of the injured trachea cross-sectional area to the non-injured area for each animal. Values represent the mean and standard deviation ($n = 3$ independent samples).

To evaluate the applicability of the 3D printed patch for repairing GI organs, the patch was used to seal 5-mm incisional defects in rat colons (**Figure 5-15c**). Leakages from GI defects are significant clinical challenges that can result in infection, sepsis, and mortality. As with the trachea, the 3D printed patch readily conforms to the colon surface and provides fluid-tight sealing within 10 s with no signs of bowel leakage following the surgery. After 4 weeks, the partially degraded patch remains adhered at the injury site and the colonic defect is repaired without signs of abscesses (**Figure 5-15c, 5-19**).

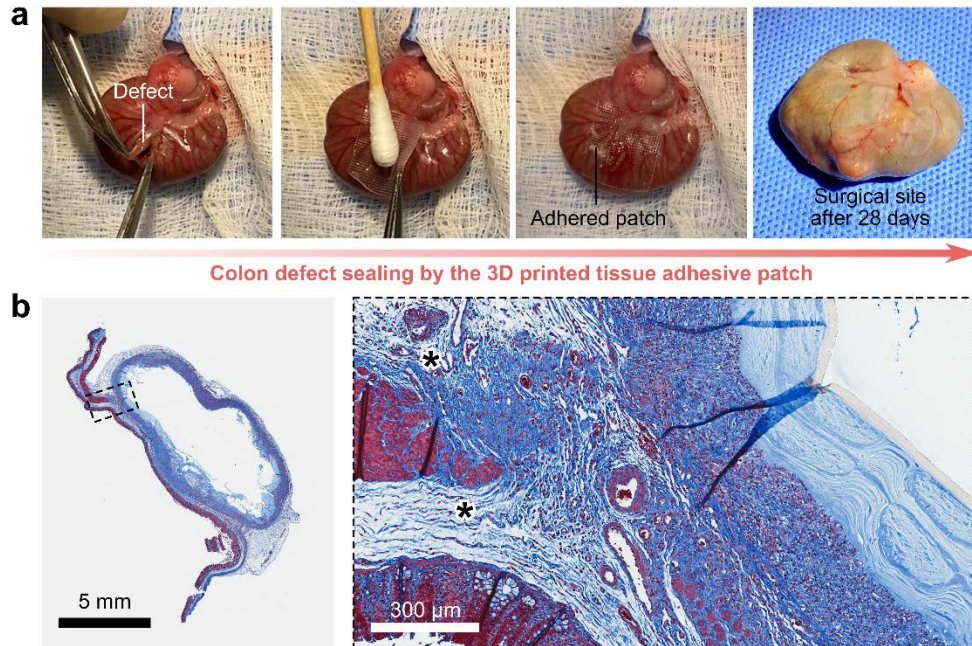


Figure 5-19. In vivo wound sealing of colonic defects in rats. (a) Experimental photographs for the rat colon defect-repair model. Surgical scissors were used to create a 10-mm incision, which was sealed with a 3D printed patch. The defects remained sealed for 28 days post-surgery. (b) Representative histology images of the colons harvested after 28 days stained with Masson's trichrome stain. * indicates the adhesive. Three independent experiments were conducted with similar results.

Addressing severely bleeding injuries is a particularly difficult challenge due to their complex, time-sensitive nature. Many tissue adhesives struggle to adhere in the presence of blood, which can interfere with tissue interactions and wash out liquid adhesives or hemostatic agents. Indeed, the NHS esters which lend adhesive functionality to the PU-PAA material can be compromised if exposed to blood, limiting the efficacy of the 3D printed patches in extremely bloody scenarios. To address this limitation, 3D printing can be leveraged to design a liquid-infused patch that resists blood during tissue repair¹²⁹⁻¹³¹ (**Figure 5-20**). The liquid-infused patch is based on the incorporation of a hydrophobic (blood-resistant) liquid into a 3D printed porous mesh structure. The efficacy of the liquid-infused patch is underpinned by the favorable thermodynamics governing the interaction between the hydrophobic fluid (i.e., oleic acid) and the textured tissue adhesive surface (**Figure 5-21**). This configuration serves as a physical barrier to preclude fouling by blood and other body fluids, which enables the application of the patch onto actively bleeding defect sites. By exerting adequate pressure, the hydrophobic liquid can be expelled through the mesh's pores as well as laterally at the interface, allowing the adhesive to form direct tissue contact and subsequently achieve adhesion (**Figure 5-20a-c**).

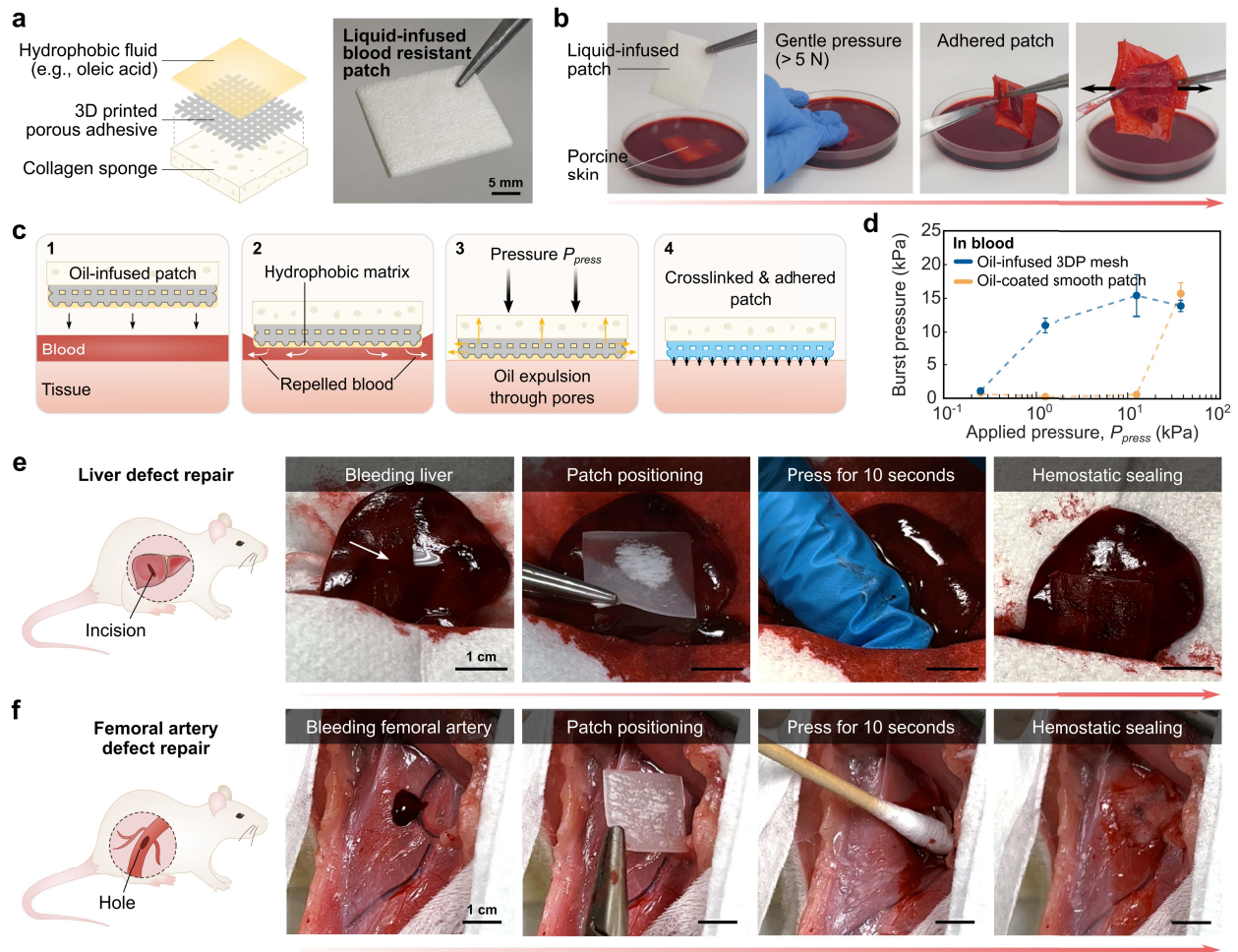


Figure 5-20. Liquid-infused 3D printed patches for blood-resistant tissue sealing. (a) Illustrated schematic and photograph of the liquid-infused 3D printed patch. A porous 3D printed pattern is integrated with a collagen sponge and infiltrated with oleic acid. (b) Photographs of the liquid-infused patch being adhered to porcine skin submerged in a blood bath. (c) Illustrated schematic of the blood-repelling, oil-dewetting, and tissue adhesion process. (d) Burst pressure vs. applied pressure for the oil-infused 3D printed mesh compared with smooth, non-porous patch (of the same material) coated with a layer of oil. Compared with the smooth patch, the porous 3D printed patch can achieve a higher burst pressure at a lower applied pressure due to drainage through the macroscopic pores. Values and error bars represent the mean and standard deviation ($n = 4$). (e) Photographs of the in vivo application of a liquid-infused 3D printed patch to repair an actively bleeding defect in the liver of a rat. (f) Photographs of the in vivo application of a liquid-infused 3D printed patch to repair an actively bleeding defect in the femoral artery of a rat.

Notably, the pressure requirement for adhering the liquid-infused mesh structure is lower than that for an oil-coated, smooth (non-porous) patch comprised of the same material (**Figure 5-20d**). This is because in the mesh structure, the hydrophobic fluid may freely drain through the pores, whereas in the smooth patch configuration, it is limited to lateral squeeze-out and may become entrapped at the tissue-patch interface. To investigate the blood-resistant adhesive performance, a series of in vivo experiments were conducted to apply the patch to actively bleeding liver and femoral artery defects in live rats (**Figure 5-20e-f**). The liquid-infused 3D printed patch achieves blood-resistant sealing of a bleeding liver injury (a 5 mm-long and 2 mm-deep incision) and a femoral artery injury (a ~2 mm snip) within 10 seconds of applied pressure. In summary, leveraging the 3D printability of the tissue adhesive to create textured, liquid-infused patches demonstrates the additional potential for treating bleeding wounds.

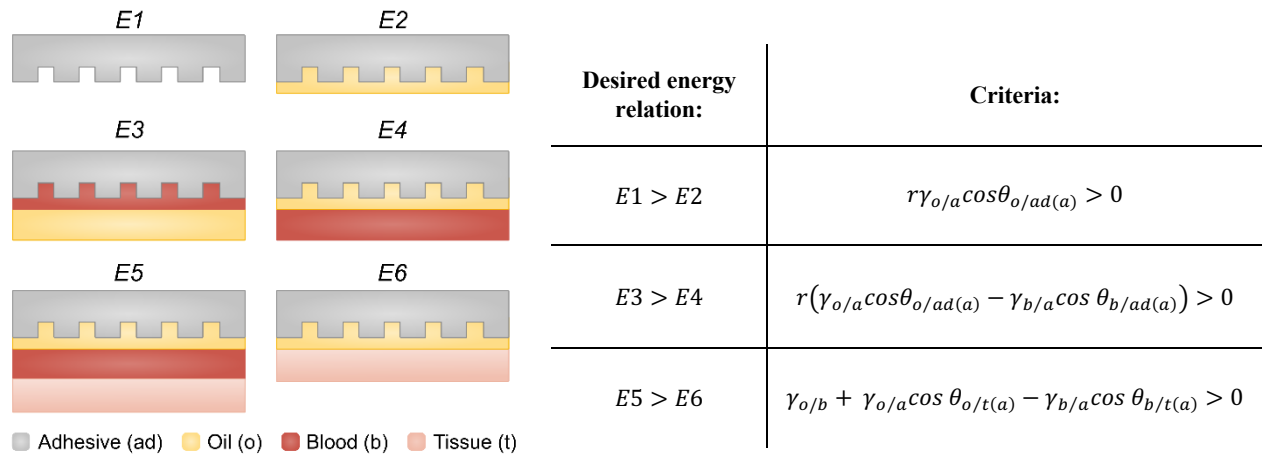


Figure 5-21. Wetting configurations and energy criteria for the liquid-infused adhesive system comprising air, the tissue adhesive material, oleic acid, and tissue. For the liquid-infused patch to be thermodynamically stable in air, the desired energy relation is $E1 > E2$. For the patch to be preferentially wetted by the oil in the presence of blood, the desired energy relation is $E3 > E4$. To ensure repelling of blood at the tissue surface, the desired energy relation is $E5 > E6$. Here, r is the ratio of the total surface area to the projected area, $\gamma_{x/y}$ is the interfacial energy between substances x and y (where $o = \text{oil}$, $a = \text{air}$, $ad = \text{adhesive}$, $b = \text{blood}$, and $t = \text{tissue}$), and $\theta_{x/y(z)}$ denotes the apparent contact angle of substance x on substance y in the presence of substance z . See the discussion below for more details.

Stability of the liquid-infused patch

The stability of the liquid-infused patch is governed by the energy relations that describe the liquid-substrate contact line^{2,3}. In the case of the textured 3D printed patch, the infusing liquid is held in place through a combination of van der Waals and capillary forces. To evaluate the thermodynamics of the system, we consider interactions between the four phases present: the oil (i.e., oleic acid), air, blood, and the tissue adhesive (**Figure 5-21**). Considering a square lattice-

printed pattern of the tissue adhesive surface with filament width a , gap width b , and thickness h , the ratio of the total surface area to the projected area is given by:

$$r = 1 + \frac{4bh}{(b+a)^2} \quad (5.1)$$

First, to determine the stable configuration of the liquid-infused 3D printed patch in air, we compare the total surface energies (denoted E_n) of Configurations E1 and E2. Configuration E1 describes a dry (i.e., not infiltrated) surface and Configuration E2 describes a fully encapsulated surface. For the oil to infiltrate the tissue adhesive, Configuration E2 should have a lower energy state than Configuration 1, such that:

$$E_1 > E_2 \quad (5.2)$$

This condition is equivalent to:

$$r\gamma_{ad/a} > r\gamma_{ad/o} \quad (5.3)$$

where $\gamma_{x/y}$ denotes the interfacial energy between substances x and y . ad denotes adhesive, a denotes air, and o denotes oil. Using Young's equation, this reduces to:

$$r\gamma_{o/a} \cos \theta_{o/ad(a)} > 0 \quad (5.4)$$

where $\theta_{o/ad(a)}$ denotes the apparent contact angle of the oil on the adhesive substrate in air. Similarly, for the tissue adhesive patch to be preferentially wetted by the oil in the presence of blood, we consider Configurations E3 and E4:

$$E_3 > E_4 \Leftrightarrow r(\gamma_{o/a} \cos \theta_{o/ad(a)} - \gamma_{b/a} \cos \theta_{b/ad(a)}) > 0 \quad (5.5)$$

Finally, we compare the surface energies of Configurations E5 and E6 to ensure repulsion of blood at the tissue interface. The corresponding energy relation that must be satisfied is:

$$E_5 > E_6 \Leftrightarrow \gamma_{o/b} + \gamma_{o/a} \cos \theta_{o/t(a)} - \gamma_{b/a} \cos \theta_{b/t(a)} > 0 \quad (5.6)$$

The system energies can thus be approximated by plugging in the relevant contact angles, interfacial energies, and geometrical parameters ($r \approx 1.22$, $\gamma_{o/a} \approx 31.92 \text{ mN m}^{-1}$, $\gamma_{b/a} \approx 72.0 \text{ mN m}^{-1}$, $\gamma_{o/b} \approx 40 \text{ mN m}^{-1}$, $\theta_{o/ad(a)} \approx 7.6^\circ$, $\theta_{b/ad(a)} \approx 72.1^\circ$, $\theta_{o/t(a)} \approx 4.2^\circ$, $\theta_{b/t(a)} \approx 84^\circ$)⁴⁻⁷. In doing so, it is evident that the thermodynamic conditions summarized in Supplementary Fig. 17 are satisfied.

5.2.5. Detailed methods

Grafting of PAA to PU

A precursor solution was prepared by combining 32 w/v % AA, 8 w/v % PU, 20 w/v % vacuum-degassed deionized water, and 40 w/v % ethanol and stirring until the PU was fully dissolved. 1.1 w/v % benzophenone and 0.1 w/v % α -ketoglutaric acid were added to the precursor solution and homogeneously mixed, then transferred to a sealed glass vial and cured in a UV crosslinker (364 nm, 15 W power) for 120 min. Benzophenone functions as a Type II free radical photoinitiator

that enters an excited triplet state under UV irradiation, generating radical sites in PU (for example, by abstracting hydrogen from carbon-hydrogen containing molecules along the polyether backbone). These radical sites may then react with acrylic acid, initiating the growth of PU-grafted PAA chains. Benzophenone ketyl radicals can eventually combine with each other to form benzopinacol, which is removed during the dialysis process. For dialysis, the cured product was transferred to a cellulose membrane (Sigma Aldrich, typical molecular weight cut-off = 14,000) and purified in a pure ethanol bath for 24 h (replacing the ethanol every 12 h) followed by in a deionized water bath for 24 h (replacing the water every 12 h) with continuous magnetic stirring. The purified PU-PAA was cut into small pieces and dried in a desiccating oven at 70 °C for 48 h.

Preparation of the 3D printable tissue adhesive ink

The dried PU-PAA was redissolved at a concentration of 20 w/w % in 70% ethanol and mixed in a 25:2 (v/v) ratio with a solution comprising 33.3 w/v % EDC and 33.3 w/v % NHS in 70% ethanol to yield around 10% (mol/mol) NHS functionalization of the carboxyl groups. The combined solution was then mixed in a 10:3 (v/v) ratio with 20 w/w % PU in 95% ethanol. To mitigate hydrolysis of NHS, the ink was prepared directly before use.

3D printing procedure

3D printing of the tissue adhesive ink and other polymer solutions was performed using a custom-designed 3D printer with a Cartesian gantry system (Aerotech). Under air pressure, inks were extruded from 5 mL syringe barrels through nozzles ranging in size from 50 to 200 μm (EFD Nordson). Printing paths were designed using Adobe Illustrator and CADFusion (Aerotech), then translated into G-code using a custom Python script. To achieve continuous printing of the tissue adhesive ink, a printing pressure of 250 kPa was selected (Ultimus V, Nordson EFD) and printing speeds ranging from 500-1800 mm/min. The structures were printed onto a glass slide (Corning) treated with hydrophobic coating (Rain-X). After printing, the structures were completely dried and sealed in plastic bags with desiccant (silica gel packets) before use.

FTIR

32 scans were recorded for droplets of polymer on a Bruker Alpha II FT-IR spectrometer with a monolithic diamond crystal at a resolution of 4 cm^{-1} . An equal number of background scans were recorded on air prior to each sample measurement. For analysis, each spectrum was normalized based on the peak around 2900 cm^{-1} . As shown in **Figure 5-6**, the stretching bands of the C=O bond and the O-H bond in carboxylic acid can be clearly observed at around 1710 cm^{-1} and 3300 cm^{-1} for the samples containing PAA, indicating the retention of PAA via grafting and entanglement. The stretching and bending vibration bands of the C-NH bond on O=C-NH-C at around 3350 cm^{-1} and 1530 cm^{-1} and the stretching vibration band of the N-H bond at around 1700 cm^{-1} can also be observed for the PU-containing spectra, indicating the presence of a urethane group²³³. The strong stretching vibration band associated with the ether bond at 1100 cm^{-1} reflects the polyether character of the ether-based PU.

¹H NMR

Proton (¹H) nuclear magnetic resonance (NMR) spectra were measured at 400 MHz on a Bruker Avance III DPX 400. Approximately 100 mg of each sample were dissolved in 500 μ L deuterated dimethylsulfoxide (DMSO-*d*6) for analysis. To evaluate the ratios of PAA:PU and NHS:PAA, each spectrum was normalized based on the peak around 2.22 ppm attributed to the methylene peak in PAA. The peaks at 7.06 ppm, attributed to the nitrogen-attached hydrogen in PU, were integrated with respect to the normalized peaks to approximate the molar ratios of PAA:PU in the final purified products (**Figure 5-7**). The NHS alkyl peaks at 2.76 ppm were integrated with respect to the normalized peaks to estimate the degree of NHS functionalization (**Figure 5-3d**).

Adhesion characterization

Adhesion tests were performed on porcine skin washed with phosphate buffer solution (PBS). 3D printed tissue adhesive samples were adhered by applying gentle pressure upon the tissue substrate for 10 s. Commercial sealants were applied according to manufacturer instructions. Unless otherwise indicated, adhesion characterizations were performed 30 minutes after initial application to allow for equilibrium swelling of the tissue adhesive material. Adhered samples were covered with gauze soaked in PBS to maintain a wet environment prior to measurement.

To measure interfacial toughness, tissue samples with widths of 2 cm were adhered to the various adhesives and tested via the standard 180-degree peel test (ASTM F2256) using a mechanical testing machine (2.5 kN load cell, Zwick/Roell Z2.5). All tests were conducted with a constant peeling speed of 50 mm min⁻¹. The measured force reached a plateau as the peeling process entered steady state. Interfacial toughness was determined by dividing two times the plateau force by the width of the tissue sample (**Figure 5-22a**). Hydrophilic nylon filters (1 μ m pore size, TISCH Scientific) were used as a stiff backing for the 3D printed tissue adhesive.

To measure shear strength, tissue samples with an adhesion area of 2 cm x 2 cm were joined using the various adhesives and tested via the standard lap shear test (ASTM F2255) using a mechanical testing machine (2.5 kN load cell, Zwick/Roell Z2.5). All tests were conducted with a constant peeling speed of 50 mm min⁻¹. Shear strength was determined by dividing the maximum force by the adhesion area (**Figure 5-22b**).

To measure burst pressure, 3 mm holes were introduced in 2.5 cm x 2.5 cm pieces of porcine skin using biopsy punches based on the ASTM F2392-04 standard defect size for burst pressure measurement. The holes were then sealed using 1.5 x 1.5 cm samples of the 3D printed tissue adhesive, or an equivalent area of Coseal, TachoSil, or Tegaderm. The size was determined based on previously reported measurements of burst pressure strength of surgical sealants²²⁶. The samples were fixed in a testing rig and PBS was injected at a constant rate of 5 mL min⁻¹ to the point of failure (i.e., fluid leakage). Pressure was recorded by a pressure transducer (PX409, Omega). The burst pressure was determined as the maximum pressure upon which a leakage formed (modified ASTM F2382-04; **Figure 5-22c**).

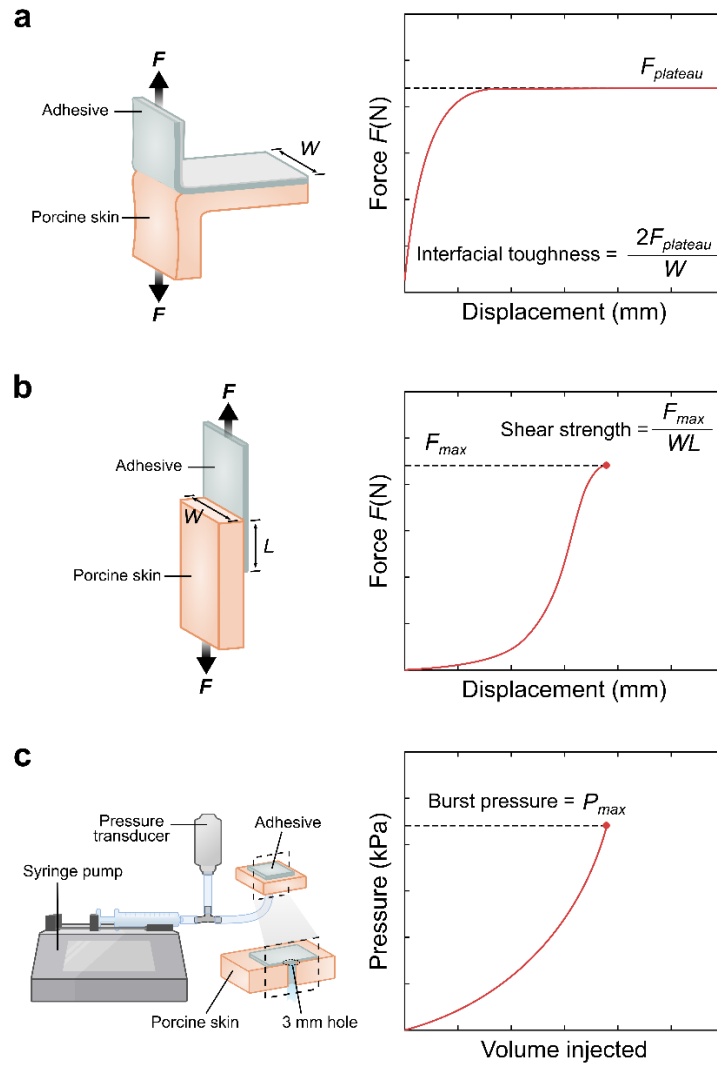


Figure 5-22. Experimental setups characterizing adhesion performance. (a) Schematic illustration of the experimental setup to measure interfacial toughness based on a 180-degree peel test (ASTM F2256). (b) Schematic illustration of the experimental setup to measure adhesive shear strength based on a lap-shear test (ASTM F2255). (c) Schematic illustration of the experimental setup to measure burst pressure based on ASTM F2392-04. Plots in a-c are generic drawings and do not represent real data.

Rheological characterization

Rheological measurements of the tissue adhesive inks were performed using a rotational rheometer (AR-G2, TA instrument) with 40-mm diameter 2° steel cone geometry at 25 °C. Apparent viscosity was measured as a function of shear rate using a continuous ramp over a logarithmic sweep from shear rate 1 to 1000 s⁻¹. Shear storage modulus (G') was measured as a function of shear stress using an oscillatory procedure with 1 Hz frequency over a logarithmic sweep from shear stress 1 to 10000 Pa. For all measurements, an aqueous solvent trap was used to minimize ink drying.

Mechanical characterization

The tensile properties of mesh samples were measured following the standard tensile test (ASTM D412) using a mechanical testing machine (2.5 kN load cell, Zwick/Roell Z2.5). Samples were fully swollen and equilibrated in PBS at 37°C before measurement. Effective Young's moduli were determined as the initial slope on the stress-strain curve.

Microscope imaging

Microscopic 3D printed structures were imaged using an epifluorescence microscope (Nikon Eclipse LV100ND). Confocal microscope images of the mesh structure were obtained by an upright confocal microscope (SP 8, Leica) with 360 nm excitation wavelength for blue fluorescent beads. ImageJ (version 2.1.0) was used for image processing and analysis.

Fabrication of the collagen fiber-inspired patches

A silicone elastomer ink was prepared by mixing Dragon Skin 30 (Smooth-On) and SE 1700 (Dow Corning) together. Specifically, Dragon Skin 30 part A, Dragon Skin 30 part B, SE 1700 base, and SE 1700 catalyst were added in a 10:10:10:1 weight ratio and mixed thoroughly using a Thinky mixer (AR-100, Thinky). The ink was printed onto a glass slide (Corning) treated with a hydrophobic coating (RainX) into the desired geometry and cured in the oven at 120 °C for 30 min. After curing and cooling, a layer of the tissue adhesive ink (prepared as described above) was printed on top of the silicone layer, following the same geometry. After drying, the patch was removed from the glass slide and evaluated using a standard tensile test.

Fabrication of the liquid-infused blood resistant patch

Tissue adhesive ink was prepared as described above and printed onto a glass slide (Corning) treated with hydrophobic coating (RainX) into a 25 cm by 25 cm repeating lattice pattern with filament width ~150 μm and gap width ~150 μm. After drying, the adhesive structure was integrated with a collagen wound dressing sponge (Puracol) of the same dimensions by exposing the uppermost surface of the printed structure to steam, allowing the surface to become slightly hydrated, then immediately placing the collagen sponge on the hydrated surface to allow crosslinking between the two substrates. The integrated patch was removed from the glass slide and infiltrated with oleic acid. To demonstrate blood-resistant tissue adhesion, samples of the oil-

infused patch were applied to porcine skin samples covered with heparinized porcine blood (Lampire Biological Laboratories, Inc.) using gentle pressure for 10–30 s.

In vitro biocompatibility

To evaluate the in vitro biocompatibility and cytotoxicity of the mesh, a LIVE/DEAD assay was used to assess Balb/c 3T3 clone A31 mouse fibroblasts (American Type Culture Collection®; CCL163™). To prepare conditioned media, 500 mg of Coseal, TachoSil, and the 3D printed tissue adhesive were each incubated in 10 ml of Dulbecco's modified Eagle's medium (DMEM) supplemented with 10 v/v % fetal bovine serum and penicillin-streptomycin (100 U mL⁻¹) at 37 °C for 24 h. The supplemented DMEM (without any material incubation) was used as a control. 3T3 cells were plated in confocal dishes (20-mm diameter) at a density of 0.5×10^5 cells cm⁻² ($N = 4$ for each group). The cells were then treated with either conditioned or control media and incubated at 37 °C for 24 h in a 5% CO₂ atmosphere. Cell viability was determined by a LIVE/DEAD viability/cytotoxicity kit for mammalian cells (Thermo Fisher Scientific). A confocal microscope (SP 8, Leica) was used to image live cells with excitation/emission at 495 nm/515 nm and dead cells at 495 nm/635 nm, respectively. Cell viability was calculated by counting live (green fluorescence) and dead (red fluorescence) cells using ImageJ (version 2.1.0).

In vivo biocompatibility

All rat studies were approved by the MIT Committee on Animal Care, and all surgical procedures and postoperative care were supervised by the MIT Division of Comparative Medicine veterinary staff. Female Sprague-Dawley rats (225-250 g, Charles River Laboratories) were used for all in vivo studies. Before implantation, the 3D printed patch was prepared using aseptic techniques and was further sterilized for 1 h under UV light. Commercially available tissue adhesives were used as provided in sterile packages following the provided user guide or manual for each product.

For implantation in the dorsal subcutaneous space, rats were anesthetized using isoflurane (2-3% isoflurane in oxygen) in an anesthetizing chamber. Anesthesia was maintained using a nose cone. The back hair was removed, and the animals were placed over a heating pad for the duration of the surgery. The subcutaneous space was accessed by a 1–2 cm skin incision per implant in the center of the animal's back. To create space for implant placement, blunt dissection was performed from the incision towards the animal shoulder blades. Samples of the 3D printed patch and TachoSil with the size of 20 mm in width and 20 mm in length were placed in the subcutaneous pocket created above the incision without detachment. The incision was closed using interrupted sutures (4-0 Vicryl, Ethicon) and 3–6 mL of saline was injected subcutaneously. Up to four implants were placed per animal ensuring no overlap between each subcutaneous pocket created. 2 or 4 weeks after the implantation, the animals were euthanized by CO₂ inhalation. Subcutaneous regions of interest were excised and fixed in 10% formalin for 24 h for histological analyses. Fixed tissue samples were placed into 70% ethanol and submitted for histological processing and H&E or Masson's trichrome (MT) staining at the Hope Babette Tang (1983) Histology Facility in the Koch Institute for Integrative Cancer Research at the Massachusetts Institute of Technology. Representative histology images of each group were shown in the corresponding figures ($n = 3$).

In vivo rat trachea defect repair

For the in vivo trachea defect repair model, rats were anesthetized using isoflurane (2-3% isoflurane in oxygen) in an anesthetizing chamber. Anesthesia was maintained using a nose cone. Hair covering the throat area was removed, and the animals were placed over a heating pad for the duration of the surgery. The trachea was exposed by a 2 cm midline skin incision followed by separation of the sternohyoid and sternothyroid muscles. A longitudinal oval-shaped defect was created by using a 1 mm-diameter biopsy punch to create two adjacent holes in the trachea. A 3D printed patch or TachoSil patch with the size of 5 mm in width and 10 mm in length was applied over the defect by gently pressing with a sterile cotton tip applicator for 10–30 s. After adhesion, leakage from the sealed defect was tested by introducing warm saline solution and checking for bubbles. Following confirmation of an air-tight seal, the muscle and skin layers were closed with sutures (4-0 Vicryl, Ethicon). 2 or 4 weeks after the surgery, the animals were euthanized by CO₂ inhalation. Tracheal regions of interest were excised and fixed in 10% formalin for 24 h for histological analyses. Fixed tissue samples were placed into 70% ethanol and submitted for histological processing and H&E or MT staining at the Hope Babette Tang (1983) Histology Facility in the Koch Institute for Integrative Cancer Research at the Massachusetts Institute of Technology. Representative histology images were shown in the corresponding figures ($n = 3$). 1, 3, and 6 weeks after surgery, the animals were imaged using Micro-CT ($n = 3$).

Micro-CT imaging of rat tracheas

Micro-CT images were obtained using a SkyScan 1276 (Bruker). To perform Micro-CT imaging, rats were anesthetized using isoflurane (1.5-2.5%) and transferred to an animal holder that was mounted into the scanner. Scans were obtained using the following parameters: pixel size 40.2 μm , source voltage 85 kV, source current 200 μA , exposure 179 ms, rotation step 230.5 mm, no frame averaging, and aluminum filter (1 mm). The images were reconstructed using NRecon software (Bruker). Luminal perimeter fraction was computed by thresholding micro-CT scans in ImageJ and taking the ratio of the injured trachea cross-sectional perimeter to the non-injured perimeter for each animal. Luminal area fraction was computed using ImageJ by taking the ratio of the injured trachea cross-sectional area to the non-injured area for each animal. After the conclusion of the 6-week timepoint, the animals were euthanized by CO₂ inhalation ($n = 3$ for each study group).

In vivo rat colon defect repair

For the in vivo colon defect repair model, rats were anesthetized using isoflurane (2-3% isoflurane in oxygen) in an anesthetizing chamber. Anesthesia was maintained using a nose cone. Abdominal hair was removed, and the animals were placed over a heating pad for the duration of the surgery. The colon was exposed by a median laparotomy. The exposed colon was packed with moistened sterile gauzes before creating a defect to prevent contamination of the abdominal cavity. A 10 mm incision was made to the colon using scissors and repaired using a 3D printed patch (10 mm in width and 20 mm in length) or sutures. After repair, warm saline was injected into the colon by a 32-gauge needle syringe to confirm formation of a fluid-tight seal. The muscle and skin layers were closed with sutures (4-0 Vicryl, Ethicon). 2 or 4 weeks after the surgery, the animals were

euthanized by CO₂ inhalation. Regions of interest were excised and fixed in 10% formalin for 24 h for histological analyses. Fixed tissue samples were placed into 70% ethanol and submitted for histological processing and H&E or MT staining at the Hope Babette Tang (1983) Histology Facility in the Koch Institute for Integrative Cancer Research at the Massachusetts Institute of Technology. Representative histology images were shown in the corresponding figures ($n = 3$).

In vivo rat liver defect repair

For the in vivo rat liver defect repair model, the rat was anesthetized using isoflurane (2-3% isoflurane in oxygen) in an anesthetizing chamber. Anesthesia was maintained using a nose cone. Abdominal hair was removed, and the animal was placed over a heating pad for the duration of the surgery. The liver was exposed by a laparotomy. An injury 5 mm in length and 2 mm in depth was made to the liver using a surgical scalpel. To seal the injury, a liquid-infused patch measuring around 2 cm by 3.5 cm was placed onto the bleeding defect site and gently pressed for 10 s. To confirm hemostasis, the region was washed with saline and observed for 30 min to check for any signs of further blood loss. At the termination of the study, the rat was euthanized by CO₂ inhalation.

In vivo rat femoral artery defect repair

For the in vivo rat femoral artery defect repair model, the rat was anesthetized using isoflurane (2-3% isoflurane in oxygen) in an anesthetizing chamber. Anesthesia was maintained using a nose cone. Leg hair was removed, and the animal was placed over a heating pad for the duration of the surgery. The femoral artery was exposed via an incision into the thigh. A snip around 2 mm in length was made to the artery using surgical scissors. To seal the injury, a liquid-infused patch measuring around 2 cm by 2 cm was placed onto the bleeding defect site and gently pressed for 10 s. To confirm hemostasis, the region was washed with saline and observed for 30 min to check for any signs of further blood loss. At the termination of the study, the rat was euthanized by CO₂ inhalation.

5.3. Bio-integrated device fabrication

Beyond the fabrication of functional patches for defect repair, the 3D printing platform provides immense versatility for constructing multimaterial, tissue-interfacing devices (**Fig. 6**). Most biomedical devices typically require sutures, tacks, or a separate adhesive layer to affix onto tissues. Although various adhesives have been developed for interfacing devices, many existing adhesive hydrogels require separate synthesis processes that are incompatible with advanced device manufacturing techniques, such as 3D printing. In contrast, the 3D printable adhesive enables devices to directly incorporate a tissue adhesive interface during the additive manufacturing process. To explore the potential technologies enabled by the 3D printing platform, several proof-of-concept devices were designed for applications including bioelectronics and drug delivery.

5.3.1. Bioelectronic patch

For instance, consider the case of a flexible, 3D printed bioelectronic patch featuring a simple LED circuit (**Figure 5-23a**). The pattern of the tissue adhesive layer contains negative space designed for the conductive electrodes to interface with the tissue, ensuring stable adhesion around their perimeters and securing electrode-to-tissue contact. When the patch is adhered to an ex vivo porcine heart connected to a power supply, the LEDs remain illuminated through dynamic movement of the heart (**Figure 5-23b**). This prototype demonstrates potential opportunities to print conformable bioelectronic devices for sensing or stimulating electrophysiological signals²³⁴.

Fabrication details

Tissue adhesive ink was prepared as described above and printed in a pattern featuring circular void spaces for electrodes onto a glass slide treated with hydrophobic coating. For the insulator layer, 20 w/v % polyurethane (HydroThane AL93A, AdvanSource biomaterials) dissolved in 1:1 tetrahydrofuran (THF) and dimethylformamide (DMF) was prepared and printed over the adhesive layer (400 μm -diameter printing nozzle, 200 kPa, 500 mm min^{-1}). Next, silver conductive ink was used to print the electrodes and circuitry (100 μm -diameter printing nozzle, 50 kPa, 800 mm min^{-1}). LEDs were attached to the circuit using a small amount of the silver ink. After drying, the bioelectronic patch was removed from the glass slide and adhered to an ex vivo porcine heart and a power source was used to run a current through the tissue to confirm illumination of the LEDs.

5.3.2. Drug delivery patches

Next, two illustrative concepts were explored for achieving localized drug delivery using the 3D printing platform to fabricate tissue adhesive, drug-loaded systems. In one example, a mock drug (fluorescein) is directly loaded into the tissue adhesive ink, enabling precise spatial patterning of a drug-releasing patch (**Figure 5-23c**). To visualize the release of fluorescein from the patch, a prototypical 3D printed patch was adhered to ex vivo porcine skin. At sequential timepoints, a small cross-sectional slice of the adhered system was cut and observed using fluorescence microscopy to capture the diffusion profile of the fluorescein into the skin (**Figure 5-23d**). In this case, the intimate consolidation between the patch and the skin allows spatially focused delivery of the mock drug into the tissue at the site of adhesion. In another example, the tissue adhesive ink is used to print the interfacial layer of a multi-material drug reservoir (**Figure 5-23e**). For this system, a therapeutic agent may be dispersed into a separate liquid or hydrogel matrix, then loaded into the adhesive reservoirs. As a visual demonstration, a mock drug solution containing blue dye was injected into the reservoirs using a syringe, and the diffusion of the dye into a gelatin hydrogel adherend was photographed to observe the release of the mock drug through the adhesive interface (**Figure 5-23f**). These prototypes illustrate the promising utility of the 3D printable tissue adhesive for localized drug delivery, which is compelling for reducing the need for high-dosage systemic delivery of pharmacological substances. In this context, the 3D printable tissue adhesive could be favorable for mitigating device displacement and leakage to the surrounding tissues. Still, further design refinement and more comprehensive studies evaluating the biocompatibility, stability, and long-term functional efficacy of each of these concepts would be necessary to bring them beyond the proof-of-concept stage.

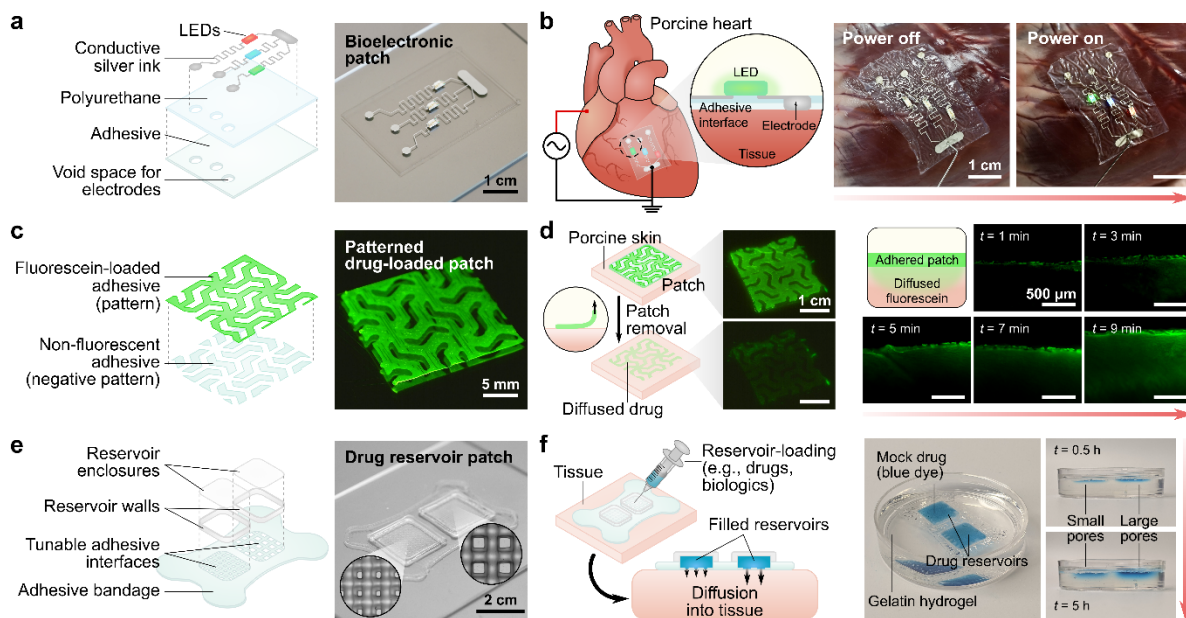


Figure 5-23. Potential applications of the 3D printable tissue adhesive platform. (a-b) Design and ex vivo demonstration of an adhesive bioelectronic patch featuring a 3D printed LED circuit adhered to a porcine heart. Application of a current through the ex vivo heart leads to illumination of the patch-mounted LEDs. (c) Design and ex vivo demonstration of a mock drug (fluorescein)-loaded patch adhered to porcine skin. (d) Fluorescent cross-sectional micrographs show the diffusion of fluorescein into porcine skin over time. (e) Design and of a mock drug (blue dye)-loaded reservoir patch with tunable interfaces. (f) Release of the dye into a gelatin tissue phantom hydrogel over time could be controlled by varying the interfacial pore size.

Fabrication details

To prepare the fluorescent mock drug-loaded ink, tissue adhesive ink was prepared as described above and mixed with a small amount of fluorescein. The non-fluorescent and fluorescent inks were printed in corresponding positive and negative patterns onto a glass slide treated with hydrophobic coating. After drying, the patch was removed from the glass slide and adhered to ex vivo porcine skin. At sequential timepoints, a small cross-sectional slice of the patch/tissue interface was cut and imaged using an epifluorescence microscope (Nikon Eclipse LV100ND) to capture the diffusion profile into the skin.

To prepare the drug reservoir patch, tissue adhesive ink was prepared as described above and printed with two different lattice dimensions at the reservoir interfaces. The reservoir walls were printed using three layers of an elastomer ink comprising 20 w/w % polyurethane (HydroThane AL93A, AdvanSource biomaterials) dissolved in 1:1 tetrahydrofuran (THF) and dimethylformamide (DMF). Before the walls were fully dried, spin-coated films of the HydroThane solution were cut to dimension and applied to provide enclosures for the reservoirs.

After drying, the patch was removed from the glass slide and adhered to a gelatin hydrogel. The mock drug solution (a mix of blue food dye and water) was injected into the reservoirs using a syringe needle, and the diffusion of the dye into the gelatin hydrogel was photographed over 5 h.

5.4. Discussion

Taken together, the development of a 3D printable tissue adhesive signifies new opportunities in technologies for tissue repair and device fabrication. *Ex vivo*, *in vitro*, and *in vivo* studies demonstrate the promising wound sealing capabilities of the material, along with its favorable biocompatibility and broad potential to be used for applications such as tissue-specific sealing, blood-resistant adhesion, and device fabrication. More generally, the unique material design offers a scalable strategy for preparing an off-the-shelf tissue adhesive with ease of processability for 3D printing or other fabrication methods. For example, the PU-PAA ink can also be dip-coated, spin-coated, and electrospun to create bioadhesive coatings and fibers.

To more rigorously validate the material platform, comprehensive biological studies would be required to fully assess the clinical efficacy of the 3D printed structures and to elucidate the influence of tuning various properties (e.g., stress-strain behavior) on adhesion behavior and biological response. Similarly, evaluating its practical applicability in fabricating specific devices will necessitate more clinically relevant analyses, such as prolonged electrophysiological monitoring or sustained drug release *in vivo*. Looking ahead, the versatile platform proposed in this work has the potential to expand the design space for creating tunable, application-specific tissue adhesive structures.

6. Future landscape of bioadhesive technology

Traditionally, bioadhesives have been developed for applications mainly revolving around hemostasis, wound dressing, and tissue sealing. With the rise of connected devices and human-machine interfaces, the development of multifunctional bioadhesives for interfacing biomedical technologies will likely define the next frontier of bioadhesive technology.

Human-interfacing devices have the potential to sense biological signals, modulate physiological functions, and improve human health. In recent years, breakthroughs in flexible electronics, miniaturized sensors, and wireless communication have enabled the development of increasingly advanced and compact biomedical devices.^{235–237} These come in many forms, from skin-mounted patches and smart contact lenses to ingestible pills and implanted devices. Despite the diverse landscape of bio-integrated devices, commercial translation of devices outside the realms of loose consumer wearables (e.g., smart watches and rings) and traditional medical implants (e.g., cardiac pacemakers and orthopedic implants) has remained relatively limited.

A crucial component underlying the capabilities of these systems is the interface they form with biological tissues.^{238,239} Establishing long-term, stable bio-integration is essential for achieving reliable signal readouts, effective delivery of therapeutic agents, and transmission of stimuli.²³⁸ Bioadhesives emerge as valuable tools in this context, as they can enable secure and conformal attachment of devices to external and internal tissue surfaces (**Figure 6-1**). Beyond the ability to bond with tissues, bioadhesives for these emerging applications require different functional properties depending on the modes of interaction between the tissue and the adhered device. (**Figure 6-2** and **Table 6-1**). This section, which is a perspective, explores recent advances and opportunities in the world of human-integrated devices, with a focus on the functional requirements of the bioadhesive interface as it pertains to different interaction modes.

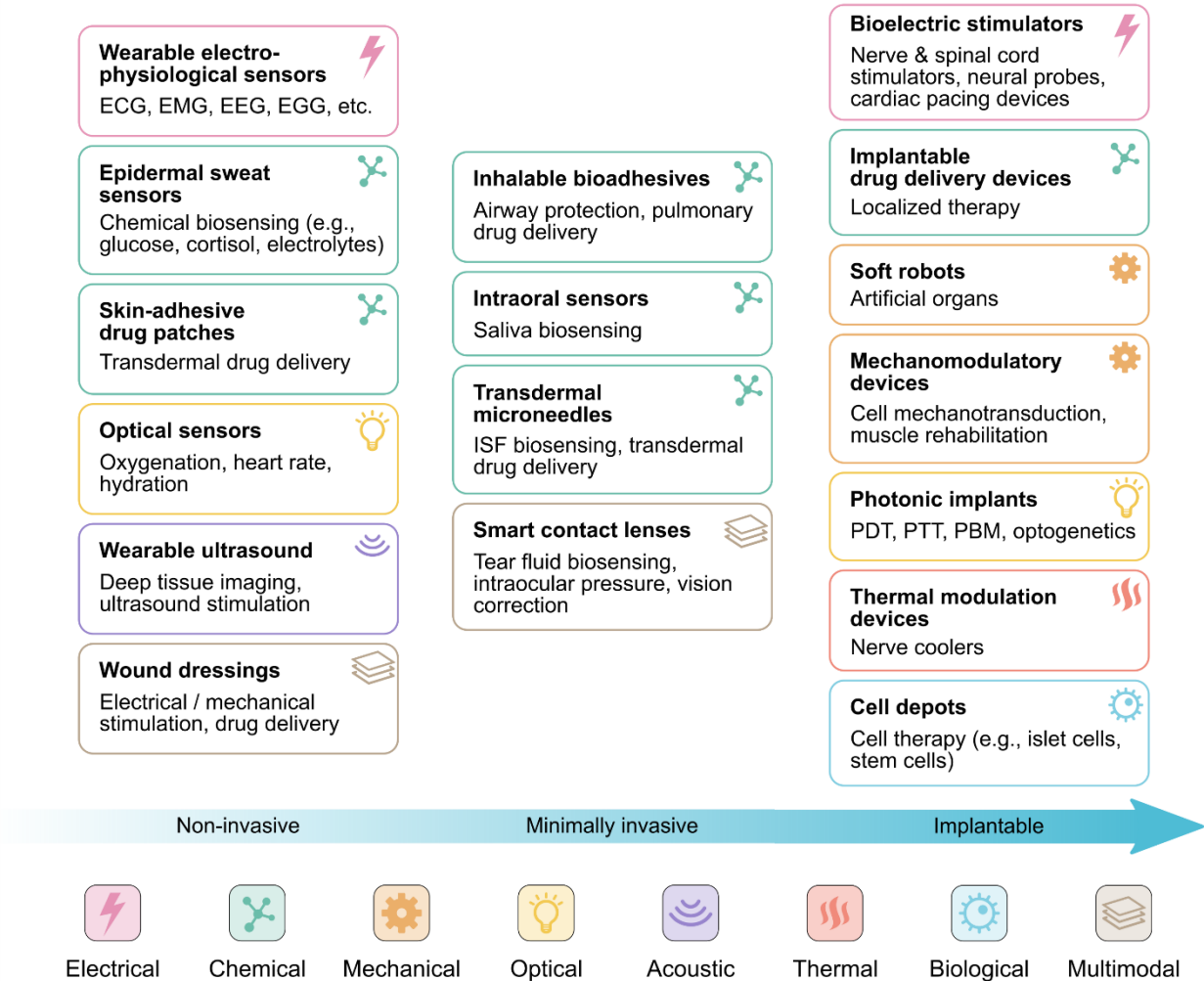


Figure 6-1. The landscape of emerging technologies for which bioadhesives may play a pivotal role, segmented by level of invasiveness and primary signal interaction type.

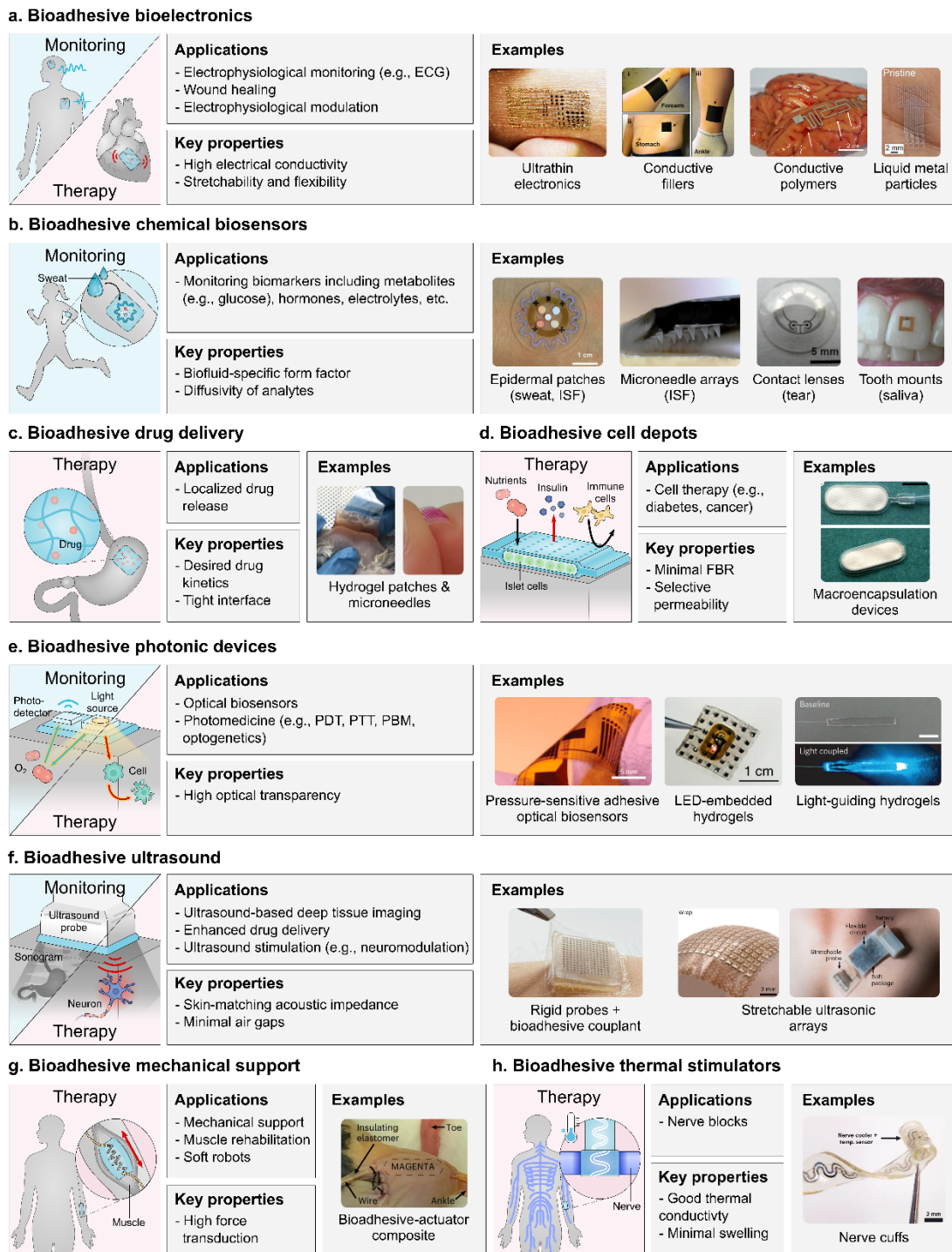


Figure 6-2. Emerging applications, key properties, and examples of: (a) bioadhesive electronics;^{240–243} (b) bioadhesive chemical sensors;^{244–247} (c) bioadhesive drug delivery devices;^{248,249} (d) bioadhesive cell depots;²⁵⁰ (e) bioadhesive photonic devices;^{251–253} (f) bioadhesive acoustic devices;^{254–256} (g) bioadhesive mechanomodulation;²⁵⁷ and (h) bioadhesive thermal stimulators.²⁵⁸ Images reproduced with permission from Ref. 240 (Copyright 2011 AAAS), Ref. 241 (Copyright 2016 American Chemical Society), Ref. 242 (Copyright 2022

Elsevier), Ref. 243 (Copyright 2022 American Chemical Society), Ref. 244 (Copyright 2016 AAAS), Ref. 245 (Copyright 2021 Springer Nature), Ref. 246 (Copyright 2021 Elsevier), Ref. 247 (Copyright 2018 Wiley), Ref. 248 (Copyright 2020 Wiley), Ref. 249 (Copyright 2021 Wiley), Ref. 250 (Copyright 2014 Elsevier), Ref. 251 (Copyright 2013 Springer Nature), Ref. 252 (Copyright 2019 Springer Nature), Ref. 253 (licensed under CC BY 4.0), Ref. 254 (Copyright 2022 AAAS), Ref. 255 (Copyright 2023 Springer Nature), Ref. 256 (Copyright 2023 Springer Nature), Ref. 257 (Copyright 2022 Springer Nature), and Ref. 258 (Copyright 2022 AAAS).

6.1. Bioadhesive bioelectronics

Many physiological systems rely on complex electrical pathways to regulate important body functions (**Figure 6-2a**). For example, the nervous system transmits signals throughout the body to control movement, sensation, and sleep; the cardiovascular system relies on electrical signals to coordinate cardiac contraction and relaxation; and the digestive system has extensive nerve connections which regulate gastrointestinal motility and appetite.^{259–262} Electrophysiological readouts of these systems, such as electroencephalograms (EEG), electrocardiograms (ECG), and electrogastrograms (EGG), can provide valuable information about their functions and pathologies. Recently, wearable electrodes that enable ambulatory electrophysiological monitoring have attracted attention due to their implications in enabling timely detection of abnormalities, facilitating personalized treatment, and empowering individuals to actively manage their health.

On the therapeutic side of bioelectronics, electrical stimulation is an area of great interest for its potential to modulate or activate biological processes. Recognition of the therapeutic effects of electricity dates back thousands of years to ancient Egyptians, who reportedly utilized shocks from electric catfish to treat pain.²⁶³ In the modern era, electrical stimulation has expanded to applications such as cardiac pacing, neural modulation, wound healing, and organ function enhancement. As our understanding of the human body's electrophysiology continues to deepen, so does the realm of electricity-based therapies, termed “electroceuticals”, across a broad spectrum of physiological systems and their pathologies.^{264–270}

The recent advent of flexible electronics has unlocked immense potential for wearable bioelectronics.^{90,271–275} For example, thin film metals, organic electronic materials, conductive nanomaterial composites, and conductive polymers have emerged as strategies to fabricate electronics with flexibility and stretchability.^{276–280} Still, the direct integration of these materials with biological tissues in a manner that ensures stable contact, low electrical resistance, and good biocompatibility is a challenge. Weak tissue-device integration can produce interfacial gaps and motion artifacts, diminishing the fidelity of transmitted electrical signals. Thus, the design of bioadhesive bioelectronics may be pivotal to enabling the maximum functionality of electrophysiological monitoring and electroceuticals.

One method to produce skin-adhesive electronics is to pattern thin film metals into wavy, serpentine, or stacked geometries, enhancing their strain tolerance.^{281,282} Using this strategy, ultra-thin electronic films (or “e-tattoos”) have emerged as a promising class of epidermal bioelectronics.^{240,283–291} Due to their two-dimensional profiles, e-tattoos adhere conformally to skin by van der Waals forces alone. However, this weak physical adhesion is vulnerable to movement and delamination during daily wear. To enhance the wear resistance of conductive metals, a recent strategy emerged utilizing liquid metal particles (LMPs) functionalized with keratin-interacting polymers, yielding skin-adhesive LMPs which could form stable adhesion with skin.²⁴³ Still, while serpentine patterns enhance the flexibility of metallic circuits, they possess limited stretchability and can crack under mild deformation.

A strategy to overcome the geometric constraints of metal circuits is to design a bioadhesive that itself is electrically conductive.^{84,292} This can be achieved by incorporating conductive fillers (e.g., carbon nanotubes or graphene) or conductive polymers (e.g., polypyrrole (PPy) or poly(3,4-ethylenedioxythiophene) polystyrene sulfonate (PEDOT)) into a bioadhesive network. For example, researchers developed a gecko-mimetic bioadhesive composite comprised of poly(dimethylsiloxane) (PDMS) filled with carbon nanotubes, simultaneously imparting adhesiveness, flexibility and stretchability, and conductivity.²⁴¹ In another example, the simultaneous polymerization of PPy and dopamine was shown to yield a functional conductive patch which remained bonded to rat hearts *in vivo* for up to four weeks.²⁹³ Despite various promising demonstrations, conductive bioadhesives are still in their nascency, and in-depth studies of their long-term *in vivo* electrical conductivity, adhesion, and biocompatibility have yet to be seen.

Beyond tissue adhesion and electrical conductivity, bioadhesives for electrical applications could benefit from the incorporation of dynamic, self-healing networks to allow conductive pathways to recover after damage.^{294–296} Moreover, for implanted devices, minimization of the FBR is a key requirement to avoid the buildup of insulating fibrotic tissue at the interface.

6.2. Bioadhesive chemical biosensors

Biological fluids such as sweat, interstitial fluid, tears, and saliva are rich in molecular analytes which can provide valuable insights into the body’s physiological state, motivating a general push toward biofluid-sampling wearables for health monitoring (**Figure 6-2b**).^{297,298} While this demand has produced significant advances in sensor technology, the availability of commercial products for on-body chemical biosensors remains limited.²⁹⁹ A notable exception is the successful commercialization of transdermal continuous glucose monitors, exemplified by devices such as the Abbott FreeStyle Libre® and Dexcom CGM, which employ semi-invasive needles to puncture the skin and measure glucose in the transcutaneous space. While these sensors have proven immensely valuable for diabetes management, their intrusive form factor and the discomfort associated with needle insertion restrict their applicability in general everyday health monitoring.

As with bioelectronics, a crucial aspect for advancing wearable chemical sensors lies in the tissue-device interface. Realizing the next generation of wearable health sensors will require tailored

bioadhesive strategies for accessing various types of biofluids. Here, our focus centers on four readily accessible biofluids: sweat, interstitial fluid, tears, and saliva.

6.2.1 Epidermal biochemical sensors

Two key biofluids that can be obtained from the epidermis are sweat and interstitial fluid (ISF). Sweat can be collected in a passive and completely non-invasive manner as it is naturally secreted onto the surface of the skin. On the other hand, sampling ISF requires strategic methods to extract it from beneath the skin.³⁰⁰ ISF can be extracted to the skin using noninvasive techniques such as ultrasonic or electrical stimulation (i.e., sonophoresis and iontophoresis), or it can be directly sampled beneath the skin using microneedle arrays.^{301–305} Both sweat and ISF contain a wealth of chemical biomarkers, including metabolites (e.g., glucose, lactate, and urea), electrolytes (e.g., sodium, potassium, and chloride ions), and hormones (e.g., cortisol), which provide a window into various health conditions and disorders. For example, glucose can be a useful biomarker for diabetes management; sodium and chloride ions can be indicators of cystic fibrosis; and cortisol variations can reflect stress levels.^{306–308} Generally, the chemical biomarkers found in ISF exhibit closer correlations with serum composition compared to those found in sweat, making ISF a suitable target biofluid for applications requiring high-accuracy readouts.³⁰⁹

Epidermal bioadhesives can be used to interface sensors for sampling sweat and ISF.^{244,309–311} To ensure the reliability and longevity of these systems, the bioadhesive must be able to withstand mechanical movement and prolonged exposure to moisture. The latter becomes particularly important when sweat or ISF is continuously secreted, as is the case with iontophoretic systems.³¹² Strategies to ensure robustness against interfacial moisture include incorporating breathable pores or designing fluidic relief channels to facilitate the removal of interfacial fluids.^{91,244,313–316}

Microneedle bioadhesives for sampling ISF beneath the skin depend on several geometrical design considerations, including the needle length, density, and morphology. Needle length and density directly determine the depth of penetration, ISF extraction, net adhesion force, and patient discomfort. Moreover, the needle morphology, whether solid, porous, or hollow, impacts the transport mechanisms involved in ISF collection.^{302,317–319} Porous and hollow microneedles generally exhibit the capacity to collect larger volumes of ISF compared to solid or hydrogel microneedles by leveraging convective forces. These considerations collectively contribute to the stability and sensing capacity of microneedle sensors.

6.2.2. Intraoral biochemical sensors

Saliva, enriched with biomarkers from the bloodstream, offers the potential to approximate serum levels through its chemical sensing and analysis.^{320–322} Early iterations of salivary sensing devices took the form of sensor-integrated mouthguards, which were limited by their bulkiness.^{323–325} To improve user acceptance, less obtrusive device form factors have been proposed, including tooth-mounted or buccal-adhesive patches.²⁴⁷ Teeth provide unique substrates for device integration, with requirements for adhesion differing greatly from those of soft tissues. Because the outer

surface of the tooth is rigid, adhesion to teeth is typically achieved using high tensile strength resins that are often paired with an acid-etch-technique to promote micromechanical interlocking with dentin.³²⁶ While this method achieves strong adhesion, the detachment procedure requires professional handling to avoid damaging the tooth, which can be impractical for interfacing sensors with short residence times. The use of photodegradable crosslinkers can facilitate debonding by equipping the bioadhesive with UV-triggered degradation.³²⁷ Nonetheless, the small surface area of individual teeth limits the size and number of components which can be integrated. In contrast to hard teeth, the buccal mucosa lining the inside of the cheek is comprised of soft epithelial tissue coated with a dynamic layer of saliva. The buccal mucosa provides a larger surface area than teeth, but it poses challenges to adhesion including continuous shear forces caused by swallowing and mucus turnover.³²⁸ The use of mechanical anchors, such as microneedle arrays, may be an effective strategy to achieve adhesion in this challenging environment.^{329,330}

6.2.3. Ocular biochemical sensors

As with the previous biofluids, tear fluid biosensors offer the ability to monitor biomarkers such as glucose, proteins, salts, and pH.^{246,331,332} Tear-based biosensors broadly come in two forms: those that make direct contact with the eye to access tear fluid, and noninvasive devices such as eyeglasses and undereye patches.^{333,334} The main drawback of noninvasive form factors is their limited and discontinuous access to tear fluid, which limits the depth of information they can provide.

For in situ tear sensing, an ideal ocular bioadhesive should exhibit conformal adhesion, oxygen permeability, and facile removal. Naturally, contact lenses offer an attractive form factor to meet these requirements. Contact lens adhesion is primarily governed by the wettability of the lens with the tear film, which generates a surface tension force pulling the lens toward the eye.³³⁵ As such, the composition of soft contact lenses is typically based on high-water-content materials such as polymer or silicone-based hydrogels.³³⁶ Additionally, the physical dimensions of the lens, including the base curve radius, diameter, and thickness, are important design parameters for ensuring a comfortable fit and sufficient oxygen transfer.³³⁷

One application that gained particular interest among contact lens sensors is continuous glucose monitoring for diabetes management.^{338–343} In 2014, Novartis and Google formed a high-profile partnership with the aim of developing a glucose-monitoring contact lens.³⁴⁴ However, the project was halted in 2017 before reaching commercialization, with the companies citing technical challenges related to inconsistent correlations between tear and blood glucose. Nonetheless, biosensing contact lenses may be useful for applications requiring a lower bar of data accuracy, such as general health monitoring. Enhancing the functionality of contact lens sensors beyond single analyte detection, such as by embedding multiplexed microfluidic channels, may be useful to enable more holistic health insights.³⁴⁵

6.3. Bioadhesive drug delivery

The targeted delivery of drugs and biologics to specific tissues is an important therapeutic approach in modern medicine (**Figure 6-2c**).³⁴⁶ Traditionally, pharmacological substances have been delivered through direct intravascular injection, which is limited by its non-specific nature and the associated risks of side effects and overdose. Implantable controlled-release drug systems have emerged as promising alternatives, enabling specific and stimulus-responsive delivery to target regions.^{347–351} However, poor integration with target tissues has been a challenge for achieving high therapeutic efficacy. Standard methods of integration, such as suturing or weak physical adhesion, provide tenuous interfacial contact which can result in uncontrolled, off-target drug release. This is a particular concern for delivering drugs that harm healthy tissues if poorly localized (e.g., chemotherapy drugs).

Achieving stable, localized drug delivery requires a multifaceted material design strategy to ensure prolonged adhesion and desired drug release kinetics.^{248,328,352–361} From the perspective of adhesion, the design of a tough matrix with tissue-bonding surface groups forms the basis for realizing robust, long-term residence. From the perspective of drug delivery, the mesh size of the matrix, drug-polymer interactions, and matrix degradation kinetics are key factors for determining the drug delivery rate.³⁶² The mesh size of the network is dependent on factors such as the degree of crosslinking, the chemical composition, and environmental conditions (e.g., temperature, pH).³⁶³ Leveraging the environment-sensitive properties of hydrogels can be used to impart stimulus-responsive temporal control over drug release.^{348,364} In addition, tissue-penetrating structures such as microneedle arrays can increase drug efficacy by overcoming physiological barriers.^{249,330,365} Besides macroscale hydrogels and patches, drug-loaded bioadhesive microparticles may also be used to minimally invasively deliver injectable or inhalable formulations.^{170,366} An advantage of using microparticles is the ability to mix distinct drug-carrying microparticles, realizing multifunctional therapeutic effects.

Therapeutic cell depots have emerged as an attractive strategy for the treatment of conditions such as Type 1 diabetes and cancer (**Figure 6-2d**).^{367–370} These devices are designed to provide an environment that protects transplanted cells from immune rejection while allowing for the essential exchange of oxygen, nutrients, and desired secretions (e.g., insulin). Despite the transformative implications of cell depots, simultaneously achieving successful immune cloaking and implant cell survival has proven to be a tremendous challenge. For these devices, the foreign body response is the dominating obstacle to their functionality. The formation of fibrous tissues around the device can physically block membrane pores, preventing nutrient exchange and resulting in cell death. Existing cell depots primarily rely on surgical fixation through sutures, making them vulnerable to inflammation and fibrous tissue formation along the loose interface. Bioadhesives can be promising tools to improve the tissue integration of these devices and extend their window of therapeutic efficacy. To this end, bioadhesives for cell depots must exhibit excellent biocompatibility and selective permeability to essential molecules. The porosity of the bioadhesive is a key design parameter for preventing cell migration while facilitating efficient transport of oxygen, nutrients, and cell secretions. Furthermore, incorporation of anti-fouling materials may help to mitigate the occurrence of host cell adhesion and fibrosis.

6.5. Bioadhesive photonic devices

Light can interact with living cells and tissues in a myriad of ways to sense biometric signals, such as blood oxygen saturation, and induce therapeutic effects, such as photothermal therapy (PTT), photodynamic therapy (PDT), photobiomodulation (PBM), and optogenetic therapy (**Figure 6-2e**).^{251,371–379} These therapeutic strategies leverage light to produce heat, activate photosensitive drugs, or stimulate light-regulated cellular processes, with applicability for a range of indications including cancer therapy, infection, wound healing, and neural modulation.^{375,380,381} Due to the finite penetration depth of light in tissues, implantable optical devices are often required to enable deep-tissue photomedicine.^{381–388} Traditional optical fibers comprised of glass and plastic are non-biodegradable and brittle, presenting an inherent mismatch between their properties and the requirements for biomedical use. A growing number of optical devices based on soft polymeric materials such as silk, agarose, and PDMS, among others, have been proposed as alternatives.^{383,389–391} Despite the improved biocompatibility of these soft photonic systems, their loose integration with tissues can hinder the spatial precision of light delivery and result in inconsistent, insufficient, or excessive light illumination. Insufficient illumination can reduce the phototherapeutic effect, while excessive illumination can induce thermal tissue damage and inflammation.^{392,393} In light of these challenges, the bioadhesives can be used to enhance the stability and precision of deep tissue-targeting phototherapies.

Transmitting light through the bioadhesive interface requires good optical transparency to minimize the loss of light intensity delivered to the tissue. Transparency is generally achieved by amorphous polymers which have low light scattering and absorption.³⁹⁴ For semicrystalline or crystalline polymers, reducing the domain size below the wavelengths of visible light can impart transparency. One method to diminish the average domain size is to disperse nanoscale fillers, such as nanocellulose and silica particles, into the polymer network.^{395–397} Furthermore, using a thin adhesive layer can enhance transmission by reducing the distance that light needs to traverse through the interface.

Highlighting the advantages of bioadhesives in photonic devices, an implantable light source for PDT was recently designed to achieve stable, long-term illumination of internal lesions.²⁵² The device was composed of an LED chip sandwiched between two PDMS nanosheets, one of which was modified with polydopamine to become bioadhesive, allowing the device to achieve suture-free residence at the site of implantation for one month. The general strategy of incorporating transparent bioadhesive materials with implantable photonic devices has immense potential to enhance the efficacy of a wide range of deep-tissue phototherapies.

6.6. Bioadhesive ultrasound

Recently, wearable ultrasound devices have attracted substantial interest for their potential to unlock continuous deep-tissue imaging and ultrasound-based stimulation (**Figure 6-2f**). The noninvasive, radiation-free characteristics of ultrasound imaging have made it a valuable tool for assessing diverse body functions, including muscular activity, cardiac function, blood flow, bone

healing, and gastric activity.^{398,310,399–401,254,256,255,402} Traditional ultrasound components are rigid and bulky, posing a challenge to their on-body integration. The emergence of flexible and stretchable ultrasonic arrays has improved wearability, but their enhanced skin conformability comes with tradeoffs in image stability and resolution.⁴⁰¹ Regardless of their form factor, a key component to the performance of ultrasound devices is the coupling agent, whose role is to maximize signal transmission by matching acoustic impedance.⁴⁰³ The most common ultrasound couplant is a wet gel, which is vulnerable to dehydration and detachment within a few hours of wear.

To concurrently address the challenges of tissue integration, image quality, and signal transmission, an ultrasound patch was recently developed consisting of a thin, rigid ultrasound probe bonded to a bioadhesive hydrogel couplant.²⁵⁴ The bioadhesive couplant was composed of a hydrogel with skin-matching acoustic impedance encapsulated by a thin layer of polyurethane to prevent the hydrogel from drying out over time.²⁰¹ The polyurethane membrane was further coated with a thin bioadhesive layer containing physical tissue interaction groups and covalent bond-forming NHS esters, imparting strong and gap-free tissue adhesion. The resulting bioadhesive ultrasound assembly was evaluated across various scenarios, including imaging of the heart, liver, and bladder, where it demonstrated excellent imaging stability over several hours. This example illustrates the significance of using multifunctional design principles to rationally design a bioadhesive interface that enables efficient device-tissue coupling, allowing even rigid devices to become wearable. Still, there is room for improvement in current bioadhesive ultrasound interfaces. For example, enabling fine adjustment over the angle of sonography, as opposed to imposing a fixed angle perpendicular to the skin, may expand the potential utility of wearable ultrasound systems.

Beyond deep tissue imaging, wearable ultrasound systems present various potential therapeutic effects.⁴⁰⁴ Ultrasound can increase the efficacy of drug delivery by overcoming physiological barriers and improving spatiotemporal control.⁴⁹ Low-intensity ultrasound can also be used to generate heat and increase circulation, which may provide rehabilitative effects for muscles. Additionally, the use of ultrasound for neuromodulation is an active area of research and development.^{405–409}

6.4. Bioadhesive mechanical support

The strategy of implanting stabilizing structures to provide mechanical support to damaged tissues has been used widely in surgery. It finds applications in various procedures, such as repairing hernias and reinforcing heart tissue damaged by myocardial infarction.^{410,411} The traditional use of sutures or tacks to fix mechanical support structures can lead to secondary complications including pain, postsurgical adhesions, and dislodgement.^{412–415} Bioadhesive mechanical supports are favorable alternatives. For example, self-adhesive hernia meshes can enhance the ease of attachment and mitigate postsurgical adverse effects.⁴¹⁶ Furthermore, bioadhesive patches can be used to provide mechanical support to infarcted heart tissue.⁴¹⁷ For instance, a viscoelastic

bioadhesive patch based on an ionically crosslinked starch gel was developed to achieve tissue-mimetic mechanical properties, leading to superior tissue remodeling in a rat model.⁴¹⁷

Another area of interest for mechanically active bioadhesives is wound healing. The phenomenon of mechanotransduction, in which physical forces are converted into biochemical signals that affect cell behavior, underlies the role that mechanical cues play in promoting wound healing and fibrosis.^{418,419} By applying controlled forces to the wound microenvironment, the healing process can be modulated to promote tissue growth and minimize scar formation.^{420–423} Bioadhesives which transmit contractile forces, such as thermosensitive or shape-memory polymers, can therefore be leveraged to enhance wound healing.^{139,424} Based on a similar principle, dynamic mechanical actuation around an implanted device can be used to mitigate the FBR and extend the functional lifespan of the device.^{425,426}

In the field of muscle rehabilitation, mechanically active devices and robotic systems have gained interest for their ability to generate forces that induce tissue regeneration (**Figure 6-2g**).⁴²⁷ However, weak interfacial coupling between actuators and tissues can lead to poor force transduction, hindering the delivery of mechanical stimuli. To address this limitation, researchers developed a bioadhesive mechanical actuator to adhere directly on muscle tissue and simulate contraction.²⁵⁷ The intimate mechanical coupling between the actuator and the tissue provided by the tough bioadhesive interface enabled efficient tissue stimulation, resulting in a slowdown of muscle atrophy.

On a larger scale, soft robotic technologies that recapitulate the mechanical motion of natural body parts have transformative potential as assistive devices and artificial organs.^{428–433} Such implants have previously leveraged mechanical bands, sutures, or suction to fix them in place; however, these methods increase device bulkiness, inflict uneven stress localization, and can elicit significant inflammation.⁴³⁴ Efficient mechanical coupling between soft robots and tissues is a crucial but challenging aspect of their performance, requiring a bioadhesive material that can achieve conformal contact over a large, non-planar surface area.⁴³⁵ Moreover, the bioadhesive must be capable of withstanding physiologically relevant shear and compressive forces over multiple cycles, demanding strength, toughness, and fatigue-resistance.

6.7. Bioadhesive thermal stimulators

Thermal bio-integrated devices offer opportunities for temperature sensing and stimulation (**Figure 6-2h**). For example, the peripheral nervous system exhibits complex thermal sensitivity and can be modulated using variations in temperature.⁴³⁶ Of particular interest is local nerve cooling, which temporarily blocks pain signals, forming the basis for potential drug-free pain relief.⁴³⁷ To harness this effect, implantable nerve coolers have been developed, but these currently rely on sutures or physical wrapping around the nerve to hold them in place.^{438,258} These weak integration methods limit the spatial precision of thermal cooling.⁴³⁹ Poor control over cooling can pose the risk of cold nerve injury, underscoring the importance of achieving proper nerve integration.⁴⁴⁰

In general, bioadhesives for thermal stimulation should be designed to exhibit good thermal conductivity and resilience. Thermal conductivity can be tuned by increasing the conduction pathways in the polymer network, such as by increasing the crosslinking density or introducing filler materials with high conductivity (e.g., graphene).⁴⁴¹ Meanwhile, thermal resilience, referring to the robustness of the bioadhesive against changes in temperature, requires the interfacial interactions (e.g., chemical and physical bonds) and physical properties of the bioadhesive to be relatively stable within the working range of temperatures.

Table 6-1. Examples of emerging bioadhesive technology platforms.

Interaction mode	Type	Use case(s)	Bioadhesive technology	Key properties	Refs
<i>Electrophysiological</i>					
Monitoring	Electrocardiography (ECG)	Arrhythmias, coronary artery disease, heart attack	Bioadhesive electrodes (epidermal)	High electrical conductivity, breathability, reversibility	442
Monitoring	Electroencephalography (EEG)	Measuring brain activity	Bioadhesive electrodes (epidermal)	High electrical conductivity, breathability, reversibility	443–446
Monitoring	Electrogastrography (EGG)	Gastric activity, gastrointestinal disorders	Bioadhesive electrodes (epidermal)	High electrical conductivity, breathability, reversibility	447–449
Stimulation	Nerve stimulation	Pain relief, retinal implants, tremors	Bioadhesive nerve cuffs (invasive), epidermal electrical stimulators (noninvasive)	High electrical conductivity, low foreign body response	450
Stimulation	Functional electrical stimulation (FES)	Muscular rehabilitation, sleep apnea	Bioadhesive electrodes (epidermal)	High electrical conductivity, breathability, reversibility	451
Stimulation	Wound electrotherapy	Wound healing, diabetic foot ulcers	Electrically conductive dressing	High electrical conductivity, proper wound healing environment, reversibility	452
Monitoring	Bioimpedance measurement	Pulmonary function, body composition, bone growth	Bioadhesive electrodes (epidermal), orthopedic implants	High electrical conductivity, breathability, reversibility	453–455
<i>Chemical biosensing</i>					
Monitoring	Sweat sensors	Metabolites, hormones, electrolytes, proteins, drugs	Epidermal patches	Robustness against moisture, breathability, reversibility	309,456,457
Monitoring	Interstitial fluid (ISF)	Metabolites, hormones, electrolytes, proteins, neurotransmitters, drugs	Epidermal patches, microneedle arrays	Robustness against moisture, breathability, reversibility	318,458,459

Monitoring	Saliva		Antibodies, bacteria, metabolites	Tooth buccal devices	mounts, adhesive	Robustness against saliva biofouling, swallowing forces, and mucus turnover	247,460
Monitoring	Tear		Salts, proteins, enzymes, lipids, metabolites	Smart contact lenses		Suitable optical properties, non-obtrusive to vision, atraumatic removal	338,340
Monitoring	Gastric fluids		Metabolites, drugs	Ingestible, gastro-retentive devices		Robustness against food, digestive fluids, and mucus turnover	461
Monitoring	Breath		Hydrogen peroxide, viruses, metabolites	Under-nose patches		Reversibility	462
<i>Drug delivery</i>							
Therapy	Bioadhesive patches		Miscellaneous	Drug-loaded patches & wound dressings		Porosity/mesh size, drug-matrix interactions, degradation kinetics	349,354,355,362
Therapy	Microneedle arrays		Miscellaneous	Microneedles (solid, hollow, porous)		Microneedle geometry and morphology	329,330,365,463,464
Therapy	Inhalable particles		Pulmonary drug delivery	Bioadhesive microparticles		Porosity/mesh size, drug-matrix interactions, degradation kinetics	170
<i>Mechanical</i>							
Stimulation	Mechanical modulation	wound	Wound healing, scar reduction	Mechanically active wound dressings		Proper wound healing environment	139,422
Stimulation	Muscular mechanomodulation		Muscle rehabilitation / regeneration	Muscle-integrated force actuators		Adhesion strength, fatigue resistance, wireless actuation	257,465

Bidirectional	Soft robots/artificial organs	Recapitulating physiological mechanics	Bioadhesive soft robots (e.g., heart sleeve, diaphragm assist)	Adhesion over large, non-planar areas, fatigue resistance	433,434
Optical					
Monitoring	Photoplethysmography	Heart rate, blood O ₂ saturation, respiration rate	On-body optoelectronic devices	High optical transparency, reversibility	466,467
Stimulation	Photomedicine	PTT, PDT, PBM, optogenetics, photosensitive drug activation	Skin-adhesive and implantable light sources, optical waveguides	High optical transparency, low FBR	382,389,468,469
Acoustic					
Bidirectional	Ultrasound	Deep tissue imaging, pain relief, on-demand drug delivery	Ultrasound patches	Skin-matching acoustic impedance	254,256,400,402,407
Monitoring	Audible biomarkers (“hearables”)	Pneumonia, asthma, COPD, sleep apnea, vocal fatigue	Skin-interfaced acoustic sensors	Breathability, reversibility	470
Thermal					
Monitoring	Temperature sensing	Miscellaneous (e.g., hydration, disease screening)	On-body temperatures sensors	Thermal conductivity, breathability, reversibility	471
Stimulation	Nerve cooling	Pain relief	Bioadhesive nerve cuffs	Thermal conductivity, thermal resilience, minimal swelling	258
Biological					
Therapy	Cell depots	Cell therapy (e.g., type 1 diabetes, cancer)	Cell microencapsulation devices	Selective permeability, low FBR	250,367,368,370

6.8. Other practical considerations

The previous sections have examined design considerations on the levels of the bioadhesive interface, bulk matrix, integrated device, and physiological environment. While these essentially determine the functional performance of a bioadhesive technology, they do not necessarily account

for other factors essential to its commercial translation, clinical adoption, and lifecycle sustainability. Here, we identify additional practical considerations for the design, development, and translation of bioadhesive technology platforms (**Figure 6-3**).

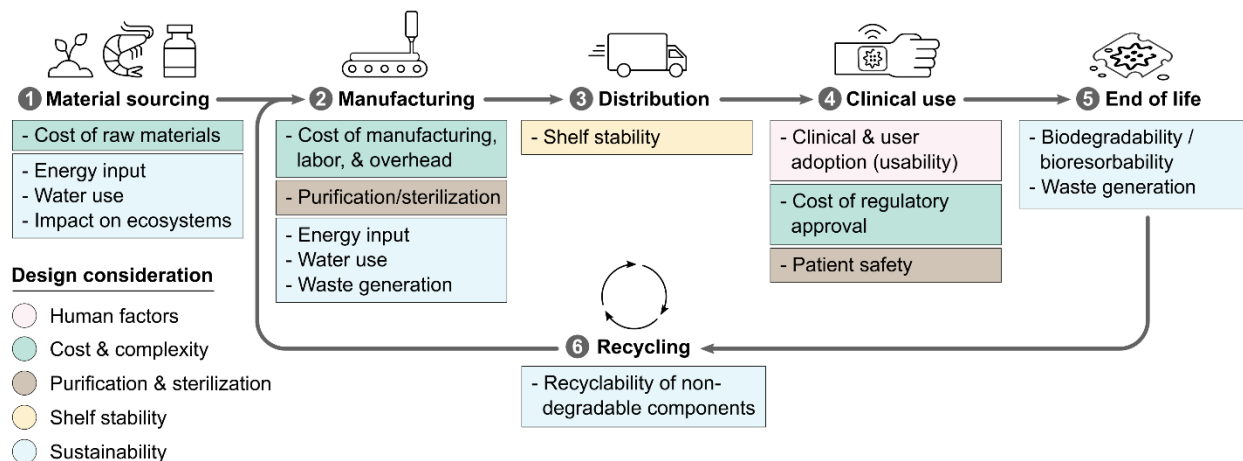


Figure 6-3. Multifaceted practical considerations of bioadhesives through their entire lifecycle from the categories of human factors, cost and complexity, purification and sterilization, shelf stability, and sustainability.

6.8.1. Human factors

In the context of bioadhesive development, human factors refer to considerations related to the usability and practicality of these materials, taking into account the needs and capabilities of healthcare professionals for safe and effective application. Considering the end user (i.e., healthcare professionals and patients) is essential to ensure safe, effective application and user acceptance of bioadhesive products. In general, providing a system that has a simple, user-friendly application process and clear instructions is required for encouraging clinical and consumer adoption. For instance, avoiding laborious pre-application steps, such as manually mixing components, can improve the usability of bioadhesives and reduce the risk of user error. Several multi-component bioadhesives (e.g., Tisseel™, Coseal™, and Vitaseal™) have evolved to be manufactured in dual-barrel syringes to eliminate the need for manual mixing, which has improved their clinical adoption. Ergonomic design considerations including the size, shape, and packaging of bioadhesives and bioadhesive devices can also enhance their user-friendliness. Furthermore, factors such as curing time and equipment requirements should be taken into account. Bioadhesives which necessitate external triggers, such as UV irradiation, may have a greater barrier to use. To evaluate such risks, Overall, designing toward intuitive and accessible products with the end user in mind can facilitate the clinical adoption and success rate of bioadhesive technologies.⁴⁷²

6.8.2. Cost and Complexity

Cost and manufacturing complexity are chief considerations in the commercial translation of bioadhesives.⁸ At the bottom line, the production cost of a bioadhesive must be sufficiently low to provide a return on investment. The calculus of cost is based on the price of raw materials, labor, manufacturing processes and overhead, and regulatory approval. Bioadhesives which require complex manufacturing steps, such as patterning intricate microstructures, may face additional challenges to achieving batch-to-batch consistency and scalability. The culmination of these costs must be balanced with the market potential of the bioadhesive, which depends on the specific clinical need(s) and the value provided by the bioadhesive material or device over existing alternatives.

6.8.3. Purification and sterilization

Purification and sterilization are critical to ensure the removal of toxic monomers, crosslinkers, solvents, bacteria, and other impurities. For instance, in the case of acrylamide-based bioadhesives, the removal of residual acrylamide monomers is essential to mitigate any potential neurotoxicity.⁴⁷³ Various purification techniques, such as filtration and dialysis, can be employed to eliminate these toxic components. Sterilization methods include the use of heat, gamma radiation, ethylene oxide gas, and electron beams.⁴⁷⁴ However, some sterilization techniques may be incompatible with preserving the functional performance of certain bioadhesive materials. For example, the use of moist heat or radiation may degrade reactive groups or alter the physical properties of a bioadhesive. Therefore, it is important to determine an appropriate sterilization method that balances effective pathogen elimination with preserving the integrity and functionality of the bioadhesive and any integrated device components.

6.8.4. Shelf stability

Environmental factors including temperature, humidity, and exposure to light can impact the integrity of a bioadhesive material. For example, bioadhesives which contain hydrolysable reactive groups are prone to degradation over time as they interact with water molecules in ambient air. A strategy to enhance the shelf stability of a bioadhesive without altering its material composition is to optimize its packaging, for example, by including desiccant to prolong the shelf life of moisture-sensitive materials or by using opaque containers to enclose light-sensitive materials. Such efforts to ensure long-term stability are important to minimize waste and enable widespread distribution.

6.8.5. Sustainability

The environmental sustainability of bioadhesive materials and devices is an increasingly important consideration. Researchers developing bioadhesive technologies should aim to minimize their environmental impact throughout their lifecycle, from raw material sourcing to processing to

disposal.⁴⁷⁵⁻⁴⁷⁸ This includes minimizing the use of environmentally hazardous reagents when possible and designing products with recyclable or biodegradable materials.^{479,480} Bio-integrated devices have attracted a great deal of interest, but in many cases these devices contain non-degradable electronic materials which can result in waste accumulation and cause environmental pollution. While the wear time of most bioadhesive wearables is relatively short (a day to a couple weeks), their degradation timeline and environmental consequences can be long-lasting. By factoring sustainability into their design rationale, scientists can contribute to environmentally conscious healthcare practices and align with global efforts toward a more sustainable future.

7. Concluding remarks

Bioadhesives have emerged as a key piece in the broad landscape of biomedical technology. Just as how their predecessors, sutures and staples, transformed the evolution of surgery, the roles of bioadhesives in repairing tissues and interfacing devices position them to be one of the most important technologies for human health in the modern era. Over the past few decades, efforts to uncover and implement tissue adhesion strategies have given rise to a diverse array of bioadhesive materials, some of which have become ubiquitous tools in the clinic today.

Still, bioadhesives face numerous limitations which call for continued innovation and improvement in the years to come. Among these, their mechanical reliability, adhesion speed with wet tissues, reversibility, and the foreign body response are principal challenges. Although there is an active research community devoted to investigating new strategies to overcome these challenges, several bottlenecks stand in the way of the commercial translation of new bioadhesive materials. Adopting a multiscale design approach to target challenges on the material, process, and commercial level will be key to bringing more effective and practical bioadhesives into the clinic.

Looking ahead, the development of personalized bioadhesives and bioadhesives with advanced functionalities beyond tissue bonding will also push the boundaries of their applications, unlocking more effective modes of healthcare monitoring and therapy by enabling efficient tissue-device integration. In this regard, a strong product/market fit is essential for successful commercial translation and adoption. At present, bio-integrated devices are increasingly being developed as components of patient-centric digital health management platforms to consolidate multiple biosignal streams and create a user-information feedback loop. Most emerging systems are focused on external wearables due to their lower barrier for user adoption and more forgiving biocompatibility requirements. To accelerate the capability and translation of these technologies, optimized skin bioadhesives will likely play an essential role in enhancing human-device signal interaction. In the longer term, implantable devices will also require advancements in multifunctional internal bioadhesives to achieve effective human-machine interfacing.

Ultimately, the successful development of bioadhesive technologies hinges on many design considerations around their functional performance, biocompatibility, manufacturability, usability, and sustainability. Continued interdisciplinary research and collaboration will be essential to realizing the full potential of bioadhesive technology platforms for transformative biomedical materials and devices.

8. References

- (1) Mackenzie, D. The History of Sutures. *Med. Hist.* **1973**, *17* (2), 158–168. <https://doi.org/10.1017/S0025727300018469>.
- (2) Muffly, T. M.; Tizzano, A. P.; Walters, M. D. The History and Evolution of Sutures in Pelvic Surgery. *J. R. Soc. Med.* **2011**, *104* (3), 107–112. <https://doi.org/10.1258/jrsm.2010.100243>.
- (3) Gaidry, A. D.; Tremblay, L.; Nakayama, D.; Ignacio, R. C. The History of Surgical Staplers: A Combination of Hungarian, Russian, and American Innovation. *Am. Surg.* **2019**, *85* (6), 563–566.
- (4) *General and Plastic Surgery Devices; Reclassification of Certain Surgical Staplers*. Federal Register. <https://www.federalregister.gov/documents/2021/10/08/2021-22041/general-and-plastic-surgery-devices-reclassification-of-certain-surgical-staplers> (accessed 2023-03-02).
- (5) Makanyengo, S. O.; Thiruchelvam, D. Literature Review on the Incidence of Primary Stapler Malfunction. *Surg. Innov.* **2020**, *27* (2), 229–234. <https://doi.org/10.1177/1553350619889274>.
- (6) Annabi, N.; Yue, K.; Tamayol, A.; Khademhosseini, A. Elastic Sealants for Surgical Applications. *Eur. J. Pharm. Biopharm.* **2015**, *95*, 27–39. <https://doi.org/10.1016/j.ejpb.2015.05.022>.
- (7) Reece, T. B.; Maxey, T. S.; Kron, I. L. A Prospectus on Tissue Adhesives. *Am. J. Surg.* **2001**, *182* (2 Suppl), 40S–44S. [https://doi.org/10.1016/s0002-9610\(01\)00742-5](https://doi.org/10.1016/s0002-9610(01)00742-5).
- (8) Taboada, G. M.; Yang, K.; Pereira, M. J. N.; Liu, S. S.; Hu, Y.; Karp, J. M.; Artzi, N.; Lee, Y. Overcoming the Translational Barriers of Tissue Adhesives. *Nat. Rev. Mater.* **2020**, *5* (4), 310–329. <https://doi.org/10.1038/s41578-019-0171-7>.
- (9) Nam, S.; Mooney, D. Polymeric Tissue Adhesives. *Chem. Rev.* **2021**, [acs.chemrev.0c00798](https://doi.org/10.1021/acs.chemrev.0c00798). <https://doi.org/10.1021/acs.chemrev.0c00798>.
- (10) Borst, H. G.; Haverich, A.; Walterbusch, G.; Maatz, W.; Messmer, B. Fibrin Adhesive: An Important Hemostatic Adjunct in Cardiovascular Operations. *J. Thorac. Cardiovasc. Surg.* **1982**, *84* (4), 548–553. [https://doi.org/10.1016/S0022-5223\(19\)38982-2](https://doi.org/10.1016/S0022-5223(19)38982-2).
- (11) Kulkarni, M. R.; Thomas, B. S.; Varghese, J. M.; Bhat, G. S. Platelet-Rich Fibrin as an Adjunct to Palatal Wound Healing after Harvesting a Free Gingival Graft: A Case Series. *J. Indian Soc. Periodontol.* **2014**, *18* (3), 399–402. <https://doi.org/10.4103/0972-124X.134591>.
- (12) Kerber, C. W.; Cromwell, L. D.; Sheptak, P. E. Intraarterial Cyanoacrylate: An Adjunct in the Treatment of Spinal/Paraspinal Arteriovenous Malformations. *AJR Am. J. Roentgenol.* **1978**, *130* (1), 99–103. <https://doi.org/10.2214/ajr.130.1.99>.
- (13) Chen, X.; Yuk, H.; Wu, J.; Nabzyk, C. S.; Zhao, X. Instant Tough Bioadhesive with Triggerable Benign Detachment. *Proc. Natl. Acad. Sci.* **2020**. <https://doi.org/10.1073/pnas.2006389117>.
- (14) Chen, H.; Cheng, J.; Ran, L.; Yu, K.; Lu, B.; Lan, G.; Dai, F.; Lu, F. An Injectable Self-Healing Hydrogel with Adhesive and Antibacterial Properties Effectively Promotes Wound Healing. *Carbohydr. Polym.* **2018**, *201*, 522–531. <https://doi.org/10.1016/j.carbpol.2018.08.090>.

- (15) Du, X.; Wu, L.; Yan, H.; Qu, L.; Wang, L.; Wang, X.; Ren, S.; Kong, D.; Wang, L. Multifunctional Hydrogel Patch with Toughness, Tissue Adhesiveness, and Antibacterial Activity for Sutureless Wound Closure. *ACS Biomater. Sci. Eng.* **2019**, *5* (5), 2610–2620. <https://doi.org/10.1021/acsbiomaterials.9b00130>.
- (16) Deng, J.; Yuk, H.; Wu, J.; Varela, C. E.; Chen, X.; Roche, E. T.; Guo, C. F.; Zhao, X. Electrical Bioadhesive Interface for Bioelectronics. *Nat. Mater.* **2021**, *20* (2), 229–236. <https://doi.org/10.1038/s41563-020-00814-2>.
- (17) Creton, C.; Ciccotti, M. Fracture and Adhesion of Soft Materials: A Review. *Rep. Prog. Phys.* **2016**, *79* (4), 046601. <https://doi.org/10.1088/0034-4885/79/4/046601>.
- (18) Zhao, X.; Chen, X.; Yuk, H.; Lin, S.; Liu, X.; Parada, G. Soft Materials by Design: Unconventional Polymer Networks Give Extreme Properties. *Chem. Rev.* **2021**, *121* (8), 4309–4372. <https://doi.org/10.1021/acs.chemrev.0c01088>.
- (19) Yuk, H.; Zhang, T.; Lin, S.; Parada, G. A.; Zhao, X. Tough Bonding of Hydrogels to Diverse Non-Porous Surfaces. *Nat. Mater.* **2016**, *15* (2), 190–196. <https://doi.org/10.1038/nmat4463>.
- (20) Ma, Z.; Bao, G.; Li, J. Multifaceted Design and Emerging Applications of Tissue Adhesives. *Adv. Mater.* **2021**, *33* (24), 2007663. <https://doi.org/10.1002/adma.202007663>.
- (21) Bouten, P. J. M.; Zonjee, M.; Bender, J.; Yauw, S. T. K.; van Goor, H.; van Hest, J. C. M.; Hoogenboom, R. The Chemistry of Tissue Adhesive Materials. *Prog. Polym. Sci.* **2014**, *39* (7), 1375–1405. <https://doi.org/10.1016/j.progpolymsci.2014.02.001>.
- (22) Tighe, B. J.; Mann, A. 11 - Adhesives and Interfacial Phenomena in Wound Healing. In *Advanced Wound Repair Therapies*; Farrar, D., Ed.; Woodhead Publishing Series in Biomaterials; Woodhead Publishing, 2011; pp 247–283. <https://doi.org/10.1533/9780857093301.2.247>.
- (23) Wallace, D. G.; Cruise, G. M.; Rhee, W. M.; Schroeder, J. A.; Prior, J. J.; Ju, J.; Maroney, M.; Duronio, J.; Ngo, M. H.; Estridge, T.; Coker, G. C. A Tissue Sealant Based on Reactive Multifunctional Polyethylene Glycol. *J. Biomed. Mater. Res.* **2001**, *58* (5), 545–555. <https://doi.org/10.1002/jbm.1053>.
- (24) Yuk, H.; Varela, C. E.; Nabzdyk, C. S.; Mao, X.; Padera, R. F.; Roche, E. T.; Zhao, X. Dry Double-Sided Tape for Adhesion of Wet Tissues and Devices. *Nature* **2019**, *575* (7781), 169–174. <https://doi.org/10.1038/s41586-019-1710-5>.
- (25) Zhang, Y.; Li, X.; Wei, W.; Liu, X. A Strong Dual-Component Bioadhesive Based on Solventless Thiol-Isocyanate Click Chemistry. *ACS Biomater. Sci. Eng.* **2021**, *7* (7), 3389–3398. <https://doi.org/10.1021/acsbiomaterials.1c00504>.
- (26) Li, J.; Celiz, A. D.; Yang, J.; Yang, Q.; Wamala, I.; Whyte, W.; Seo, B. R.; Vasilyev, N. V.; Vlassak, J. J.; Suo, Z.; Mooney, D. J. Tough Adhesives for Diverse Wet Surfaces. *Science* **2017**, *357* (6349), 378–381. <https://doi.org/10.1126/science.aah6362>.
- (27) Quan, W.-Y.; Hu, Z.; Liu, H.-Z.; Ouyang, Q.-Q.; Zhang, D.-Y.; Li, S.-D.; Li, P.-W.; Yang, Z.-M. Mussel-Inspired Catechol-Functionalized Hydrogels and Their Medical Applications. *Molecules* **2019**, *24* (14), 2586. <https://doi.org/10.3390/molecules24142586>.
- (28) Saiz-Poseu, J.; Mancebo-Aracil, J.; Nador, F.; Busqué, F.; Ruiz-Molina, D. The Chemistry behind Catechol-Based Adhesion. *Angew. Chem. Int. Ed.* **2019**, *58* (3), 696–714. <https://doi.org/10.1002/anie.201801063>.
- (29) Bovone, G.; Dudaryeva, O. Y.; Marco-Dufort, B.; Tibbitt, M. W. Engineering Hydrogel Adhesion for Biomedical Applications via Chemical Design of the Junction. *ACS Biomater. Sci. Eng.* **2021**. <https://doi.org/10.1021/acsbiomaterials.0c01677>.

- (30) Zhang, Y.; Qi, Y.; Ulrich, S.; Barboiu, M.; Ramström, O. Dynamic Covalent Polymers for Biomedical Applications. *Mater. Chem. Front.* **2020**, *4* (2), 489–506. <https://doi.org/10.1039/c9qm00598f>.
- (31) Hua, Y.; Gan, Y.; Li, P.; Song, L.; Shi, C.; Bao, C.; Yang, Y.; Zhou, Q.; Lin, Q.; Zhu, L. Moldable and Removable Wound Dressing Based on Dynamic Covalent Cross-Linking of Thiol-Aldehyde Addition. *ACS Biomater. Sci. Eng.* **2019**, *5* (8), 4048–4053. <https://doi.org/10.1021/acsbomaterials.9b00459>.
- (32) Yang, S.; Bai, J.; Sun, X.; Zhang, J. Robust and Healable Poly(Disulfides) Supramolecular Adhesives Enabled by Dynamic Covalent Adaptable Networks and Noncovalent Hydrogen-Bonding Interactions. *Chem. Eng. J.* **2023**, *461*, 142066. <https://doi.org/10.1016/j.cej.2023.142066>.
- (33) Chen, M.; Wu, Y.; Chen, B.; Tucker, A. M.; Jagota, A.; Yang, S. Fast, Strong, and Reversible Adhesives with Dynamic Covalent Bonds for Potential Use in Wound Dressing. *Proc. Natl. Acad. Sci.* **2022**, *119* (29), e2203074119. <https://doi.org/10.1073/pnas.2203074119>.
- (34) Belowich, M. E.; Stoddart, J. F. Dynamic Imine Chemistry. *Chem. Soc. Rev.* **2012**, *41* (6), 2003–2024. <https://doi.org/10.1039/C2CS15305J>.
- (35) Hofman, A. H.; van Hees, I. A.; Yang, J.; Kamperman, M. Bioinspired Underwater Adhesives by Using the Supramolecular Toolbox. *Adv. Mater.* **2018**, *30* (19), 1704640. <https://doi.org/10.1002/adma.201704640>.
- (36) Chen, S.; Zhang, K.; Li, Z.; Wu, Y.; Zhu, B.; Zhu, J. Hydrogen-Bonded Supramolecular Adhesives: Synthesis, Responsiveness, and Application. *Supramol. Mater.* **2023**, *2*, 100032. <https://doi.org/10.1016/j.supmat.2023.100032>.
- (37) Fan, H.; Gong, J. P. Bioinspired Underwater Adhesives. *Adv. Mater.* **2021**, *33* (44), 2102983. <https://doi.org/10.1002/adma.202102983>.
- (38) Ahn, B. K. Perspectives on Mussel-Inspired Wet Adhesion. *J. Am. Chem. Soc.* **2017**, *139* (30), 10166–10171. <https://doi.org/10.1021/jacs.6b13149>.
- (39) Lee, B. P.; Messersmith, P. B.; Israelachvili, J. N.; Waite, J. H. Mussel-Inspired Adhesives and Coatings. *Annu. Rev. Mater. Res.* **2011**, *41* (1), 99–132. <https://doi.org/10.1146/annurev-matsci-062910-100429>.
- (40) Kord Forooshani, P.; Lee, B. P. Recent Approaches in Designing Bioadhesive Materials Inspired by Mussel Adhesive Protein. *J. Polym. Sci. Part Polym. Chem.* **2017**, *55* (1), 9–33. <https://doi.org/10.1002/pola.28368>.
- (41) Waite, J. H. Mussel Adhesion – Essential Footwork. *J. Exp. Biol.* **2017**, *220* (4), 517–530. <https://doi.org/10.1242/jeb.134056>.
- (42) Guo, Q.; Chen, J.; Wang, J.; Zeng, H.; Yu, J. Recent Progress in Synthesis and Application of Mussel-Inspired Adhesives. *Nanoscale* **2020**, *12* (3), 1307–1324. <https://doi.org/10.1039/C9NR09780E>.
- (43) Guo, Z.; Xia, J.; Mi, S.; Sun, W. Mussel-Inspired Naturally Derived Double-Network Hydrogels and Their Application in 3D Printing: From Soft, Injectable Bioadhesives to Mechanically Strong Hydrogels. *ACS Biomater. Sci. Eng.* **2020**, *6* (3), 1798–1808. <https://doi.org/10.1021/acsbomaterials.9b01864>.
- (44) Montazerian, H.; Mitra, S.; Hassani Najafabadi, A.; Seyedmahmoud, R.; Zheng, Y.; Dokmeci, M. R.; Annabi, N.; Khademhosseini, A.; Weiss, P. S. Catechol Conjugation for Bioadhesion in Photo-Cross-Linkable Biomaterials. *ACS Mater. Lett.* **2023**, 1672–1683. <https://doi.org/10.1021/acsmaterialslett.3c00193>.

- (45) Yang, J.; Bai, R.; Suo, Z. Topological Adhesion of Wet Materials. *Adv. Mater.* **2018**, *30* (25), 1800671. <https://doi.org/10.1002/adma.201800671>.
- (46) Gao, Y.; Chen, J.; Han, X.; Pan, Y.; Wang, P.; Wang, T.; Lu, T. A Universal Strategy for Tough Adhesion of Wet Soft Material. *Adv. Funct. Mater.* **2020**, *30* (36), 2003207. <https://doi.org/10.1002/adfm.202003207>.
- (47) Roma-Luciw, R.; Sarraf, L.; Morcellet, M. Complexes of Poly(Acrylic Acid) with Some Divalent, Trivalent and Tetravalent Metal Ions. *Eur. Polym. J.* **2001**, *37* (9), 1741–1745. [https://doi.org/10.1016/S0014-3057\(01\)00066-0](https://doi.org/10.1016/S0014-3057(01)00066-0).
- (48) Gao, Y.; Wu, K.; Suo, Z. Photodetachable Adhesion. *Adv. Mater.* **2019**, *31* (6), 1806948. <https://doi.org/10.1002/adma.201806948>.
- (49) J. Delaney, L.; Isguven, S.; R. Eisenbrey, J.; J. Hickok, N.; Forsberg, F. Making Waves: How Ultrasound-Targeted Drug Delivery Is Changing Pharmaceutical Approaches. *Mater. Adv.* **2022**, *3* (7), 3023–3040. <https://doi.org/10.1039/D1MA01197A>.
- (50) Ma, Z.; Bourquard, C.; Gao, Q.; Jiang, S.; De Iure-Grimmel, T.; Huo, R.; Li, X.; He, Z.; Yang, Z.; Yang, G.; Wang, Y.; Lam, E.; Gao, Z.; Supponen, O.; Li, J. Controlled Tough Bioadhesion Mediated by Ultrasound. *Science* **2022**, *377* (6607), 751–755. <https://doi.org/10.1126/science.abn8699>.
- (51) Kim, W.-S.; Yun, I.-H.; Lee, J.-J.; Jung, H.-T. Evaluation of Mechanical Interlock Effect on Adhesion Strength of Polymer–Metal Interfaces Using Micro-Patterned Surface Topography. *Int. J. Adhes. Adhes.* **2010**, *30* (6), 408–417. <https://doi.org/10.1016/j.ijadhadh.2010.05.004>.
- (52) Webster, I. Recent Developments in Pressure-Sensitive Adhesives for Medical Applications. *Int. J. Adhes. Adhes.* **1997**, *17* (1), 69–73. [https://doi.org/10.1016/S0143-7496\(96\)00024-3](https://doi.org/10.1016/S0143-7496(96)00024-3).
- (53) *DuPont™ Liveo™ Medical Grade Pressure Sensitive Adhesives (PSAs)*. <https://www.dupont.com/products/LiveoMedicalGradeMGPressureSensitiveAdhesives.html> (accessed 2023-05-11).
- (54) *Dressing and Device Securement : 3M Medical | 3M United States*. https://www.3m.com/3M/en_US/medical-us/dressing-and-device-securement/ (accessed 2023-05-11).
- (55) *Soft skin adhesives | Silicones | Products*. [Elkem.com](https://www.elkem.com/products/silicones/medical-grade-silicones/soft-skin-adhesives/). <https://www.elkem.com/products/silicones/medical-grade-silicones/soft-skin-adhesives/> (accessed 2023-05-11).
- (56) *Pushing boundaries in health tech: 3M launches new medical adhesive offering premium wear time, up to 28 days*. 3M News Center. <https://news.3m.com/2023-02-06-Pushing-boundaries-in-health-tech-3M-launches-new-medical-adhesive-offering-premium-wear-time,-up-to-28-days> (accessed 2023-05-11).
- (57) Fitzgerald, D. M.; Colson, Y. L.; Grinstaff, M. W. Advancing Pressure-Sensitive Adhesives for Internal Wound Closure. *Nat. Rev. Mater.* **2023**, *8* (1), 3–5. <https://doi.org/10.1038/s41578-022-00516-y>.
- (58) Zhu, M.; Zhang, F.; Chen, X. Bioinspired Mechanically Interlocking Structures. *Small Struct.* **2020**, *1* (3), 2000045. <https://doi.org/10.1002/sstr.202000045>.
- (59) Kochhar, J. S.; Quek, T. C.; Soon, W. J.; Choi, J.; Zou, S.; Kang, L. Effect of Microneedle Geometry and Supporting Substrate on Microneedle Array Penetration into Skin. *J. Pharm. Sci.* **2013**, *102* (11), 4100–4108. <https://doi.org/10.1002/jps.23724>.

- (60) Yang, S. Y.; O’Cearbhaill, E. D.; Sisk, G. C.; Park, K. M.; Cho, W. K.; Villiger, M.; Bouma, B. E.; Pomahac, B.; Karp, J. M. A Bio-Inspired Swellable Microneedle Adhesive for Mechanical Interlocking with Tissue. *Nat. Commun.* **2013**, *4* (1), 1702. <https://doi.org/10.1038/ncomms2715>.
- (61) Han, D.; Morde, R. S.; Mariani, S.; La Mattina, A. A.; Vignali, E.; Yang, C.; Barillaro, G.; Lee, H. 4D Printing of a Bioinspired Microneedle Array with Backward-Facing Barbs for Enhanced Tissue Adhesion. *Adv. Funct. Mater.* **2020**, *30* (11), 1909197. <https://doi.org/10.1002/adfm.201909197>.
- (62) Seong, K.-Y.; Seo, M.-S.; Hwang, D. Y.; O’Cearbhaill, E. D.; Sreenan, S.; Karp, J. M.; Yang, S. Y. A Self-Adherent, Bullet-Shaped Microneedle Patch for Controlled Transdermal Delivery of Insulin. *J. Controlled Release* **2017**, *265*, 48–56. <https://doi.org/10.1016/j.jconrel.2017.03.041>.
- (63) Writer, L. M. H. S. *Harvard entrepreneurs weave silk with science*. Harvard Gazette. <https://news.harvard.edu/gazette/story/2012/06/harvard-entrepreneurs-weave-silk-with-science/> (accessed 2023-05-22).
- (64) Inc, M. B. *Micron Biomedical Initiates First-Ever Microneedle Vaccine Clinical Trial in Children*. <https://www.prnewswire.com/news-releases/micron-biomedical-initiates-first-ever-microneedle-vaccine-clinical-trial-in-children-301331844.html> (accessed 2023-05-22).
- (65) SofusaTM | Medication Delivery Platform Enabling A Distinct Therapeutic Advantage Through Nanotechnology | Technology. <http://www.sofusa.com/technology/> (accessed 2023-05-22).
- (66) Stinson, J. A.; Boopathy, A. V.; Cieslewicz, B. M.; Zhang, Y.; Hartman, N. W.; Miller, D. P.; Dirckx, M.; Hurst, B. L.; Tarbet, E. B.; Kluge, J. A.; Kosuda, K. M. Enhancing Influenza Vaccine Immunogenicity and Efficacy through Infection Mimicry Using Silk Microneedles. *Vaccine* **2021**, *39* (38), 5410–5421. <https://doi.org/10.1016/j.vaccine.2021.07.064>.
- (67) Stinson, J. A.; Palmer, C. R.; Miller, D. P.; Li, A. B.; Lightner, K.; Jost, H.; Weldon, W. C.; Oberste, M. S.; Kluge, J. A.; Kosuda, K. M. Thin Silk Fibroin Films as a Dried Format for Temperature Stabilization of Inactivated Polio Vaccine. *Vaccine* **2020**, *38* (7), 1652–1660. <https://doi.org/10.1016/j.vaccine.2019.12.062>.
- (68) Makvandi, P.; Kirkby, M.; Hutton, A. R. J.; Shabani, M.; Yiu, C. K. Y.; Baghbantaraghdari, Z.; Jamaledin, R.; Carlotti, M.; Mazzolai, B.; Mattoli, V.; Donnelly, R. F. Engineering Microneedle Patches for Improved Penetration: Analysis, Skin Models and Factors Affecting Needle Insertion. *Nano-Micro Lett.* **2021**, *13* (1), 93. <https://doi.org/10.1007/s40820-021-00611-9>.
- (69) Chimutengwende-Gordon, M.; Dowling, R.; Pendegrass, C.; Blunn, G. Determining the Porous Structure for Optimal Soft-Tissue Ingrowth: An in Vivo Histological Study. *PLoS ONE* **2018**, *13* (10), e0206228. <https://doi.org/10.1371/journal.pone.0206228>.
- (70) Matos, G. R. M. Surface Roughness of Dental Implant and Osseointegration. *J. Maxillofac. Oral Surg.* **2021**, *20* (1), 1–4. <https://doi.org/10.1007/s12663-020-01437-5>.
- (71) Yabe, A.; Okada, M.; Hara, E. S.; Torii, Y.; Matsumoto, T. Self-Adhering Implantable Device of Titanium: Enhanced Soft-Tissue Adhesion by Sandblast Pretreatment. *Colloids Surf. B Biointerfaces* **2022**, *211*, 112283. <https://doi.org/10.1016/j.colsurfb.2021.112283>.

- (72) Ban, S.; Iwaya, Y.; Kono, H.; Sato, H. Surface Modification of Titanium by Etching in Concentrated Sulfuric Acid. *Dent. Mater.* **2006**, *22* (12), 1115–1120. <https://doi.org/10.1016/j.dental.2005.09.007>.
- (73) Syam, S.; Wu, C.-J.; Lan, W.-C.; Ou, K.-L.; Huang, B.-H.; Lin, Y.-Y.; Saito, T.; Tsai, H.-Y.; Chuo, Y.-C.; Yen, M.-L.; Liu, C.-M.; Hou, P.-J. The Potential of a Surface-Modified Titanium Implant with Tetrapeptide for Osseointegration Enhancement. *Appl. Sci.* **2021**, *11* (6), 2616. <https://doi.org/10.3390/app11062616>.
- (74) Carpenter, R. D.; Klosterhoff, B. S.; Torstrick, F. B.; Foley, K. T.; Burkus, J. K.; Lee, C. S. D.; Gall, K.; Guldberg, R. E.; Safranski, D. L. Effect of Porous Orthopaedic Implant Material and Structure on Load Sharing with Simulated Bone Ingrowth: A Finite Element Analysis Comparing Titanium and PEEK. *J. Mech. Behav. Biomed. Mater.* **2018**, *80*, 68–76. <https://doi.org/10.1016/j.jmbbm.2018.01.017>.
- (75) Wang, W.; Liu, Y.; Xie, Z. Gecko-Like Dry Adhesive Surfaces and Their Applications: A Review. *J. Bionic Eng.* **2021**, *18* (5), 1011–1044. <https://doi.org/10.1007/s42235-021-00088-7>.
- (76) Mahdavi, A.; Ferreira, L.; Sundback, C.; Nichol, J. W.; Chan, E. P.; Carter, D. J. D.; Bettinger, C. J.; Patanavanich, S.; Chignozha, L.; Ben-Joseph, E.; Galakatos, A.; Pryor, H.; Pomerantseva, I.; Masiakos, P. T.; Faquin, W.; Zumbuehl, A.; Hong, S.; Borenstein, J.; Vacanti, J.; Langer, R.; Karp, J. M. A Biodegradable and Biocompatible Gecko-Inspired Tissue Adhesive. *Proc. Natl. Acad. Sci.* **2008**, *105* (7), 2307–2312. <https://doi.org/10.1073/pnas.0712117105>.
- (77) Autumn, K.; Liang, Y. A.; Hsieh, S. T.; Zesch, W.; Chan, W. P.; Kenny, T. W.; Fearing, R.; Full, R. J. Adhesive Force of a Single Gecko Foot-Hair. *Nature* **2000**, *405* (6787), 681–685. <https://doi.org/10.1038/35015073>.
- (78) *Geckos Climb by the Hairs of Their Toes* | *Science*. <https://www-science-org.libproxy.mit.edu/doi/10.1126/science.288.5472.1717a> (accessed 2023-05-14).
- (79) Autumn, K.; Sitti, M.; Liang, Y. A.; Peattie, A. M.; Hansen, W. R.; Sponberg, S.; Kenny, T. W.; Fearing, R.; Israelachvili, J. N.; Full, R. J. Evidence for van Der Waals Adhesion in Gecko Setae. *Proc. Natl. Acad. Sci.* **2002**, *99* (19), 12252–12256. <https://doi.org/10.1073/pnas.192252799>.
- (80) Kim, J.-K.; Varenberg, M. Contact Splitting in Dry Adhesion and Friction: Reducing the Influence of Roughness. *Beilstein J. Nanotechnol.* **2019**, *10*, 1–8. <https://doi.org/10.3762/bjnano.10.1>.
- (81) Arzt, E.; Gorb, S.; Spolenak, R. From Micro to Nano Contacts in Biological Attachment Devices. *Proc. Natl. Acad. Sci.* **2003**, *100* (19), 10603–10606. <https://doi.org/10.1073/pnas.1534701100>.
- (82) *Surface energy and the contact of elastic solids* | *Proceedings of the Royal Society of London. A. Mathematical and Physical Sciences*. <https://royalsocietypublishing.org/doi/10.1098/rspa.1971.0141> (accessed 2023-05-18).
- (83) Zeng, H.; Pesika, N.; Tian, Y.; Zhao, B.; Chen, Y.; Tirrell, M.; Turner, K. L.; Israelachvili, J. N. Frictional Adhesion of Patterned Surfaces and Implications for Gecko and Biomimetic Systems. *Langmuir* **2009**, *25* (13), 7486–7495. <https://doi.org/10.1021/la900877h>.
- (84) Drotlef, D.-M.; Amjadi, M.; Yunusa, M.; Sitti, M. Bioinspired Composite Microfibers for Skin Adhesion and Signal Amplification of Wearable Sensors. *Adv. Mater.* **2017**, *29* (28), 1701353. <https://doi.org/10.1002/adma.201701353>.

- (85) Bae, W. G.; Kim, D.; Kwak, M. K.; Ha, L.; Kang, S. M.; Suh, K. Y. Enhanced Skin Adhesive Patch with Modulus-Tunable Composite Micropillars. *Adv. Healthc. Mater.* **2013**, *2* (1), 109–113. <https://doi.org/10.1002/adhm.201200098>.
- (86) Kerst, C. F. Gecko Inspired Adhesives: Permanent Practical Manufacturing, New Materials, and Applications. Ph.D., Stanford University, United States -- California. <https://www.proquest.com/docview/2509703362/abstract/9B16EAA90FB4407CPQ/1> (accessed 2023-05-24).
- (87) Tramacere, F.; Pugno, N. M.; Kuba, M. J.; Mazzolai, B. Unveiling the Morphology of the Acetabulum in Octopus Suckers and Its Role in Attachment. *Interface Focus* **2015**, *5* (1), 20140050. <https://doi.org/10.1098/rsfs.2014.0050>.
- (88) Baik, S.; Kim, D. W.; Park, Y.; Lee, T.-J.; Ho Bhang, S.; Pang, C. A Wet-Tolerant Adhesive Patch Inspired by Protuberances in Suction Cups of Octopi. *Nature* **2017**, *546* (7658), 396–400. <https://doi.org/10.1038/nature22382>.
- (89) Baik, S.; Kim, J.; Lee, H. J.; Lee, T. H.; Pang, C. Highly Adaptable and Biocompatible Octopus-Like Adhesive Patches with Meniscus-Controlled Unfoldable 3D Microtips for Underwater Surface and Hairy Skin. *Adv. Sci.* **2018**, *5* (8), 1800100. <https://doi.org/10.1002/advs.201800100>.
- (90) Chun, S.; Son, W.; Kim, D. W.; Lee, J.; Min, H.; Jung, H.; Kwon, D.; Kim, A.-H.; Kim, Y.-J.; Lim, S. K.; Pang, C.; Choi, C. Water-Resistant and Skin-Adhesive Wearable Electronics Using Graphene Fabric Sensor with Octopus-Inspired Microsuckers. *ACS Appl. Mater. Interfaces* **2019**, *11* (18), 16951–16957. <https://doi.org/10.1021/acsami.9b04206>.
- (91) Kim, D. W.; Baik, S.; Min, H.; Chun, S.; Lee, H. J.; Kim, K. H.; Lee, J. Y.; Pang, C. Highly Permeable Skin Patch with Conductive Hierarchical Architectures Inspired by Amphibians and Octopi for Omnidirectionally Enhanced Wet Adhesion. *Adv. Funct. Mater.* **2019**, *29* (13), 1807614. <https://doi.org/10.1002/adfm.201807614>.
- (92) Huang, R.; Zhang, X.; Li, W.; Shang, L.; Wang, H.; Zhao, Y. Suction Cups-Inspired Adhesive Patch with Tailorable Patterns for Versatile Wound Healing. *Adv. Sci.* **2021**, *8* (17), 2100201. <https://doi.org/10.1002/advs.202100201>.
- (93) Lee, Y.-W.; Chun, S.; Son, D.; Hu, X.; Schneider, M.; Sitti, M. A Tissue Adhesion-Controllable and Biocompatible Small-Scale Hydrogel Adhesive Robot. *Adv. Mater.* **2022**, *34* (13), 2109325. <https://doi.org/10.1002/adma.202109325>.
- (94) Wang, H.; Su, X.; Chai, Z.; Tian, Z.; Xie, W.; Wang, Y.; Wan, Z.; Deng, M.; Yuan, Z.; Huang, J. A Hydra Tentacle-Inspired Hydrogel with Underwater Ultra-Stretchability for Adhering Adipose Surfaces. *Chem. Eng. J.* **2022**, *428*, 131049. <https://doi.org/10.1016/j.cej.2021.131049>.
- (95) Smith, A. M. Cephalopod Sucker Design and the Physical Limits to Negative Pressure. *J. Exp. Biol.* **1996**, *199* (4), 949–958. <https://doi.org/10.1242/jeb.199.4.949>.
- (96) Baik, S.; Lee, H. J.; Kim, D. W.; Min, H.; Pang, C. Capillarity-Enhanced Organ-Attachable Adhesive with Highly Drainable Wrinkled Octopus-Inspired Architectures. *ACS Appl. Mater. Interfaces* **2019**, *11* (29), 25674–25681. <https://doi.org/10.1021/acsami.9b05511>.
- (97) Zhao, X. Multi-Scale Multi-Mechanism Design of Tough Hydrogels: Building Dissipation into Stretchy Networks. *Soft Matter* **2014**, *10* (5), 672–687. <https://doi.org/10.1039/C3SM52272E>.

- (98) Fuchs, S.; Shariati, K.; Ma, M. Specialty Tough Hydrogels and Their Biomedical Applications. *Adv. Healthc. Mater.* **2020**, *9* (2), e1901396. <https://doi.org/10.1002/adhm.201901396>.
- (99) Gong, J. p.; Katsuyama, Y.; Kurokawa, T.; Osada, Y. Double-Network Hydrogels with Extremely High Mechanical Strength. *Adv. Mater.* **2003**, *15* (14), 1155–1158. <https://doi.org/10.1002/adma.200304907>.
- (100) Azuma, C.; Yasuda, K.; Tanabe, Y.; Taniguro, H.; Kanaya, F.; Nakayama, A.; Chen, Y. M.; Gong, J. P.; Osada, Y. Biodegradation of High-Toughness Double Network Hydrogels as Potential Materials for Artificial Cartilage. *J. Biomed. Mater. Res. A* **2007**, *81A* (2), 373–380. <https://doi.org/10.1002/jbm.a.31043>.
- (101) Liu, J.; Wang, S.; Shen, Q.; Kong, L.; Huang, G.; Wu, J. Tough Underwater Super-Tape Composed of Semi-Interpenetrating Polymer Networks with a Water-Repelling Liquid Surface. *ACS Appl. Mater. Interfaces* **2021**, *13* (1), 1535–1544. <https://doi.org/10.1021/acsami.0c18916>.
- (102) *An off-the-shelf bioadhesive patch for sutureless repair of gastrointestinal defects | Science Translational Medicine.* <https://www.science.org/doi/10.1126/scitranslmed.abh2857> (accessed 2023-05-14).
- (103) Karami, P.; Wyss, C. S.; Khoushabi, A.; Schmocker, A.; Broome, M.; Moser, C.; Bourban, P.-E.; Pioletti, D. P. Composite Double-Network Hydrogels To Improve Adhesion on Biological Surfaces. *ACS Appl. Mater. Interfaces* **2018**, *10* (45), 38692–38699. <https://doi.org/10.1021/acsami.8b10735>.
- (104) Rahman, M. A.; Bowland, C.; Ge, S.; Acharya, S. R.; Kim, S.; Cooper, V. R.; Chen, X. C.; Irlle, S.; Sokolov, A. P.; Savara, A.; Saito, T. Design of Tough Adhesive from Commodity Thermoplastics through Dynamic Crosslinking. *Sci. Adv.* **2021**, *7* (42), eabk2451. <https://doi.org/10.1126/sciadv.abk2451>.
- (105) Xie, C.; Wang, X.; He, H.; Ding, Y.; Lu, X. Mussel-Inspired Hydrogels for Self-Adhesive Bioelectronics. *Adv. Funct. Mater.* **2020**, *30* (25), 1909954. <https://doi.org/10.1002/adfm.201909954>.
- (106) Han, L.; Lu, X.; Liu, K.; Wang, K.; Fang, L.; Weng, L.-T.; Zhang, H.; Tang, Y.; Ren, F.; Zhao, C.; Sun, G.; Liang, R.; Li, Z. Mussel-Inspired Adhesive and Tough Hydrogel Based on Nanoclay Confined Dopamine Polymerization. *ACS Nano* **2017**, *11* (3), 2561–2574. <https://doi.org/10.1021/acs.nano.6b05318>.
- (107) Verma, N.; Moore, E.; Blau, W.; Volkov, Y.; Babu, R. Cytotoxicity Evaluation of Nanoclays in Human Epithelial Cell Line A549 Using High Content Screening and Real-Time Impedance Analysis. *J. Nanoparticle Res.* **2012**, *14*, 1137. <https://doi.org/10.1007/s11051-012-1137-5>.
- (108) Ou, L.; Song, B.; Liang, H.; Liu, J.; Feng, X.; Deng, B.; Sun, T.; Shao, L. Toxicity of Graphene-Family Nanoparticles: A General Review of the Origins and Mechanisms. *Part. Fibre Toxicol.* **2016**, *13* (1), 57. <https://doi.org/10.1186/s12989-016-0168-y>.
- (109) Liao, C.; Li, Y.; Tjong, S. C. Graphene Nanomaterials: Synthesis, Biocompatibility, and Cytotoxicity. *Int. J. Mol. Sci.* **2018**, *19* (11), 3564. <https://doi.org/10.3390/ijms19113564>.
- (110) Wegst, U. G. K.; Bai, H.; Saiz, E.; Tomsia, A. P.; Ritchie, R. O. Bioinspired Structural Materials. *Nat. Mater.* **2015**, *14* (1), 23–36. <https://doi.org/10.1038/nmat4089>.
- (111) Ni, J.; Lin, S.; Qin, Z.; Veysset, D.; Liu, X.; Sun, Y.; Hsieh, A. J.; Radovitzky, R.; Nelson, K. A.; Zhao, X. Strong Fatigue-Resistant Nanofibrous Hydrogels Inspired by Lobster Underbelly. *Matter* **2021**, *4* (6), 1919–1934. <https://doi.org/10.1016/j.matt.2021.03.023>.

- (112) Mo, C.; Long, H.; Raney, J. R. Tough, Aorta-Inspired Soft Composites. *Proc. Natl. Acad. Sci.* **2022**, *119* (28), e2123497119. <https://doi.org/10.1073/pnas.2123497119>.
- (113) Zhao, X. Designing Toughness and Strength for Soft Materials. *Proc. Natl. Acad. Sci.* **2017**, *114* (31), 8138–8140. <https://doi.org/10.1073/pnas.1710942114>.
- (114) Pinkas, O.; Haneman, O.; Chemke, O.; Zilberman, M. Fiber-Reinforced Composite Hydrogels for Bioadhesive and Sealant Applications. *Polym. Adv. Technol.* **2017**, *28* (9), 1162–1169. <https://doi.org/10.1002/pat.4009>.
- (115) Béguin, P.; Aubert, J. P. The Biological Degradation of Cellulose. *FEMS Microbiol. Rev.* **1994**, *13* (1), 25–58. <https://doi.org/10.1111/j.1574-6976.1994.tb00033.x>.
- (116) Saheb, D. N.; Jog, J. P. Natural Fiber Polymer Composites: A Review. *Adv. Polym. Technol.* **1999**, *18* (4), 351–363. [https://doi.org/10.1002/\(SICI\)1098-2329\(199924\)18:4<351::AID-ADV6>3.0.CO;2-X](https://doi.org/10.1002/(SICI)1098-2329(199924)18:4<351::AID-ADV6>3.0.CO;2-X).
- (117) Nishiguchi, A.; Taguchi, T. Engineering an Injectable Tough Tissue Adhesive through Nanocellulose Reinforcement. *ACS Appl. Bio Mater.* **2020**, *3* (12), 9093–9100. <https://doi.org/10.1021/acsabm.0c01317>.
- (118) Gao, Y.; Han, X.; Chen, J.; Pan, Y.; Yang, M.; Lu, L.; Yang, J.; Suo, Z.; Lu, T. Hydrogel–Mesh Composite for Wound Closure. *Proc. Natl. Acad. Sci.* **2021**, *118* (28). <https://doi.org/10.1073/pnas.2103457118>.
- (119) Wu, J.; Yuk, H.; Sarrafian, T. L.; Guo, C. F.; Griffiths, L. G.; Nabzdyk, C. S.; Zhao, X. An Off-the-Shelf Bioadhesive Patch for Sutureless Repair of Gastrointestinal Defects. *Sci. Transl. Med.* **2022**, *14* (630), eabh2857. <https://doi.org/10.1126/scitranslmed.abh2857>.
- (120) Fung, Y. C. Elasticity of Soft Tissues in Simple Elongation. *Am. J. Physiol.* **1967**, *213* (6), 1532–1544. <https://doi.org/10.1152/ajplegacy.1967.213.6.1532>.
- (121) Purslow, P. P.; Wess, T. J.; Hukins, D. W. Collagen Orientation and Molecular Spacing during Creep and Stress-Relaxation in Soft Connective Tissues. *J. Exp. Biol.* **1998**, *201* (Pt 1), 135–142. <https://doi.org/10.1242/jeb.201.1.135>.
- (122) Screen, H. R. C. Investigating Load Relaxation Mechanics in Tendon. *J. Mech. Behav. Biomed. Mater.* **2008**, *1* (1), 51–58. <https://doi.org/10.1016/j.jmbbm.2007.03.002>.
- (123) Silver, F. H.; Kelkar, N.; Deshmukh, T. Molecular Basis for Mechanical Properties of ECMs: Proposed Role of Fibrillar Collagen and Proteoglycans in Tissue Biomechanics. *Biomolecules* **2021**, *11* (7), 1018. <https://doi.org/10.3390/biom11071018>.
- (124) Trębacz, H.; Barzycka, A. Mechanical Properties and Functions of Elastin: An Overview. *Biomolecules* **2023**, *13* (3), 574. <https://doi.org/10.3390/biom13030574>.
- (125) Nia, H. T.; Han, L.; Li, Y.; Ortiz, C.; Grodzinsky, A. Poroelasticity of Cartilage at the Nanoscale. *Biophys. J.* **2011**, *101* (9), 2304–2313. <https://doi.org/10.1016/j.bpj.2011.09.011>.
- (126) Yang, Z.; Ma, Z.; Liu, S.; Li, J. Tissue Adhesion with Tough Hydrogels: Experiments and Modeling. *Mech. Mater.* **2021**, *157*, 103800. <https://doi.org/10.1016/j.mechmat.2021.103800>.
- (127) Lim, C. Y.; Owens, N. A.; Wampler, R. D.; Ying, Y.; Granger, J. H.; Porter, M. D.; Takahashi, M.; Shimazu, K. Succinimidyl Ester Surface Chemistry: Implications of the Competition between Aminolysis and Hydrolysis on Covalent Protein Immobilization. *Langmuir* **2014**, *30* (43), 12868–12878. <https://doi.org/10.1021/la503439g>.
- (128) Mao, X.; Yuk, H.; Zhao, X. Hydration and Swelling of Dry Polymers for Wet Adhesion. *J. Mech. Phys. Solids* **2020**, *137*, 103863. <https://doi.org/10.1016/j.jmps.2020.103863>.

- (129) Epstein, A. K.; Wong, T.-S.; Belisle, R. A.; Boggs, E. M.; Aizenberg, J. Liquid-Infused Structured Surfaces with Exceptional Anti-Biofouling Performance. *Proc. Natl. Acad. Sci.* **2012**, *109* (33), 13182–13187. <https://doi.org/10.1073/pnas.1201973109>.
- (130) Wu, S. J.; Yuk, H.; Wu, J.; Nabzdyk, C. S.; Zhao, X. A Multifunctional Origami Patch for Minimally Invasive Tissue Sealing. *Adv. Mater.* **2021**, *33* (11), 2007667. <https://doi.org/10.1002/adma.202007667>.
- (131) Bao, G.; Gao, Q.; Cau, M.; Ali-Mohamad, N.; Strong, M.; Jiang, S.; Yang, Z.; Valiei, A.; Ma, Z.; Amabili, M.; Gao, Z.-H.; Mongeau, L.; Kastrup, C.; Li, J. Liquid-Infused Microstructured Bioadhesives Halt Non-Compressible Hemorrhage. *Nat. Commun.* **2022**, *13* (1), 1–14. <https://doi.org/10.1038/s41467-022-32803-1>.
- (132) Geraldini, N. R.; Guan, J. H.; Dodd, L. E.; Maiello, P.; Xu, B. B.; Wood, D.; Newton, M. I.; Wells, G. G.; McHale, G. Double-Sided Slippery Liquid-Infused Porous Materials Using Conformable Mesh. *Sci. Rep.* **2019**, *9* (1), 13280. <https://doi.org/10.1038/s41598-019-49887-3>.
- (133) Yuk, H.; Wu, J.; Sarrafian, T. L.; Mao, X.; Varela, C. E.; Roche, E. T.; Griffiths, L. G.; Nabzdyk, C. S.; Zhao, X. Rapid and Coagulation-Independent Haemostatic Sealing by a Paste Inspired by Barnacle Glue. *Nat. Biomed. Eng.* **2021**, *5* (10), 1131–1142. <https://doi.org/10.1038/s41551-021-00769-y>.
- (134) Thavarajah, D.; De Lacy, P.; Hussain, R.; Redfern, R. M. Postoperative Cervical Cord Compression Induced by Hydrogel (DuraSeal): A Possible Complication. *Spine* **2010**, *35* (1), E25. <https://doi.org/10.1097/BRS.0b013e3181b9fc45>.
- (135) Blackburn, S. L.; Smyth, M. D. Hydrogel-Induced Cervicomedullary Compression after Posterior Fossa Decompression for Chiari Malformation. Case Report. *J. Neurosurg.* **2007**, *106* (4 Suppl), 302–304. <https://doi.org/10.3171/ped.2007.106.4.302>.
- (136) Mulder, M.; Crosier, J.; Dunn, R. Cauda Equina Compression by Hydrogel Dural Sealant after a Laminotomy and Discectomy: Case Report. *Spine* **2009**, *34* (4), E144–148. <https://doi.org/10.1097/BRS.0b013e31818d5427>.
- (137) Barrett, D. G.; Bushnell, G. G.; Messersmith, P. B. Mechanically Robust, Negative-Swelling, Mussel-Inspired Tissue Adhesives. *Adv. Healthc. Mater.* **2013**, *2* (5), 745–755. <https://doi.org/10.1002/adhm.201200316>.
- (138) Tian, G.; Yang, D.; Liang, C.; Liu, Y.; Chen, J.; Zhao, Q.; Tang, S.; Huang, J.; Xu, P.; Liu, Z.; Qi, D. A Nonswelling Hydrogel with Regenerable High Wet Tissue Adhesion for Bioelectronics. *Adv. Mater.* **2023**, *35* (18), 2212302. <https://doi.org/10.1002/adma.202212302>.
- (139) Theocharidis, G.; Yuk, H.; Roh, H.; Wang, L.; Mezghani, I.; Wu, J.; Kafanas, A.; Contreras, M.; Sumpio, B.; Li, Z.; Wang, E.; Chen, L.; Guo, C. F.; Jayaswal, N.; Katopodi, X.-L.; Kalavros, N.; Nabzdyk, C. S.; Vlachos, I. S.; Veves, A.; Zhao, X. A Strain-Programmed Patch for the Healing of Diabetic Wounds. *Nat. Biomed. Eng.* **2022**, *6* (10), 1118–1133. <https://doi.org/10.1038/s41551-022-00905-2>.
- (140) Annabi, N.; Zhang, Y.-N.; Assmann, A.; Sani, E. S.; Cheng, G.; Lassaletta, A. D.; Vegh, A.; Dehghani, B.; Ruiz-Esparza, G. U.; Wang, X.; Gangadharan, S.; Weiss, A. S.; Khademhosseini, A. Engineering a Highly Elastic Human Protein-Based Sealant for Surgical Applications. *Sci. Transl. Med.* **2017**, *9* (410). <https://doi.org/10.1126/scitranslmed.aai7466>.
- (141) Annabi, N.; Mithieux, S. M.; Zorlutuna, P.; Camci-Unal, G.; Weiss, A. S.; Khademhosseini, A. Engineered Cell-Laden Human Protein-Based Elastomer.

- Biomaterials* **2013**, *34* (22), 5496–5505.
<https://doi.org/10.1016/j.biomaterials.2013.03.076>.
- (142) Anderson, J. M.; Rodriguez, A.; Chang, D. T. Foreign Body Reaction to Biomaterials. *Semin. Immunol.* **2008**, *20* (2), 86–100. <https://doi.org/10.1016/j.smim.2007.11.004>.
- (143) Fatehi Hassanabad, A.; Zarzycki, A. N.; Jeon, K.; Dundas, J. A.; Vasanthan, V.; Deniset, J. F.; Fedak, P. W. M. Prevention of Post-Operative Adhesions: A Comprehensive Review of Present and Emerging Strategies. *Biomolecules* **2021**, *11* (7), 1027. <https://doi.org/10.3390/biom11071027>.
- (144) Klopffleisch, R.; Jung, F. The Pathology of the Foreign Body Reaction against Biomaterials. *J. Biomed. Mater. Res. A* **2017**, *105* (3), 927–940. <https://doi.org/10.1002/jbm.a.35958>.
- (145) Zhang, L.; Cao, Z.; Bai, T.; Carr, L.; Ella-Menye, J.-R.; Irvin, C.; Ratner, B. D.; Jiang, S. Zwitterionic Hydrogels Implanted in Mice Resist the Foreign-Body Reaction. *Nat. Biotechnol.* **2013**, *31* (6), 553–556. <https://doi.org/10.1038/nbt.2580>.
- (146) Jansen, L. E.; Amer, L. D.; Chen, E. Y.-T.; Nguyen, T. V.; Saleh, L. S.; Emrick, T.; Liu, W. F.; Bryant, S. J.; Peyton, S. R. Zwitterionic PEG-PC Hydrogels Modulate the Foreign Body Response in a Modulus-Dependent Manner. *Biomacromolecules* **2018**, *19* (7), 2880–2888. <https://doi.org/10.1021/acs.biomac.8b00444>.
- (147) Doloff, J. C.; Veiseh, O.; de Mezerville, R.; Sforza, M.; Perry, T. A.; Haupt, J.; Jamiel, M.; Chambers, C.; Nash, A.; Aghlara-Fotovvat, S.; Stelzel, J. L.; Bauer, S. J.; Neshat, S. Y.; Hancock, J.; Romero, N. A.; Hidalgo, Y. E.; Leiva, I. M.; Munhoz, A. M.; Bayat, A.; Kinney, B. M.; Hodges, H. C.; Miranda, R. N.; Clemens, M. W.; Langer, R. The Surface Topography of Silicone Breast Implants Mediates the Foreign Body Response in Mice, Rabbits and Humans. *Nat. Biomed. Eng.* **2021**, *5* (10), 1115–1130. <https://doi.org/10.1038/s41551-021-00739-4>.
- (148) Veiseh, O.; Doloff, J. C.; Ma, M.; Vegas, A. J.; Tam, H. H.; Bader, A. R.; Li, J.; Langan, E.; Wyckoff, J.; Loo, W. S.; Jhunjunwala, S.; Chiu, A.; Siebert, S.; Tang, K.; Hollister-Lock, J.; Aresta-Dasilva, S.; Bochenek, M.; Mendoza-Elias, J.; Wang, Y.; Qi, M.; Lavin, D. M.; Chen, M.; Dholakia, N.; Thakrar, R.; Lacík, I.; Weir, G. C.; Oberholzer, J.; Greiner, D. L.; Langer, R.; Anderson, D. G. Size- and Shape-Dependent Foreign Body Immune Response to Materials Implanted in Rodents and Non-Human Primates. *Nat. Mater.* **2015**, *14* (6), 643–651. <https://doi.org/10.1038/nmat4290>.
- (149) Hilger, C.; Clark, E.; Swiontek, K.; Chiriack, A. M.; Caimmi, D. P.; Demoly, P.; Bourrain, J. L. Anaphylaxis to Bovine Serum Albumin Tissue Adhesive in a Non-Meat-Allergic Patient. *J. Investig. Allergol. Clin. Immunol.* **2020**, *30* (5), 369–371. <https://doi.org/10.18176/jiaci.0522>.
- (150) Mitsuhata, H.; Horiguchi, Y.; Saitoh, J.; Saitoh, K.; Fukuda, H.; Hirabayasi, Y.; Togashi, H.; Shimizu, R. An Anaphylactic Reaction to Topical Fibrin Glue. *Anesthesiology* **1994**, *81* (4), 1074–1077. <https://doi.org/10.1097/00000542-199410000-00034>.
- (151) Saffarzadeh, M.; Mulpuri, A.; Arneja, J. S. Recalcitrant Anaphylaxis Associated with Fibrin Sealant: Treatment with “TISSEEL-Ectomy.” *Plast. Reconstr. Surg. Glob. Open* **2021**, *9* (1), e3382. <https://doi.org/10.1097/GOX.0000000000003382>.
- (152) Shupak, R. P.; Blackmore, S.; Kim, R. Y. Skin Hypersensitivity Following Application of Tissue Adhesive (2-Octyl Cyanoacrylate). *Bayl. Univ. Med. Cent. Proc.* **2021**, *34* (6), 736–738. <https://doi.org/10.1080/08998280.2021.1935140>.

- (153) Aguado, B. A.; Grim, J. C.; Rosales, A. M.; Watson-Capps, J. J.; Anseth, K. S. Engineering Precision Biomaterials for Personalized Medicine. *Sci. Transl. Med.* **2018**, *10* (424), eaam8645. <https://doi.org/10.1126/scitranslmed.aam8645>.
- (154) Pahlevanzadeh, F.; Setayeshmehr, M.; Bakhsheshi-Rad, H. R.; Emadi, R.; Kharaziha, M.; Poursamar, S. A.; Ismail, A. F.; Sharif, S.; Chen, X.; Berto, F. A Review on Antibacterial Biomaterials in Biomedical Applications: From Materials Perspective to Bioinks Design. *Polymers* **2022**, *14* (11), 2238. <https://doi.org/10.3390/polym14112238>.
- (155) Sarasam, A. R.; Krishnaswamy, R. K.; Madihally, S. V. Blending Chitosan with Polycaprolactone: Effects on Physicochemical and Antibacterial Properties. *Biomacromolecules* **2006**, *7* (4), 1131–1138. <https://doi.org/10.1021/bm050935d>.
- (156) Li, W.; Thian, E. S.; Wang, M.; Wang, Z.; Ren, L. Surface Design for Antibacterial Materials: From Fundamentals to Advanced Strategies. *Adv. Sci.* **2021**, *8* (19), 2100368. <https://doi.org/10.1002/advs.202100368>.
- (157) Wang, F.; Wang, S.; Nan, L.; Lu, J.; Zhu, Z.; Yang, J.; Zhang, D.; Liu, J.; Zhao, X.; Wu, D. Conductive Adhesive and Antibacterial Zwitterionic Hydrogel Dressing for Therapy of Full-Thickness Skin Wounds. *Front. Bioeng. Biotechnol.* **2022**, *10*.
- (158) Zheng, L.; Sundaram, H. S.; Wei, Z.; Li, C.; Yuan, Z. Applications of Zwitterionic Polymers. *React. Funct. Polym.* **2017**, *118*, 51–61. <https://doi.org/10.1016/j.reactfunctpolym.2017.07.006>.
- (159) Drago, L.; Bortolin, M.; De Vecchi, E.; Agrappi, S.; Weinstein, R. L.; Mattina, R.; Francetti, L. Antibiofilm Activity of Sandblasted and Laser-Modified Titanium against Microorganisms Isolated from Peri-Implantitis Lesions. *J. Chemother.* **2016**, *28* (5), 383–389. <https://doi.org/10.1080/1120009X.2016.1158489>.
- (160) Kargar, M.; Chang, Y.-R.; Khalili Hoseinabad, H.; Pruden, A.; Ducker, W. A. Colloidal Crystals Delay Formation of Early Stage Bacterial Biofilms. *ACS Biomater. Sci. Eng.* **2016**, *2* (6), 1039–1048. <https://doi.org/10.1021/acsbiomaterials.6b00163>.
- (161) Pascual, G.; Sotomayor, S.; Rodríguez, M.; Pérez-Köhler, B.; Kühnhardt, A.; Fernández-Gutiérrez, M.; San Román, J.; Bellón, J. M. Cytotoxicity of Cyanoacrylate-Based Tissue Adhesives and Short-Term Preclinical In Vivo Biocompatibility in Abdominal Hernia Repair. *PLoS ONE* **2016**, *11* (6), e0157920. <https://doi.org/10.1371/journal.pone.0157920>.
- (162) Li, Y.; Li, G.; Chen, Y.; Zhao, X.; Wang, Y.; Liu, J.; Li, Z. Gradient Modulus Tissue Adhesive Composite for Dynamic Wound Closure. *Adv. Funct. Mater.* **2022**, *32* (45), 2207306. <https://doi.org/10.1002/adfm.202207306>.
- (163) Kelly, B. A.; Chowienczyk, P. Vascular Compliance. In *An Introduction to Vascular Biology: From Basic Science to Clinical Practice*; Halliday, A. W., Hunt, B. J., Poston, L., Schachter, M., Eds.; Cambridge University Press: Cambridge, 2002; pp 33–48. <https://doi.org/10.1017/CBO9780511545948.003>.
- (164) Abbott, W. M.; Megerman, J.; Hasson, J. E.; L'Italien, G.; Warnock, D. F. Effect of Compliance Mismatch on Vascular Graft Patency. *J. Vasc. Surg.* **1987**, *5* (2), 376–382. [https://doi.org/10.1016/0741-5214\(87\)90148-0](https://doi.org/10.1016/0741-5214(87)90148-0).
- (165) Zhou, J.; Fung, Y. C. The Degree of Nonlinearity and Anisotropy of Blood Vessel Elasticity. *Proc. Natl. Acad. Sci.* **1997**, *94* (26), 14255–14260. <https://doi.org/10.1073/pnas.94.26.14255>.
- (166) Bhupathi, S. S.; Chalasani, S.; Rokey, R. Stiff Heart Syndrome. *Clin. Med. Res.* **2011**, *9* (2), 92–99. <https://doi.org/10.3121/cm.2010.899>.

- (167) Lang, N.; Pereira, M. J.; Lee, Y.; Friehs, I.; Vasilyev, N. V.; Feins, E. N.; Ablasser, K.; O’Cearbhaill, E. D.; Xu, C.; Fabozzo, A.; Padera, R.; Wasserman, S.; Freudenthal, F.; Ferreira, L. S.; Langer, R.; Karp, J. M.; del Nido, P. J. A Blood-Resistant Surgical Glue for Minimally Invasive Repair of Vessels and Heart Defects. *Sci. Transl. Med.* **2014**, *6* (218), 218ra6. <https://doi.org/10.1126/scitranslmed.3006557>.
- (168) Kurzawski, J.; Janion-Sadowska, A.; Sadowski, M. A Novel Minimally Invasive Method of Successful Tissue Glue Injection in Patients with Iatrogenic Pseudoaneurysm. *Br. J. Radiol.* **2018**, *91* (1087), 20170538. <https://doi.org/10.1259/bjr.20170538>.
- (169) Zhou, F.; Yang, Y.; Zhang, W.; Liu, S.; Shaikh, A. B.; Yang, L.; Lai, Y.; Ouyang, H.; Zhu, W. Bioinspired, Injectable, Tissue-Adhesive and Antibacterial Hydrogel for Multiple Tissue Regeneration by Minimally Invasive Therapy. *Appl. Mater. Today* **2022**, *26*, 101290. <https://doi.org/10.1016/j.apmt.2021.101290>.
- (170) Mei, X.; Li, J.; Wang, Z.; Zhu, D.; Huang, K.; Hu, S.; Popowski, K. D.; Cheng, K. An Inhaled Bioadhesive Hydrogel to Shield Non-Human Primates from SARS-CoV-2 Infection. *Nat. Mater.* **2023**, 1–10. <https://doi.org/10.1038/s41563-023-01475-7>.
- (171) Song, R.; Murphy, M.; Li, C.; Ting, K.; Soo, C.; Zheng, Z. Current Development of Biodegradable Polymeric Materials for Biomedical Applications. *Drug Des. Devel. Ther.* **2018**, *12*, 3117–3145. <https://doi.org/10.2147/DDDT.S165440>.
- (172) Tamariz, E.; Rios-Ramírez, A.; Tamariz, E.; Rios-Ramírez, A. Biodegradation of Medical Purpose Polymeric Materials and Their Impact on Biocompatibility. In *Biodegradation - Life of Science*; IntechOpen, 2013. <https://doi.org/10.5772/56220>.
- (173) Brugmans, M. C. P.; Söntjens, S. H. M.; Cox, M. A. J.; Nandakumar, A.; Bosman, A. W.; Mes, T.; Janssen, H. M.; Bouten, C. V. C.; Baaijens, F. P. T.; Driessen-Mol, A. Hydrolytic and Oxidative Degradation of Electrospun Supramolecular Biomaterials: In Vitro Degradation Pathways. *Acta Biomater.* **2015**, *27*, 21–31. <https://doi.org/10.1016/j.actbio.2015.08.034>.
- (174) Williams, D. F.; Zhong, S. P. Biodeterioration/Biodegradation of Polymeric Medical Devices in Situ. *Int. Biodeterior. Biodegrad.* **1994**, *34* (2), 95–130. [https://doi.org/10.1016/0964-8305\(94\)90002-7](https://doi.org/10.1016/0964-8305(94)90002-7).
- (175) Santerre, J. P.; Woodhouse, K.; Laroche, G.; Labow, R. S. Understanding the Biodegradation of Polyurethanes: From Classical Implants to Tissue Engineering Materials. *Biomaterials* **2005**, *26* (35), 7457–7470. <https://doi.org/10.1016/j.biomaterials.2005.05.079>.
- (176) Azevedo, H. S.; Reis, R. L. Enzymatic Degradation of Biodegradable Polymers and Strategies to Control Their Degradation Rate. *Biodegrad. Syst. Tissue Eng. Regen. Med.*
- (177) Santerre, J. P.; Labow, R. S.; Duguay, D. G.; Erfle, D.; Adams, G. A. Biodegradation Evaluation of Polyether and Polyester-Urethanes with Oxidative and Hydrolytic Enzymes. *J. Biomed. Mater. Res.* **1994**, *28* (10), 1187–1199. <https://doi.org/10.1002/jbm.820281009>.
- (178) Crippa, S.; Salvia, R.; Falconi, M.; Butturini, G.; Landoni, L.; Bassi, C. Anastomotic Leakage in Pancreatic Surgery. *HPB* **2007**, *9* (1), 8–15. <https://doi.org/10.1080/13651820600641357>.
- (179) Tian, F.; Appert, H. E.; Howard, J. M. The Disintegration of Absorbable Suture Materials on Exposure to Human Digestive Juices: An Update. *Am. Surg.* **1994**, *60* (4), 287–291.
- (180) Leggat, P. A.; Smith, D. R.; Kedjarune, U. Surgical Applications of Cyanoacrylate Adhesives: A Review of Toxicity. *ANZ J. Surg.* **2007**, *77* (4), 209–213. <https://doi.org/10.1111/j.1445-2197.2007.04020.x>.

- (181) Chen, M. H.; Wang, L. L.; Chung, J. J.; Kim, Y.-H.; Atluri, P.; Burdick, J. A. Methods To Assess Shear-Thinning Hydrogels for Application As Injectable Biomaterials. *ACS Biomater. Sci. Eng.* **2017**, *3* (12), 3146–3160. <https://doi.org/10.1021/acsbiomaterials.7b00734>.
- (182) Lapomarda, A.; Pulidori, E.; Cerqueni, G.; Chiesa, I.; De Blasi, M.; Geven, M. A.; Montemurro, F.; Duce, C.; Mattioli-Belmonte, M.; Tiné, M. R.; Vozzi, G.; De Maria, C. Pectin as Rheology Modifier of a Gelatin-Based Biomaterial Ink. *Materials* **2021**, *14* (11), 3109. <https://doi.org/10.3390/ma14113109>.
- (183) Pang, Y.; Liu, J.; Moussa, Z. L.; Collins, J. E.; McDonnell, S.; Hayward, A. M.; Jajoo, K.; Langer, R.; Traverso, G. Endoscopically Injectable Shear-Thinning Hydrogels Facilitating Polyp Removal. *Adv. Sci.* **2019**, *6* (19), 1901041. <https://doi.org/10.1002/adv.201901041>.
- (184) Kovalchick, C.; Molinari, A.; Ravichandran, G. Rate Dependent Adhesion Energy and Nonsteady Peeling of Inextensible Tapes. *J. Appl. Mech.* **2013**, *81* (041016). <https://doi.org/10.1115/1.4025273>.
- (185) Capella-Monsonís, H.; Kearns, S.; Kelly, J.; Zeugolis, D. I. Battling Adhesions: From Understanding to Prevention. *BMC Biomed. Eng.* **2019**, *1* (1), 5. <https://doi.org/10.1186/s42490-019-0005-0>.
- (186) Dumville, J. C.; Coulthard, P.; Worthington, H. V.; Riley, P.; Patel, N.; Darcey, J.; Esposito, M.; Elst, M. van der; Waes, O. J. F. van. Tissue Adhesives for Closure of Surgical Incisions. *Cochrane Database Syst. Rev.* **2014**, No. 11. <https://doi.org/10.1002/14651858.CD004287.pub4>.
- (187) *Carbodiimide Crosslinker Chemistry - US*. //www.thermofisher.com/us/en/home/life-science/protein-biology/protein-biology-learning-center/protein-biology-resource-library/pierce-protein-methods/carbodiimide-crosslinker-chemistry.html (accessed 2021-04-20).
- (188) Cheung, R. C. F.; Ng, T. B.; Wong, J. H.; Chan, W. Y. Chitosan: An Update on Potential Biomedical and Pharmaceutical Applications. *Mar. Drugs* **2015**, *13* (8), 5156–5186. <https://doi.org/10.3390/md13085156>.
- (189) Ahmadi, F.; Oveisi, Z.; Samani, S. M.; Amoozgar, Z. Chitosan Based Hydrogels: Characteristics and Pharmaceutical Applications. *Res. Pharm. Sci.* **2015**, *10* (1), 1–16.
- (190) Howell, C.; Grinthal, A.; Sunny, S.; Aizenberg, M.; Aizenberg, J. Designing Liquid-Infused Surfaces for Medical Applications: A Review. *Adv. Mater.* **2018**, *30* (50), 1802724. <https://doi.org/10.1002/adma.201802724>.
- (191) Smith, J. D.; Dhiman, R.; Anand, S.; Reza-Garduno, E.; Cohen, R. E.; McKinley, G. H.; Varanasi, K. K. Droplet Mobility on Lubricant-Impregnated Surfaces. *Soft Matter* **2013**, *9* (6), 1772–1780. <https://doi.org/10.1039/C2SM27032C>.
- (192) Barca, F.; Caporossi, T.; Rizzo, S. Silicone Oil: Different Physical Properties and Clinical Applications. *BioMed Res. Int.* **2014**, *2014*. <https://doi.org/10.1155/2014/502143>.
- (193) Woodward, R. B.; Schramm, C. H. SYNTHESIS OF PROTEIN ANALOGS. *J. Am. Chem. Soc.* **1947**, *69* (6), 1551–1552. <https://doi.org/10.1021/ja01198a526>.
- (194) Carr, L.; Cheng, G.; Xue, H.; Jiang, S. Engineering the Polymer Backbone To Strengthen Nonfouling Sulfobetaine Hydrogels. *Langmuir* **2010**, *26* (18), 14793–14798. <https://doi.org/10.1021/la1028004>.
- (195) Yue, W.-W.; Li, H.-J.; Xiang, T.; Qin, H.; Sun, S.-D.; Zhao, C.-S. Grafting of Zwitterion from Polysulfone Membrane via Surface-Initiated ATRP with Enhanced Antifouling

- Property and Biocompatibility. *J. Membr. Sci.* **2013**, *446*, 79–91. <https://doi.org/10.1016/j.memsci.2013.06.029>.
- (196) Wu, J.; Lin, W.; Wang, Z.; Chen, S.; Chang, Y. Investigation of the Hydration of Nonfouling Material Poly(Sulfobetaine Methacrylate) by Low-Field Nuclear Magnetic Resonance. *Langmuir* **2012**, *28* (19), 7436–7441. <https://doi.org/10.1021/la300394c>.
- (197) Shao, Q.; Jiang, S. Molecular Understanding and Design of Zwitterionic Materials. *Adv. Mater.* **2015**, *27* (1), 15–26. <https://doi.org/10.1002/adma.201404059>.
- (198) Jiang, S.; Cao, Z. Ultralow-Fouling, Functionalizable, and Hydrolyzable Zwitterionic Materials and Their Derivatives for Biological Applications. *Adv. Mater.* **2010**, *22* (9), 920–932. <https://doi.org/10.1002/adma.200901407>.
- (199) He, H.; Xiao, Z.; Zhou, Y.; Chen, A.; Xuan, X.; Li, Y.; Guo, X.; Zheng, J.; Xiao, J.; Wu, J. Zwitterionic Poly(Sulfobetaine Methacrylate) Hydrogels with Optimal Mechanical Properties for Improving Wound Healing in Vivo. *J. Mater. Chem. B* **2019**, *7* (10), 1697–1707. <https://doi.org/10.1039/C8TB02590H>.
- (200) Wang, W. Polyurethane for Biomedical Applications: A Review of Recent Developments. *Des. Manuf. Med. Devices* **37**.
- (201) Yu, Y.; Yuk, H.; Parada, G. A.; Wu, Y.; Liu, X.; Nabzdyk, C. S.; Youcef-Toumi, K.; Zang, J.; Zhao, X. Multifunctional “Hydrogel Skins” on Diverse Polymers with Arbitrary Shapes. *Adv. Mater.* **2019**, *31* (7), 1807101. <https://doi.org/10.1002/adma.201807101>.
- (202) Wong, T.-S.; Kang, S. H.; Tang, S. K. Y.; Smythe, E. J.; Hatton, B. D.; Grinthal, A.; Aizenberg, J. Bioinspired Self-Repairing Slippery Surfaces with Pressure-Stable Omniphobicity. *Nature* **2011**, *477* (7365), 443–447. <https://doi.org/10.1038/nature10447>.
- (203) Kreder, M. J.; Alvarenga, J.; Kim, P.; Aizenberg, J. Design of Anti-Icing Surfaces: Smooth, Textured or Slippery? *Nat. Rev. Mater.* **2016**, *1* (1), 15003. <https://doi.org/10.1038/natrevmats.2015.3>.
- (204) Villegas, M.; Zhang, Y.; Abu Jarad, N.; Soleymani, L.; Didar, T. F. Liquid-Infused Surfaces: A Review of Theory, Design, and Applications. *ACS Nano* **2019**, *13* (8), 8517–8536. <https://doi.org/10.1021/acsnano.9b04129>.
- (205) Amini, S.; Kolle, S.; Petrone, L.; Ahanotu, O.; Sunny, S.; Sutanto, C. N.; Hoon, S.; Cohen, L.; Weaver, J. C.; Aizenberg, J.; Vogel, N.; Miserez, A. Preventing Mussel Adhesion Using Lubricant-Infused Materials. *Science* **2017**, *357* (6352), 668–673. <https://doi.org/10.1126/science.aai8977>.
- (206) Bohn, H. F.; Federle, W. Insect Aquaplaning: Nepenthes Pitcher Plants Capture Prey with the Peristome, a Fully Wettable Water-Lubricated Anisotropic Surface. *Proc. Natl. Acad. Sci. U. S. A.* **2004**, *101* (39), 14138–14143. <https://doi.org/10.1073/pnas.0405885101>.
- (207) Yashima, S.; Takase, N.; Kurokawa, T.; Gong, J. P. Friction of Hydrogels with Controlled Surface Roughness on Solid Flat Substrates. *Soft Matter* **2014**, *10* (18), 3192–3199. <https://doi.org/10.1039/C3SM52883A>.
- (208) Langley, K. R.; Thoroddsen, S. T. Gliding on a Layer of Air: Impact of a Large-Viscosity Drop on a Liquid Film. *J. Fluid Mech.* **2019**, *878*. <https://doi.org/10.1017/jfm.2019.682>.
- (209) Walls, D. J.; Meiburg, E.; Fuller, G. G. The Shape Evolution of Liquid Droplets in Miscible Environments. *J. Fluid Mech.* **2018**, *852*, 422–452. <https://doi.org/10.1017/jfm.2018.535>.
- (210) Boreyko, J. B.; Polizos, G.; Datskos, P. G.; Sarles, S. A.; Collier, C. P. Air-Stable Droplet Interface Bilayers on Oil-Infused Surfaces. *Proc. Natl. Acad. Sci.* **2014**, *111* (21), 7588–7593. <https://doi.org/10.1073/pnas.1400381111>.

- (211) Yuk, H.; Wu, J.; Mao, X.; Varela, C. E.; Roche, E. T.; Nabzdyk, C. S.; Zhao, X. *Barnacle-Inspired Paste for Instant Hemostatic Tissue Sealing*; preprint; Bioengineering, 2020. <https://doi.org/10.1101/2020.12.12.422505>.
- (212) Leslie, D. C.; Waterhouse, A.; Berthet, J. B.; Valentin, T. M.; Watters, A. L.; Jain, A.; Kim, P.; Hatton, B. D.; Nedder, A.; Donovan, K.; Super, E. H.; Howell, C.; Johnson, C. P.; Vu, T. L.; Bolgen, D. E.; Rifai, S.; Hansen, A. R.; Aizenberg, M.; Super, M.; Aizenberg, J.; Ingber, D. E. A Bioinspired Omniphobic Surface Coating on Medical Devices Prevents Thrombosis and Biofouling. *Nat. Biotechnol.* **2014**, *32* (11), 1134–1140. <https://doi.org/10.1038/nbt.3020>.
- (213) Duarte, A. P.; Coelho, J. F.; Bordado, J. C.; Cidade, M. T.; Gil, M. H. Surgical Adhesives: Systematic Review of the Main Types and Development Forecast. *Prog. Polym. Sci.* **2012**, *37* (8), 1031–1050. <https://doi.org/10.1016/j.progpolymsci.2011.12.003>.
- (214) Wang, S.; Li, J.; Pan, Y.; Liu, F.; Zeng, L.; Gao, Y.; Lu, T. A Double-Network Strategy for the Tough Tissue Adhesion of Hydrogels with Long-Term Stability under Physiological Environment. *Soft Matter* **2022**, *18* (33), 6192–6199. <https://doi.org/10.1039/D2SM00688J>.
- (215) Chia, H. N.; Wu, B. M. Recent Advances in 3D Printing of Biomaterials. *J. Biol. Eng.* **2015**, *9* (1), 4. <https://doi.org/10.1186/s13036-015-0001-4>.
- (216) Lai, J.; Wang, C.; Wang, M. 3D Printing in Biomedical Engineering: Processes, Materials, and Applications. *Appl. Phys. Rev.* **2021**, *8* (2), 021322. <https://doi.org/10.1063/5.0024177>.
- (217) Do, A.-V.; Khorsand, B.; Geary, S. M.; Salem, A. K. 3D Printing of Scaffolds for Tissue Regeneration Applications. *Adv. Healthc. Mater.* **2015**, *4* (12), 1742–1762. <https://doi.org/10.1002/adhm.201500168>.
- (218) ten Kate, J.; Smit, G.; Breedveld, P. 3D-Printed Upper Limb Prostheses: A Review. *Disabil. Rehabil. Assist. Technol.* **2017**, *12* (3), 300–314. <https://doi.org/10.1080/17483107.2016.1253117>.
- (219) Prasad, L. K.; Smyth, H. 3D Printing Technologies for Drug Delivery: A Review. *Drug Dev. Ind. Pharm.* **2016**, *42* (7), 1019–1031. <https://doi.org/10.3109/03639045.2015.1120743>.
- (220) Lewis, J. A. Direct Ink Writing of 3D Functional Materials. *Adv. Funct. Mater.* **2006**, *16* (17), 2193–2204. <https://doi.org/10.1002/adfm.200600434>.
- (221) Naficy, S.; Spinks, G. M.; Wallace, G. G. Thin, Tough, pH-Sensitive Hydrogel Films with Rapid Load Recovery. *ACS Appl. Mater. Interfaces* **2014**, *6* (6), 4109–4114. <https://doi.org/10.1021/am405708v>.
- (222) Gorbachev, A. A.; Tretinnikov, O. N.; Shkrabatovskaya, L. V.; Prihodchenko, L. K. Photoinduced Graft-Polymerization of Acrylic Acid on Polyethylene and Polypropylene Surfaces: Comparative Study Using IR-ATR Spectroscopy. *J. Appl. Spectrosc.* **2014**, *81* (5), 754–757. <https://doi.org/10.1007/s10812-014-0001-z>.
- (223) Rånby, B.; Guo, F. Z. “Surface-Photografting”: New Applications to Synthetic Fibers. *Polym. Adv. Technol.* **1994**, *5* (12), 829–836. <https://doi.org/10.1002/pat.1994.220051210>.
- (224) Schneider, M. H.; Tran, Y.; Tabeling, P. Benzophenone Absorption and Diffusion in Poly(Dimethylsiloxane) and Its Role in Graft Photo-Polymerization for Surface Modification. *Langmuir* **2011**, *27* (3), 1232–1240. <https://doi.org/10.1021/la103345k>.

- (225) Michel, R.; Poirier, L.; Poelvoorde, Q. van; Legagneux, J.; Manassero, M.; Corté, L. Interfacial Fluid Transport Is a Key to Hydrogel Bioadhesion. *Proc. Natl. Acad. Sci.* **2019**, *116* (3), 738–743. <https://doi.org/10.1073/pnas.1813208116>.
- (226) Shea, L. Comparison of TissuePatchTM3 with Other Commonly Used Surgical Sealants. **2009**.
- (227) National High Blood Pressure Education Program. *The Seventh Report of the Joint National Committee on Prevention, Detection, Evaluation, and Treatment of High Blood Pressure*; National Heart, Lung, and Blood Institute (US): Bethesda (MD), 2004.
- (228) Javaheri, S. Chapter 32 - Heart Failure as a Consequence of Sleep-Disordered Breathing. In *Heart Failure: A Companion to Braunwald's Heart Disease (Second Edition)*; Mann, D. L., Ed.; W.B. Saunders: Philadelphia, 2011; pp 477–494. <https://doi.org/10.1016/B978-1-4160-5895-3.10032-4>.
- (229) Ling, Y.; Pang, W.; Liu, J.; Page, M.; Xu, Y.; Zhao, G.; Stalla, D.; Xie, J.; Zhang, Y.; Yan, Z. Bioinspired Elastomer Composites with Programmed Mechanical and Electrical Anisotropies. *Nat. Commun.* **2022**, *13* (1), 524. <https://doi.org/10.1038/s41467-022-28185-z>.
- (230) Loh, X. J.; Tan, K. K.; Li, X.; Li, J. The in Vitro Hydrolysis of Poly(Ester Urethane)s Consisting of Poly[(R)-3-Hydroxybutyrate] and Poly(Ethylene Glycol). *Biomaterials* **2006**, *27* (9), 1841–1850. <https://doi.org/10.1016/j.biomaterials.2005.10.038>.
- (231) Daniels, J. IBS20.01 Airway Fistulas. *J. Thorac. Oncol.* **2019**, *14* (10), S111–S112. <https://doi.org/10.1016/j.jtho.2019.08.239>.
- (232) Fang, A. H.; Chao, W.; Ecker, M. Review of Colonic Anastomotic Leakage and Prevention Methods. *J. Clin. Med.* **2020**, *9* (12), 4061. <https://doi.org/10.3390/jcm9124061>.
- (233) Liu, X.; Ding, S.; Wang, F.; Shi, Y.; Wang, X.; Wang, Z. Controlling Energy Dissipation during Deformation by Selection of the Hard-Segment Component for Thermoplastic Polyurethanes. *Ind. Eng. Chem. Res.* **2022**, *61* (25), 8821–8831. <https://doi.org/10.1021/acs.iecr.2c01018>.
- (234) Li, S.; Cong, Y.; Fu, J. Tissue Adhesive Hydrogel Bioelectronics. *J. Mater. Chem. B* **2021**, *9* (22), 4423–4443. <https://doi.org/10.1039/D1TB00523E>.
- (235) Chen, X.; A. Rogers, J.; P. Lacour, S.; Hu, W.; Kim, D.-H. Materials Chemistry in Flexible Electronics. *Chem. Soc. Rev.* **2019**, *48* (6), 1431–1433. <https://doi.org/10.1039/C9CS90019E>.
- (236) Huang, S.; Liu, Y.; Zhao, Y.; Ren, Z.; Guo, C. F. Flexible Electronics: Stretchable Electrodes and Their Future. *Adv. Funct. Mater.* **2019**, *29* (6), 1805924. <https://doi.org/10.1002/adfm.201805924>.
- (237) Gao, W.; Ota, H.; Kiriya, D.; Takei, K.; Javey, A. Flexible Electronics toward Wearable Sensing. *Acc. Chem. Res.* **2019**, *52* (3), 523–533. <https://doi.org/10.1021/acs.accounts.8b00500>.
- (238) Ray, T. R.; Choi, J.; Bhandodkar, A. J.; Krishnan, S.; Gutruf, P.; Tian, L.; Ghaffari, R.; Rogers, J. A. Bio-Integrated Wearable Systems: A Comprehensive Review. *Chem. Rev.* **2019**, *119* (8), 5461–5533. <https://doi.org/10.1021/acs.chemrev.8b00573>.
- (239) Yuk, H.; Wu, J.; Zhao, X. Hydrogel Interfaces for Merging Humans and Machines. *Nat. Rev. Mater.* **2022**, *7* (12), 935–952. <https://doi.org/10.1038/s41578-022-00483-4>.
- (240) Kim, D.-H.; Lu, N.; Ma, R.; Kim, Y.-S.; Kim, R.-H.; Wang, S.; Wu, J.; Won, S. M.; Tao, H.; Islam, A.; Yu, K. J.; Kim, T.; Chowdhury, R.; Ying, M.; Xu, L.; Li, M.; Chung, H.-J.;

- Keum, H.; McCormick, M.; Liu, P.; Zhang, Y.-W.; Omenetto, F. G.; Huang, Y.; Coleman, T.; Rogers, J. A. Epidermal Electronics. *Science* **2011**, *333* (6044), 838–843. <https://doi.org/10.1126/science.1206157>.
- (241) Kim, T.; Park, J.; Sohn, J.; Cho, D.; Jeon, S. Bioinspired, Highly Stretchable, and Conductive Dry Adhesives Based on 1D–2D Hybrid Carbon Nanocomposites for All-in-One ECG Electrodes. *ACS Nano* **2016**, *10* (4), 4770–4778. <https://doi.org/10.1021/acsnano.6b01355>.
- (242) Wang, X.; Sun, X.; Gan, D.; Soubrier, M.; Chiang, H.-Y.; Yan, L.; Li, Y.; Li, J.; Yu, S.; Xia, Y.; Wang, K.; Qin, Q.; Jiang, X.; Han, L.; Pan, T.; Xie, C.; Lu, X. Bioadhesive and Conductive Hydrogel-Integrated Brain-Machine Interfaces for Conformal and Immune-Evasive Contact with Brain Tissue. *Matter* **2022**, *5* (4), 1204–1223. <https://doi.org/10.1016/j.matt.2022.01.012>.
- (243) Ding, L.; Hang, C.; Yang, S.; Qi, J.; Dong, R.; Zhang, Y.; Sun, H.; Jiang, X. In Situ Deposition of Skin-Adhesive Liquid Metal Particles with Robust Wear Resistance for Epidermal Electronics. *Nano Lett.* **2022**, *22* (11), 4482–4490. <https://doi.org/10.1021/acs.nanolett.2c01270>.
- (244) Koh, A.; Kang, D.; Xue, Y.; Lee, S.; Pielak, R. M.; Kim, J.; Hwang, T.; Min, S.; Banks, A.; Bastien, P.; Manco, M. C.; Wang, L.; Ammann, K. R.; Jang, K.-I.; Won, P.; Han, S.; Ghaffari, R.; Paik, U.; Slepian, M. J.; Balooch, G.; Huang, Y.; Rogers, J. A. A Soft, Wearable Microfluidic Device for the Capture, Storage, and Colorimetric Sensing of Sweat. *Sci. Transl. Med.* **2016**, *8* (366), 366ra165–366ra165. <https://doi.org/10.1126/scitranslmed.aaf2593>.
- (245) Wang, Z.; Luan, J.; Seth, A.; Liu, L.; You, M.; Gupta, P.; Rathi, P.; Wang, Y.; Cao, S.; Jiang, Q.; Zhang, X.; Gupta, R.; Zhou, Q.; Morrissey, J. J.; Scheller, E. L.; Rudra, J. S.; Singamaneni, S. Microneedle Patch for the Ultrasensitive Quantification of Protein Biomarkers in Interstitial Fluid. *Nat. Biomed. Eng.* **2021**, *5* (1), 64–76. <https://doi.org/10.1038/s41551-020-00672-y>.
- (246) Thomas, N.; Lähdesmäki, I.; Parviz, B. A. A Contact Lens with an Integrated Lactate Sensor. *Sens. Actuators B Chem.* **2012**, *162* (1), 128–134. <https://doi.org/10.1016/j.snb.2011.12.049>.
- (247) Tseng, P.; Napier, B.; Garbarini, L.; Kaplan, D. L.; Omenetto, F. G. Functional, RF-Trilayer Sensors for Tooth-Mounted, Wireless Monitoring of the Oral Cavity and Food Consumption. *Adv. Mater.* **2018**, *30* (18), 1703257. <https://doi.org/10.1002/adma.201703257>.
- (248) Jung, H.; Kim, M. K.; Lee, J. Y.; Choi, S. W.; Kim, J. Adhesive Hydrogel Patch with Enhanced Strength and Adhesiveness to Skin for Transdermal Drug Delivery. *Adv. Funct. Mater.* **2020**, *30* (42), 2004407. <https://doi.org/10.1002/adfm.202004407>.
- (249) Ziesmer, J.; Tajpara, P.; Hempel, N.-J.; Ehrström, M.; Melican, K.; Eidsmo, L.; Sotiriou, G. A. Vancomycin-Loaded Microneedle Arrays against Methicillin-Resistant Staphylococcus Aureus Skin Infections. *Adv. Mater. Technol.* **2021**, *6* (7), 2001307. <https://doi.org/10.1002/admt.202001307>.
- (250) Lathuilière, A.; Cosson, S.; Lutolf, M. P.; Schneider, B. L.; Aebischer, P. A High-Capacity Cell Macroencapsulation System Supporting the Long-Term Survival of Genetically Engineered Allogeneic Cells. *Biomaterials* **2014**, *35* (2), 779–791. <https://doi.org/10.1016/j.biomaterials.2013.09.071>.

- (251) Choi, M.; Choi, J. W.; Kim, S.; Nizamoglu, S.; Hahn, S. K.; Yun, S. H. Light-Guiding Hydrogels for Cell-Based Sensing and Optogenetic Synthesis in Vivo. *Nat. Photonics* **2013**, *7* (12), 987–994. <https://doi.org/10.1038/nphoton.2013.278>.
- (252) Yamagishi, K.; Kirino, I.; Takahashi, I.; Amano, H.; Takeoka, S.; Morimoto, Y.; Fujie, T. Tissue-Adhesive Wirelessly Powered Optoelectronic Device for Metronomic Photodynamic Cancer Therapy. *Nat. Biomed. Eng.* **2019**, *3* (1), 27–36. <https://doi.org/10.1038/s41551-018-0261-7>.
- (253) Barrios, C. A. Pressure Sensitive Adhesive Tape: A Versatile Material Platform for Optical Sensors. *Sensors* **2020**, *20* (18), 5303. <https://doi.org/10.3390/s20185303>.
- (254) Wang, C.; Chen, X.; Wang, L.; Makihata, M.; Liu, H.-C.; Zhou, T.; Zhao, X. Bioadhesive Ultrasound for Long-Term Continuous Imaging of Diverse Organs. *Science* **2022**, *377* (6605), 517–523. <https://doi.org/10.1126/science.abo2542>.
- (255) Hu, H.; Ma, Y.; Gao, X.; Song, D.; Li, M.; Huang, H.; Qian, X.; Wu, R.; Shi, K.; Ding, H.; Lin, M.; Chen, X.; Zhao, W.; Qi, B.; Zhou, S.; Chen, R.; Gu, Y.; Chen, Y.; Lei, Y.; Wang, C.; Wang, C.; Tong, Y.; Cui, H.; Abdal, A.; Zhu, Y.; Tian, X.; Chen, Z.; Lu, C.; Yang, X.; Mu, J.; Lou, Z.; Eghtedari, M.; Zhou, Q.; Oberai, A.; Xu, S. Stretchable Ultrasonic Arrays for the Three-Dimensional Mapping of the Modulus of Deep Tissue. *Nat. Biomed. Eng.* **2023**, 1–14. <https://doi.org/10.1038/s41551-023-01038-w>.
- (256) Lin, M.; Zhang, Z.; Gao, X.; Bian, Y.; Wu, R. S.; Park, G.; Lou, Z.; Zhang, Z.; Xu, X.; Chen, X.; Kang, A.; Yang, X.; Yue, W.; Yin, L.; Wang, C.; Qi, B.; Zhou, S.; Hu, H.; Huang, H.; Li, M.; Gu, Y.; Mu, J.; Yang, A.; Yaghi, A.; Chen, Y.; Lei, Y.; Lu, C.; Wang, R.; Wang, J.; Xiang, S.; Kistler, E. B.; Vasconcelos, N.; Xu, S. A Fully Integrated Wearable Ultrasound System to Monitor Deep Tissues in Moving Subjects. *Nat. Biotechnol.* **2023**, 1–10. <https://doi.org/10.1038/s41587-023-01800-0>.
- (257) Nam, S.; Seo, B. R.; Najibi, A. J.; McNamara, S. L.; Mooney, D. J. Active Tissue Adhesive Activates Mechanosensors and Prevents Muscle Atrophy. *Nat. Mater.* **2022**, 1–11. <https://doi.org/10.1038/s41563-022-01396-x>.
- (258) Reeder, J. T.; Xie, Z.; Yang, Q.; Seo, M.-H.; Yan, Y.; Deng, Y.; Jenkins, K. R.; Krishnan, S. R.; Liu, C.; McKay, S.; Patnaude, E.; Johnson, A.; Zhao, Z.; Kim, M. J.; Xu, Y.; Huang, I.; Avila, R.; Felicelli, C.; Ray, E.; Guo, X.; Ray, W. Z.; Huang, Y.; MacEwan, M. R.; Rogers, J. A. Soft, Bioresorbable Coolers for Reversible Conduction Block of Peripheral Nerves. *Science* **2022**, *377* (6601), 109–115. <https://doi.org/10.1126/science.abl8532>.
- (259) Schwartz, A. R.; Bennett, M. L.; Smith, P. L.; De Backer, W.; Hedner, J.; Boudewyns, A.; Van de Heyning, P.; Ejnell, H.; Hochban, W.; Knaack, L.; Podszus, T.; Penzel, T.; Peter, J. H.; Goding, G. S.; Erickson, D. J.; Testerman, R.; Ottenhoff, F.; Eisele, D. W. Therapeutic Electrical Stimulation of the Hypoglossal Nerve in Obstructive Sleep Apnea. *Arch. Otolaryngol. Neck Surg.* **2001**, *127* (10), 1216–1223. <https://doi.org/10.1001/archotol.127.10.1216>.
- (260) Rutten, W. L. C. Selective Electrical Interfaces with the Nervous System. *Annu. Rev. Biomed. Eng.* **2002**, *4* (1), 407–452. <https://doi.org/10.1146/annurev.bioeng.4.020702.153427>.
- (261) Trohman, R. G.; Kim, M. H.; Pinski, S. L. Cardiac Pacing: The State of the Art. *The Lancet* **2004**, *364* (9446), 1701–1719. [https://doi.org/10.1016/S0140-6736\(04\)17358-3](https://doi.org/10.1016/S0140-6736(04)17358-3).

- (262) Chen, J. D. Z.; Yin, J.; Wei, W. Electrical Therapies for Gastrointestinal Motility Disorders. *Expert Rev. Gastroenterol. Hepatol.* **2017**, *11* (5), 407–418. <https://doi.org/10.1080/17474124.2017.1298441>.
- (263) Kellaway, P. The Part Played by Electric Fish in the Early History of Bioelectricity and Electrotherapy. *Bull. Hist. Med.* **1946**, *20* (2), 112–137.
- (264) Jünger, M.; Arnold, A.; Zuder, D.; Stahl, H.-W.; Heising, S. Local Therapy and Treatment Costs of Chronic, Venous Leg Ulcers with Electrical Stimulation (Dermapulse): A Prospective, Placebo Controlled, Double Blind Trial. *Wound Repair Regen. Off. Publ. Wound Heal. Soc. Eur. Tissue Repair Soc.* **2008**, *16* (4), 480–487. <https://doi.org/10.1111/j.1524-475X.2008.00393.x>.
- (265) Li, Z.; Feng, H.; Zheng, Q.; Li, H.; Zhao, C.; Ouyang, H.; Noreen, S.; Yu, M.; Su, F.; Liu, R.; Li, L.; Wang, Z. L.; Li, Z. Photothermally Tunable Biodegradation of Implantable Triboelectric Nanogenerators for Tissue Repairing. *Nano Energy* **2018**, *54*, 390–399. <https://doi.org/10.1016/j.nanoen.2018.10.020>.
- (266) Nazari-Vanani, R.; Vafaiee, M.; Asadian, E.; Mohammadpour, R.; Rafii-Tabar, H.; Sasanpour, P. Enhanced Proliferation and Migration of Fibroblast Cells by Skin-Attachable and Self-Cleaning Triboelectric Nanogenerator. *Biomater. Adv.* **2023**, *149*, 213364. <https://doi.org/10.1016/j.bioadv.2023.213364>.
- (267) Reilly, J. P. *Applied Bioelectricity: From Electrical Stimulation to Electropathology*; Springer Science & Business Media, 2012.
- (268) Reilly, J. P.; Antoni, H. *Electrical Stimulation and Electropathology*; Cambridge University Press, 1992.
- (269) Meng, X.; Xiao, X.; Jeon, S.; Kim, D.; Park, B.-J.; Kim, Y.-J.; Rubab, N.; Kim, S.; Kim, S.-W. An Ultrasound-Driven Bioadhesive Triboelectric Nanogenerator for Instant Wound Sealing and Electrically Accelerated Healing in Emergencies. *Adv. Mater.* **2023**, *35* (12), 2209054. <https://doi.org/10.1002/adma.202209054>.
- (270) Wang, C.; Jiang, X.; Kim, H.-J.; Zhang, S.; Zhou, X.; Chen, Y.; Ling, H.; Xue, Y.; Chen, Z.; Qu, M.; Ren, L.; Zhu, J.; Libanori, A.; Zhu, Y.; Kang, H.; Ahadian, S.; Dokmeci, M. R.; Servati, P.; He, X.; Gu, Z.; Sun, W.; Khademhosseini, A. Flexible Patch with Printable and Antibacterial Conductive Hydrogel Electrodes for Accelerated Wound Healing. *Biomaterials* **2022**, *285*, 121479. <https://doi.org/10.1016/j.biomaterials.2022.121479>.
- (271) Wang, C.; Wang, C.; Huang, Z.; Xu, S. Materials and Structures toward Soft Electronics. *Adv. Mater.* **2018**, *30* (50), 1801368. <https://doi.org/10.1002/adma.201801368>.
- (272) Zhang, Y.; Tao, T. H. Skin-Friendly Electronics for Acquiring Human Physiological Signatures. *Adv. Mater.* **2019**, *31* (49), 1905767. <https://doi.org/10.1002/adma.201905767>.
- (273) Ma, Y.; Zhang, Y.; Cai, S.; Han, Z.; Liu, X.; Wang, F.; Cao, Y.; Wang, Z.; Li, H.; Chen, Y.; Feng, X. Flexible Hybrid Electronics for Digital Healthcare. *Adv. Mater.* **2020**, *32* (15), 1902062. <https://doi.org/10.1002/adma.201902062>.
- (274) Wang, C.; He, K.; Li, J.; Chen, X. Conformal Electrodes for On-Skin Digitalization. *SmartMat* **2021**, *2* (3), 252–262. <https://doi.org/10.1002/smm2.1068>.
- (275) Keplinger, C.; Sun, J.-Y.; Foo, C. C.; Rothmund, P.; Whitesides, G. M.; Suo, Z. Stretchable, Transparent, Ionic Conductors. *Science* **2013**, *341* (6149), 984–987. <https://doi.org/10.1126/science.1240228>.
- (276) Pitsalidis, C.; Pappa, A.-M.; Boys, A. J.; Fu, Y.; Moysidou, C.-M.; van Niekerk, D.; Saez, J.; Savva, A.; Iandolo, D.; Owens, R. M. Organic Bioelectronics for In Vitro Systems. *Chem. Rev.* **2022**, *122* (4), 4700–4790. <https://doi.org/10.1021/acs.chemrev.1c00539>.

- (277) Xu, F.; Zhu, Y. Highly Conductive and Stretchable Silver Nanowire Conductors. *Adv. Mater.* **2012**, *24* (37), 5117–5122. <https://doi.org/10.1002/adma.201201886>.
- (278) Kramer, R. K.; Majidi, C.; Wood, R. J. Masked Deposition of Gallium-Indium Alloys for Liquid-Embedded Elastomer Conductors. *Adv. Funct. Mater.* **2013**, *23* (42), 5292–5296. <https://doi.org/10.1002/adfm.201203589>.
- (279) Wang, Y.; Zhu, C.; Pfattner, R.; Yan, H.; Jin, L.; Chen, S.; Molina-Lopez, F.; Lissel, F.; Liu, J.; Rabiah, N. I.; Chen, Z.; Chung, J. W.; Linder, C.; Toney, M. F.; Murmann, B.; Bao, Z. A Highly Stretchable, Transparent, and Conductive Polymer. *Sci. Adv.* **2017**, *3* (3), e1602076. <https://doi.org/10.1126/sciadv.1602076>.
- (280) Choi, G. M.; Lim, S.-M.; Lee, Y.-Y.; Yi, S.-M.; Lee, Y.-J.; Sun, J.-Y.; Joo, Y.-C. PEDOT:PSS/Polyacrylamide Nanoweb: Highly Reliable Soft Conductors with Swelling Resistance. *ACS Appl. Mater. Interfaces* **2019**, *11* (10), 10099–10107. <https://doi.org/10.1021/acsami.9b00314>.
- (281) Choi, C.; Lee, Y.; Cho, K. W.; Koo, J. H.; Kim, D.-H. Wearable and Implantable Soft Bioelectronics Using Two-Dimensional Materials. *Acc. Chem. Res.* **2019**, *52* (1), 73–81. <https://doi.org/10.1021/acs.accounts.8b00491>.
- (282) Xue, Z.; Song, H.; Rogers, J. A.; Zhang, Y.; Huang, Y. Mechanically-Guided Structural Designs in Stretchable Inorganic Electronics. *Adv. Mater.* **2020**, *32* (15), 1902254. <https://doi.org/10.1002/adma.201902254>.
- (283) Wang, S.; Li, M.; Wu, J.; Kim, D.-H.; Lu, N.; Su, Y.; Kang, Z.; Huang, Y.; Rogers, J. A. Mechanics of Epidermal Electronics. *J. Appl. Mech.* **2012**, *79* (031022). <https://doi.org/10.1115/1.4005963>.
- (284) Yeo, W.-H.; Kim, Y.-S.; Lee, J.; Ameen, A.; Shi, L.; Li, M.; Wang, S.; Ma, R.; Jin, S. H.; Kang, Z.; Huang, Y.; Rogers, J. A. Multifunctional Epidermal Electronics Printed Directly Onto the Skin. *Adv. Mater.* **2013**, *25* (20), 2773–2778. <https://doi.org/10.1002/adma.201204426>.
- (285) Wang, L.; Lu, N. Conformability of a Thin Elastic Membrane Laminated on a Soft Substrate With Slightly Wavy Surface. *J. Appl. Mech.* **2016**, *83* (041007). <https://doi.org/10.1115/1.4032466>.
- (286) Xu, B.; Akhtar, A.; Liu, Y.; Chen, H.; Yeo, W.-H.; Park, S. I.; Boyce, B.; Kim, H.; Yu, J.; Lai, H.-Y.; Jung, S.; Zhou, Y.; Kim, J.; Cho, S.; Huang, Y.; Bretl, T.; Rogers, J. A. An Epidermal Stimulation and Sensing Platform for Sensorimotor Prosthetic Control, Management of Lower Back Exertion, and Electrical Muscle Activation. *Adv. Mater.* **2016**, *28* (22), 4462–4471. <https://doi.org/10.1002/adma.201504155>.
- (287) Kabiri Ameri, S.; Ho, R.; Jang, H.; Tao, L.; Wang, Y.; Wang, L.; Schnyer, D. M.; Akinwande, D.; Lu, N. Graphene Electronic Tattoo Sensors. *ACS Nano* **2017**, *11* (8), 7634–7641. <https://doi.org/10.1021/acsnano.7b02182>.
- (288) Wang, Y.; Qiu, Y.; Ameri, S. K.; Jang, H.; Dai, Z.; Huang, Y.; Lu, N. Low-Cost, Mm-Thick, Tape-Free Electronic Tattoo Sensors with Minimized Motion and Sweat Artifacts. *Npj Flex. Electron.* **2018**, *2* (1), 1–7. <https://doi.org/10.1038/s41528-017-0019-4>.
- (289) Gong, S.; Yap, L. W.; Zhu, B.; Zhai, Q.; Liu, Y.; Lyu, Q.; Wang, K.; Yang, M.; Ling, Y.; Lai, D. T. H.; Marzbanrad, F.; Cheng, W. Local Crack-Programmed Gold Nanowire Electronic Skin Tattoos for In-Plane Multisensor Integration. *Adv. Mater.* **2019**, *31* (41), 1903789. <https://doi.org/10.1002/adma.201903789>.
- (290) Alberto, J.; Leal, C.; Fernandes, C.; Lopes, P. A.; Paisana, H.; de Almeida, A. T.; Tavakoli, M. Fully Untethered Battery-Free Biomonitoring Electronic Tattoo with

- Wireless Energy Harvesting. *Sci. Rep.* **2020**, *10* (1), 5539. <https://doi.org/10.1038/s41598-020-62097-6>.
- (291) Gogurla, N.; Kim, Y.; Cho, S.; Kim, J.; Kim, S. Multifunctional and Ultrathin Electronic Tattoo for On-Skin Diagnostic and Therapeutic Applications. *Adv. Mater.* **2021**, *33* (24), 2008308. <https://doi.org/10.1002/adma.202008308>.
- (292) Gan, D.; Huang, Z.; Wang, X.; Jiang, L.; Wang, C.; Zhu, M.; Ren, F.; Fang, L.; Wang, K.; Xie, C.; Lu, X. Graphene Oxide-Templated Conductive and Redox-Active Nanosheets Incorporated Hydrogels for Adhesive Bioelectronics. *Adv. Funct. Mater.* **2020**, *30* (5), 1907678. <https://doi.org/10.1002/adfm.201907678>.
- (293) Liang, S.; Zhang, Y.; Wang, H.; Xu, Z.; Chen, J.; Bao, R.; Tan, B.; Cui, Y.; Fan, G.; Wang, W.; Wang, W.; Liu, W. Paintable and Rapidly Bondable Conductive Hydrogels as Therapeutic Cardiac Patches. *Adv. Mater.* **2018**, *30* (23), 1704235. <https://doi.org/10.1002/adma.201704235>.
- (294) Deng, Z.; Wang, H.; Ma, P. X.; Guo, B. Self-Healing Conductive Hydrogels: Preparation, Properties and Applications. *Nanoscale* **2020**, *12* (3), 1224–1246. <https://doi.org/10.1039/C9NR09283H>.
- (295) Lu, Y.; Liu, Z.; Yan, H.; Peng, Q.; Wang, R.; Barkey, M. E.; Jeon, J.-W.; Wujcik, E. K. Ultrastretchable Conductive Polymer Complex as a Strain Sensor with a Repeatable Autonomous Self-Healing Ability. *ACS Appl. Mater. Interfaces* **2019**, *11* (22), 20453–20464. <https://doi.org/10.1021/acsami.9b05464>.
- (296) Han, L.; Yan, L.; Wang, K.; Fang, L.; Zhang, H.; Tang, Y.; Ding, Y.; Weng, L.-T.; Xu, J.; Weng, J.; Liu, Y.; Ren, F.; Lu, X. Tough, Self-Healable and Tissue-Adhesive Hydrogel with Tunable Multifunctionality. *NPG Asia Mater.* **2017**, *9* (4), e372–e372. <https://doi.org/10.1038/am.2017.33>.
- (297) Bandodkar, A. J.; Wang, J. Non-Invasive Wearable Electrochemical Sensors: A Review. *Trends Biotechnol.* **2014**, *32* (7), 363–371. <https://doi.org/10.1016/j.tibtech.2014.04.005>.
- (298) Bariya, M.; Nyein, H. Y. Y.; Javey, A. Wearable Sweat Sensors. *Nat. Electron.* **2018**, *1* (3), 160–171. <https://doi.org/10.1038/s41928-018-0043-y>.
- (299) Luo, Y.; Abidian, M. R.; Ahn, J.-H.; Akinwande, D.; Andrews, A. M.; Antonietti, M.; Bao, Z.; Berggren, M.; Berkey, C. A.; Bettinger, C. J.; Chen, J.; Chen, P.; Cheng, W.; Cheng, X.; Choi, S.-J.; Chortos, A.; Dagdeviren, C.; Dauskardt, R. H.; Di, C.; Dickey, M. D.; Duan, X.; Facchetti, A.; Fan, Z.; Fang, Y.; Feng, J.; Feng, X.; Gao, H.; Gao, W.; Gong, X.; Guo, C. F.; Guo, X.; Hartel, M. C.; He, Z.; Ho, J. S.; Hu, Y.; Huang, Q.; Huang, Y.; Huo, F.; Hussain, M. M.; Javey, A.; Jeong, U.; Jiang, C.; Jiang, X.; Kang, J.; Karnaushenko, D.; Khademhosseini, A.; Kim, D.-H.; Kim, I.-D.; Kireev, D.; Kong, L.; Lee, C.; Lee, N.-E.; Lee, P. S.; Lee, T.-W.; Li, F.; Li, J.; Liang, C.; Lim, C. T.; Lin, Y.; Lipomi, D. J.; Liu, J.; Liu, K.; Liu, N.; Liu, R.; Liu, Y.; Liu, Y.; Liu, Z.; Liu, Z.; Loh, X. J.; Lu, N.; Lv, Z.; Magdassi, S.; Malliaras, G. G.; Matsuhisa, N.; Nathan, A.; Niu, S.; Pan, J.; Pang, C.; Pei, Q.; Peng, H.; Qi, D.; Ren, H.; Rogers, J. A.; Rowe, A.; Schmidt, O. G.; Sekitani, T.; Seo, D.-G.; Shen, G.; Sheng, X.; Shi, Q.; Someya, T.; Song, Y.; Stavrinidou, E.; Su, M.; Sun, X.; Takei, K.; Tao, X.-M.; Tee, B. C. K.; Thean, A. V.-Y.; Trung, T. Q.; Wan, C.; Wang, H.; Wang, J.; Wang, M.; Wang, S.; Wang, T.; Wang, Z. L.; Weiss, P. S.; Wen, H.; Xu, S.; Xu, T.; Yan, H.; Yan, X.; Yang, H.; Yang, L.; Yang, S.; Yin, L.; Yu, C.; Yu, G.; Yu, J.; Yu, S.-H.; Yu, X.; Zamburg, E.; Zhang, H.; Zhang, X.; Zhang, X.; Zhang, X.; Zhang, Y.; Zhang, Y.; Zhao, S.; Zhao, X.; Zheng, Y.; Zheng, Y.-Q.; Zheng, Z.; Zhou, T.; Zhu, B.; Zhu, M.; Zhu, R.; Zhu, Y.; Zhu, Y.; Zou, G.; Chen, X. Technology Roadmap

- for Flexible Sensors. *ACS Nano* **2023**, *17* (6), 5211–5295.
<https://doi.org/10.1021/acsnano.2c12606>.
- (300) Zhao, J.; Guo, H.; Li, J.; Bandodkar, A. J.; Rogers, J. A. Body-Interfaced Chemical Sensors for Noninvasive Monitoring and Analysis of Biofluids. *Trends Chem.* **2019**, *1* (6), 559–571. <https://doi.org/10.1016/j.trechm.2019.07.001>.
- (301) Miller, P. R.; Skoog, S. A.; Edwards, T. L.; Wheeler, D. R.; Xiao, X.; Brozik, S. M.; Polsky, R.; Narayan, R. J. Hollow Microneedle-Based Sensor for Multiplexed Transdermal Electrochemical Sensing. *J. Vis. Exp. JoVE* **2012**, No. 64, 4067.
<https://doi.org/10.3791/4067>.
- (302) Samant, P. P.; Prausnitz, M. R. Mechanisms of Sampling Interstitial Fluid from Skin Using a Microneedle Patch. *Proc. Natl. Acad. Sci.* **2018**, *115* (18), 4583–4588.
<https://doi.org/10.1073/pnas.1716772115>.
- (303) Bollella, P.; Sharma, S.; Cass, A. E. G.; Antiochia, R. Microneedle-Based Biosensor for Minimally-Invasive Lactate Detection. *Biosens. Bioelectron.* **2019**, *123*, 152–159.
<https://doi.org/10.1016/j.bios.2018.08.010>.
- (304) Li, J.; Lu, H.; Wang, Y.; Yang, S.; Zhang, Y.; Wei, W.; Qiao, Y.; Dai, W.; Ge, R.; Dong, H. Interstitial Fluid Biomarkers' Minimally Invasive Monitoring Using Microneedle Sensor Arrays. *Anal. Chem.* **2022**, *94* (2), 968–974.
<https://doi.org/10.1021/acs.analchem.1c03827>.
- (305) Mitragotri, S.; Coleman, M.; Kost, J.; Langer, R. Analysis of Ultrasonically Extracted Interstitial Fluid as a Predictor of Blood Glucose Levels. *J. Appl. Physiol.* **2000**, *89* (3), 961–966. <https://doi.org/10.1152/jappl.2000.89.3.961>.
- (306) Lee, H.; Choi, T. K.; Lee, Y. B.; Cho, H. R.; Ghaffari, R.; Wang, L.; Choi, H. J.; Chung, T. D.; Lu, N.; Hyeon, T.; Choi, S. H.; Kim, D.-H. A Graphene-Based Electrochemical Device with Thermoresponsive Microneedles for Diabetes Monitoring and Therapy. *Nat. Nanotechnol.* **2016**, *11* (6), 566–572. <https://doi.org/10.1038/nnano.2016.38>.
- (307) Green, A.; Dodds, P.; Pennock, C. A Study of Sweat Sodium and Chloride; Criteria for the Diagnosis of Cystic Fibrosis. *Ann. Clin. Biochem.* **1985**, *22* (2), 171–174.
<https://doi.org/10.1177/000456328502200212>.
- (308) Torrente-Rodríguez, R. M.; Tu, J.; Yang, Y.; Min, J.; Wang, M.; Song, Y.; Yu, Y.; Xu, C.; Ye, C.; IsHak, W. W.; Gao, W. Investigation of Cortisol Dynamics in Human Sweat Using a Graphene-Based Wireless mHealth System. *Matter* **2020**, *2* (4), 921–937.
<https://doi.org/10.1016/j.matt.2020.01.021>.
- (309) Kim, J.; Sempionatto, J. R.; Imani, S.; Hartel, M. C.; Barfidokht, A.; Tang, G.; Campbell, A. S.; Mercier, P. P.; Wang, J. Simultaneous Monitoring of Sweat and Interstitial Fluid Using a Single Wearable Biosensor Platform. *Adv. Sci.* **2018**, *5* (10), 1800880.
<https://doi.org/10.1002/advs.201800880>.
- (310) Gao, W.; Emaminejad, S.; Nyein, H. Y. Y.; Challa, S.; Chen, K.; Peck, A.; Fahad, H. M.; Ota, H.; Shiraki, H.; Kiriya, D.; Lien, D.-H.; Brooks, G. A.; Davis, R. W.; Javey, A. Fully Integrated Wearable Sensor Arrays for Multiplexed in Situ Perspiration Analysis. *Nature* **2016**, *529* (7587), 509–514. <https://doi.org/10.1038/nature16521>.
- (311) Rose, D. P.; Ratterman, M. E.; Griffin, D. K.; Hou, L.; Kelley-Loughnane, N.; Naik, R. R.; Hagen, J. A.; Papautsky, I.; Heikenfeld, J. C. Adhesive RFID Sensor Patch for Monitoring of Sweat Electrolytes. *IEEE Trans. Biomed. Eng.* **2015**, *62* (6), 1457–1465.
<https://doi.org/10.1109/TBME.2014.2369991>.

- (312) Hansen, D.; Zajforoushan Moghaddam, S.; Eiler, J.; Hansen, K.; Thormann, E. Performance of Polymeric Skin Adhesives during Perspiration. *ACS Appl. Polym. Mater.* **2020**, *2* (4), 1535–1542. <https://doi.org/10.1021/acsapm.9b01214>.
- (313) Nyein, H. Y. Y.; Tai, L.-C.; Ngo, Q. P.; Chao, M.; Zhang, G. B.; Gao, W.; Bariya, M.; Bullock, J.; Kim, H.; Fahad, H. M.; Javey, A. A Wearable Microfluidic Sensing Patch for Dynamic Sweat Secretion Analysis. *ACS Sens.* **2018**, *3* (5), 944–952. <https://doi.org/10.1021/acssensors.7b00961>.
- (314) Miyamoto, A.; Lee, S.; Cooray, N. F.; Lee, S.; Mori, M.; Matsuhisa, N.; Jin, H.; Yoda, L.; Yokota, T.; Itoh, A.; Sekino, M.; Kawasaki, H.; Ebihara, T.; Amagai, M.; Someya, T. Inflammation-Free, Gas-Permeable, Lightweight, Stretchable on-Skin Electronics with Nanomeshes. *Nat. Nanotechnol.* **2017**, *12* (9), 907–913. <https://doi.org/10.1038/nnano.2017.125>.
- (315) Yang, X.; Li, L.; Wang, S.; Lu, Q.; Bai, Y.; Sun, F.; Li, T.; Li, Y.; Wang, Z.; Zhao, Y.; Shi, Y.; Zhang, T. Ultrathin, Stretchable, and Breathable Epidermal Electronics Based on a Facile Bubble Blowing Method. *Adv. Electron. Mater.* **2020**, *6* (11), 2000306. <https://doi.org/10.1002/aelm.202000306>.
- (316) Min, H.; Baik, S.; Kim, J.; Lee, J.; Bok, B.-G.; Song, J. H.; Kim, M.-S.; Pang, C. Tough Carbon Nanotube-Implanted Bioinspired Three-Dimensional Electrical Adhesive for Isotropically Stretchable Water-Repellent Bioelectronics. *Adv. Funct. Mater.* **2022**, *32* (8), 2107285. <https://doi.org/10.1002/adfm.202107285>.
- (317) Bollella, P.; Sharma, S.; Cass, A. E. G.; Tasca, F.; Antiochia, R. Minimally Invasive Glucose Monitoring Using a Highly Porous Gold Microneedles-Based Biosensor: Characterization and Application in Artificial Interstitial Fluid. *Catalysts* **2019**, *9* (7), 580. <https://doi.org/10.3390/catal9070580>.
- (318) Madden, J.; O'Mahony, C.; Thompson, M.; O'Riordan, A.; Galvin, P. Biosensing in Dermal Interstitial Fluid Using Microneedle Based Electrochemical Devices. *Sens. Bio-Sens. Res.* **2020**, *29*, 100348. <https://doi.org/10.1016/j.sbsr.2020.100348>.
- (319) Yi, K.; Wang, Y.; Shi, K.; Chi, J.; Lyu, J.; Zhao, Y. Aptamer-Decorated Porous Microneedles Arrays for Extraction and Detection of Skin Interstitial Fluid Biomarkers. *Biosens. Bioelectron.* **2021**, *190*, 113404. <https://doi.org/10.1016/j.bios.2021.113404>.
- (320) Kaufman, E.; Lamster, I. B. Analysis of Saliva for Periodontal Diagnosis. *J. Clin. Periodontol.* **2000**, *27* (7), 453–465. <https://doi.org/10.1034/j.1600-051x.2000.027007453.x>.
- (321) Pfafe, T.; Cooper-White, J.; Beyerlein, P.; Kostner, K.; Punyadeera, C. Diagnostic Potential of Saliva: Current State and Future Applications. *Clin. Chem.* **2011**, *57* (5), 675–687. <https://doi.org/10.1373/clinchem.2010.153767>.
- (322) Lee, Y.-H.; Wong, D. T. Saliva: An Emerging Biofluid for Early Detection of Diseases. *Am. J. Dent.* **2009**, *22* (4), 241–248.
- (323) Kim, J.; Valdés-Ramírez, G.; Bandodkar, A. J.; Jia, W.; Martinez, A. G.; Ramírez, J.; Mercier, P.; Wang, J. Non-Invasive Mouthguard Biosensor for Continuous Salivary Monitoring of Metabolites. *Analyst* **2014**, *139* (7), 1632–1636. <https://doi.org/10.1039/C3AN02359A>.
- (324) Kim, J.; Imani, S.; de Araujo, W. R.; Warchall, J.; Valdés-Ramírez, G.; Paixão, T. R. L. C.; Mercier, P. P.; Wang, J. Wearable Salivary Uric Acid Mouthguard Biosensor with Integrated Wireless Electronics. *Biosens. Bioelectron.* **2015**, *74*, 1061–1068. <https://doi.org/10.1016/j.bios.2015.07.039>.

- (325) Arakawa, T.; Kuroki, Y.; Nitta, H.; Chouhan, P.; Toma, K.; Sawada, S.; Takeuchi, S.; Sekita, T.; Akiyoshi, K.; Minakuchi, S.; Mitsubayashi, K. Mouthguard Biosensor with Telemetry System for Monitoring of Saliva Glucose: A Novel Cavitas Sensor. *Biosens. Bioelectron.* **2016**, *84*, 106–111. <https://doi.org/10.1016/j.bios.2015.12.014>.
- (326) Perdigão, J.; Frankenberger, R.; Rosa, B. T.; Breschi, L. New Trends in Dentin/Enamel Adhesion. *Am. J. Dent.* **2000**, *13* (Spec No), 25D-30D.
- (327) Matsunaga, S.; Tamura, A.; Fushimi, M.; Santa, H.; Arisaka, Y.; Nikaido, T.; Tagami, J.; Yui, N. Light-Embrittled Dental Resin Cements Containing Photodegradable Polyrotaxane Cross-Linkers for Attenuating Debonding Strength. *ACS Appl. Polym. Mater.* **2020**, *2* (12), 5756–5766. <https://doi.org/10.1021/acsapm.0c01024>.
- (328) Hu, S.; Pei, X.; Duan, L.; Zhu, Z.; Liu, Y.; Chen, J.; Chen, T.; Ji, P.; Wan, Q.; Wang, J. A Mussel-Inspired Film for Adhesion to Wet Buccal Tissue and Efficient Buccal Drug Delivery. *Nat. Commun.* **2021**, *12* (1), 1689. <https://doi.org/10.1038/s41467-021-21989-5>.
- (329) Zhu, T.; Yu, X.; Yi, X.; Guo, X.; Li, L.; Hao, Y.; Wang, W. Lidocaine-Loaded Hyaluronic Acid Adhesive Microneedle Patch for Oral Mucosal Topical Anesthesia. *Pharmaceutics* **2022**, *14* (4), 686. <https://doi.org/10.3390/pharmaceutics14040686>.
- (330) Caffarel-Salvador, E.; Kim, S.; Soares, V.; Tian, R. Y.; Stern, S. R.; Minahan, D.; Yona, R.; Lu, X.; Zakaria, F. R.; Collins, J.; Wainer, J.; Wong, J.; McManus, R.; Tamang, S.; McDonnell, S.; Ishida, K.; Hayward, A.; Liu, X.; Hubálek, F.; Fels, J.; Vegge, A.; Frederiksen, M. R.; Rahbek, U.; Yoshitake, T.; Fujimoto, J.; Roxhed, N.; Langer, R.; Traverso, G. A Microneedle Platform for Buccal Macromolecule Delivery. *Sci. Adv.* **2021**, *7* (4), eabe2620. <https://doi.org/10.1126/sciadv.abe2620>.
- (331) Hagan, S.; Martin, E.; Enríquez-de-Salamanca, A. Tear Fluid Biomarkers in Ocular and Systemic Disease: Potential Use for Predictive, Preventive and Personalised Medicine. *EPMA J.* **2016**, *7* (1), 15. <https://doi.org/10.1186/s13167-016-0065-3>.
- (332) Yu, L.; Yang, Z.; An, M. Lab on the Eye: A Review of Tear-Based Wearable Devices for Medical Use and Health Management. *Biosci. Trends* **2019**, *13* (4), 308–313. <https://doi.org/10.5582/bst.2019.01178>.
- (333) Sempionatto, J. R.; Brazaca, L. C.; García-Carmona, L.; Bolat, G.; Campbell, A. S.; Martin, A.; Tang, G.; Shah, R.; Mishra, R. K.; Kim, J.; Zucolotto, V.; Escarpa, A.; Wang, J. Eyeglasses-Based Tear Biosensing System: Non-Invasive Detection of Alcohol, Vitamins and Glucose. *Biosens. Bioelectron.* **2019**, *137*, 161–170. <https://doi.org/10.1016/j.bios.2019.04.058>.
- (334) Xu, J.; Tao, X.; Liu, X.; Yang, L. Wearable Eye Patch Biosensor for Noninvasive and Simultaneous Detection of Multiple Biomarkers in Human Tears. *Anal. Chem.* **2022**, *94* (24), 8659–8667. <https://doi.org/10.1021/acs.analchem.2c00614>.
- (335) Hayashi, T. T.; Fatt, I. Forces Retaining a Contact Lens on the Eye between Blinks. *Am. J. Optom. Physiol. Opt.* **1980**, *57* (8), 485–507. <https://doi.org/10.1097/00006324-198008000-00003>.
- (336) Musgrave, C. S. A.; Fang, F. Contact Lens Materials: A Materials Science Perspective. *Materials* **2019**, *12* (2), 261. <https://doi.org/10.3390/ma12020261>.
- (337) Farandos, N. M.; Yetisen, A. K.; Monteiro, M. J.; Lowe, C. R.; Yun, S. H. Contact Lens Sensors in Ocular Diagnostics. *Adv. Healthc. Mater.* **2015**, *4* (6), 792–810. <https://doi.org/10.1002/adhm.201400504>.

- (338) Yao, H.; Shum, A. J.; Cowan, M.; Lähdesmäki, I.; Parviz, B. A. A Contact Lens with Embedded Sensor for Monitoring Tear Glucose Level. *Biosens. Bioelectron.* **2011**, *26* (7), 3290–3296. <https://doi.org/10.1016/j.bios.2010.12.042>.
- (339) Ascaso, F. J.; Huerva, V. Noninvasive Continuous Monitoring of Tear Glucose Using Glucose-Sensing Contact Lenses. *Optom. Vis. Sci.* **2016**, *93* (4), 426. <https://doi.org/10.1097/OPX.0000000000000698>.
- (340) Yao, H.; Liao, Y.; Lingley, A. R.; Afanasiev, A.; Lähdesmäki, I.; Otis, B. P.; Parviz, B. A. A Contact Lens with Integrated Telecommunication Circuit and Sensors for Wireless and Continuous Tear Glucose Monitoring. *J. Micromechanics Microengineering* **2012**, *22* (7), 075007. <https://doi.org/10.1088/0960-1317/22/7/075007>.
- (341) Kim, J.; Kim, M.; Lee, M.-S.; Kim, K.; Ji, S.; Kim, Y.-T.; Park, J.; Na, K.; Bae, K.-H.; Kyun Kim, H.; Bien, F.; Young Lee, C.; Park, J.-U. Wearable Smart Sensor Systems Integrated on Soft Contact Lenses for Wireless Ocular Diagnostics. *Nat. Commun.* **2017**, *8* (1), 14997. <https://doi.org/10.1038/ncomms14997>.
- (342) Park, J.; Kim, J.; Kim, S.-Y.; Cheong, W. H.; Jang, J.; Park, Y.-G.; Na, K.; Kim, Y.-T.; Heo, J. H.; Lee, C. Y.; Lee, J. H.; Bien, F.; Park, J.-U. Soft, Smart Contact Lenses with Integrations of Wireless Circuits, Glucose Sensors, and Displays. *Sci. Adv.* **2018**, *4* (1), eaap9841. <https://doi.org/10.1126/sciadv.aap9841>.
- (343) Xie, M.; Yao, G.; Zhang, T.; Wang, Q.; Mo, X.; Dong, Q.; Lou, W.; Lu, F.; Pan, T.; Gao, M.; Jiang, D.; Zhao, K.; Lin, Y. Multifunctional Flexible Contact Lens for Eye Health Monitoring Using Inorganic Magnetic Oxide Nanosheets. *J. Nanobiotechnology* **2022**, *20* (1), 202. <https://doi.org/10.1186/s12951-022-01415-8>.
- (344) Senior, M. Novartis Signs up for Google Smart Lens. *Nat. Biotechnol.* **2014**, *32* (9), 856–856. <https://doi.org/10.1038/nbt0914-856>.
- (345) Yang, X.; Yao, H.; Zhao, G.; Ameer, G. A.; Sun, W.; Yang, J.; Mi, S. Flexible, Wearable Microfluidic Contact Lens with Capillary Networks for Tear Diagnostics. *J. Mater. Sci.* **2020**, *55* (22), 9551–9561. <https://doi.org/10.1007/s10853-020-04688-2>.
- (346) Langer, R. Drug Delivery and Targeting. *Nature* **1998**, *392* (6679 Suppl), 5–10.
- (347) Graham, N. B.; McNeill, M. E. Hydrogels for Controlled Drug Delivery. *Biomaterials* **1984**, *5* (1), 27–36. [https://doi.org/10.1016/0142-9612\(84\)90063-2](https://doi.org/10.1016/0142-9612(84)90063-2).
- (348) Qiu, Y.; Park, K. Environment-Sensitive Hydrogels for Drug Delivery. *Adv. Drug Deliv. Rev.* **2001**, *53* (3), 321–339. [https://doi.org/10.1016/S0169-409X\(01\)00203-4](https://doi.org/10.1016/S0169-409X(01)00203-4).
- (349) Bhattarai, N.; Gunn, J.; Zhang, M. Chitosan-Based Hydrogels for Controlled, Localized Drug Delivery. *Adv. Drug Deliv. Rev.* **2010**, *62* (1), 83–99. <https://doi.org/10.1016/j.addr.2009.07.019>.
- (350) Xu, J.; Strandman, S.; Zhu, J. X. X.; Barralet, J.; Cerruti, M. Genipin-Crosslinked Catechol-Chitosan Mucoadhesive Hydrogels for Buccal Drug Delivery. *Biomaterials* **2015**, *37*, 395–404. <https://doi.org/10.1016/j.biomaterials.2014.10.024>.
- (351) das Neves, J.; Bahia, M. F. Gels as Vaginal Drug Delivery Systems. *Int. J. Pharm.* **2006**, *318* (1), 1–14. <https://doi.org/10.1016/j.ijpharm.2006.03.012>.
- (352) Mirani, B.; Pagan, E.; Currie, B.; Siddiqui, M. A.; Hosseinzadeh, R.; Mostafalu, P.; Zhang, Y. S.; Ghahary, A.; Akbari, M. An Advanced Multifunctional Hydrogel-Based Dressing for Wound Monitoring and Drug Delivery. *Adv. Healthc. Mater.* **2017**, *6* (19), 1700718. <https://doi.org/10.1002/adhm.201700718>.

- (353) Livnat, M.; Beyar, R.; Seliktar, D. Endoluminal Hydrogel Films Made of Alginate and Polyethylene Glycol: Physical Characteristics and Drug-Eluting Properties. *J. Biomed. Mater. Res. A* **2005**, *75A* (3), 710–722. <https://doi.org/10.1002/jbm.a.30474>.
- (354) Alvarez-Lorenzo, C.; Anguiano-Igea, S.; Varela-García, A.; Vivero-Lopez, M.; Concheiro, A. Bioinspired Hydrogels for Drug-Eluting Contact Lenses. *Acta Biomater.* **2019**, *84*, 49–62. <https://doi.org/10.1016/j.actbio.2018.11.020>.
- (355) Kim, Y. E.; Jung, H. Y.; Park, N.; Kim, J. Adhesive Composite Hydrogel Patch for Sustained Transdermal Drug Delivery To Treat Atopic Dermatitis. *Chem. Mater.* **2023**, *35* (3), 1209–1217. <https://doi.org/10.1021/acs.chemmater.2c03234>.
- (356) Chen, J.; Wang, D.; Wang, L.-H.; Liu, W.; Chiu, A.; Shariati, K.; Liu, Q.; Wang, X.; Zhong, Z.; Webb, J.; Schwartz, R. E.; Bouklas, N.; Ma, M. An Adhesive Hydrogel with “Load-Sharing” Effect as Tissue Bandages for Drug and Cell Delivery. *Adv. Mater.* **2020**, *32* (43), 2001628. <https://doi.org/10.1002/adma.202001628>.
- (357) Wright, Z. M.; Holt, B. D.; Sydlik, S. A. Covalently-Controlled Drug Delivery via Therapeutic Methacrylic Tissue Adhesives. *J. Mater. Chem. B* **2017**, *5* (37), 7743–7755. <https://doi.org/10.1039/C7TB01151B>.
- (358) Kakinoki, S.; Taguchi, T. Antitumor Effect of an Injectable In-Situ Forming Drug Delivery System Composed of a Novel Tissue Adhesive Containing Doxorubicin Hydrochloride. *Eur. J. Pharm. Biopharm.* **2007**, *67* (3), 676–681. <https://doi.org/10.1016/j.ejpb.2007.03.020>.
- (359) Lurtz, C.; Voss, K.; Hahn, V.; Schauer, F.; Wegmann, J.; Odermatt, E. K.; Schmitz, K.-P.; Sternberg, K. In Vitro Degradation and Drug Release of a Biodegradable Tissue Adhesive Based on Functionalized 1,2-Ethylene Glycol Bis(Dilactic Acid) and Chitosan. *J. Mater. Sci. Mater. Med.* **2013**, *24* (3), 667–678. <https://doi.org/10.1007/s10856-012-4826-9>.
- (360) Zhang, M.; An, H.; Gu, Z.; Huang, Z.; Zhang, F.; Wen, Y.; Zhang, P. Mimosa-Inspired Stimuli-Responsive Curling Bioadhesive Tape Promotes Peripheral Nerve Regeneration. *Adv. Mater.* *n/a* (n/a), 2212015. <https://doi.org/10.1002/adma.202212015>.
- (361) Freedman, B. R.; Kuttler, A.; Beckmann, N.; Nam, S.; Kent, D.; Schuleit, M.; Ramazani, F.; Accart, N.; Rock, A.; Li, J.; Kurz, M.; Fisch, A.; Ullrich, T.; Hast, M. W.; Tinguely, Y.; Weber, E.; Mooney, D. J. Enhanced Tendon Healing by a Tough Hydrogel with an Adhesive Side and High Drug-Loading Capacity. *Nat. Biomed. Eng.* **2022**, *6* (10), 1167–1179. <https://doi.org/10.1038/s41551-021-00810-0>.
- (362) Li, J.; Mooney, D. J. Designing Hydrogels for Controlled Drug Delivery. *Nat. Rev. Mater.* **2016**, *1* (12), 1–17. <https://doi.org/10.1038/natrevmats.2016.71>.
- (363) Lin, C.-C.; Metters, A. T. Hydrogels in Controlled Release Formulations: Network Design and Mathematical Modeling. *Adv. Drug Deliv. Rev.* **2006**, *58* (12), 1379–1408. <https://doi.org/10.1016/j.addr.2006.09.004>.
- (364) Bagherifard, S.; Tamayol, A.; Mostafalu, P.; Akbari, M.; Comotto, M.; Annabi, N.; Ghaderi, M.; Sonkusale, S.; Dokmeci, M. R.; Khademhosseini, A. Dermal Patch with Integrated Flexible Heater for on Demand Drug Delivery. *Adv. Healthc. Mater.* **2016**, *5* (1), 175–184. <https://doi.org/10.1002/adhm.201500357>.
- (365) Lee, J. W.; Park, J.-H.; Prausnitz, M. R. Dissolving Microneedles for Transdermal Drug Delivery. *Biomaterials* **2008**, *29* (13), 2113–2124. <https://doi.org/10.1016/j.biomaterials.2007.12.048>.

- (366) Daly, A. C.; Riley, L.; Segura, T.; Burdick, J. A. Hydrogel Microparticles for Biomedical Applications. *Nat. Rev. Mater.* **2020**, *5* (1), 20–43. <https://doi.org/10.1038/s41578-019-0148-6>.
- (367) Liu, W.; Wang, Y.; Wang, J.; Lanier, O. L.; Wechsler, M. E.; Peppas, N. A.; Gu, Z. Macroencapsulation Devices for Cell Therapy. *Engineering* **2022**, *13*, 53–70. <https://doi.org/10.1016/j.eng.2021.10.021>.
- (368) Orive, G.; Santos, E.; Poncelet, D.; Hernández, R. M.; Pedraz, J. L.; Wahlberg, L. U.; De Vos, P.; Emerich, D. Cell Encapsulation: Technical and Clinical Advances. *Trends Pharmacol. Sci.* **2015**, *36* (8), 537–546. <https://doi.org/10.1016/j.tips.2015.05.003>.
- (369) Song, S.; Roy, S. Progress and Challenges in Macroencapsulation Approaches for Type 1 Diabetes (T1D) Treatment: Cells, Biomaterials, and Devices. *Biotechnol. Bioeng.* **2016**, *113* (7), 1381–1402. <https://doi.org/10.1002/bit.25895>.
- (370) Wang, L.-H.; Ernst, A. U.; An, D.; Datta, A. K.; Epel, B.; Kotecha, M.; Ma, M. A Bioinspired Scaffold for Rapid Oxygenation of Cell Encapsulation Systems. *Nat. Commun.* **2021**, *12* (1), 5846. <https://doi.org/10.1038/s41467-021-26126-w>.
- (371) Yun, S. H.; Kwok, S. J. J. Light in Diagnosis, Therapy and Surgery. *Nat. Biomed. Eng.* **2017**, *1*, 0008. <https://doi.org/10.1038/s41551-016-0008>.
- (372) Lee, G.-H.; Moon, H.; Kim, H.; Lee, G. H.; Kwon, W.; Yoo, S.; Myung, D.; Yun, S. H.; Bao, Z.; Hahn, S. K. Multifunctional Materials for Implantable and Wearable Photonic Healthcare Devices. *Nat. Rev. Mater.* **2020**, *5* (2), 149–165. <https://doi.org/10.1038/s41578-019-0167-3>.
- (373) Zhi, D.; Yang, T.; O'Hagan, J.; Zhang, S.; Donnelly, R. F. Photothermal Therapy. *J. Controlled Release* **2020**, *325*, 52–71. <https://doi.org/10.1016/j.jconrel.2020.06.032>.
- (374) Huang, X.; Jain, P. K.; El-Sayed, I. H.; El-Sayed, M. A. Plasmonic Photothermal Therapy (PPTT) Using Gold Nanoparticles. *Lasers Med. Sci.* **2008**, *23* (3), 217–228. <https://doi.org/10.1007/s10103-007-0470-x>.
- (375) Dolmans, D. E. J. G. J.; Fukumura, D.; Jain, R. K. Photodynamic Therapy for Cancer. *Nat. Rev. Cancer* **2003**, *3* (5), 380–387. <https://doi.org/10.1038/nrc1071>.
- (376) Ong, F. L. L.; Loh, C. H.; Oh, C. C. Wearable Devices for Photodynamic Therapy – A Systematic Review. *JAAD Int.* **2023**, *11*, 59–62. <https://doi.org/10.1016/j.jdin.2023.01.010>.
- (377) Hamblin, M. R. Mechanisms and Applications of the Anti-Inflammatory Effects of Photobiomodulation. *AIMS Biophys.* **2017**, *4* (3), 337–361. <https://doi.org/10.3934/biophys.2017.3.337>.
- (378) Williams, J. C.; Denison, T. From Optogenetic Technologies to Neuromodulation Therapies. *Sci. Transl. Med.* **2013**, *5* (177), 177ps6-177ps6. <https://doi.org/10.1126/scitranslmed.3003100>.
- (379) Pan, J.; Zhang, Z.; Jiang, C.; Zhang, L.; Tong, L. A Multifunctional Skin-like Wearable Optical Sensor Based on an Optical Micro-/Nanofibre. *Nanoscale* **2020**, *12* (33), 17538–17544. <https://doi.org/10.1039/D0NR03446K>.
- (380) Tariq, R.; Khalid, U. A.; Kanwal, S.; Adnan, F.; Qasim, M. Photodynamic Therapy: A Rational Approach Toward COVID-19 Management. *J. Explor. Res. Pharmacol.* **2021**, *6* (2), 44–52. <https://doi.org/10.14218/JERP.2020.00036>.
- (381) Park, S. I.; Brenner, D. S.; Shin, G.; Morgan, C. D.; Copits, B. A.; Chung, H. U.; Pullen, M. Y.; Noh, K. N.; Davidson, S.; Oh, S. J.; Yoon, J.; Jang, K.-I.; Samineni, V. K.; Norman, M.; Grajales-Reyes, J. G.; Vogt, S. K.; Sundaram, S. S.; Wilson, K. M.; Ha, J. S.;

- Xu, R.; Pan, T.; Kim, T.; Huang, Y.; Montana, M. C.; Golden, J. P.; Bruchas, M. R.; Gereau, R. W.; Rogers, J. A. Soft, Stretchable, Fully Implantable Miniaturized Optoelectronic Systems for Wireless Optogenetics. *Nat. Biotechnol.* **2015**, *33* (12), 1280–1286. <https://doi.org/10.1038/nbt.3415>.
- (382) Nizamoglu, S.; Gather, M. C.; Humar, M.; Choi, M.; Kim, S.; Kim, K. S.; Hahn, S. K.; Scarcelli, G.; Randolph, M.; Redmond, R. W.; Yun, S. H. Bioabsorbable Polymer Optical Waveguides for Deep-Tissue Photomedicine. *Nat. Commun.* **2016**, *7* (1), 10374. <https://doi.org/10.1038/ncomms10374>.
- (383) Parker, S. T.; Domachuk, P.; Amsden, J.; Bressner, J.; Lewis, J. A.; Kaplan, D. L.; Omenetto, F. G. Biocompatible Silk Printed Optical Waveguides. *Adv. Mater.* **2009**, *21* (23), 2411–2415. <https://doi.org/10.1002/adma.200801580>.
- (384) Shan, D.; Zhang, C.; Kalaba, S.; Mehta, N.; Kim, G. B.; Liu, Z.; Yang, J. Flexible Biodegradable Citrate-Based Polymeric Step-Index Optical Fiber. *Biomaterials* **2017**, *143*, 142–148. <https://doi.org/10.1016/j.biomaterials.2017.08.003>.
- (385) Dupuis, A.; Guo, N.; Gao, Y.; Godbout, N.; Lacroix, S.; Dubois, C.; Skorobogatiy, M. Prospective for Biodegradable Microstructured Optical Fibers. *Opt. Lett.* **2007**, *32* (2), 109–111. <https://doi.org/10.1364/OL.32.000109>.
- (386) Feng, J.; Zheng, Y.; Bhusari, S.; Villiou, M.; Pearson, S.; Campo, A. del. Printed Degradable Optical Waveguides for Guiding Light into Tissue. *Adv. Funct. Mater.* **2020**, *30* (45), 2004327. <https://doi.org/10.1002/adfm.202004327>.
- (387) Chen, G.; Hou, K.; Yu, N.; Wei, P.; Chen, T.; Zhang, C.; Wang, S.; Liu, H.; Cao, R.; Zhu, L.; Hsiao, B. S.; Zhu, M. Temperature-Adaptive Hydrogel Optical Waveguide with Soft Tissue-Affinity for Thermal Regulated Interventional Photomedicine. *Nat. Commun.* **2022**, *13* (1), 7789. <https://doi.org/10.1038/s41467-022-35440-w>.
- (388) Jeong, S.-H.; Lee, M.-G.; Kim, C.-C.; Park, J.; Baek, Y.; Park, B. I.; Doh, J.; Sun, J.-Y. An Implantable Ionic Therapeutic Platform for Photodynamic Therapy with Wireless Capacitive Power Transfer. *Mater. Horiz.* **2023**. <https://doi.org/10.1039/D2MH01548J>.
- (389) Jain, A.; Yang, A. H. J.; Erickson, D. Gel-Based Optical Waveguides with Live Cell Encapsulation and Integrated Microfluidics. *Opt. Lett.* **2012**, *37* (9), 1472–1474. <https://doi.org/10.1364/OL.37.001472>.
- (390) Missinne, J.; Kalathimekkad, S.; Hoe, B. V.; Bosman, E.; Vanfleteren, J.; Steenberge, G. V. Stretchable Optical Waveguides. *Opt. Express* **2014**, *22* (4), 4168–4179. <https://doi.org/10.1364/OE.22.004168>.
- (391) Sykes, E. A.; Albanese, A.; Chan, W. C. W. Implantable Waveguides. *Nat. Photonics* **2013**, *7* (12), 940–941. <https://doi.org/10.1038/nphoton.2013.308>.
- (392) Kinsey, J. H.; Cortese, D. A.; Neel, H. B. Thermal Considerations in Murine Tumor Killing Using Hematoporphyrin Derivative Phototherapy. *Cancer Res.* **1983**, *43* (4), 1562–1567.
- (393) Horimatsu, T.; Muto, M.; Yoda, Y.; Yano, T.; Ezoe, Y.; Miyamoto, S.; Chiba, T. Tissue Damage in the Canine Normal Esophagus by Photoactivation with Talaporfin Sodium (Laserphyrin): A Preclinical Study. *PLOS ONE* **2012**, *7* (6), e38308. <https://doi.org/10.1371/journal.pone.0038308>.
- (394) Lin, Y.; Bilotti, E.; Bastiaansen, C. W. M.; Peijs, T. Transparent Semi-Crystalline Polymeric Materials and Their Nanocomposites: A Review. *Polym. Eng. Sci.* **2020**, *60* (10), 2351–2376. <https://doi.org/10.1002/pen.25489>.

- (395) Althues, H.; Henle, J.; Kaskel, S. Functional Inorganic Nanofillers for Transparent Polymers. *Chem. Soc. Rev.* **2007**, *36* (9), 1454. <https://doi.org/10.1039/b608177k>.
- (396) Tummala, G. K.; Rojas, R.; Mihranyan, A. Poly(Vinyl Alcohol) Hydrogels Reinforced with Nanocellulose for Ophthalmic Applications: General Characteristics and Optical Properties. *J. Phys. Chem. B* **2016**, *120* (51), 13094–13101. <https://doi.org/10.1021/acs.jpcc.6b10650>.
- (397) Takeoka, Y.; Asai, F.; Gao, G.; He, J.; Liu, S. Transparent and Mechanically High-Performance Soft Materials Consisting of Colloidal Building Blocks. *Acc. Mater. Res.* **2022**, *3* (8), 799–811. <https://doi.org/10.1021/accounts.2c00059>.
- (398) Protopappas, V. C.; Baga, D. A.; Fotiadis, D. I.; Likas, A. C.; Papachristos, A. A.; Malizos, K. N. An Ultrasound Wearable System for the Monitoring and Acceleration of Fracture Healing in Long Bones. *IEEE Trans. Biomed. Eng.* **2005**, *52* (9), 1597–1608. <https://doi.org/10.1109/TBME.2005.851507>.
- (399) Yang, X.; Chen, Z.; Hettiarachchi, N.; Yan, J.; Liu, H. A Wearable Ultrasound System for Sensing Muscular Morphological Deformations. *IEEE Trans. Syst. Man Cybern. Syst.* **2021**, *51* (6), 3370–3379. <https://doi.org/10.1109/TSMC.2019.2924984>.
- (400) Kenny, J.-É. S. Functional Hemodynamic Monitoring With a Wireless Ultrasound Patch. *J. Cardiothorac. Vasc. Anesth.* **2021**, *35* (5), 1509–1515. <https://doi.org/10.1053/j.jvca.2021.01.040>.
- (401) Wang, C.; Qi, B.; Lin, M.; Zhang, Z.; Makihata, M.; Liu, B.; Zhou, S.; Huang, Y.; Hu, H.; Gu, Y.; Chen, Y.; Lei, Y.; Lee, T.; Chien, S.; Jang, K.-I.; Kistler, E. B.; Xu, S. Continuous Monitoring of Deep-Tissue Haemodynamics with Stretchable Ultrasonic Phased Arrays. *Nat. Biomed. Eng.* **2021**, *5* (7), 749–758. <https://doi.org/10.1038/s41551-021-00763-4>.
- (402) Hu, H.; Huang, H.; Li, M.; Gao, X.; Yin, L.; Qi, R.; Wu, R. S.; Chen, X.; Ma, Y.; Shi, K.; Li, C.; Maus, T. M.; Huang, B.; Lu, C.; Lin, M.; Zhou, S.; Lou, Z.; Gu, Y.; Chen, Y.; Lei, Y.; Wang, X.; Wang, R.; Yue, W.; Yang, X.; Bian, Y.; Mu, J.; Park, G.; Xiang, S.; Cai, S.; Corey, P. W.; Wang, J.; Xu, S. A Wearable Cardiac Ultrasound Imager. *Nature* **2023**, *613* (7945), 667–675. <https://doi.org/10.1038/s41586-022-05498-z>.
- (403) Ginzler, E.; MacNEIL, R.; Ginzler, R.; Zuber, M.; Sinclair, A. N. Acoustic Properties of the Elastomeric Materials AqualeneTM and ACETM.
- (404) Mitragotri, S. Healing Sound: The Use of Ultrasound in Drug Delivery and Other Therapeutic Applications. *Nat. Rev. Drug Discov.* **2005**, *4* (3), 255–260. <https://doi.org/10.1038/nrd1662>.
- (405) Miller, D.; Smith, N.; Bailey, M.; Czarnota, G.; Hynynen, K.; Makin, I. Overview of Therapeutic Ultrasound Applications and Safety Considerations. *J. Ultrasound Med. Off. J. Am. Inst. Ultrasound Med.* **2012**, *31* (4), 623–634.
- (406) Winkler, S. L.; Urbisci, A. E.; Best, T. M. Sustained Acoustic Medicine for the Treatment of Musculoskeletal Injuries: A Systematic Review and Meta-Analysis. *BMC Sports Sci. Med. Rehabil.* **2021**, *13* (1), 159. <https://doi.org/10.1186/s13102-021-00383-0>.
- (407) Uddin, S. M. Z.; Komatsu, D. E.; Motyka, T.; Petterson, S. Low-Intensity Continuous Ultrasound Therapies—A Systematic Review of Current State-of-the-Art and Future Perspectives. *J. Clin. Med.* **2021**, *10* (12), 2698. <https://doi.org/10.3390/jcm10122698>.
- (408) Jarit, P.; Klyve, D.; Walters, R. Long Duration Sonophoresis of Diclofenac to Augment Rehabilitation of Common Musculoskeletal Injuries. *Glob. J. Orthop. Res.* **2023**, *4* (2), 584.

- (409) Yang, Y.; Yuan, J.; Field, R. L.; Ye, D.; Hu, Z.; Xu, K.; Xu, L.; Gong, Y.; Yue, Y.; Kravitz, A. V.; Bruchas, M. R.; Cui, J.; Brestoff, J. R.; Chen, H. Induction of a Torpor-like Hypothermic and Hypometabolic State in Rodents by Ultrasound. *Nat. Metab.* **2023**, 1–15. <https://doi.org/10.1038/s42255-023-00804-z>.
- (410) Wang See, C.; Kim, T.; Zhu, D. Hernia Mesh and Hernia Repair: A Review. *Eng. Regen.* **2020**, *1*, 19–33. <https://doi.org/10.1016/j.engreg.2020.05.002>.
- (411) Nguyen-Truong, M.; Li, Y. V.; Wang, Z. Mechanical Considerations of Electrospun Scaffolds for Myocardial Tissue and Regenerative Engineering. *Bioengineering* **2020**, *7* (4), 122. <https://doi.org/10.3390/bioengineering7040122>.
- (412) Beldi, G.; Wagner, M.; Bruegger, L. E.; Kurmann, A.; Candinas, D. Mesh Shrinkage and Pain in Laparoscopic Ventral Hernia Repair: A Randomized Clinical Trial Comparing Suture versus Tack Mesh Fixation. *Surg. Endosc.* **2011**, *25* (3), 749–755. <https://doi.org/10.1007/s00464-010-1246-0>.
- (413) Karahasanoglu, T.; Onur, E.; Baca, B.; Hamzaoglu, I.; Pekmezci, S.; Bolser, D. E.; Kilic, N.; Altug, T. Spiral Tacks May Contribute to Intra-Abdominal Adhesion Formation. *Surg. Today* **2004**, *34* (10), 860–864. <https://doi.org/10.1007/s00595-004-2831-4>.
- (414) Gungor, B.; Malazgirt, Z.; Topgül, K.; Gök, A.; Bilgin, M.; Yürüker, S. Comparative Evaluation of Adhesions to Intraperitoneally Placed Fixation Materials: A Laparoscopic Study in Rats. *Indian J. Surg.* **2010**, *72* (6), 475–480. <https://doi.org/10.1007/s12262-010-0168-3>.
- (415) Peach, G.; Tan, L. C. Small Bowel Obstruction and Perforation Due to a Displaced Spiral Tacker: A Rare Complication of Laparoscopic Inguinal Hernia Repair. *Hernia* **2008**, *12* (3), 303–305. <https://doi.org/10.1007/s10029-007-0289-1>.
- (416) Ben Yehuda, A.; Nyska, A.; Szold, A. Mesh Fixation Using Novel Bio-Adhesive Coating Compared to Tack Fixation for IPOM Hernia Repair: In Vivo Evaluation in a Porcine Model. *Surg. Endosc.* **2019**, *33* (7), 2364–2375. <https://doi.org/10.1007/s00464-019-06806-x>.
- (417) Lin, X.; Liu, Y.; Bai, A.; Cai, H.; Bai, Y.; Jiang, W.; Yang, H.; Wang, X.; Yang, L.; Sun, N.; Gao, H. A Viscoelastic Adhesive Epicardial Patch for Treating Myocardial Infarction. *Nat. Biomed. Eng.* **2019**, *3* (8), 632–643. <https://doi.org/10.1038/s41551-019-0380-9>.
- (418) Kuehlmann, B.; Bonham, C. A.; Zucal, I.; Prantl, L.; Gurtner, G. C. Mechanotransduction in Wound Healing and Fibrosis. *J. Clin. Med.* **2020**, *9* (5), 1423. <https://doi.org/10.3390/jcm9051423>.
- (419) Barnes, L. A.; Marshall, C. D.; Leavitt, T.; Hu, M. S.; Moore, A. L.; Gonzalez, J. G.; Longaker, M. T.; Gurtner, G. C. Mechanical Forces in Cutaneous Wound Healing: Emerging Therapies to Minimize Scar Formation. *Adv. Wound Care* **2018**, *7* (2), 47–56. <https://doi.org/10.1089/wound.2016.0709>.
- (420) Thompson, J. T.; Marks, M. W. Negative Pressure Wound Therapy. *Clin. Plast. Surg.* **2007**, *34* (4), 673–684. <https://doi.org/10.1016/j.cps.2007.07.005>.
- (421) Gurtner, G. C.; Werner, S.; Barrandon, Y.; Longaker, M. T. Wound Repair and Regeneration. *Nature* **2008**, *453* (7193), 314–321. <https://doi.org/10.1038/nature07039>.
- (422) Wong, V. W.; Beasley, B.; Zepeda, J.; Dauskardt, R. H.; Yock, P. G.; Longaker, M. T.; Gurtner, G. C. A Mechanomodulatory Device to Minimize Incisional Scar Formation. *Adv. Wound Care* **2013**, *2* (4), 185–194. <https://doi.org/10.1089/wound.2012.0396>.

- (423) Harn, H. I.-C.; Ogawa, R.; Hsu, C.-K.; Hughes, M. W.; Tang, M.-J.; Chuong, C.-M. The Tension Biology of Wound Healing. *Exp. Dermatol.* **2019**, *28* (4), 464–471. <https://doi.org/10.1111/exd.13460>.
- (424) Blacklow, S. O.; Li, J.; Freedman, B. R.; Zeidi, M.; Chen, C.; Mooney, D. J. Bioinspired Mechanically Active Adhesive Dressings to Accelerate Wound Closure. *Sci. Adv.* **2019**, *5* (7), eaaw3963. <https://doi.org/10.1126/sciadv.aaw3963>.
- (425) Dolan, E. B.; Varela, C. E.; Mendez, K.; Whyte, W.; Levey, R. E.; Robinson, S. T.; Maye, E.; O'Dwyer, J.; Beatty, R.; Rothman, A.; Fan, Y.; Hochstein, J.; Rothenbucher, S. E.; Wylie, R.; Starr, J. R.; Monaghan, M.; Dockery, P.; Duffy, G. P.; Roche, E. T. An Actuatable Soft Reservoir Modulates Host Foreign Body Response. *Sci. Robot.* **2019**, *4* (33), eaax7043. <https://doi.org/10.1126/scirobotics.aax7043>.
- (426) Whyte, W.; Goswami, D.; Wang, S. X.; Fan, Y.; Ward, N. A.; Levey, R. E.; Beatty, R.; Robinson, S. T.; Sheppard, D.; O'Connor, R.; Monahan, D. S.; Trask, L.; Mendez, K. L.; Varela, C. E.; Horvath, M. A.; Wylie, R.; O'Dwyer, J.; Domingo-Lopez, D. A.; Rothman, A. S.; Duffy, G. P.; Dolan, E. B.; Roche, E. T. Dynamic Actuation Enhances Transport and Extends Therapeutic Lifespan in an Implantable Drug Delivery Platform. *Nat. Commun.* **2022**, *13* (1), 4496. <https://doi.org/10.1038/s41467-022-32147-w>.
- (427) Seo, B. R.; Payne, C. J.; McNamara, S. L.; Freedman, B. R.; Kwee, B. J.; Nam, S.; de Lázaro, I.; Darnell, M.; Alvarez, J. T.; Dellacherie, M. O.; Vandenburg, H. H.; Walsh, C. J.; Mooney, D. J. Skeletal Muscle Regeneration with Robotic Actuation–Mediated Clearance of Neutrophils. *Sci. Transl. Med.* **2021**, *13* (614), eabe8868. <https://doi.org/10.1126/scitranslmed.abe8868>.
- (428) Kung, R. T. V.; Rosenberg, M. Heart Booster: A Pericardial Support Device. *Ann. Thorac. Surg.* **1999**, *68* (2), 764–767. [https://doi.org/10.1016/S0003-4975\(99\)00524-X](https://doi.org/10.1016/S0003-4975(99)00524-X).
- (429) Kwon, M. H.; Cevasco, M.; Schmitto, J. D.; Chen, F. Y. Ventricular Restraint Therapy for Heart Failure: A Review, Summary of State of the Art, and Future Directions. *J. Thorac. Cardiovasc. Surg.* **2012**, *144* (4), 771–777.e1. <https://doi.org/10.1016/j.jtcvs.2012.06.014>.
- (430) Payne, C. J.; Wamala, I.; Bautista-Salinas, D.; Saeed, M.; Van Story, D.; Thalhofer, T.; Horvath, M. A.; Abah, C.; del Nido, P. J.; Walsh, C. J.; Vasilyev, N. V. Soft Robotic Ventricular Assist Device with Septal Bracing for Therapy of Heart Failure. *Sci. Robot.* **2017**, *2* (12), eaan6736. <https://doi.org/10.1126/scirobotics.aan6736>.
- (431) Zrinscak, D.; Lorenzon, L.; Maselli, M.; Cianchetti, M. Soft Robotics for Physical Simulators, Artificial Organs and Implantable Assistive Devices. *Prog. Biomed. Eng.* **2023**, *5* (1), 012002. <https://doi.org/10.1088/2516-1091/acb57a>.
- (432) Yang, X.; An, C.; Liu, S.; Cheng, T.; Bunpetch, V.; Liu, Y.; Dong, S.; Li, S.; Zou, X.; Li, T.; Ouyang, H.; Wu, Z.; Yang, W. Soft Artificial Bladder Detrusor. *Adv. Healthc. Mater.* **2018**, *7* (6), 1701014. <https://doi.org/10.1002/adhm.201701014>.
- (433) Hu, L.; Bonnemain, J.; Saeed, M. Y.; Singh, M.; Quevedo Moreno, D.; Vasilyev, N. V.; Roche, E. T. An Implantable Soft Robotic Ventilator Augments Inspiration in a Pig Model of Respiratory Insufficiency. *Nat. Biomed. Eng.* **2023**, *7* (2), 110–123. <https://doi.org/10.1038/s41551-022-00971-6>.
- (434) Roche, E. T.; Horvath, M. A.; Wamala, I.; Alazmani, A.; Song, S.-E.; Whyte, W.; Machaidze, Z.; Payne, C. J.; Weaver, J. C.; Fishbein, G.; Kuebler, J.; Vasilyev, N. V.; Mooney, D. J.; Pigula, F. A.; Walsh, C. J. Soft Robotic Sleeve Supports Heart Function. *Sci. Transl. Med.* **2017**, *9* (373), eaaf3925. <https://doi.org/10.1126/scitranslmed.aaf3925>.

- (435) Horvath, M. A.; Varela, C. E.; Dolan, E. B.; Whyte, W.; Monahan, D. S.; Payne, C. J.; Wamala, I. A.; Vasilyev, N. V.; Pigula, F. A.; Mooney, D. J.; Walsh, C. J.; Duffy, G. P.; Roche, E. T. Towards Alternative Approaches for Coupling of a Soft Robotic Sleeve to the Heart. *Ann. Biomed. Eng.* **2018**, *46* (10), 1534–1547. <https://doi.org/10.1007/s10439-018-2046-2>.
- (436) Rutkove, S. B. Effects of Temperature on Neuromuscular Electrophysiology. *Muscle Nerve* **2001**, *24* (7), 867–882. <https://doi.org/10.1002/mus.1084>.
- (437) Janssen, R. Thermal Influences on Nervous System Function. *Neurosci. Biobehav. Rev.* **1992**, *16* (3), 399–413. [https://doi.org/10.1016/S0149-7634\(05\)80209-X](https://doi.org/10.1016/S0149-7634(05)80209-X).
- (438) Borgdorff, P.; Versteeg, P. G. A. An Implantable Nerve Cooler for the Exercising Dog. *Eur. J. Appl. Physiol.* **1984**, *53* (2), 175–179. <https://doi.org/10.1007/BF00422583>.
- (439) Paggi, V.; Akouissi, O.; Micera, S.; Lacour, S. P. Compliant Peripheral Nerve Interfaces. *J. Neural Eng.* **2021**, *18* (3), 031001. <https://doi.org/10.1088/1741-2552/abcdbe>.
- (440) Jia, J.; Pollock, M. Cold Nerve Injury Is Enhanced by Intermittent Cooling. *Muscle Nerve* **1999**, *22* (12), 1644–1652. [https://doi.org/10.1002/\(SICI\)1097-4598\(199912\)22:12<1644::AID-MUS5>3.0.CO;2-F](https://doi.org/10.1002/(SICI)1097-4598(199912)22:12<1644::AID-MUS5>3.0.CO;2-F).
- (441) Tang, N.; Peng, Z.; Guo, R.; An, M.; Chen, X.; Li, X.; Yang, N.; Zang, J. Thermal Transport in Soft PAAm Hydrogels. *Polymers* **2017**, *9* (12), 688. <https://doi.org/10.3390/polym9120688>.
- (442) Chung, H. U.; Kim, B. H.; Lee, J. Y.; Lee, J.; Xie, Z.; Ibler, E. M.; Lee, K.; Banks, A.; Jeong, J. Y.; Kim, J.; Ogle, C.; Grande, D.; Yu, Y.; Jang, H.; Assem, P.; Ryu, D.; Kwak, J. W.; Namkoong, M.; Park, J. B.; Lee, Y.; Kim, D. H.; Ryu, A.; Jeong, J.; You, K.; Ji, B.; Liu, Z.; Huo, Q.; Feng, X.; Deng, Y.; Xu, Y.; Jang, K.-I.; Kim, J.; Zhang, Y.; Ghaffari, R.; Rand, C. M.; Schau, M.; Hamvas, A.; Weese-Mayer, D. E.; Huang, Y.; Lee, S. M.; Lee, C. H.; Shanbhag, N. R.; Paller, A. S.; Xu, S.; Rogers, J. A. Binodal, Wireless Epidermal Electronic Systems with in-Sensor Analytics for Neonatal Intensive Care. *Science* **2019**, *363* (6430), eaau0780. <https://doi.org/10.1126/science.aau0780>.
- (443) Nurse, E. S.; Marlow, K.; Hennessy, P. J.; Knight-Sadler, R.; Nelson, T.; Freestone, D. R.; Slater, K. D.; Cook, M. J. Water-Soluble Adhesive for Stable Long-Term Ambulatory EEG Recordings. *Clin. Neurophysiol.* **2022**, *142*, 258–261. <https://doi.org/10.1016/j.clinph.2022.07.490>.
- (444) Lee, S. M.; Kim, J. H.; Byeon, H. J.; Choi, Y. Y.; Park, K. S.; Lee, S.-H. A Capacitive, Biocompatible and Adhesive Electrode for Long-Term and Cap-Free Monitoring of EEG Signals. *J. Neural Eng.* **2013**, *10* (3), 036006. <https://doi.org/10.1088/1741-2560/10/3/036006>.
- (445) Zhang, A.; Shyam, A. B.; Cunningham, A. M.; Williams, C.; Brissenden, A.; Bartley, A.; Amsden, B.; Docoslis, A.; Kontopoulou, M.; Ameri, S. K. Adhesive Wearable Sensors for Electroencephalography from Hairy Scalp. *Adv. Healthc. Mater.* *n/a* (n/a), 2300142. <https://doi.org/10.1002/adhm.202300142>.
- (446) Wang, C.; Wang, H.; Wang, B.; Miyata, H.; Wang, Y.; Nayeem, M. O. G.; Kim, J. J.; Lee, S.; Yokota, T.; Onodera, H.; Someya, T. On-Skin Paintable Biogel for Long-Term High-Fidelity Electroencephalogram Recording. *Sci. Adv.* **2022**, *8* (20), eabo1396. <https://doi.org/10.1126/sciadv.abo1396>.
- (447) Vujic, A.; Tong, S.; Picard, R.; Maes, P. Going with Our Guts: Potentials of Wearable Electrogastrography (EGG) for Affect Detection. In *Proceedings of the 2020 International*

- Conference on Multimodal Interaction; ICMI '20; Association for Computing Machinery: New York, NY, USA, 2020; pp 260–268. <https://doi.org/10.1145/3382507.3418882>.*
- (448) Kumar, G. P.; Prakash, S. O.; Sangeetha, B.; Asha, R.; Suganthi, L.; Divya, B. Wireless Real-Time Electrogastrography Monitoring System. *J. Comput. Theor. Nanosci.* **2020**, *17* (8), 3724–3732. <https://doi.org/10.1166/jctn.2020.9268>.
- (449) Vujic, A.; Krause, C.; Tso, G.; Lin, J.; Han, B.; Maes, P. Gut-Brain Computer Interfacing (GBCI) : Wearable Monitoring of Gastric Myoelectric Activity. *Annu. Int. Conf. IEEE Eng. Med. Biol. Soc. IEEE Eng. Med. Biol. Soc. Annu. Int. Conf.* **2019**, *2019*, 5886–5889. <https://doi.org/10.1109/EMBC.2019.8856568>.
- (450) Grishin, A. A.; Moshonkina, T. R.; Solopova, I. A.; Gorodnichev, R. M.; Gerasimenko, Y. P. A Five-Channel Noninvasive Electrical Stimulator of the Spinal Cord for Rehabilitation of Patients with Severe Motor Disorders. *Biomed. Eng.* **2017**, *50* (5), 300–304. <https://doi.org/10.1007/s10527-017-9642-6>.
- (451) Kapadia, N.; Moineau, B.; Popovic, M. R. Functional Electrical Stimulation Therapy for Retraining Reaching and Grasping After Spinal Cord Injury and Stroke. *Front. Neurosci.* **2020**, *14*.
- (452) Song, J. W.; Ryu, H.; Bai, W.; Xie, Z.; Vázquez-Guardado, A.; Nandoliya, K.; Avila, R.; Lee, G.; Song, Z.; Kim, J.; Lee, M.-K.; Liu, Y.; Kim, M.; Wang, H.; Wu, Y.; Yoon, H.-J.; Kwak, S. S.; Shin, J.; Kwon, K.; Lu, W.; Chen, X.; Huang, Y.; Ameer, G. A.; Rogers, J. A. Bioresorbable, Wireless, and Battery-Free System for Electrotherapy and Impedance Sensing at Wound Sites. *Sci. Adv.* **2023**, *9* (8), eade4687. <https://doi.org/10.1126/sciadv.ade4687>.
- (453) Sel, K.; Brown, A.; Jang, H.; Krumholz, H. M.; Lu, N.; Jafari, R. A Wrist-Worn Respiration Monitoring Device Using Bio-Impedance. In *2020 42nd Annual International Conference of the IEEE Engineering in Medicine & Biology Society (EMBC); 2020; pp 3989–3993. <https://doi.org/10.1109/EMBC44109.2020.9176367>.*
- (454) Frerichs, I.; Vogt, B.; Wacker, J.; Paradiso, R.; Braun, F.; Rapin, M.; Caldani, L.; Chételat, O.; Weiler, N. Wearable Electrical Impedance Tomography for Chest Monitoring. *Eur. Respir. J.* **2020**, *56* (suppl 64). <https://doi.org/10.1183/13993003.congress-2020.1355>.
- (455) Groenendaal, W.; Lee, S.; Hoof, C. van. Wearable Bioimpedance Monitoring: Viewpoint for Application in Chronic Conditions. *JMIR Biomed. Eng.* **2021**, *6* (2), e22911. <https://doi.org/10.2196/22911>.
- (456) Wang, M.; Yang, Y.; Min, J.; Song, Y.; Tu, J.; Mukasa, D.; Ye, C.; Xu, C.; Heflin, N.; McCune, J. S.; Hsiai, T. K.; Li, Z.; Gao, W. A Wearable Electrochemical Biosensor for the Monitoring of Metabolites and Nutrients. *Nat. Biomed. Eng.* **2022**, *6* (11), 1225–1235. <https://doi.org/10.1038/s41551-022-00916-z>.
- (457) Nyein, H. Y. Y.; Bariya, M.; Tran, B.; Ahn, C. H.; Brown, B. J.; Ji, W.; Davis, N.; Javey, A. A Wearable Patch for Continuous Analysis of Thermoregulatory Sweat at Rest. *Nat. Commun.* **2021**, *12* (1), 1823. <https://doi.org/10.1038/s41467-021-22109-z>.
- (458) Kim, Y.; Prausnitz, M. R. Sensitive Sensing of Biomarkers in Interstitial Fluid. *Nat. Biomed. Eng.* **2021**, *5* (1), 3–5. <https://doi.org/10.1038/s41551-020-00679-5>.
- (459) Friedel, M.; Thompson, I. A. P.; Kasting, G.; Polsky, R.; Cunningham, D.; Soh, H. T.; Heikenfeld, J. Opportunities and Challenges in the Diagnostic Utility of Dermal Interstitial Fluid. *Nat. Biomed. Eng.* **2023**, 1–15. <https://doi.org/10.1038/s41551-022-00998-9>.

- (460) Lee, Y.; Howe, C.; Mishra, S.; Lee, D. S.; Mahmood, M.; Piper, M.; Kim, Y.; Tieu, K.; Byun, H.-S.; Coffey, J. P.; Shayan, M.; Chun, Y.; Costanzo, R. M.; Yeo, W.-H. Wireless, Intraoral Hybrid Electronics for Real-Time Quantification of Sodium Intake toward Hypertension Management. *Proc. Natl. Acad. Sci.* **2018**, *115* (21), 5377–5382. <https://doi.org/10.1073/pnas.1719573115>.
- (461) Nan, K.; Feig, V. R.; Ying, B.; Howarth, J. G.; Kang, Z.; Yang, Y.; Traverso, G. Mucosa-Interfacing Electronics. *Nat. Rev. Mater.* **2022**, *7* (11), 908–925. <https://doi.org/10.1038/s41578-022-00477-2>.
- (462) Ates, H. C.; Dincer, C. Wearable Breath Analysis. *Nat. Rev. Bioeng.* **2023**, *1* (2), 80–82. <https://doi.org/10.1038/s44222-022-00011-7>.
- (463) Chew, S. W. T.; Shah, A. H.; Zheng, M.; Chang, H.; Wiraja, C.; Steele, T. W. J.; Xu, C. A Self-adhesive Microneedle Patch with Drug Loading Capability through Swelling Effect. *Bioeng. Transl. Med.* **2020**, *5* (2). <https://doi.org/10.1002/btm2.10157>.
- (464) Waghule, T.; Singhvi, G.; Dubey, S. K.; Pandey, M. M.; Gupta, G.; Singh, M.; Dua, K. Microneedles: A Smart Approach and Increasing Potential for Transdermal Drug Delivery System. *Biomed. Pharmacother.* **2019**, *109*, 1249–1258. <https://doi.org/10.1016/j.biopha.2018.10.078>.
- (465) Cezar, C. A.; Roche, E. T.; Vandeburgh, H. H.; Duda, G. N.; Walsh, C. J.; Mooney, D. J. Biologic-Free Mechanically Induced Muscle Regeneration. *Proc. Natl. Acad. Sci.* **2016**, *113* (6), 1534–1539. <https://doi.org/10.1073/pnas.1517517113>.
- (466) Kim, J.; Salvatore, G. A.; Araki, H.; Chiarelli, A. M.; Xie, Z.; Banks, A.; Sheng, X.; Liu, Y.; Lee, J. W.; Jang, K.-I.; Heo, S. Y.; Cho, K.; Luo, H.; Zimmerman, B.; Kim, J.; Yan, L.; Feng, X.; Xu, S.; Fabiani, M.; Gratton, G.; Huang, Y.; Paik, U.; Rogers, J. A. Battery-Free, Stretchable Optoelectronic Systems for Wireless Optical Characterization of the Skin. *Sci. Adv.* **2016**, *2* (8), e1600418. <https://doi.org/10.1126/sciadv.1600418>.
- (467) Kim, J.; Gutruf, P.; Chiarelli, A. M.; Heo, S. Y.; Cho, K.; Xie, Z.; Banks, A.; Han, S.; Jang, K.-I.; Lee, J. W.; Lee, K.-T.; Feng, X.; Huang, Y.; Fabiani, M.; Gratton, G.; Paik, U.; Rogers, J. A. Miniaturized Battery-Free Wireless Systems for Wearable Pulse Oximetry. *Adv. Funct. Mater.* **2017**, *27* (1), 1604373. <https://doi.org/10.1002/adfm.201604373>.
- (468) Kim, A.; Zhou, J.; Samaddar, S.; Song, S. H.; Elzey, B. D.; Thompson, D. H.; Ziaie, B. An Implantable Ultrasonically-Powered Micro-Light-Source (μ Light) for Photodynamic Therapy. *Sci. Rep.* **2019**, *9* (1), 1395. <https://doi.org/10.1038/s41598-019-38554-2>.
- (469) Attili, S. K.; Lesar, A.; McNeill, A.; Camacho-Lopez, M.; Moseley, H.; Ibbotson, S.; Samuel, I. D. W.; Ferguson, J. An Open Pilot Study of Ambulatory Photodynamic Therapy Using a Wearable Low-irradiance Organic Light-emitting Diode Light Source in the Treatment of Nonmelanoma Skin Cancer. *Br. J. Dermatol.* **2009**, *161* (1), 170–173. <https://doi.org/10.1111/j.1365-2133.2009.09096.x>.
- (470) Jeong, H.; Yoo, J.-Y.; Ouyang, W.; Greane, A. L. J. X.; Wiebe, A. J.; Huang, I.; Lee, Y. J.; Lee, J. Y.; Kim, J.; Ni, X.; Kim, S.; Huynh, H. L.-T.; Zhong, I.; Chin, Y. X.; Gu, J.; Johnson, A. M.; Brancaccio, T.; Rogers, J. A. Closed-Loop Network of Skin-Interfaced Wireless Devices for Quantifying Vocal Fatigue and Providing User Feedback. *Proc. Natl. Acad. Sci.* **2023**, *120* (9), e2219394120. <https://doi.org/10.1073/pnas.2219394120>.
- (471) Shin, J.; Wang, H.; Kwon, K.; Ostojich, D.; Christiansen, Z.; Berkovich, J.; Park, Y.; Li, Z.; Lee, G.; Nasif, R.; Chung, T. S.; Su, C.-J.; Lim, J.; Kubota, H.; Ikoma, A.; Lu, Y.-A.; Lin, D. H.; Xu, S.; Banks, A.; Chang, J.-K.; Rogers, J. A. Wireless, Soft Sensors of Skin

- Hydration with Designs Optimized for Rapid, Accurate Diagnostics of Dermatological Health. *Adv. Healthc. Mater.* **2023**, *12* (4), 2202021.
<https://doi.org/10.1002/adhm.202202021>.
- (472) Sawyer, D. An Introduction to Human Factors in Medical Devices.
- (473) Amended Final Report on the Safety Assessment of Polyacrylamide and Acrylamide Residues in Cosmetics. *Int. J. Toxicol.* **2005**, *24 Suppl 2*, 21–50.
<https://doi.org/10.1080/10915810590953842>.
- (474) Harrington, R. E.; Guda, T.; Lambert, B.; Martin, J. 3.1.4 - Sterilization and Disinfection of Biomaterials for Medical Devices. In *Biomaterials Science (Fourth Edition)*; Wagner, W. R., Sakiyama-Elbert, S. E., Zhang, G., Yaszemski, M. J., Eds.; Academic Press, 2020; pp 1431–1446. <https://doi.org/10.1016/B978-0-12-816137-1.00091-X>.
- (475) Zhang, X.; Fevre, M.; Jones, G. O.; Waymouth, R. M. Catalysis as an Enabling Science for Sustainable Polymers. *Chem. Rev.* **2018**, *118* (2), 839–885.
<https://doi.org/10.1021/acs.chemrev.7b00329>.
- (476) Horváth, I. T. Introduction: Sustainable Chemistry. *Chem. Rev.* **2018**, *118* (2), 369–371.
<https://doi.org/10.1021/acs.chemrev.7b00721>.
- (477) Biswal, T.; BadJena, S. K.; Pradhan, D. Sustainable Biomaterials and Their Applications: A Short Review. *Mater. Today Proc.* **2020**, *30*, 274–282.
<https://doi.org/10.1016/j.matpr.2020.01.437>.
- (478) Jarach, N.; Dodiuk, H. Debondable, Recyclable and/or Biodegradable Naturally-Based Adhesives. In *Biobased Adhesives*; John Wiley & Sons, Ltd, 2023; pp 427–461.
<https://doi.org/10.1002/9781394175406.ch15>.
- (479) Liu, Y.; Li, H.; Feng, Q.; Su, H.; Li, D.; Shang, Y.; Chen, H.; Li, B.; Dong, H. A Three-Dimensional-Printed Recyclable, Flexible, and Wearable Device for Visualized UV, Temperature, and Sweat pH Sensing. *ACS Omega* **2022**, *7* (11), 9834–9845.
<https://doi.org/10.1021/acsomega.2c00128>.
- (480) Kostag, M.; El Seoud, O. A. Sustainable Biomaterials Based on Cellulose, Chitin and Chitosan Composites - A Review. *Carbohydr. Polym. Technol. Appl.* **2021**, *2*, 100079.
<https://doi.org/10.1016/j.carpta.2021.100079>.